MODELING OF MOLECULAR AND PARTICULATE TRANSPORT IN DRY SPENT NUCLEAR FUEL CANISTERS

A Dissertation

Presented to

the Faculty of the Graduate School

University of Missouri-Columbia

In Partial Fulfillment

of the Requirements for the Degree

Doctor of Philosophy

---

by

ANDREW M. CASELLA

Dr. Sudarshan K. Loyalka — Dissertation Supervisors

Dr. Brady D. Hanson

AUGUST 2007

The undersigned, appointed by the Dean of the Graduate School, have examined the dissertation entitled

MODELING OF MOLECULAR AND PARTICULATE TRANSPORT

IN DRY SPENT NUCLEAR FUEL CANISTERS

presented by ANDREW M. CASELLA

a candidate for the degree of Doctor of Philosophy in Nuclear Engineering

and hereby certify that in their opinion it is worthy of acceptance.

_____

Dr. Sudarshan K. Loyalka

_____

Dr. Brady D. Hanson

_____

Dr. Paul C.H. Chan

_____

Dr. Tushar K. Ghosh

_____

Dr. Mark A. Prelas

_____

Dr. Robert V. Tompson

ACKNOWLEDGEMENTS

This research was performed while I was under appointment to the U.S. Department of Energy Nuclear Engineering and Health Physics Fellowship Program sponsored by the U.S. Department of Energy's Office of Nuclear Energy, Science, and Technology. Additional support was provided through a G. Ellsworth Huggins Fellowship from the University of Missouri and graduate scholarships from the American Nuclear Society. The support provided by these sources allowed me to fully focus on my studies. For this, I am very grateful.

I am indebted to my thesis supervisors Dr. Sudarshan K. Loyalka of the University of Missouri-Columbia and Dr. Brady D. Hanson of Pacific Northwest National Laboratory (PNNL) for their guidance throughout the development of this thesis. I also owe a great deal of gratitude to the additional members of my thesis committee, the staff members of the Nuclear Science and Engineering Institute, and the staff members at PNNL that provided help when needed.

Whatever professional or academic endeavor one undertakes in life is always much easier when things are running smoothly away from the office. I was fortunate enough to enjoy continuous support throughout my doctoral studies from my family and from my wonderful bride-to-be, Amanda. Certainly, if everyone enjoyed such support, the world would be a much better place.

TABLE OF CONTENTS

LIST OF FIGURES

LIST OF TABLES

ABSTRACT

The transportation and storage of spent nuclear fuel is one of the prominent issues facing the commercial nuclear industry today, as there is still no general consensus regarding the near- and long-term strategy for managing the back-end of the nuclear fuel cycle. The debate continues over whether the fuel cycle should remain open, in which case spent fuel will be stored at on-site reactor facilities, interim facilities, or a geologic repository; or if the fuel cycle should be closed, in which case spent fuel will be recycled.

Currently, commercial spent nuclear fuel is stored at on-site reactor facilities either in pools or in dry storage containers. Increasingly, spent fuel is being moved to dry storage containers due to decreased costs relative to pools. As the number of dry spent fuel containers increases and the roles they play in the nuclear fuel cycle increase, more regulations will be enacted to ensure that they function properly. Accordingly, they will have to be carefully analyzed for normal conditions, as well as any off-normal conditions of concern. This thesis addresses the phenomena associated with one such concern; the formation of a microscopic through-wall breach in a dry storage container. Particular emphasis is placed on the depressurization of the canister, release of radioactivity, and plugging of the breach due to deposition of suspended particulates.

The depressurization of a dry storage container upon the formation of a breach depends on the temperature and quantity of the fill gas, the pressure differential across the breach, and the size of the breach. The first model constructed in this thesis is capable of determining the depressurization time for a breached container as long as the associated parameters just identified allow for laminar flow through the breach. The

parameters can be manipulated to quantitatively determine their effect on depressurization. This model is expanded to account for the presence of suspended particles. If these particles are transported with the fill gas into the breach, they may be deposited, leading to a restriction of flow and eventually to the plugging of the breach. This model uses an analytical solution to the problem of particle deposition in convective-diffusive fully-developed laminar flow through a straight cylindrical tube. Since the cylindrical flow geometry is a requirement for the use of this equation, it is assumed that all deposited particles are distributed uniformly both axially and circumferentially along the breach. The model is capable of monitoring the pressure, temperature, quantity of fill gas, breach radius, particle transmission fraction, and flow velocity through the breach as functions of time.

The depressurization time can be significantly affected by the release of fission gases or helium generated from alpha decay if the cladding of a fuel rod within the canister is breached. To better quantify this phenomenon, a Monte Carlo model of molecular transport through nano-scale flow pathways in the spent fuel is developed in this thesis. This model is applied to cylindrical, conical, elliptical, and helical pathways.

Finally, in order to remove some of the restrictions of the model of canister depressurization accounting for suspended particles, a Monte Carlo program was written to model the movement of particles through the breach. This program is capable of accounting for any transport mechanism specified but is focused in this work on laminar convective-diffusive flow. Each test particle is tracked as it is carried through the breach and if it impacts the breach wall, the three-dimensional location of the impact is recorded. In this way, the axial and circumferential deposition patterns can be recorded. This

program can model any flow geometry as long as a velocity profile can be provided. In this thesis, the program is expanded to account for flow through straight and torroidal cylindrical tubes.

CHAPTER 1: INTRODUCTION

When spent fuel is removed from a commercial nuclear reactor core, it is immediately transferred to a pool where decay heat from short-lived fission products can be transported away by the water. Each commercial reactor in the U.S. has a spent fuel storage pool that was constructed at the same time as the reactor itself. These pools were designed to accommodate a relatively small amount of spent fuel since those designing the pools believed that the spent fuel would soon be taken to another facility for reprocessing. However, commercial reprocessing in the U.S. was not pursued and attention was instead focused on the construction of a geological repository where the spent fuel could be transported after a short cooling period in the storage pools. The construction and opening of this repository is described in the Nuclear Waste Policy Act of 1982 [1.1]. However, the opening of this repository has been delayed significantly. While work toward opening the repository has continued, the U.S. government has recently announced that reprocessing of commercial spent nuclear fuel is to be reconsidered as part of the Global Nuclear Energy Partnership (GNEP) [1.2].

As the debate over repositories and reprocessing continues, spent fuel inventories at commercial nuclear plants are growing. The space in storage pools for these inventories is diminishing and utilities are being forced to develop new ways to store their spent fuel. According to the National Research Council, "In 2000, the nuclear power industry projected that roughly three or four plants per year would run out of needed storage space in their pools without additional interim storage capacity [1.3]." The current solution to this problem has been to construct Independent Spent Fuel

Storage Installations (ISFSI) where spent fuel is stored in additional pools or in dry storage containers. The majority of these ISFSI are storing spent fuel in dry containers due to the reduced cost relative to pools. Currently, 4500 metric tones of uranium (MTU) are in storage at 22 sites with operating commercial nuclear power reactors, and 1700 MTU are in storage at 6 sites where commercial reactors are no longer operating [1.3].

Regardless of what decisions are made relating to the ultimate disposition of spent nuclear fuel, it is evident that it will be spending some time in dry storage containers. For the purpose of this work, a dry storage container is defined as a metal cask in which intact spent fuel assemblies are contained under a pressurized, inert fill gas. When the geologic repository opens, the spent fuel will be transported in shipping casks and stored in waste packages, both of which will be dry storage containers as defined above. If GNEP reaches fruition, spent fuel assemblies will need to be transported to a reprocessing facility and temporarily stored. In this scenario, the transportation and the storage will be in dry storage containers. Until either of these options is realized, the spent fuel will need to be stored in dry storage containers at ISFSI.

Since dry storage containers are to play an integral role in whatever future fuel cycle is chosen, it is necessary to analyze them for normal and off-normal conditions. Under any conditions, these containers must be able to contain the radioactivity housed within them. The possible release of radioactivity from nuclear facilities and nuclear material containers has been of concern since the beginning of the nuclear era. In order to deal with this concern, a system for determining the effect of various types of radiation on biological systems has been developed. This system assigns two values, A_1 and A_2, to each radioisotope based on the radiological consequences that that radioisotope might

have on biological systems if it is released to the environment. These two values are the limits for non-dispersible and dispersible materials, respectively, that can be placed in a nuclear material transport package. The process for determining each of these values for a given radioisotope is given in the International Atomic Energy Agency (IAEA) safety series No. 7 [1.4]. Tables of these values are located in the current IAEA safety standards [1.5] and in the Appendix of 10CFR71 [1.6]. Although these values are determined for limits in transport casks, they are useful in determining ways to engineer spent fuel containers that minimize the possible impact of the materials that they contain on the environment.

There are essentially three factors to consider when determining the importance of a given radionuclide in the total threat to the environment from a breached dry storage container. The first of these is the activity of the radionuclide, the second is the A_2 value of the radionuclide as described above, and the third is the chemical class of the radionuclide. The chemical class of a radionuclide is described in NUREG/CR-6672 [1.7]. What is meant by the chemical form of the radionuclide can be most easily explained by the case of ruthenium. Normally, ruthenium exists as RuO_2, but when exposed to oxygen, it can be transformed to RuO_3 or RuO_4 which are much more volatile. Essentially, the form determines the mobility of the radionuclide and thus its propensity for dispersion and eventual release. The A_2 value of a radionuclide is constant over time and thus this portion of the threat posed from a given radionuclide can be assessed for the lifetime of the dry storage container. However, as a radionuclide decays over time, its activity declines. Also, the form of a radionuclide may vary for different conditions. So,

the total importance of the radionuclide must be determined over time and for given physical conditions.

The activities that can be expected from each radionuclide within the dry storage container are shown in Table 1.1 which is a copy of a table from NUREG/CR-6672 [1.7]. The activity for each radionuclide presented in Table 1.1 was generated with the ORIGEN2 code [1.8, 1.9], which can calculate the activities for over 800 radionuclides. The most important of these radionuclides to consider are those that have a high activity to A_2 ratio. NUREG/CR-6672 utilized the RADSEL code [1.10] to determine these ratios. The radionuclides included in Table 1.1 are those determined to have the highest activity to A_2 ratios three years after discharge from the reactor.

Table 1.1. Generic High Burnup, Three-Year Cooled, Fuel Assembly Inventories for RADTRAN Calculations (Ci/assembly) [1.7]

Generic BWR Assembly	
Nuclide	**Amount (Ci)**
Co-60	6.40e+01
Kr-85	1.74e+03
Sr-90	1.59e+04
Y-90	1.59e+04
Ru-106	1.42e+04
Cs-134	2.15e+04
Cs-137	2.59e+04
Ce-144	1.03e+04
Pm-147	8.49e+03
Pu-238	1.67e+03
Pu-239	7.44e+01
Pu-240	1.36e+02
Pu-241	2.91e+04
Am-241	2.05e+02
Am-242M	8.09e+00
Am-243	1.22e+01
Cm-242	1.82e+02
Cm-243	1.42e+01
Cm-244	2.95e+03

Generic PWR Assembly	
Nuclide	**Amount (Ci)**
Co-60	5.78e+01
Kr-85	1.74e+03
Sr-90	5.36e+04
Y-90	5.36e+04
Ru-106	4.43e+04
Cs-134	6.99e+04
Cs-137	7.90e+04
Ce-144	3.87e+04
Pm-147	2.58e+04
Eu-154	8.42e+03
Pu-238	4.81e+03
Pu-239	2.14e+02
Pu-240	4.28e+02
Pu-241	6.52e+04
Am-241	4.36e+02
Am-242M	1.33e+01
Am-243	2.51e+01
Cm-242	3.76e+02
Cm-243	2.88e+01
Cm-244	5.62e+03

In order to associate the A_2 values of the radionuclides presented in Table 1.1, Table 1.2 was compiled from the values listed in the appendix of 10CFR71 [1.6]. Officially, these A_2 values are determined in Terebecquerels, but they are presented in Curies in Table 1.2 in order to remain consistent with Table 1.1. The A_2 value is a limit so the smaller the value, the larger the effect of the associated radionuclide.

Table 1.2. A_2 Values Associated with Table 1.1

Radionuclide	A_2 (Ci)
Co-60	11
Kr-85	270
Sr-90	8.1
Y-90	8.1
Ru-106	5.4
Cs-134	19
Cs-137	16
Ce-144	5.4
Pm-147	54
Eu-154	16
Pu-238	0.027
Pu-239	0.027
Pu-240	0.027
Pu-241	1.6
Am-241	0.027
Am-242m	0.027
Am-243	0.027
Cm-242	0.27
Cm-243	0.027
Cm-244	0.054

From the data in Tables 1.1 and 1.2, a good understanding can be gained of the important radionuclides in the spent fuel and their relative threat to the environment if released. The remaining piece of information to be addressed is the chemical class into which each radionuclide is placed. There are five chemical classes: Noble (non-condensable) gases, condensable gases, single element group, fission products found in Chalk River Unidentified Deposits (CRUD), and all other fission products. The only

non-condensable gas in that appears in Table 1.1 is Kr-85. The only condensable gases that appear in Table 1.1 are Cs-134 and Cs-137. As the class "single element group" suggests, it contains only one element, ruthenium. As discussed earlier, the volatility of this element depends on the degree to which it has been oxidized. The vast majority of the activity in CRUD is due to Co-60, and thus the only element that appears in Table 1.1 that is in the "fission products found in CRUD" class is Co-60. The Co-60 exists in the CRUD in a particulate form. The rest of the radionuclides that appear in Table 1.1 are in the "all other fission products" class and exist in particulate form. This demonstrates that the vast majority of the radioactivity within the dry storage container is in particulate form. Thus, if a large release of radioactivity to the environment is to occur, then this radioactivity must be released in the form of particulates.

The many scenarios in which particulates can escape from the dry storage container are classified into two categories. These categories are catastrophic releases and long-term releases. In the catastrophic case, the dry storage container sustains a massive breach through a dramatic external event such as an explosion or a physical collision. In this case, the situation will most likely be observed and dealt with relatively quickly. In the long-term case, the dry storage container sustains a microscopic breach through which small amounts of fill gas and any associated radioactivity can be released slowly. Such cases can be caused by faulty seals or welds. In addition, they may be created through relatively minor physical impacts, chemical corrosion, or stress-crack corrosion. The focus of this thesis will be on the release of particulate radioactivity through such breaches regardless of their source of formation.

Due to the nature of the system, there are two fundamental phenomena that will be investigated in this work. These phenomena are cask depressurization and particle release. Cask depressurization is important because it is the fundamental mechanism through which suspended particulates can be transported from the cask. The effect of this phenomenon depends on the physical conditions within the dry storage cask.

When the spent fuel is removed from the storage pool, it is vacuum dried and transferred to a dry storage cask. The dry storage cask is then backfilled with an inert gas such as nitrogen or helium, and sealed with welds or bolts. Immediately, the temperature of the backfill gas begins to rise due to the decay heat from the spent fuel. Since the volume is constant, this leads to an increase in pressure within the container. Even if the breach forms immediately with a faulty seal or weld, the pressure within the container will be higher than the atmospheric pressure outside of the container. This high pressure will act to push the backfill gas from the container. This is a negative effect in the sense that any radioactivity suspended in the backfill gas will be released from the container. However, there is a positive effect associated with this effect because the flow from the container prevents the diffusion of oxygen from the atmosphere into the container. Thus, if particulates are present in the backfill gas, the main concern associated with the breach formation is the release of radioactivity to the environment. If particulates are not present, then the main concern is the depressurization time of the cask over which an inert atmosphere can be maintained within the container. Once the container has been depressurized, then oxygen can begin to diffuse through the breach into the container. As the decay heat from the spent fuel decreases with time, the temperature and thus the pressure within the container will decrease as well. This can lead to convective flow of

oxygen into the container, leading to oxidation of fuel rod cladding and any exposed fuel. This oxidation can transform radionuclides into more mobile forms. Accordingly, this work is dedicated to the depressurization of a dry storage container with a microscopic breach and the release of associated particulate activity.

The thesis is organized into 9 chapters. Chapter 2 is dedicated to physically characterizing modern spent fuel storage systems. An analysis of the time-dependent thermal conditions within spent fuel canisters is provided in Chapter 3. Chapter 4 provides a model of the depressurization time of a canister in which no particulates are suspended and compares the results of this model with an existing model. Chapter 5 presents an analysis of the source terms of radioactivity within a spent fuel canister. A Monte Carlo model for characterizing helium flow through nano-scale cracks in the spent fuel rods is described in Chapter 6. In Chapter 7, the depressurization model of Chapter 4 is expanded to account for the particulate release through and deposition within a breach. The focus of Chapter 8 is a Monte Carlo model of particulate motion that removes several of the limitations of the model described in Chapter 7. Finally, Chapter 9 concludes this thesis and provides several suggestions for future work.

REFERENCES

1.1 Nuclear Waste Policy Act of 1982. Pub. L. 97-425 (1/7/1983).

1.2 Global Nuclear Energy Partnership, <http://www.gnep.energy.gov/> (9/01/2006).

1.3 National Research Council of the National Academies, "Safety and Security of Commercial Spent Nuclear Fuel Storage" (2006).

1.4 IAEA safety series No. 7, "Explanatory Material for the IAEA Regulations for the Safe Transport of Radioactive Material (1985 Edition) 2nd Ed., International Atomic Energy Agency, Vienna (1987).

1.5 IAEA Safety Standards for protecting people and the environment, "Regulations for the Safe Transport of Radioactive Material 2005 Edition," Safety Requirements No. TS-R-1, International Atomic Energy Agency, Vienna (2005).

1.6 10CFR71. Packaging and Transportation of Radioactive Material. Appendix A. Determination of A_1 and A_2. <http://www.nrc.gov/reading-rm/doc-collections/cfr/part071/> (6/23/2007).

1.7 Sprung, J. L., et al., "Reexamination of Spent Fuel Shipment Risk Estimates," NUREG/CR-6672, Vols. 1,2 SAND2000-0234 (3/2000).

1.8 Croff, A.G., "A User's Manual for the ORIGEN2 Computer Code," ORNL/TM-7175 (7/1980).

1.9 Croff, A.G., "ORIGEN2: A Versatile Computer Code for Calculating the Nuclide Compositions and Characteristics of Nuclear Materials," *Nuclear Technology*, 62, (9/1983), p. 335.

1.10 RADSEL, unpublished Sandia code, available upon request.

CHAPTER 2: DESCRIPTION OF COMMERCIAL DRY STORAGE SYSTEMS

The main physical container that is used in dry storage of spent nuclear fuel is referred to as a "cask". Inside this cask, there is a matrix of axially oriented dividers known as a "basket". This basket forms a grid that divides the volume of the cask into individual spaces for spent fuel assemblies. Although nearly all current dry storage technologies share these general characteristics, there are several different competing designs. Current spent fuel dry storage technologies are divided into two categories. These categories are bare-fuel casks and canister-based casks. In bare-fuel casks, complete spent fuel assemblies including the fuel and cladding are placed directly into a basket that is part of the cask itself. In canister-based casks, the spent fuel assemblies are placed into a basket that is physically part of the metal canister. This canister/basket system is placed into an "overpack" which completes the cask system. A lid is welded onto the canister and the lid of the overpack into which the closed canister is placed is secured with bolts. Since the canister-based cask conforms more accurately to the definition of a dry storage container presented in Chapter 1, it will be the focus of the work in this thesis.

Spent fuel casks can be classified by their intended use as well. In this scheme, a dry storage cask is categorized as a single-purpose, a dual-purpose, or a multi-purpose cask. A single-purpose cask is only licensed for spent fuel storage, a dual-purpose cask is licensed for storage and transportation, and a multi-purpose cask is licensed for storage, transportation, and geologic disposal. Currently, there are no multi-purpose casks on the

market [2.1]. However, the relatively recently proposed Transportation, Aging, and Disposal canister-based system will be classified as such when it comes into use [2.2].

As was mentioned in Chapter 1, spent fuel is increasingly transported to independent fuel storage installations (ISFSIs). An ISFSI is defined as, "…a complex designed and constructed for the interim storage of spent nuclear fuel, solid reactor-related GTCC waste, and other radioactive materials associated with spent fuel and reactor related GTCC waste storage" [2.3]. In this definition, the acronym GTCC refers to "greater than class C" waste. "Class C waste is waste that not only must meet more rigorous requirements on waste form to ensure stability but also requires additional measures at the disposal facility to protect against inadvertent intrusion. The physical form and characteristics of Class C waste must meet both the minimum and stability requirements set forth in § 61.56" [2.4]. One can continue to investigate these definitions created by the Nuclear Regulatory Commission (NRC) for further detail, but for the current purposes, any site where a spent fuel dry storage system is located will be defined as an ISFSI.

According to the NRC, as of August 2006, spent nuclear fuel was stored in dry storage at ISFSIs at 27 sites with general licenses and 15 sites with site-specific licenses [2.5]. Figure 2.1 shows the locations of these sites. Under a general license for storing spent nuclear fuel in dry storage, a nuclear power plant licensee is authorized to store spent fuel in NRC-approved casks at a site that is licensed to operate a nuclear power reactor. If spent fuel is to be stored at a location other than a site licensed to operate a nuclear power reactor, a site-specific license must be sought. In order to grant a site-specific license, the NRC must do a complete safety analysis of the ISFSI [2.6]. There

are numerous vendors that manufacture dry storage systems, but only a few designs from these vendors have been approved for use. Table 2.1 lists the designs that have been approved by the NRC for general use as of August 7, 2006 [2.7].

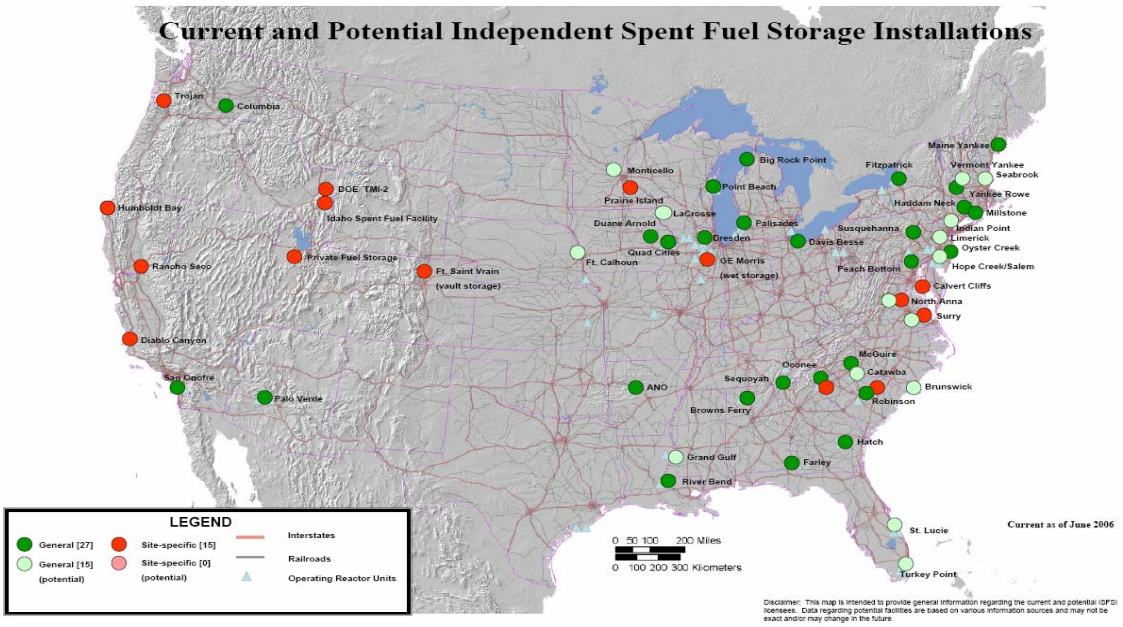

Figure 2.1: U.S. ISFSI Locations as of June 2006 [2.4]

Table 2.1: Dry Storage Systems Approved for General Use

Vendor	Storage Design Model	Certificate of Compliance Issue Date
BNG Fuel Solutions Corp.	VSC-24	5/7/1993
	FuelSolutions	2/15/2001
General Nuclear Systems, Inc.	CASTOR V/21	8/17/1990
Holtec International	HI-STAR 100	10/4/1999
	HI-STORM 100	6/1/2000
NAC International, Inc.	NAC S/T	8/17/1990
	NAC-C28 S/T	8/17/1990
	NAC-UMS	11/20/2000
	NAC-MPC	4/10/2000
Transnuclear, Inc.	NUHOMS-24P	1/23/1995
	NUHOMS-52B	1/23/1995
	NUHOMS-61BT	1/23/1995
	NUHOMS-32PT	1/23/1995
	NUHOMS-24PHB	1/23/1995
	NUHOMS-24PTH	1/23/1995
	TN-32	4/19/2000
	TN-68	5/28/2000
	Advanced NUHOMS-24PT1	2/5/2003

In addition to systems that have been approved for general use, several systems have been approved for use at specific sites. The business of manufacturing and vending dry storage systems for spent nuclear fuel has been very dynamic. Several venders have merged or changed companies over the past few years. In addition, the variety of designs to handle spent fuel of various sizes and characteristics has steadily increased. Although there appears to be a growing diversity in the designs of storage systems, the overall design is fairly uniform. Thus, we will be considering a generic case and the implications of deviating from this case. As can be seen in Table 2.1, a large portion of the available designs that have received a general license are produced by Transnuclear. For this reason, we will base our generic container on parameters associated with one of their

designs. Figure 2.2 is a schematic of one such design, the Transnuclear NUHOMS®-32PT Dry Shielded Canister (DSC) components [2.8].

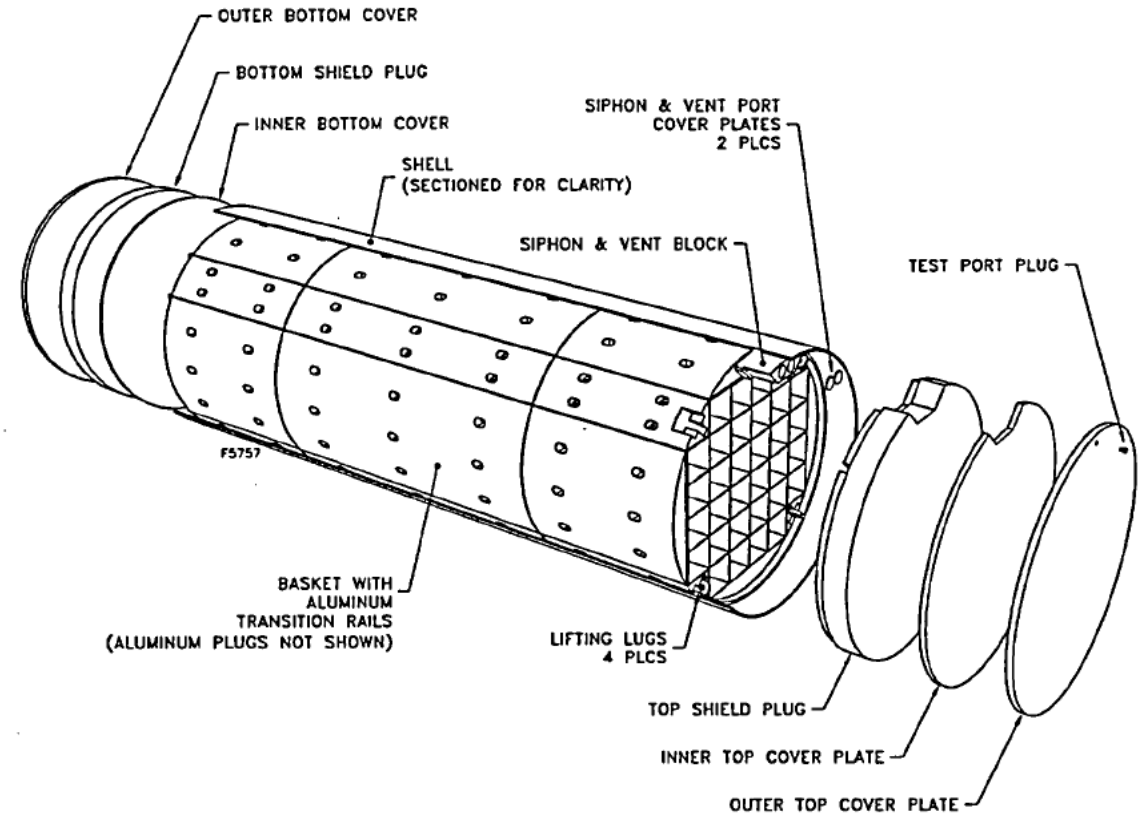

Figure 2.2: NUHOMS®-32PT DSC Components [2.8]

Figure 2.3 is a schematic of the Transnuclear NUHOMS®-24PT2 DSC components [2.9]. Figures 2.2 and 2.3 provide a good visualization of the basic design characteristics associated with dry storage containers. Figure 2.2 shows the overall structure of the container including the basket grid into which the assemblies are placed. Figure 2.3 shows that the container is not solid and gives a better understanding of the thicknesses that should be used to describe breaches considered in the latter sections of this thesis.

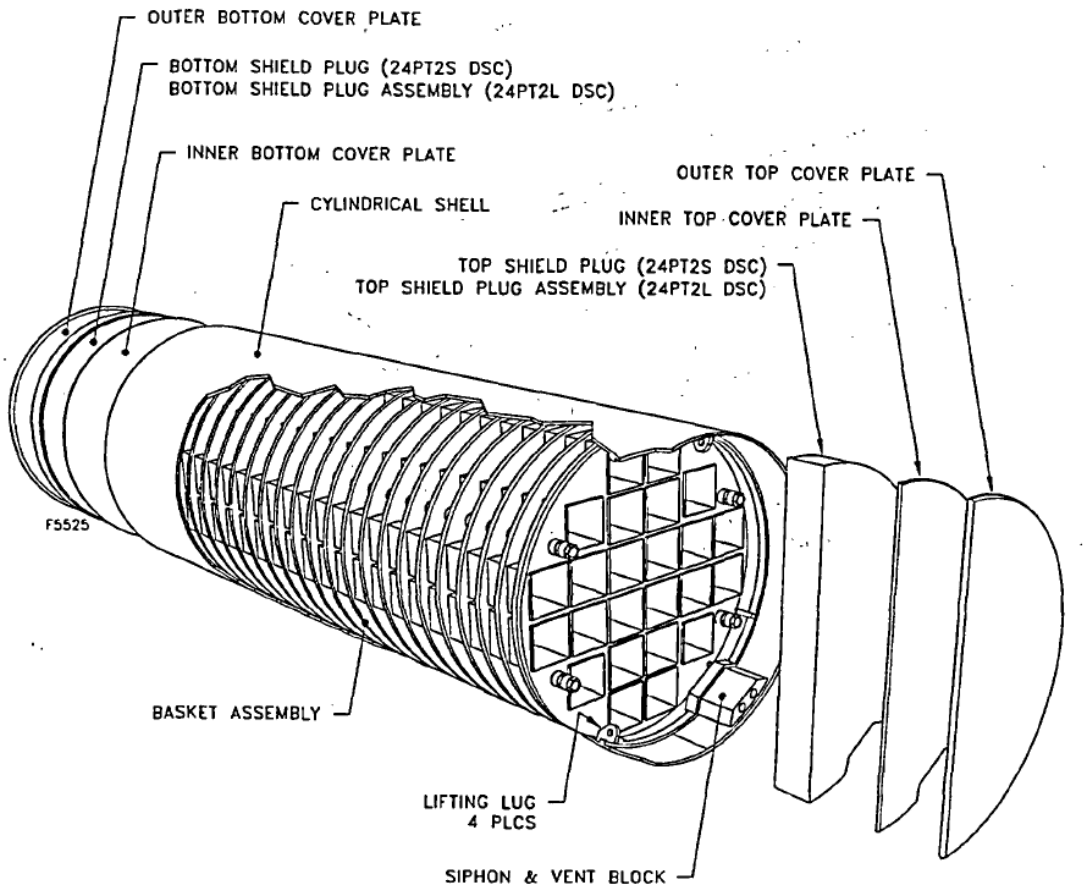

Figure 2.3: NUHOMS®-24PT2 DSC Components [2.9]

Notice in Fig. 2.2 and Fig. 2.3 that the number and the size of the spaces within the basket vary. This is a common design specification that is changed to adequately accommodate fuel from different reactors. For example, fuel from a boiling water reactor (BWR) differs in size and decay heat generation compared to fuel from a pressurized water reactor (PWR). Another design parameter that is commonly varied is the length of the container. Figure 2.4 shows a cross section of a NUHOMS®-24P DSC [2.8]. Notice by comparison to Fig. 2.3 that the space between the guide sleeves of the basket and the canister shell is open space except for the presence of a periodic structural plate.

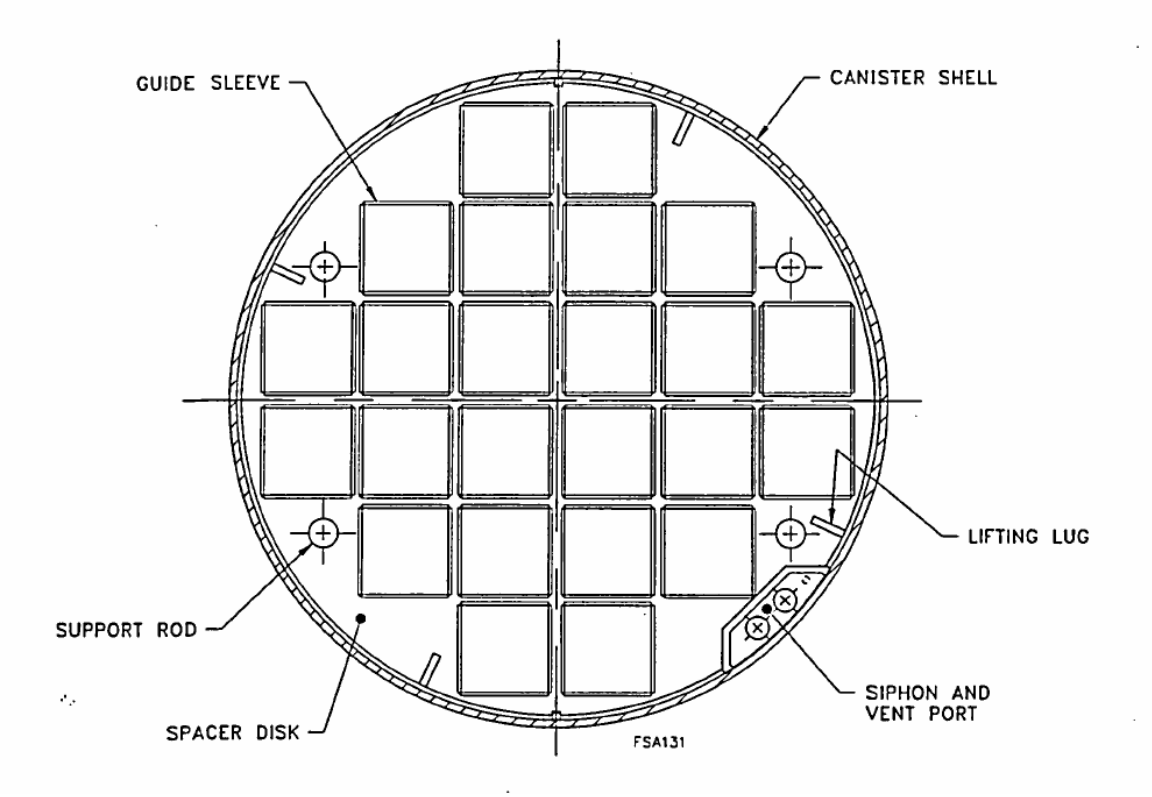

Figure 2.4: NUHOMS®-24P Dry Shielded Canister Cross Section [2.8]

As stated earlier in this chapter, spent fuel dry storage systems are arranged into two categories, bare-fuel casks and canister-based casks. The NUHOMS® systems that are displayed in Fig. 2.2 through Fig. 2.4 are in the canister-based cask category. This means that these canisters are to be placed into an "overpack" known as a horizontal storage module (HSM). In the case of the NUHOMS® systems, this overpack is mostly composed of concrete. A schematic of the overpack used in the NUHOMS® system is displayed in Fig. 2.5 [2.9]. Although the HSM provides additional containment, it is appropriate to discuss leaks through the DSC's discussed above and neglect leakage through the overpack. This is due to the fact that in order to facilitate heat transfer, air is allowed to flow between the DSC and the overpack. It is possible that any particulates

leaving through the DSC will stick to the overpack and not be released to the outer environment, but that situation will not be considered in this analysis. Instead, this work will focus on the release of the radioactive particulates from the DSC's themselves.

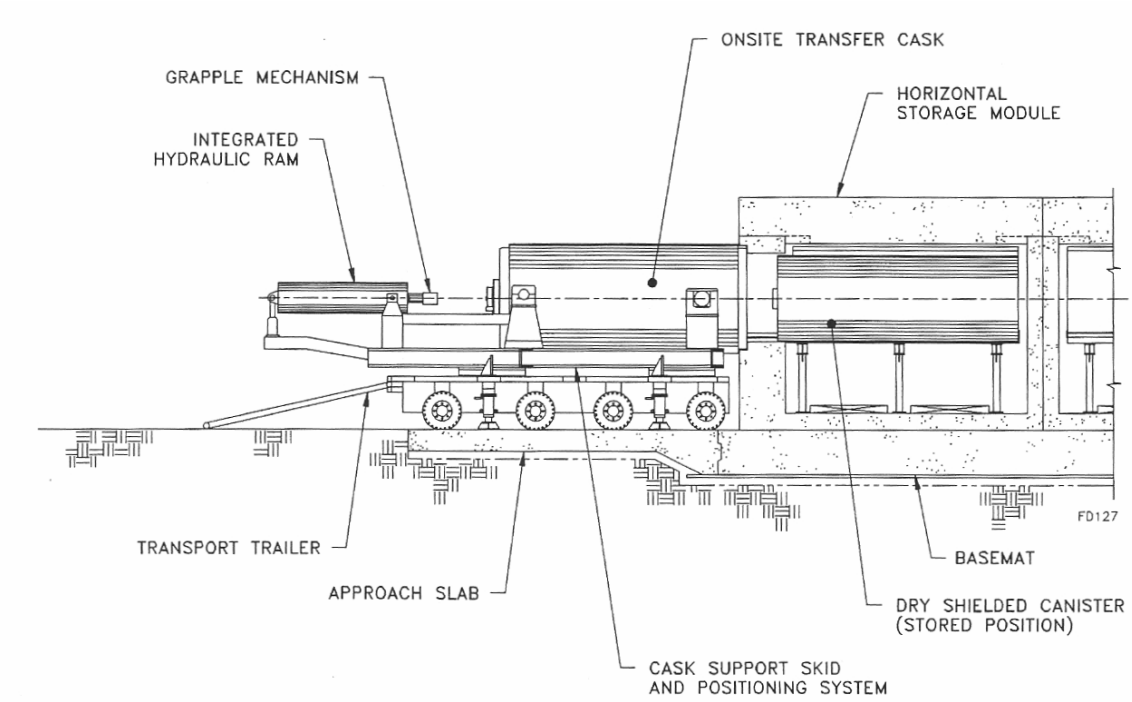

Figure 2.5: NUHOMS® Schematic including the Overpack [2.8]

Another important characteristic to be considered is the orientation of the spent fuel storage systems. In the case of NUHOMS® systems, the DSC's are stored in horizontal positions. This is important because it affects the heat transfer properties within the DSC. Since there is very little vertical displacement within the horizontally oriented systems, the effects of convection are minimal. Thus, heat transfer within the DSC's is limited to conduction and thermal radiation. There are several designs however that offer vertical storage orientations, including the Transnuclear TN-32 and TN-68.

Virtually all canister-based dry storage containers have the same characteristics as those presented above. They consist of a steel cylinder in which a basket is placed to support and separate the spent fuel assemblies. This cylinder is placed in an overpack, but there is air between the container and the overpack for the purpose of heat transfer. Thus, the figures and systems listed and described in this chapter will be referred to in future analysis of dry storage systems.

REFERENCES

2.1 National Research Council of the National Academies, "Safety and Security of Commercial Spent Nuclear fuel Storage" (2006).

2.2 Zabransky, D.K., "Preliminary Transportation, Aging, and Disposal Canister System Performance Specification, Revision B," DOE/RW-0585, WMO-TADCS-0000001 (11/ 2006).

2.3 10CFR72.3, "Licensing Requirements for the Independent Storage of Spent Nuclear Fuel, High-Level Radioactive Waste, and Reactor-Related Greater Than Class C Waste," <http://www.nrc.gov/reading-rm/doc-collections/cfr/part072/> (6/23/2007).

2.4 10CFR61.55, "Licensing Requirements for Land Disposal of Radioactive Waste," <http://www.nrc.gov/reading-rm/doc-collections/cfr/part061/> (6/23/2007).

2.5 <http://www.nrc.gov/reading-rm/doc-collections/fact-sheets/dry-cask-storage.html> (9/12/2006).

2.6 <http://www.nrc.gov/waste/spent-fuel-storage/licensing.html#site> (9/12/2006).

2.7 <http://www.nrc.gov/waste/spent-fuel-storage/designs.html> (9/01/2006).

2.8 Standardized NUHOMS® Horizontal Modular Storage System for Irradiated Nuclear Fuel, Final Safety Analysis Report (6/2004).

2.9 Johnson, E.R., Saverot, P.M., "Monograph of Spent Nuclear Fuel Storage Technologies," Institute of Nuclear Materials Management (3/1997).

CHAPTER 3: THERMAL ANALYSIS

To some extent, the behavior of particulates within the spent fuel container is determined by the characteristics of the particulates themselves. However, the physical conditions within the container play an appreciable role as well. These physical conditions can be characterized upon determination of the heat distribution throughout the container. The first step in determining the heat distribution is to assess the rate at which heat is generated by the decay of the spent fuel, which can be calculated with a computer code such as the ORIGEN-ARP module in the SCALE5 suite from Oak Ridge National Laboratory (ORNL) [3.1]. The decay mechanisms of the many radionuclides leading to heat generation in the spent fuel will include α^{2+}, β^{-}, and γ decay. It is reasonable to assume that all of the α^{2+} and β^{-} particles will be deposited within the fuel rods, but some γ rays will escape the fuel rods and be deposited elsewhere. Thus, after determining the heat generated by the decay of the spent fuel, the next step is to determine how much of this heat is deposited within the fuel. Next, the rate at which heat is transferred from the fuel rods must be determined. This heat transfer rate is very difficult to determine due to the complicated geometry associated with the assemblies within the container, and because heat is transferred throughout the container through the three mechanisms of conduction, convection, and thermal radiation. In addition, the rate at which heat is transferred from the outer wall of the container to the surrounding environment must be considered since the temperature difference between the spent fuel and the container wall can determine the extent to which each of the heat transfer mechanisms is involved. For the purposes of characterizing suspended particle behavior

within the spent fuel container, the goal of the thermal analysis of the container is to determine the time-dependent heat transfer rate to the fill gas. This information will allow for the computation of the time-dependent temperature and pressure of the fill gas.

Essentially, the crux of the thermal analysis is to determine the extent of the roles played by each of the three mechanisms of heat transfer, and many models have been developed to address this problem. Two of the most prominent models are the "coupled effective thermal conductivity and edge conductance model" [3.2] and the effective "thermal conductivity model" [3.3]. All of these models make assumptions and one must decide which assumptions allow the individual models to be more accurate. In a fundamental numerical study by Burns et al. [3.4], it is assumed that the heat transferred from the fuel to the cladding is by way of conduction, and that the subsequent transfer of heat from the cladding to the fill gas is through a combination of thermal radiation and natural convection. The study concludes that the rate of heat transfer via thermal radiation is a factor of three larger than the rate of heat transfer via convection. Ultimately, such ratios of transfer mechanism importance are what is needed to accurately model the system. Canaan and Klein performed both numerical and experimental studies to attempt to clarify these ratios [3.5, 3.6]. The focus of their studies was to clarify the role of convection heat transport. They concluded that for helium with low Rayleigh numbers, heat transfer is mainly through radiation and conduction, but for nitrogen and high Rayleigh numbers, the transfer is through radiation and convection. In general, the relative importance of convection is the largest uncertainty in characterizing the heat transfer in spent fuel containers. The difficulty associated with this parameter arises from the complex geometry of the assemblies.

Many studies have attempted to determine the effects of cylinder arrangement on the relative importance of natural convection in heat transfer [3.7, 3.8, 3.9].

In addition to the complex geometries involved, the difficulty associated with this problem stems from the fact that the exact conditions of the system are not well known. For example, it has been observed that for high-burnup fuel, there is no fuel-clad gap. Instead, the fuel has expanded and has become fused to the cladding. In this case, heat from the fuel can be transferred directly to the cladding through conduction. However, if the fuel contracts and is not in contact with the cladding, the heat from the fuel must first be transferred to the helium within the fuel rod and then transferred to the cladding. In addition to heat transfer through conduction, heat can be transferred through radiation from the fuel. The condition of the cladding will also introduce uncertainty into the analysis of the system. Some cladding will be coated with a layer of Chalk River Unidentified Deposits (CRUD) that affects all three mechanisms of heat transfer from the fuel rod and cladding. Also, it has been observed that the cladding tends to absorb hydrogen to form hydrides or can be oxidized in certain cases. Small breaches in the cladding will also affect the heat transfer properties of the fuel. Many of these complexities must be neglected and accounted for with correction factors. Even if the exact condition of every spent fuel rod in a storage container were known at the beginning of storage, these conditions would change over time.

Because the time-dependent thermal conditions within the storage container are difficult to characterize, assumptions must be made in order to address issues associated with the storage container. Some methods for producing estimates for container thermal behavior will be addressed in this chapter. As was mentioned earlier, the first step in the

thermal analysis is to use the ORIGEN-ARP module of the SCALE5 code to determine the decay heat generated by the spent fuel. The inputs to this code can be made to match the power history of the reactor from which the spent fuel was discharged. For demonstration purposes, generic histories can be used to calculate the decay heat. For example, for a PWR using 17 x 17 fuel assemblies of 4.5% enriched UO_2 fuel, running to a burnup of 50 GWd/MTU, using a power history of three 18 month cycles with 30 day down times, the heat curve in Fig. 3.1 can be generated using the express form of the ORIGEN-ARP module.

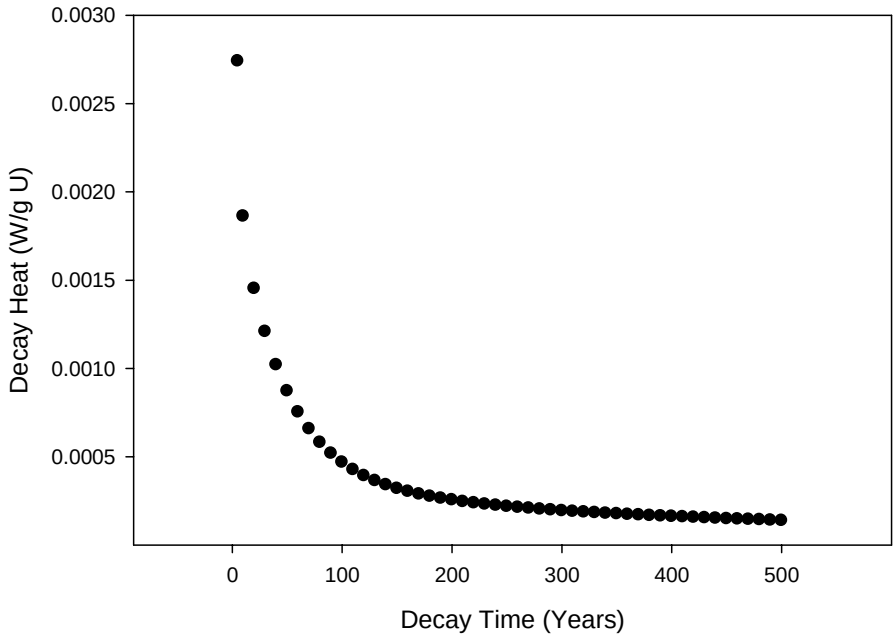

Figure 3.1: Decay Heat Curve for 4.5% Enriched 17x17 PWR Fuel with a Burnup of 50 GWd/MTU

The tabulated data used to create Fig. 3.1 are presented in Table 3.1. In order to generate the curve for Fig. 3.1, the ORIGEN-ARP module must be executed for several different decay times. The output from these evaluations can then be recorded and tabulated to generate a heat curve like that in Fig. 3.1. An example of the ORIGEN-ARP express

form input screen is shown in Fig. 3.2. The input values in Fig. 3.2 are those used to generate heat values in Fig. 3.1. The only value that was changed to generate different data points was the decay time. The power history value of "90% up" tells the program that over the fuel history, the reactor was down 10% of the time for refueling and maintenance. The average power value is the total burnup of the fuel divided by the total time that the reactor was "up" or online. The inputs of "3" cycles, "90%" up, and "30.86" Average Power correspond to three 540.07 day operation cycles separated by 30.86 day power down periods for refueling and maintenance. In order to calculate the total decay heat output, click "Plot Setup" and choose "total watts" from the "Output Units" toolbar. The "Plot Setup" screen is displayed in Fig. 3.3.

Table 3.1: Tabulated Data Used to Generate Figure 3.1

Time (years)	Heat (W/g U)	Time (years)	Heat (W/g U)	Time (years)	Heat (W/g U)
5	2.74E-03	170	2.88E-04	340	1.78E-04
10	1.86E-03	180	2.75E-04	350	1.75E-04
20	1.45E-03	190	2.64E-04	360	1.72E-04
30	1.21E-03	200	2.54E-04	370	1.69E-04
40	1.02E-03	210	2.45E-04	380	1.66E-04
50	8.71E-04	220	2.37E-04	390	1.63E-04
60	7.52E-04	230	2.30E-04	400	1.60E-04
70	6.57E-04	240	2.24E-04	410	1.58E-04
80	5.80E-04	250	2.18E-04	420	1.55E-04
90	5.18E-04	260	2.12E-04	430	1.53E-04
100	4.67E-04	270	2.07E-04	440	1.51E-04
110	4.26E-04	280	2.02E-04	450	1.48E-04
120	3.92E-04	290	1.98E-04	460	1.46E-04
130	3.63E-04	300	1.93E-04	470	1.44E-04
140	3.40E-04	310	1.89E-04	480	1.42E-04
150	3.19E-04	320	1.86E-04	490	1.40E-04
160	3.02E-04	330	1.82E-04	500	1.38E-04

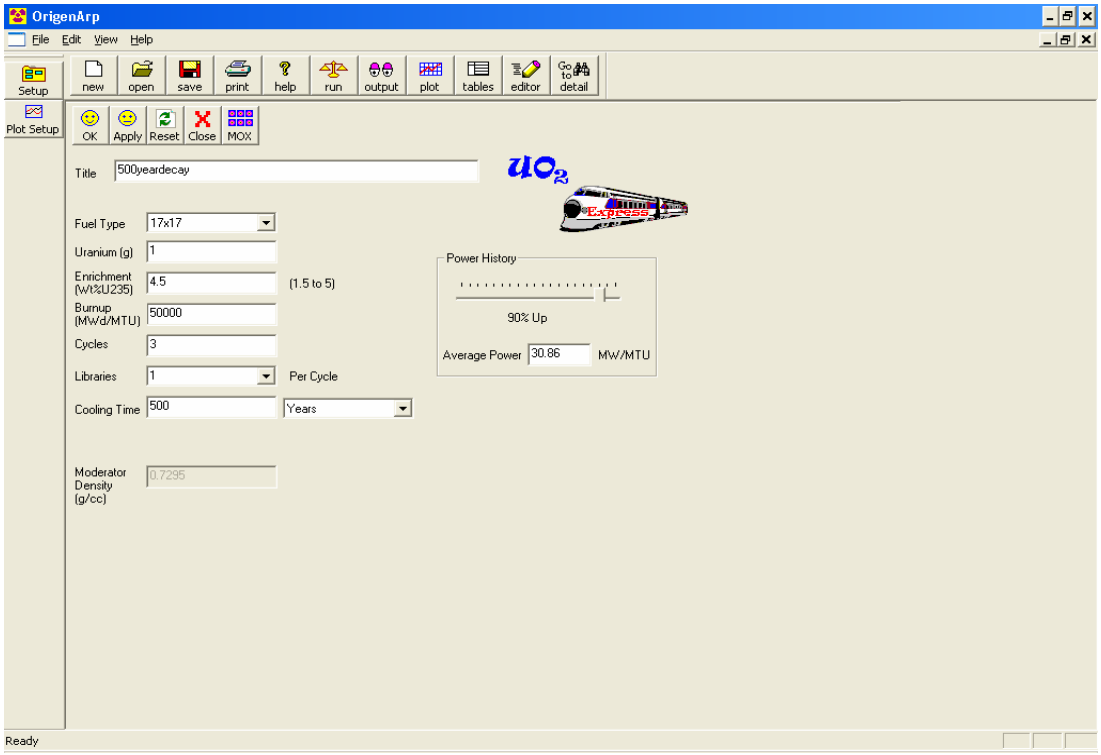

Figure 3.2: ORIGEN-ARP Express Form for Generating the Heat Curve in Figure 3.1

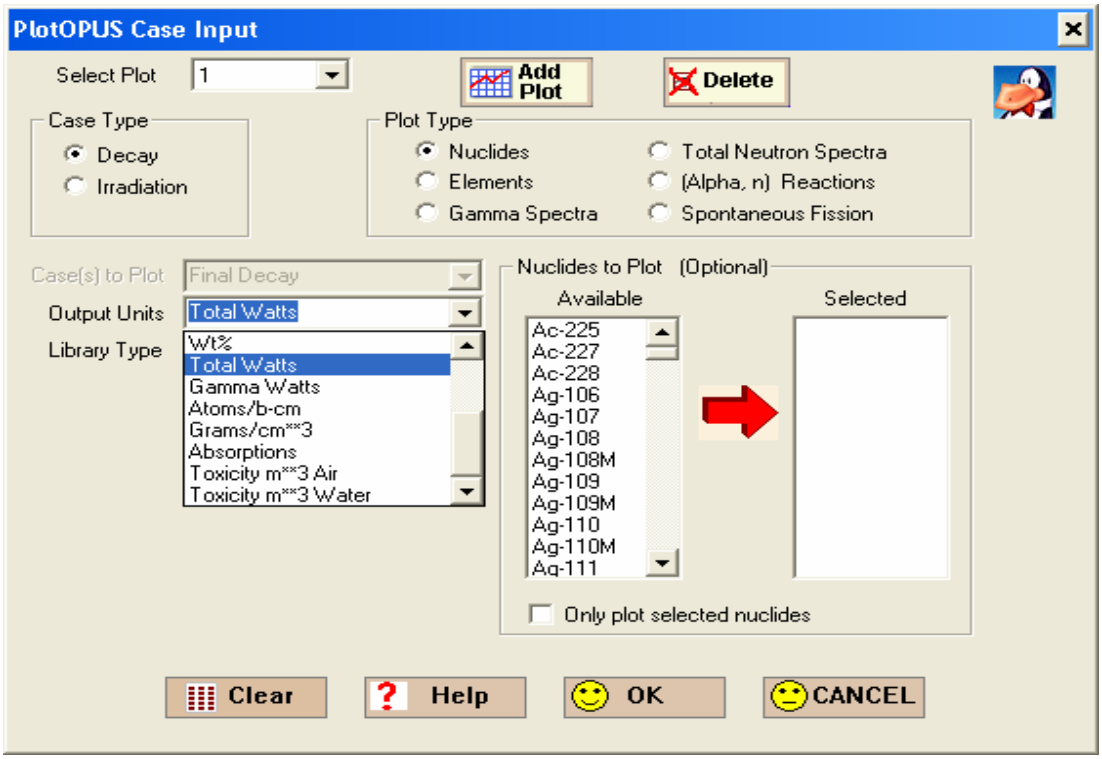

Figure 3.3: How to Generate Total Decay Heat Output

A numerical fit to the data in Table 3.1 can be generated using the "Fit" command in Mathematica®. This fit can be manufactured using whatever mathematical form is desired as long as the result is within the set accuracy range. For example, the heat curve in Fig. 3.1 appears to be a logarithmic curve. Using the Fit function in Mathematica® with the parameters {Log[x], x, 1/x, 1} produces the result

$$Q[t] = 0.00276172 + \frac{0.00399301}{t} + 1.37628 \times 10^{-6} t - 0.000528891 \; Log[t] \qquad (3.1)$$

where $Q[t]$ is the decay heat generation at time t. Equation 3.1 is plotted along with the decay heat data in Fig. 3.4 and is shown to be a fairly good match over the data range. However, although it is difficult to tell from Fig. 3.4, Eq. 3.1 indicates an increase in decay heat at long decay times and it is suggested that other mathematical fits be made for more accurate matching over smaller time scales of particular interest.

It was mentioned earlier that the ORIGEN-ARP input can be modified to model the power history of the reactor from which the spent fuel is removed. It is important to quantify the difference that various reactor histories can have on the decay heat from the spent fuel that they produce. If all of the parameters used in the first example above are kept constant except for the burnup and the average power, what effect would this have on the heat curve? If the burnup is set to 60 GWd/MTU, and the corresponding average power is set to 37.04 MW/MTU, then the heat curve that appears in Fig. 3.5 results. The heat curve from Fig. 3.1 is shown in Fig. 3.5 as well for comparison. For short decay times, the variation is appreciable, but for long decay times, the curves are nearly identical.

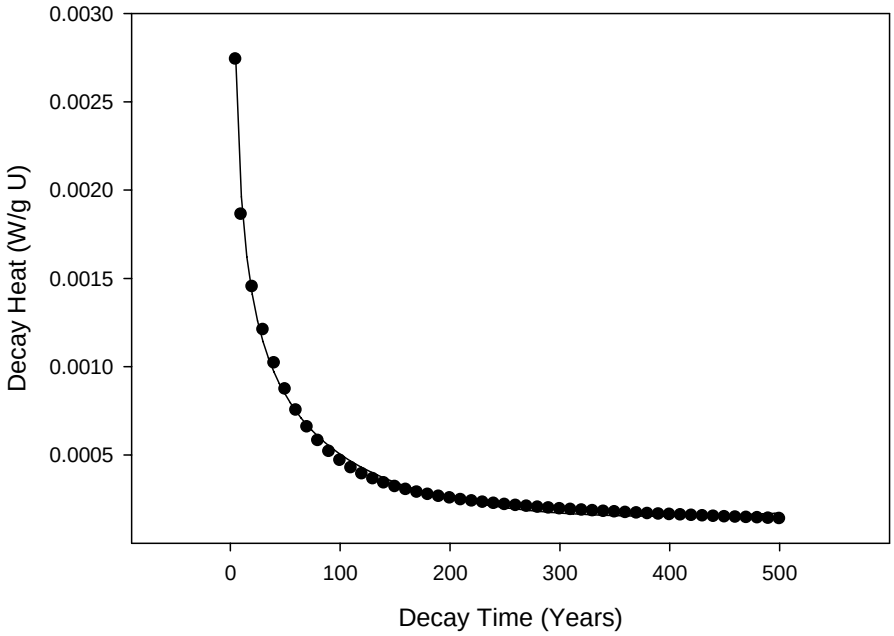

Figure 3.4: Test of Data Fit Accuracy

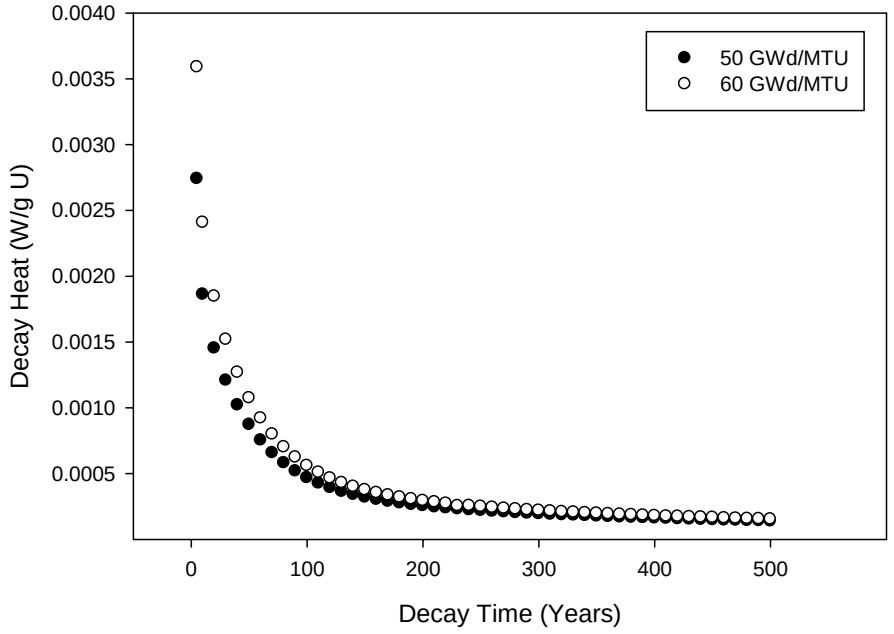

Figure 3.5: Effect of Higher Burnup on Heat Curves

Burnup is not the only factor that can affect the decay heat produced by spent fuel. Various reactor assembly designs can produce different decay heat curves for the

same burnup. For example, a 7 x 7 BWR spent fuel assembly that has been irradiated to a burnup of 50 GWd/MTU under the same conditions as the PWR spent fuel characterized in Figure 3.1 will generate a different decay heat curve. The decay curves from the BWR and the PWR are shown in Fig. 3.6. The curves nearly match except that the decay heat is slightly less for the BWR.

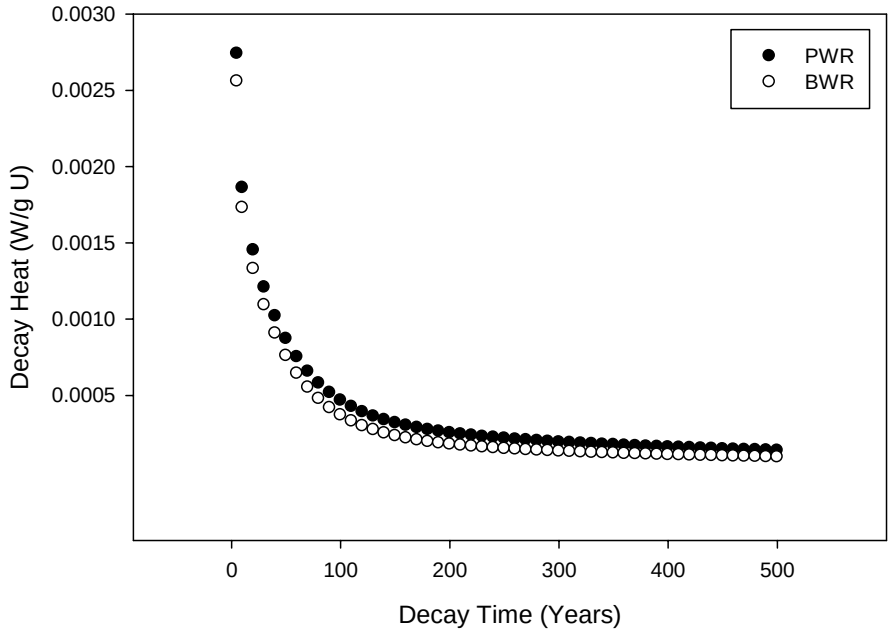

Figure 3.6: Comparison of Heat Curves of PWR and BWR Spent Fuel with a Burnup of 50 GWD/MT

The decay heat that appears in Fig. 3.1, Fig. 3.4, and Fig. 3.6 is in units of watts per gram of uranium. In order to determine the total heat generation within the dry storage container, it is necessary to determine the total number of grams of uranium placed in it. This information is available from the fuel manufacturer for the specific spent fuel assemblies being analyzed. However, for a general analysis, generic data must be used. Some generic data is available for 17 x 17 PWR assemblies and 7 x 7 BWR assemblies as considered above [3.10]. For a Westinghouse 17 x 17 standard PWR

assembly, the number of metric tons of initial heavy metal is 0.46360, the enrichment is 1.6 - 3.8%, the average design burnup is 38 GWd/MTIHM, and the maximum design burnup is 50 GWd/ MTIHM. For a General Electric 7 x 7 Humboldt Bay BWR assembly, the number of metric tons of initial heavy metal is 0.77, but information regarding enrichment and burnup is not available. Since there are 10^6 grams in a metric ton, the decay heat in units of W/MTU (or W/MTIHM as they are the same in this case), can be obtained by multiplying the values in Fig. 3.1, Fig. 3.4, or Fig. 3.6 by 10^6. This number can then be multiplied by 0.46360 to determine the decay heat from a 17 x 17 PWR spent fuel assembly or by 0.77 to determine the decay heat from a 7 x 7 BWR spent fuel assembly. Finally, the decay heat per assembly must be multiplied by the number of assemblies that are to be stored in a given container. For a NUHOMS®-32PT DSC as described in Chapter 2, the total heat load associated with the spent fuel characterized in Fig. 3.1 after a decay time of 10 years would be

$$1.861\times10^{-6}\,\frac{kW}{gU}\times10^{6}\,\frac{gU}{MTU}\times0.46360\,\frac{MTU}{assembly}\times32\,\frac{assemblies}{cask}=27.6\,\frac{kW}{cask}$$

Ultimately, the quantification of the temperature and pressure of the fill gas over time is the desired goal. The first step in the process of determining these values is to determine the amount of heat that is deposited within the spent fuel. The total heat from spent fuel decay from an example case has been characterized with Eq. 3.1, but the fraction of this decay heat that is deposited within the fuel must now be determined. As can be seen in Fig. 3.3, the ORIGEN-ARP user interface includes the option of calculating the fraction of the decay heat that is due to gamma decay. The results of this

calculation are compared with the total decay heat in Fig. 3.7 which demonstrates that a larger fraction of decay heat is generated by alpha and beta decay than gamma decay.

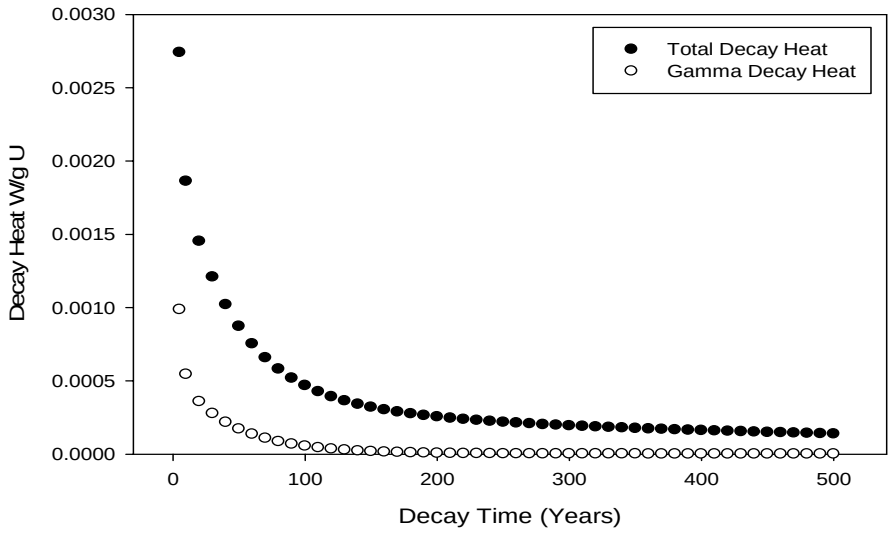

Figure 3.7: Comparison of Total Decay Heat and Decay Heat due to Gamma Decay

Since the heat generated by gamma decay is much lower than the heat generated by alpha and beta decay (after 10 years it is lower by an order of magnitude or more), it will be assumed in this work that all of the decay heat is deposited within the fuel. However, a radiation transport code such as Monte Carlo N-Particle (MCNP) can be used to calculate the fraction of gamma energy that is deposited within the fuel, the fill gas, the canister wall, and the overpack in addition to the fraction of the gamma energy that escapes the container [3.11]. This calculation will provide relevant data for analyses for the first few decades of decay only and will be left for future work.

As mentioned earlier, the heat transfer from the spent fuel is complicated and the system must be simplified. One simplification is to neglect the effects of the cladding. In

this scenario, the heat generated and deposited within the fuel can either stay in the fuel, be transported from the fuel via thermal radiation, or be transported via conduction and/or convection to the fill gas. This can be expressed mathematically as

$$\dot{Q}_d = \dot{Q}_s - \dot{Q}_r - \dot{Q}_{fg} \tag{3.2}$$

where $\dot{Q}_s$ is the rate of heat generated from the radioactive decay, $\dot{Q}_d$ is the net rate of heat deposition within the fuel, $\dot{Q}_r$ is the rate that heat is transferred from the fuel via radiative transfer, and $\dot{Q}_{fg}$ is the rate that heat is transferred to the fill gas. Another heat balance must be generated for the fill gas. This balance can be stated as

$$\dot{Q}_{net} = \dot{Q}_{fg} - \dot{Q}_{out} \tag{3.3}$$

where $\dot{Q}_{net}$ is the net heat transfer rate to the fill gas, and $\dot{Q}_{out}$ is the rate of heat flow from the fill gas to the container wall or basket. Ultimately, the goal is to determine the value of $\dot{Q}_{net}$. Combining Eq. 3.2 and Eq. 3.3 and rearranging gives the following equation for $\dot{Q}_{net}$

$$\dot{Q}_{net} = \dot{Q}_s - \dot{Q}_r - \dot{Q}_d - \dot{Q}_{out} \tag{3.4}$$

To be more specific, the value of $\dot{Q}_{out}$ relies heavily on how quickly the heat is transferred from the container wall to the outside environment, and thus on the

temperature of the wall. This means that another heat balance on the outer wall is required for completeness. In order to obtain any results, either assumptions must be made or experiments must be conducted. As mentioned earlier, several models currently exist in which several assumptions have been made and justified. In addition, many of the designs for dry storage containers that are currently available have been tested and several aspects of heat transfer have been quantified.

As stated in Table 2.1, the CASTOR V/21 storage cask designed by General Nuclear Systems, Inc. has been approved by the NRC for general use. Extensive testing of this cask design was performed at Pacific Northwest National Laboratory in the mid 1980's [3.12]. Figure 3.8 is a cross sectional view of the Castor V/21 storage system that appears to illustrate that the system is a canister based cask. In the Castor V/21 system, the canister appears to be part of the basket system that in Fig. 3.8 is referred to as the "basket barrel". In the upper right quadrant of Fig. 3.8, an arc appears that is labeled "cask body". This cask body appears to be the overpack of the system. The problem is that the basket is not sealed. The primary lid of the system is bolted to the cask body and there is no lid for the basket portion of the container. However, if the basket were sealed, this would be an excellent example of the canister-based system that is being focused on in this study. If this system were a canister based system, the objective would be to model the transport of particulates through any small breaches that may form in what is labeled as the basket barrel in Fig. 3.8. Even though this system does not directly correlate to the system being modeled, it can serve as a useful case to demonstrate analysis. Thermal data for more closely correlated systems have been produced, but are not available, apparently for proprietary reasons.

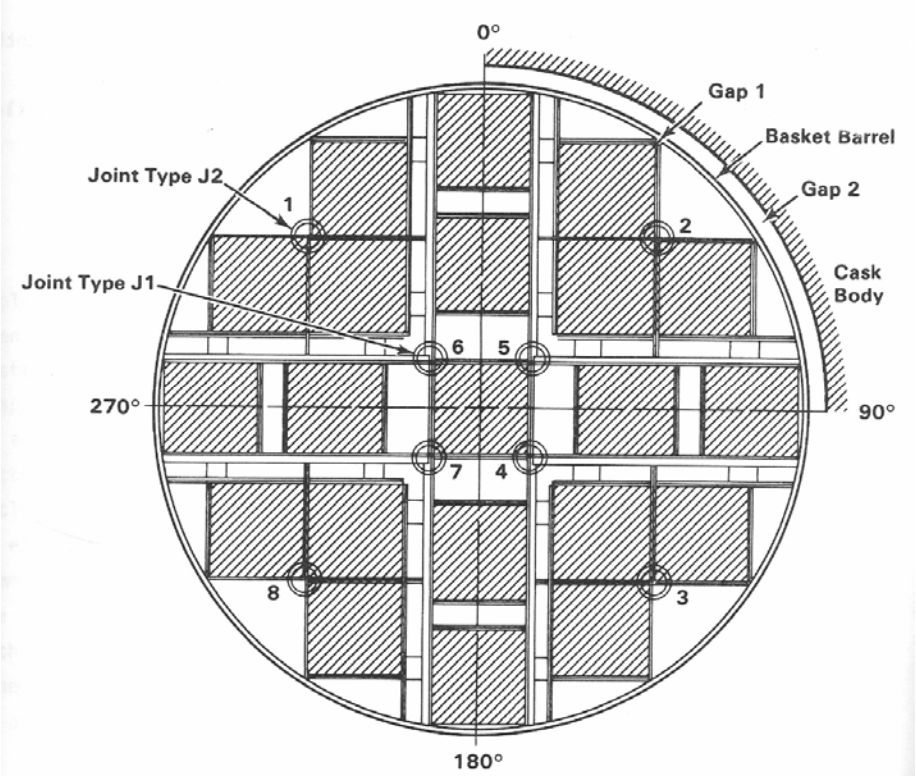

Figure 3.8: Cross-section of the Castor V/21 Dry Storage Container [3.12]

In order to try to characterize the effects of each of the heat transfer mechanisms involved, several tests involving the Castor V/21 design were considered. First, in order to determine the effect of convection, the heat transfer was measured for the cask when it was in a vertical and when it was in a horizontal position. The results were that heat transfer was more effective for the vertical orientation, suggesting that convection plays a significant role in heat transfer if the container is stored vertically. However, this role is diminished if the cask is stored horizontally. In addition, the heat transfer was tested for the two when the container was backfilled with nitrogen and when it was backfilled with helium. Since these two gases have different densities and thermal conductivities, the effects of conduction and convection could be more accurately characterized. Finally, the

heat transfer with no fill gas (creating a vacuum) was measured in order to characterize the effects of thermal radiation. The results of these tests for the estimated peak cladding temperatures are presented in Table 3.2.

Table 3.2: Castor V/21 Heat Transfer Experimental Data [3.12]

Orientation	Backfill	Heat Load (kW)	Ambient Temp. (C)	Measured Guide Tube Temp. (C)	Estimated Peak Clad Temp. (C)
Vertical	Helium	28.4	27	347	352
Vertical	Nitrogen	28.4	24	358	368
Vertical	Vacuum	28.4	25	414	424
Horizontal	Helium	28.4	24	360	365
Horizontal	Nitrogen	28.4	24	395	405

In future chapters, it will be necessary to know the rate at which heat is deposited in the fill gas in order to determine the temperature and pressure of the fill gas as a function of time. In order to determine the parameter values necessary to calculate the heat deposition rate, approximations must be made, models must be constructed, and experiments must be performed. The information in Table 3.2 can be used to obtain estimates of the necessary values.

Although it is a gross misrepresentation of the actual physical situation, the spent fuel assemblies will be modeled as one large cylindrical mass of fuel and cladding at the center of the container. The rest of the volume within the container will be modeled as the fill gas. The first problem to address in this model is the effect of radiative transport from the assemblies which is governed by

$$\dot{Q}_r = e\sigma T^4 \tag{3.5}$$

where e is the emissivity of the material and σ is the Stefan-Boltzmann constant. In Table 3.2, the temperature of the fuel for the case of no fill gas is listed as 414 ºC. Due to the absence of fill gas in this case, it can be assumed that all of the heat transfer is by way of radiative transfer. The equation describing the heat balance on the fuel for this situation is

$$\dot{Q}_s = \dot{Q}_r + \dot{Q}_d \tag{3.6}$$

which is simply Eq. 3.2 with the term for the heat transfer to the fill gas removed. Over short time intervals, the time rate of change of the heat generation from the spent fuel decay is close to zero. The fact that the decay heat for all experiments recorded in Table 3.2 is constant at 28.4 kW is evidence of this claim. Thus, over short periods of time, the system can be described as a pseudo-steady state in which the rate of heat deposition in the fuel is negligible. Applying this condition to Eq. 3.6 and combining it with Eq. 3.5, leads to the conclusion

$$\dot{Q}_s = e\sigma T^4 \tag{3.7}$$

The heat source on the left hand side of Eq. 3.7 is 28.4 kW, the temperature on the right hand side is 414 ºC, and the value of the Stefan-Boltzmann constant is 5.68 x 10^{-8} W/m^2 K^4. These parameters can be used to determine an effective value of e in this system. The resulting value is 2.25 per square meter of surface area from which the heat is being radiated. For the fuel used in the experiment above, the length of each assembly

was 3.658 meters, each fuel rod had a diameter of 10.7 millimeters, there were 204 fuel rods per assembly, and twenty-one assemblies were placed into the storage container. These values correspond to a total radiative surface area of roughly 527 per square meter, resulting in a value of 0.0043 for the effective emissivity of the system under consideration. If the assumption is made that the emissivity for the system is constant with respect to temperature, then the equation for the radiative transport of heat from the spent fuel assemblies in the system is known.

Heat transfer through conduction and convection must now be addressed. The general equations that describe these mechanisms are respectively,

$$q = -A\,k\,\nabla T \tag{3.8}$$

$$q = -A\,h\,\nabla T \tag{3.9}$$

where k is the thermal conductivity and h is the convective heat transfer coefficient. It is important to note that the temperatures that appear in Eq. 3.8 and Eq. 3.9 are not the same. However, since both equations are of the same form, it can be estimated that the heat transfer due to the combined effects of conduction and convection are described by an equation

$$q = -l\,\nabla T \tag{3.10}$$

where l is a combined thermal transport coefficient that takes into account the effects of both conduction and convection. Upon analysis of another experiment reported in Table 3.2, it is seen that for the case where the container was stored in a horizontal orientation and backfilled with helium, the fuel temperature was reportedly 360 ºC. Later in the report [3.12], it was stated that the wall of the canister had a temperature of 200 ºC. Also, Table 3.2 states that the ambient temperature was 24 ºC. Using this data, it can be determined that the value of l is 177.3 W/K. If it is assumed that the cask body is a black body, then all of the heat that is transferred from the fuel through thermal radiation will be deposited within it. All heat conducted through the fill gas will also be deposited within the cask body. Thus, assuming a relatively steady state like before, for the experimental conditions reported, it can be claimed that the effective heat transfer through the cask is 28.4 kW/(200-24) = 159.1 W/K (ΔºC = ΔK). Thus, the overall equation for the heat transfer through the cask taking into account these assumptions is

$$\dot{Q}_S = 2\times10^{-10} T_f^4 + 177.3(T_f - T_w) \tag{3.11}$$

where T_f is the temperature the fuel and T_w is the temperature of the canister wall. The equation for the canister wall can be given from the arguments above as

$$T_w = \frac{\dot{Q}_S}{159.1} + 297 \tag{3.12}$$

if the ambient temperature is assumed to be constant. Eq. 3.12 can be substituted into Eq 3.11 and rearranged to give

$$\dot{Q}_S(t) = 9.46 \times 10^{-11} T_f^4(t) + 83.9(T_f(t) - 297) \tag{3.13}$$

where the time argument has been inserted to explicitly display the dependence on time. Equations 3.12 and 3.13 can now be used to determine the temperature of the canister wall and the fuel respectively as functions of time. These two values must then be used to determine the temperature of the fill gas as a function of time. The simplest way to do this is to average the two values. Figure 3.9 displays the time-dependent curves describing the fuel temperature, wall temperature, and fill-gas temperature if Eq. 3.1 is used to describe the decay heat from the spent fuel over time and the result is scaled up to account for the total quantity of fuel within the cask. The rise in temperature between 400 and 500 years is due to the mathematical fit used to generate Eq. 3.1 that was mentioned earlier. More accurate fits for specific time-intervals can be generated as needed.

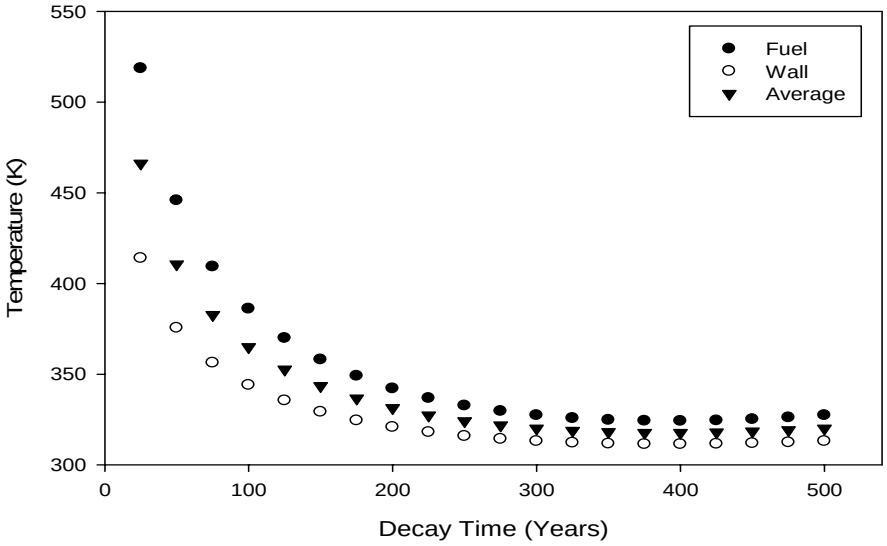

Figure 3.9: Estimated Temperature Curves for the V/21

In the thermal analysis just presented, numerous assumptions and estimates were made. However, the resulting temperature curve for the fill gas as presented in Fig. 3.9 looks a lot like other temperature curves that have been created for spent fuel containers. The temperature does appear to drop too rapidly however. Assumptions can be modified to make the curve more accurate. Justifications need to be made however as to which modification should be made. More accurate heat transfer analyses can be performed with computational fluid dynamic codes such as FLUENT [3.13].

REFERENCES

3.1 ORIGEN-ARP 5.1, <http://www.ornl.gov/sci/origen-arp/origen-arp_5.1.pdf> (6/19/2007).

3.2 Manteuffel, R.D., Todreas, N.E., "Effective Thermal Conductivity and Edge Conductance Model for a Spent Fuel Assembly," *Nuclear Technology*, 105 (1994) p. 41.

3.3 Bahney, R.H., Lots, T.L., "Spent Nuclear Feul Effective Thermal Conductivity Report," Document Identifier BBA00000-01717-5705-00010 REV 00 (7/11/1996).

3.4 Burns, S.P., Canaan, R.E., Klein, D.E., "A Numerical Analysis of Spent Nuclear Fuel Thermal Characteristics," *Proceedings of the 4th International Conference on High Level Radioactive Waste Management*, 2 (1993) p. 1778.

3.5 Canaan, R.E., Klein, D.E., "A Numerical Investigation of Natural Convection Heat Transfer within Horizontal Spent-fuel Assemblies," *Nuclear Technology*, 123 (8/1998) p. 193-208.

3.6 Canaan, R.E., Klein, D.E., "An Experimental Investigation of Natural Convection Heat Transfer within Horizontal Spent Fuel Assemblies," *Nuclear Technology*, 116 (1996) p. 306-317.

3.7 Triplett, C.E., et al., "A Comparison of Natural Convection Heat Transfer for a Staggered Versus an Aligned Array of Horizontal Spent Nuclear Fuel Rods within a Rectangular Enclosure," *Nuclear Technology*, 130, (4/2000) p. 99-110.

3.8 Keyhani, M., Dalton, T., "Natural Convection Heat Transfer in Horizontal Rod-Bundle Enclosures," *Transactions of the American Society of Mechanical Engineers*, 118 (8/1996).

3.9 Sparrow, E.M., Niethammer, J.E., "Effect of Vertical Separation Distance and Cylinder-to-Cylinder Temperature Imbalance on Natural Convection for a Pair of Horizontal Cylinders," *Transactions of the American Society of Mechanical Engineers*, 103 (11/1981).

3.10 Office of Civilian Radioactive Waste Management, "Characteristics of Spent Fuel, High-level Waste, and Other Radioactive Wastes Which May Require Long-Term Isolation," Appendix 2A. "Physical Descriptions of LWR Fuel Assemblies," DOE/RW-0184, Volume 3 of 6 (12/1987).

3.11 MCNP, <http://mcnp-green.lanl.gov/index.html> (7/16/2007).

3.12 Creer, J.M., et al. “The Castor-V/21 Spent Fuel Storage Cask: Testing and Analyses,” NP-4887, Research Project 2406-4, PNL-5917, UC-85, Interim Report, (11/1986).

3.13 FLUENT, <http://www.fluent.com/> (6/21/2007).

CHAPTER 4: DEPRESSURIZATION

As discussed in Chapter 1, the first phenomenon to be studied upon the formation of a small breach in spent fuel canister wall is the depressurization time. The depressurization time will depend on the pressure differential across the breach, the size of the breach, the temperature within the canister, and the amount of fill gas. Ideally, the free volume is composed solely of the backfill gas that is pumped into the canister at the time that it is sealed. This backfill gas will be inert and will most likely be helium. If this is the case, then the only release from the canister on account of the breach formation will be helium. The health concerns associated with spent nuclear fuel containers stem from the possibility of radioactivity present in the backfill gas in the form of fission gases or radioactive aerosol particulates.

As an introduction to this problem, one can look at a simplistic case; that of a canister in which the free volume is occupied by only backfill gas and the breach shape is a straight right cylinder. This problem was addressed by E. Zwahlen in his Ph.D. dissertation [4.1]. Figure 4.1 shows the system that Zwahlen analyzed [4.1]. Notice that although he is modeling a waste container, the container in Fig. 4.1 contains no waste. He does however define "*V*" in the figure as the "gas void volume", representing the free volume surrounding the waste.

Zwahlen's analysis used argon as a fill gas. He assumed that the waste container was filled with argon to a pressure of 1 atm. at a temperature of 298 K. The waste container was then immediately sealed off and the heat from the spent fuel was allowed to heat up the argon causing a rise in the pressure inside the container. Under these

conditions, the argon would reach an equilibrium temperature of 558 K and a pressure of 1.87 atm. [4.1].

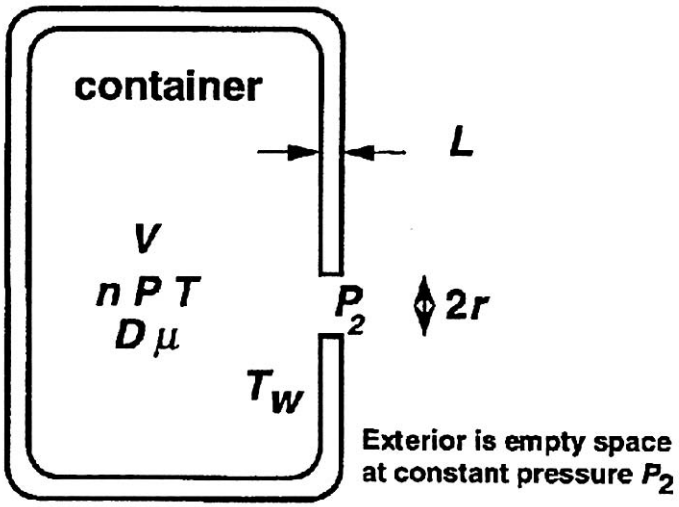

Figure 4.1: "Waste Container with a Hole" [4.1]

Figure 4.2 shows the expected temperature of the fill gas inside the waste container as a function of time according to Zwahlen's analysis [4.1]. Zwahlen obtained this temperature information from the *Yucca Mountain Site Characterization Plan* [4.2], which in turn took this information from an analysis done at Lawrence Livermore national Laboratory in 1984 [4.3]. This work was done using a three-dimensional implicit finite-element code called TACO3D. Two observations should be made about the information presented in Fig. 4.2. First of all, the curves in the figure, "neglect the few years for the container to heat up to its maximum temperature" [4.1]. Also, the time in Fig. 4.2 represents the time after the spent fuel has been placed into the container, which occurs 10 years after it has been discharged from the reactor [4.1].

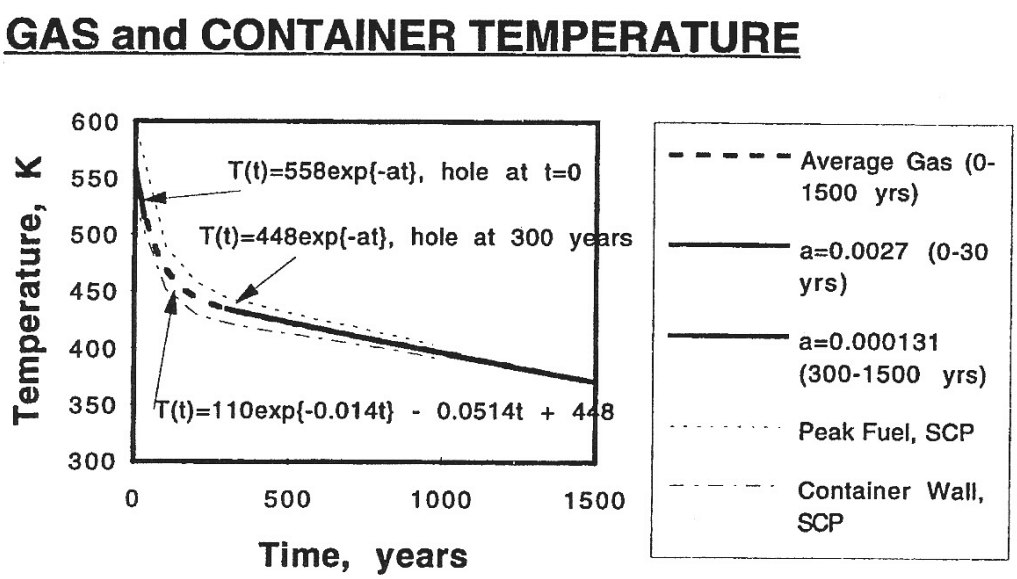

Figure 4.2: "Gas and Container Absolute-Temperature as a Function of Time after Waste Container Emplacement" [4.1]

The model used to generate Fig. 4.2 used the thermal properties of dry air or helium inside the container and the thermal properties of 100% humid air outside the container. It is stated in the analysis that the current designs call for the canisters to be backfilled with argon instead of helium. The problem of helium having a higher thermal conductivity than argon is recognized, but the importance of this fact is downplayed because it is expected that the main method of heat transfer in the container will be thermal radiation [4.3]. Figure 4.3 shows a comparison of the fill gas temperatures predicted by Zwahlen's fit for the waste container in his analysis and the fill gas temperatures predicted for an intact Castor V/21 as calculated in Chapter 3. Obviously there is some discrepancy which illustrates the importance of an accurate thermal analysis. Figure 4.4 shows the results of the thermal analysis in Chapter 3, re-evaluated with an ambient temperature of 400 K instead of 297 K.

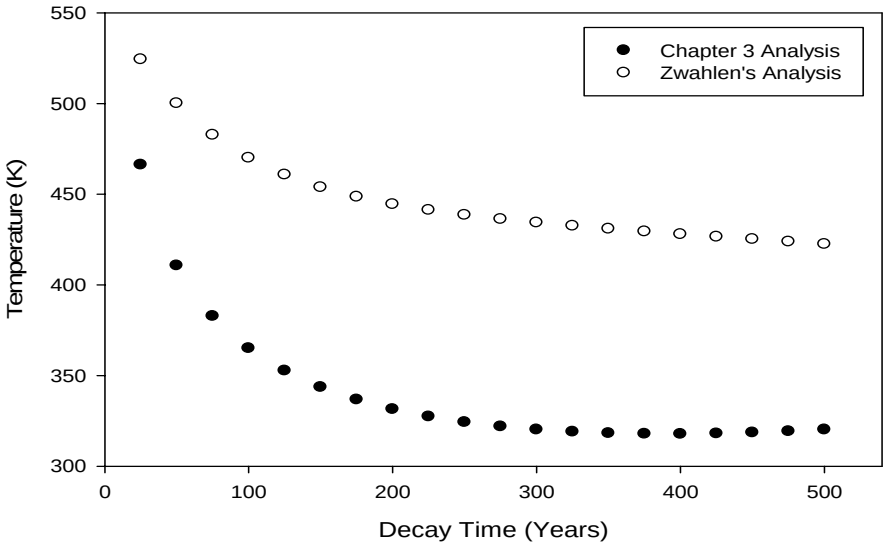

Fig. 4.3: Comparison of Zwahlen's Heat Curve to the Heat Curve Derived in Chapter 3

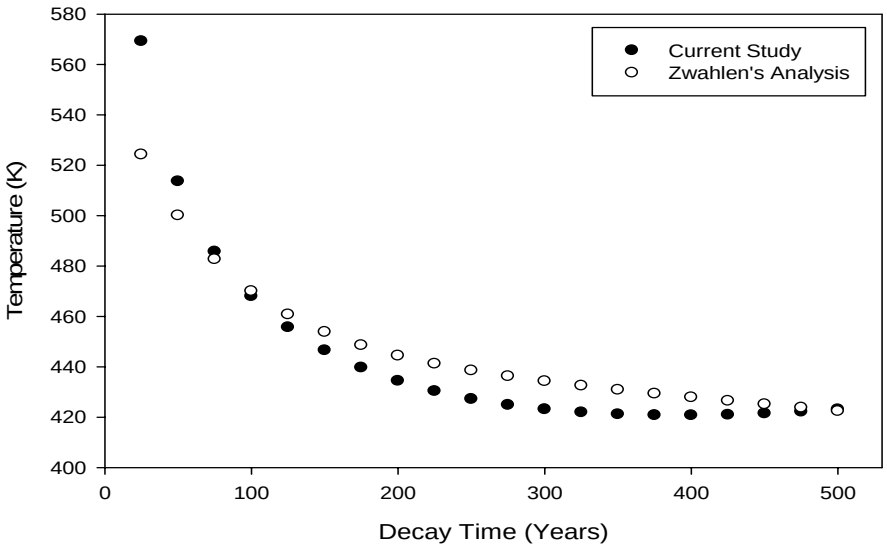

Fig. 4.4: Effect of Changing the Ambient Temperature on the Heat Curve Derived in Chapter 3

Although the magnitudes of the curves being compared in Fig. 4.4 are roughly the same, the shapes of the curves are different. The motivation behind using a higher ambient temperature is that the thermal analysis used by Zwahlen was performed for

spent fuel containers that had already been placed within the Yucca Mountain repository. Therefore, the ambient temperature may be different from that presented in Table 3.2. However, if the ambient temperature were higher during the experiments which generated the data in Table 3.2, the temperatures measured at the cladding and in the guide tubes may have been higher as well. Therefore the heat curve generated for Fig. 4.4 is not fully justified and is presented for comparison only.

Figure 4.2 represents the expected temperature for the cask and fill gas if no breach is formed. Some explanation is needed for the different equations and parameters that appear in Fig. 4.2. It is most appropriate that this explanation appear in the next few paragraphs in the form of a summary of the approach that Zwahlen took toward solving the problem of determining the spent fuel canister depressurization time after the formation of a through-wall breach. Note that since he allowed the temperature inside the container to reach a maximum before introducing a breach, the pressure correspondingly rises to a maximum. Since the fill gas is an inert gas and the pressure does not exceed 2 atmospheres, it is reasonable to assume that the fill gas can be accurately described by the ideal gas law

$$PV = nRT \tag{4.1}$$

In fact, the maximum pressure of 1.87 atm. for the canister interior was calculated using the ideal gas law with the temperature determined from a finite element method [4.3]. Since the pressure inside the container is higher than the pressure outside of the container, when a breach in the container wall forms, the flow will be from inside the

container to outside the container. The flow rate out of the container and the corresponding time it takes for the pressures inside and outside the container to equilibrate depend on the size of the breach. Note from Fig. 4.1 that the size of the breach is characterized by the radius r and the length L. Since Zwahlen considered only right cylindrical breaches, the length was always considered to be the container wall thickness which was 1 centimeter. Zwahlen calculated that for breaches with $r \geq 50$ μm, the flow from the container can be described as orifice flow. For breaches with $r < 5$ μm, the flow is in the slip region and for smaller values, Knudsen flow may occur. For breaches with 5 μm < r < 50 μm, the flow is laminar and can be described by the Poiseuille Equation

$$\frac{dn_{cv}(t)}{dt} = -\frac{\pi r^4 \left(P^2(t) - P_a^2\right)}{16 \mu L R T_w} \tag{4.2}$$

where n_{cv} is the number of moles of fill gas in the free volume V of the canister, r is the radius of the breach, μ is the viscosity of the fill gas, L is the container wall thickness, P_a is the atmospheric pressure on the outside of the container, and T_w is the temperature of the container wall [4.1].

Although Zwahlen addressed orifice flow for breaches with larger radii, it is the smaller breaches that result in Pouseuille flow that will be the focus of this work. Zwahlen realized that if he rearranged the ideal gas law and differentiated with respect to time, he would obtain an equation for the molar rate of fill gas loss from the container with respect to time. This resulting equation for the molar flow rate of fill gas through the breach is

$$\frac{dn_{cv}(t)}{dt} = \frac{V}{RT(t)^2}\left[T(t)\frac{dP(t)}{dt} - P(t)\frac{dT(t)}{dt}\right] \tag{4.3}$$

Zwahlen then reasoned that according to the conservation of mass, the rate at which moles of gas are leaving through the breach as described by the left-hand side (LHS) of Eq. 4.2 must be equal to the rate of loss of fill gas on the LHS of Eq. 4.3. Thus he combined the two equations to form

$$\frac{V}{RT(t)^2}\left[T(t)\frac{dP(t)}{dt} - P(t)\frac{dT(t)}{dt}\right] = -\frac{\pi r^4\left(P^2(t) - P_a^2\right)}{16\mu LRT_w} \tag{4.4}$$

Unfortunately, Eq. 4.4 is one equation with two unknowns. In order to move forward toward a solution, Zwahlen made some assumptions. First, he assumed that the log derivative with respect to time was a constant

$$\frac{1}{T(t)}\frac{dT(t)}{dt} = -a \tag{4.5}$$

The "*a*" that appears on the right-hand side (RHS) of Eq. 4.5 is the same "*a*" that appears in Fig. 4.2. There are three different equations describing the time dependent temperature of the container as a function of *a*, since *a* is not actually a constant as claimed in Eq. 4.5. However, *a* assumes a mostly constant value for the time period 0 – 30 years and another mostly constant value for the time period 300 – 1500 years. Two of the equations in Fig. 4.2 represent each of these time periods over which the value of *a* can be considered constant. The third equation in Fig. 4.2 is a mathematical fit to the entire temperature

curve. Zwahlen also defined the ratios $P(t)/P_a = p(t)$ and $T(t)/T_w = T^*$. Plugging these ratios and Eq. 4.5 into Eq. 4.4 gives,

$$\frac{dp(t)}{dt} + ap(t) = -\Omega\left(p^2(t) - 1\right) \tag{4.6}$$

where,

$$\Omega = \frac{\pi r^4 T^* P_a}{16 \mu L V} \tag{4.7}$$

is a constant if T^* and μ are taken to be constant. Equation 4.6 can be rearranged into the form,

$$\frac{dp(t)}{dt} = -\Omega p^2(t) - ap(t) + \Omega \tag{4.8}$$

which can in turn be integrated and solved for $p(t)$ if all parameters in Eq. 4.7 are given set constant values. The resulting equation can be solved for $p(t) = P_a$ to determine the depressurization time. The result is a depressurization time of about 850 years if the breach has a 5 μm radius and forms at time $t = 0$. The depressurization times are much smaller for breaches with larger radii. Figure 4.5 is a plot of the pressure inside the container as a function of time that appeared in Zwahlen's thesis [4.1].

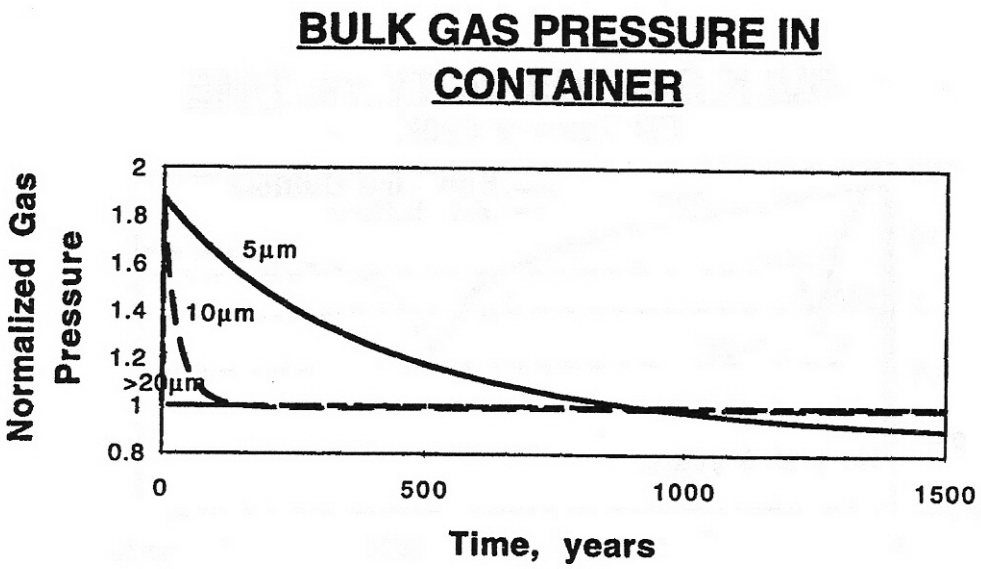

Figure 4.5: "Normalized Bulk Gas Pressure in the Waste Container as a Function of time For a Hole at 0 Years" [4.1]

Zwahlen's methods in addressing this problem involved many assumptions that may or may not cause an unacceptable degree of error in his solutions. In order to verify or improve upon Zwahlen's work, a more general description of this problem using the same input parameters has been constructed. Initially, a closed system was considered, which can be completely described with information from Zwahlen's thesis. This system is represented by Fig. 4.6.

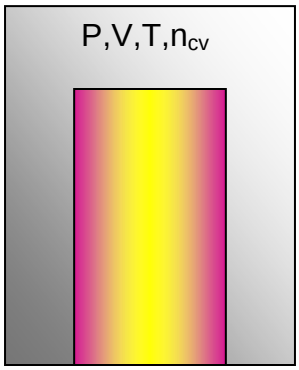

Figure 4.6: Closed System

The temperature of the closed system as a function of time, taken from Fig. 4.2 is

$$T_{closed}(t) = 110e^{-0.014t} - 0.0514t + 448 \tag{4.9}$$

and the time-depended pressure within the canister can be determined from Eqs. 4.1 and 4.9. The first step in moving from a closed system analysis to an open system is to evaluate the energy balance for the closed system

$$\frac{dE_{cv}}{dt} = \frac{dU_{cv}}{dt} = \dot{Q} = n_{cv}c_v \frac{dT_{closed}}{dt} \tag{4.10}$$

where E_{cv} is the total energy of the control volume, U_{cv} is the internal energy of the control volume, $\dot{Q}$ is the net rate of heat transfer to the control volume, n_{cv} is the number of moles in the control volume, c_v is the specific heat at constant volume of the backfill gas in the control volume and T_{closed} is the time dependent temperature defined by Eq. 4.9. The temperature here is labeled with the subscript "*closed* " in order to distinguish it from the temperature of the open system to be analyzed next. The subscript "*cv* " has also been added to the parameters referring to the control volume in order to clarify the system being considered. This system or control volume is the fill gas that resides in the free volume of the dry storage container.

The total energy of the system is equal to the sum of the potential energy, kinetic energy, and internal energy of the system. Since the system is stationary, the changes in kinetic energy and potential energy of the system with respect to time are zero. Thus, the time derivative of the total energy of the system is equal to the time derivative of the

internal energy with respect to time. According to the first law of thermodynamics, the time derivative of the total energy of the system with respect to time is equal to the net rate of heat transfer to the system plus the work done on the system. Since no work is being done, the change in the energy is equal to the net rate of heat transferred to the system, which in the ideal gas approximation is equal to the RHS of Eq. 4.10.

The characterization is now adjusted to describe an open system, represented by Fig. 4.7.

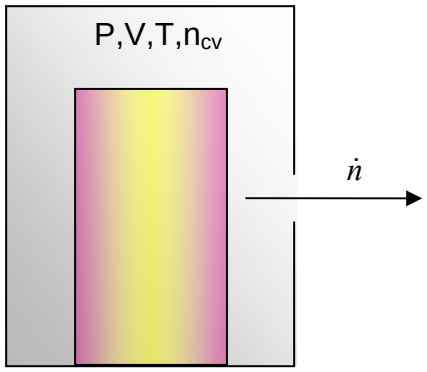

Figure 4.7: Open System

For the open system, a mass balance, an energy balance, an equation of state, and a flow equation are now constructed. The equation of state and the flow equation are given by Eq. 4.3 and Eq. 4.2 respectively. The mass balance and the energy balance are given respectively by,

$$\frac{dn_{cv}}{dt} = -\dot{n} \tag{4.11}$$

and

$$\frac{dU_{cv}}{dt} = \dot{Q} - \dot{n}h \tag{4.12}$$

In Eq. 4.12, it is assumed that the change in internal energy of the system due to heat transfer to the system is the same for the closed system and the open system. The *h* in Eq. 4.12 is the specific enthalpy of the gas molecules leaving the system through the breach in the wall. Eq. 4.2, 4.3, 4.11 and 4.12 can be combined and rearranged to produce three equations with three unknowns

$$\frac{dU_{cv}(t)}{dt} = n_{cv}(0)c_v \frac{dT_{closed}}{dt} + \frac{dn_{cv}}{dt}h \tag{4.13}$$

$$\frac{dn_{cv}(t)}{dt} = \frac{V}{RT(t)^2}\left[T(t)\frac{dP(t)}{dt} - P(t)\frac{dT(t)}{dt}\right] \tag{4.14}$$

$$\frac{dn_{cv}(t)}{dt} = -\frac{\pi r^4 (P^2 - P_a^2)}{16\mu LRT_w} \tag{4.15}$$

In Eq. 4.13, the number of moles in the control volume is denoted specifically as the initial number of moles because it is assumed that the change in internal energy due to heat transfer was the same for the closed system and the open system. Also, in Eq. 4.15, T_w was set equal to *T(t)* and μ was not treated as a constant. Instead, tabulated data for argon and for helium was obtained from the CRC Handbook of Chemistry and Physics [4.4]. These data were extrapolated using Sutherland's formula, [4.5]

$$\mu = \mu'\left(\frac{T}{T'}\right)^{\frac{3}{2}}\frac{T'+S}{T+S} \tag{4.16}$$

where S is a constant evaluated after the values of the viscosity are substituted in for their corresponding temperatures. Notice that all three equations are differential equations with derivatives taken with respect to time. Thus, all three equations can be solved simultaneously with the numerical differential equation solver "NDSolve" in Mathematica®. This method produces a depressurization time of approximately 550 years if the backfill gas in the container is argon. This calculation using argon as the backfill gas was performed to produce results directly comparable to those of Zwahlen. However, it is now commonly established that the backfill gas will be helium rather than argon due to reduced cost and a higher thermal conductivity. For this reason, the depressurization time with helium as a backfill gas was calculated as well. The result was that a depressurization time of approximately 475 years is expected for helium. Fig. 4.8 is a plot of the resulting pressures from Zwahlen's analysis as well as the pressure curves generated from the model constructed in this chapter in which the backfill gas is helium or argon.

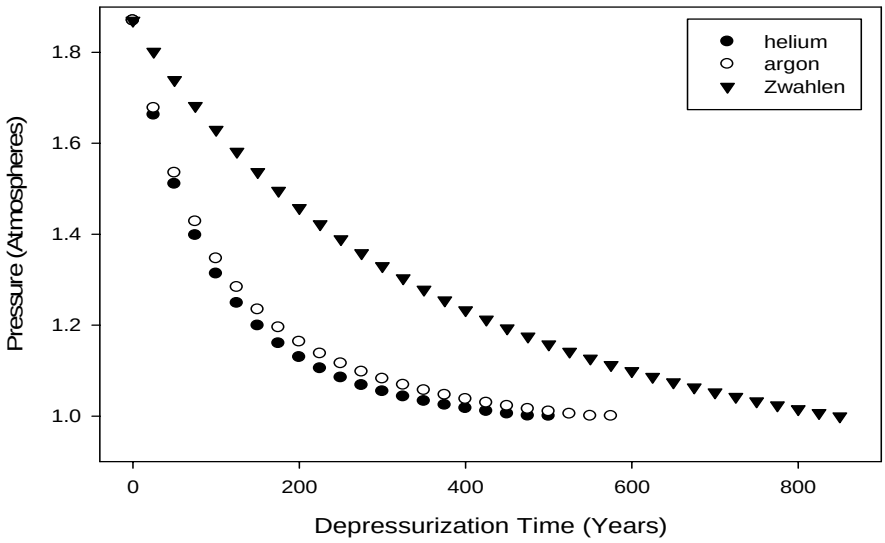

Figure 4.8: Depressurization Results for r = 5 μm

The current method was used to calculate the depressurization time for helium and argon for varying breach radii and wall thicknesses. These results are tabulated in Table 4.1 and Table 4.2 respectively. The system behaves as expected with larger breach radii leading to shorter depressurization times and thicker walls leading to longer depressurization times. The depressurization time is much more sensitive however to the breach radius than the wall thickness. The reason for this phenomenon is apparent upon a quick inspection of Eq. 4.15. Notice that the change in the number of moles in the system with respect to time is proportional to the inverse of the wall thickness, yet it is proportional to the breach radius raised to the fourth power.

Table 4.1. Depressurization Times for Various Breach Radii

Radius (μm)	Argon (years)	Helium (years)
5	550	475
6	265	218
7	141	120
8	90	78
9	63	55
10	46	40
15	14	12
20	5.5	4.8
25	2.6	2.3
30	1.4	1.2
35	0.8	0.7

Table 4.2. Depressurization Times for Various Wall Thicknesses

Length (cm)	Argon (years)	Helium (years)
0.5	276	226
0.75	427	358
1	550	475
1.25	653	575
1.5	741	659

Another characteristic parameter of this system that is of interest is the flow rate of the gas from the system as a function of time. The molar flow rate out of the system is one of the three unknown variables that appear in Eqs. 4.13 - 4.15. Thus, this value can be determined with Mathematica in the same fashion as the time dependent pressure was determined. The curve of the molar flow rate out vs. time appears in Fig. 4.9. The initial flow rates out for several different breach radii are tabulated in Table 4.3. The results presented in Figs. 4.6 through 4.7 and Tables 4.1 through 4.3 were presented at the ANS National Conference in Reno, Nevada on June 6, 2006 [4.6].

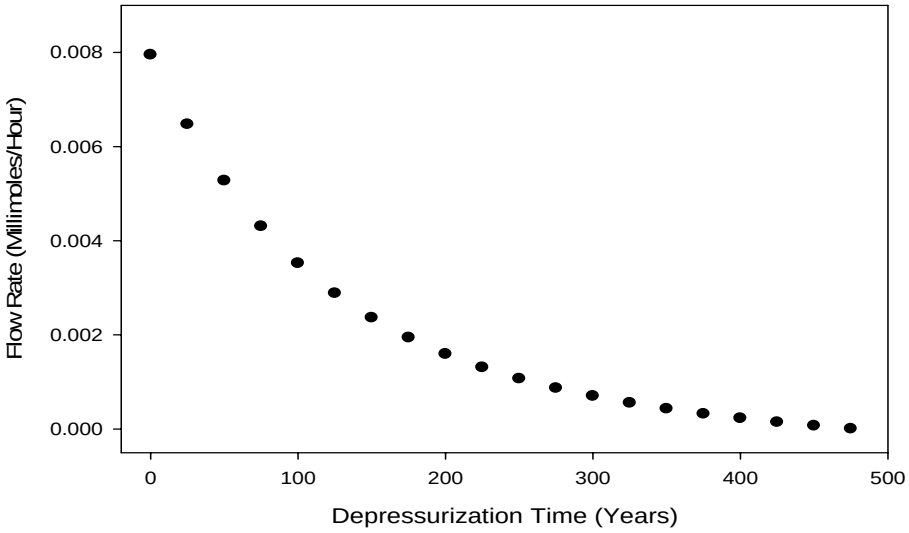

Figure 4.9: Time-Dependent Molar Flow Rate out for He, for r = 5 μm

Table 4.3: Initial Flow Rates Out for Various Breach Radii

Radius (μm)	Argon (mmol/hr)	Helium (mmol/hr)
5	0.007	0.008
6	0.014	0.017
7	0.025	0.031
8	0.043	0.052
9	0.069	0.083
10	0.11	0.131
15	0.53	0.64
20	1.7	2
25	4.1	5
30	8.5	10
35	16	19

The results presented above were generated with a model that used a heat deposition rate within the fill gas determined from Eq. 4.10. To a large extent, the accuracy of these results depends on how accurately Eq. 4.9 describes the time-dependent temperature curve of the canister if no through-wall breach forms. Figures 4.3 and 4.4

show the effect that varying a physical parameter (the ambient air temperature in this case) can have on the time-dependent temperature curve of a spent fuel storage canister. In order to quantify the effect that the time-dependent temperature function used to determine the rate of heat deposition in the fill gas has on the depressurization time of a spent fuel canister with a breach according to the model constructed in this chapter, simple modifications of Eq. 4.9 were used to generate depressurization plots. These plots are displayed in Fig. 4.10. For a better understanding of the system, the temperature curves associated with the depressurization plots in Fig. 4.10 are presented in Fig. 4.11 and the quantities of fill gas remaining within the container as a function of time for each case in Fig. 4.10 are presented in Fig. 4.12. Table 4.4 lists the depressurization time, the final temperature of the canister at the time of pressure equilibrium, and the number of moles remaining at the time of pressure equilibrium for each of the cases considered in Figs. 4.10 - 4.12. The modified closed system time-dependent temperature curves used to generate the data in Figs. 4.10 - 4.12 and Table 4.4 are

$$T(t) = 110e^{-0.014t} - 0.0514t + 348 \tag{4.17}$$

$$T(t) = 110e^{-0.014t} - 0.0514t + 398 \tag{4.18}$$

$$T(t) = 110e^{-0.014t} - 0.0514t + 498 \tag{4.19}$$

$$T(t) = 110e^{-0.014t} - 0.0514t + 548 \tag{4.20}$$

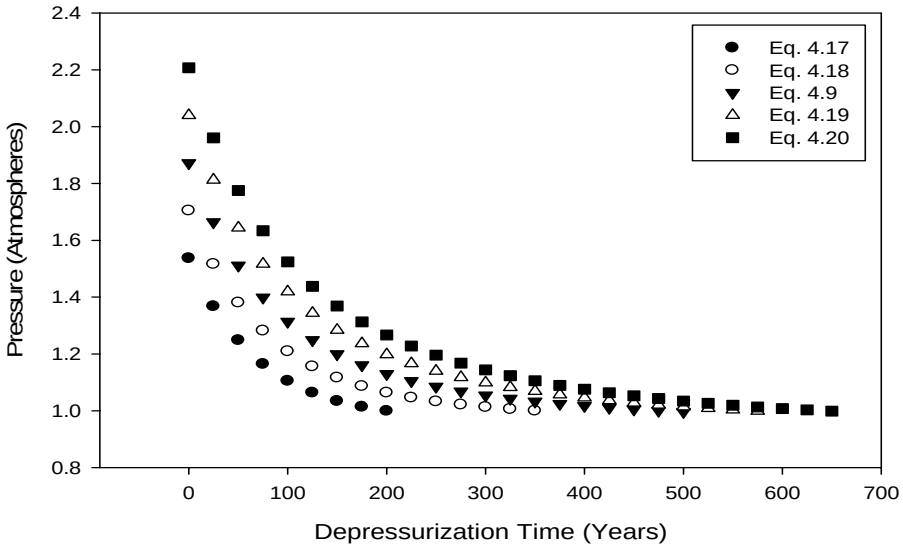

Figure 4.10: Effect of Thermal Conditions on Depressurization Time

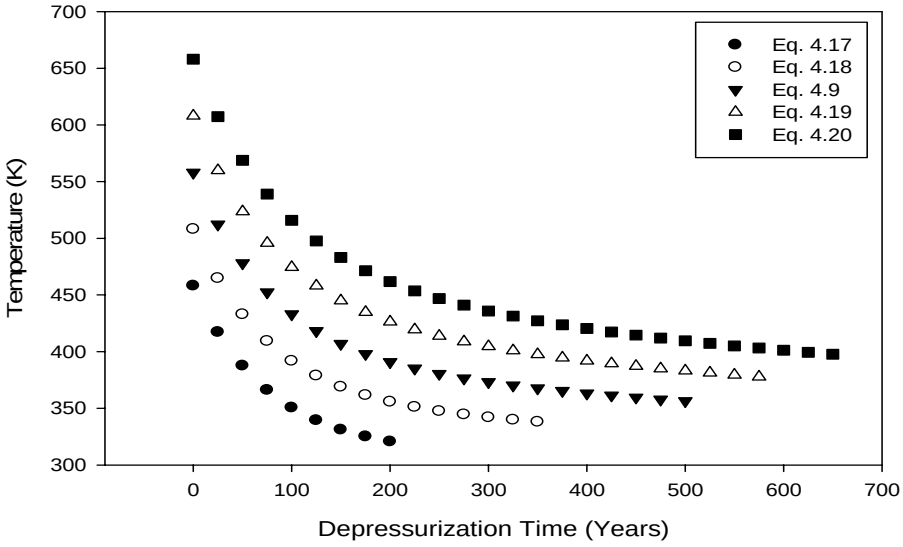

Figure 4.11: Effect of Thermal Conditions on Open-System Temperature

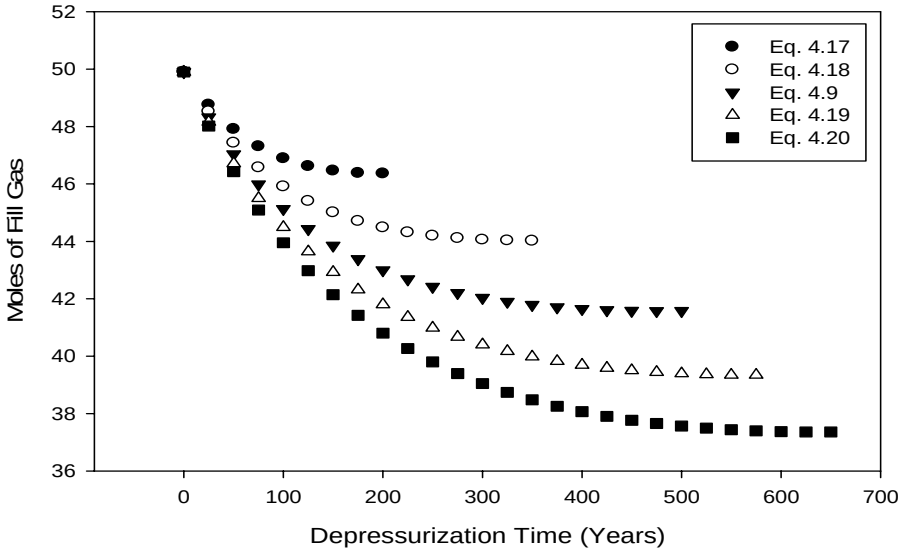

Figure 4.12: Effect of Thermal Conditions Fill Gas Loss During Depressurization Time

Table 4.4: Depressurization Parameters for Models Using Eqs. 4.9, 4.17-4.20

$T_{closed}(t)$	Depressurization Time	Final Temperature	Number of Moles
4.17	198 Years	321 K	46.4
4.18	348 Years	338 K	44.0
4.9	475 Years	358 K	41.6
4.19	570 Years	378 K	39.3
4.20	642 Years	398 K	37.4

Figures 4.10 - 4.12 and Table 4.4 demonstrate the importance of developing a good thermal model for the canister being considered. Once an appropriate quantification of the net heat flow to the fill gas has been made, the model presented in this chapter can be used to determine the depressurization time for a cask that incurs a cylindrical pinhole breach. The thermal analysis used in the model constructed in this chapter will be used for all other models constructed in this study. A more in-depth thermal study is left for future analyses of specific spent fuel storage canisters.

REFERENCES

4.1 Zwahlen, E., "Release Rate and Dose Rate Calculations of Radioactive Contaminants at the Proposed Yucca Mountain Repository," PhD Dissertation, University of California at Berkely, U.S.A. (1995).

4.2 U.S. Department of Energy, Office of Civilian Radioactive Waste Management, "Site Characterization Plan: Yucca Mountain Site, Nevada Research and Development Area, Nevada," DOE/RW-1099, U.S. Government Printing Office, Washington, D.C. (1988) p. 7-41.

4.3 O'NEAL, W.C., et al., "Preclosure Analysis of Conceptual Waste Package Designs for a Nuclear Waste Repository in Tuff," UCRL-53595, Lawrence Livermore National Laboratory, Livermore, California (1984).

4.4 Lide, D., Handbook of Chemistry and Physics, Chemical Rubber Company, 82nd Edition (2001-2002) p. 6-20.

4.5 Chapman, S., Cowling, T.G., The Mathematical Theory of Non-Uniform Gases, 3rd Edition, Cambridge University Press (1990) p. 232-233.

4.6 Casella, A., Loyalka, S.K., Hanson, B., "Pinhole Breaches in Spent Fuel Containers: Some Modeling Considerations," 94 (2006) p. 80-81.

CHAPTER 5: RADIOACTIVE SOURCE TERM

Now that the depressurization of a spent fuel canister and the associated flow of fill gas from the container have been analyzed, the possible radioactivity available for release needs to be characterized. As was mentioned in the first chapter of this thesis, the vast majority of the radioactivity within the spent fuel canister is in particulate form. For this reason, the quantity and characteristics of radioactive particulate matter within the canister will be analyzed in this chapter. Additionally, in this chapter, the flow of gases through nano-scopic pores in fuel and clad breaches will be discussed. A Monte Carlo program that has been developed to model such gas behavior will be described and its results reported in the next chapter. Even though the conditions within the fuel rods will be at relatively high pressure, the gas flows considered in the next chapter are modeled in the Monte Carlo program as if they are in the free molecular flow regime. There are reasons behind this decision. First, it has recently been suspected, due to experimental evidence, that certain fission products move through the silicon carbide layers of TRISO fuel by way of vapor transport [5.1]. If the pathways through the silicon carbide are sufficiently small, then rarefied gas conditions can lead to molecular flows within these pathways. The program presented in the next chapter was developed in order to attempt to model this phenomenon. If similarly small flow pathways develop within the spent fuel or through the fuel rod cladding, then molecular flows may occur. Even if the flows are not as rarefied as implied by the free molecular flow Monte Carlo program presented in the next chapter, the program provides a basis upon which to build future programs

that take into consideration particle-particle interactions through a Direct Simulation Monte Carlo technique.

The transport of radioactivity associated with fission gases is not the sole reason that it is relevant to consider the molecular flow of gases through spent fuel and its cladding. Of equal or greater importance is the build up helium associated with the alpha decay of transuranics formed through neutron absorption while the fuel was being irradiated. If the helium and fission gases can be transported through the fuel matrix where they are formed to the fuel-clad gap, then they can contribute to an increase in the pressure within the cladding.

In order to determine the conditions promoting transport of gas and particles from within the fuel rod to the volume of the canister, it is important to characterize the pressure within the fuel rod over time. The baseline pressure within a fuel rod is the pressure associated with the backfill gas. Fuel rods are generally backfilled with helium to promote heat transfer. The rods are generally filled with helium to a pressure between 2 and 3.5 MPa at an assumed initial temperature of 300 K [5.2]. Any subsequent pressure due to the initial fill gas can be calculated from these initial values by using the ideal gas law. This backfill pressure is the pressure in the fuel-clad gap and plenum. So if fission gases are trapped within the fuel matrix itself, then the pressure they experience may be very different.

It has been proposed that the total amount of fission gas produced in a fuel rod is linearly related to the burnup that the rod experiences through the ratio 31 cm^3 (STP)/MWd, where STP is defined to be 273 K and 0.1 MPa [5.3, 5.4]. This gas is formed in the fuel matrix and the majority of it stays there. Only the fraction that is

transported to the fuel-clad gap and the plenum will contribute to the internal pressure exerted on the cladding. Thus, the volume of fission gases in the open space within a fuel rod is equal to the product of the ratio 31 cm^3 (STP)/MWd, the burnup of the rod (MWD/MTU), and the mass of the rod (MTU). The ideal gas law can be used to determine the moles of gas that this volume constitutes. The fraction of the fission gases produced that escapes to the fuel-clad gap and the plenum is called the fission gas release fraction (FGR). The product of the volume of gas produced and the FGR will specify the volume of fission gas that is released to the interior volume of the fuel rod. This gas volume will be at STP and the ideal gas law can be used to determine the volume and pressure contribution this gas volume will contribute according to the conditions within the fuel rod. Although the FGR tends to increase with burnup, in nearly all observed cases, it has been determined to be less that 5%. Fuel that is subjected to operational transients leading to thermal spiking may exhibit a larger FGR than this. Table 5.1 shows the experimentally determined FGR for several fuel irradiated fuel rods [5.3]. The majority of the fission gas is composed of isotopes of krypton and xenon. All of these isotopes are stable except for Kr-85, which has a 10 year half-life. Since roughly 4.61% of the krypton in the fission gas is Kr-85, it is assumed that the amount of fission gas within a fuel rod is constant over time. Although the FGR increases over time as more fission gas escapes the fuel matrix, this increase is apparently very small. It is currently generally assumed that fission escape from the fuel matrix through diffusion, and that this diffusion decreases rapidly with temperature decrease over time. This was the same assumption made for the movement of vapors through TRISO fuels mentioned earlier. It is suggested in this work however that since the spent fuel is porous at the rim and

fractured on a nano-scopic scale throughout, it is possible that the transport of gas out of the fuel matrix may occur by way of molecular transport. This is the justification of the Monte Carlo program to be discussed in the next chapter.

Table 5.1: Observed Fission Gas Release Fractions [5.3]

Row No.	Fuel Vendor	Reference	Burnup (MWD/kgU)				
			20	40	50	60	80
			Fraction of Fission Gas Released (%)				
1	CE	Garde (1986), Fig. 4 Best Est.	0.5	0.8	1	2	N/A
2	CE	Garde (1986, Fig.4) High Value	1	3.3	3.8	4.5	N/A
3	CE	Garde (1986, Table 4) Average of 12 measurements	N/A	N/A	0.94	N/A	N/A
4	Siemens	Manzel et al. (1997, Fig. 1) Best Est.	6	6.6	7.5	8.6	14
5	Siemens	Manzel et al. (1997) High Value	N/A	8	9	10	N/A
6	Framatome	Morel et al. (1994, Fig. 4) Best Est.	0.3	0.8	1.8	3	N/A
7	Siemens	Van Swam et al. (1997a, Fig. 9) Best Est.	N/A	1	3	4.5	8
8	Siemens	Van Swam et al. (1997a, Fig. 9 High Value	N/A	N/A	3.2	5	9
9	B&W	Bain et al. (1985, Fig. 4), Best Est.	N/A	1.5	1.6	N/A	N/A
10	B&W	Bain et al. (1985, Fig. 4) High Value	N/A	3.4	3.8	N/A	N/A
11	N/A	Median for CCDF	1.69	2.14	2.98	4.53	11.00
12	N/A	Average High Values	N/A	4.90	4.95	6.50	N/A
13	N/A	Average High/Median	N/A	2.29	1.64	1.44	N/A
14	CE	Manaktala (1993, Fig. 3-5) Maine Yankee	12 to 15	N/A	N/A	N/A	N/A
15	Westing-house	Barner (1985, ATM-101, p. 4.9) (10 rods)	0.15 to 0.27	N/A	N/A	N/A	N/A
16	CE	Guenther et al. (1988a ATM-103, p. 4.15)	0.25 (@ 30 MWd/kgU)		N/A	N/A	N/A
17	CE	Guenther et al. (1991 ATM-104, p. 8.9) (3 rods measured)	N/A	0.38, 0.62, 1.10	N/A	N/A	N/A
18	CE	Guenther et al. (1988b, ATM-106, p.2.1) (3 rods measured)	N/A	1.4, 7.4, 11.2	N/A	N/A	N/A
19	GE	Lanning et al. (1997, Transients, Tbl. 2.2)	3.5-38	3.5-44.1	13-14.4	22-34	N/A

The creation of helium within the fuel and subsequent transport from the fuel into the fuel-clad gap and plenum may also be governed by molecular transport. The

importance of helium production and release is greater over longer periods of time. Assuming that all helium produced by alpha decay is immediately released into the free volume inside the cladding of the fuel rod with a burnup of 36 MWd/kgU at 100ºC, the partial pressure of helium in the free volume is estimated to be [5.3, 5.5, 5.6]

$$P_{He}(MPa) = 0.019953t^{0.65} \quad , t \leq 1{,}000\ years$$
$$P_{He}(MPa) = 0.17783t^{0.3333} \quad , t > 1{,}000\ years \tag{5.1}$$

The contributions of the initial backfill helium gas, fission gases, and helium production from alpha-decay over time are compared in Table 5.2 [5.3].

Table 5.2: Pressure Contribution Over Time from Helium and Fission Gases [5.3]

Time (yr.)	Temperature (°C)	Helium Pressure (MPa)	Fission Gas Pressure (MPa)[a]	Total Pressure (MPa)	He % of total Pres.
1	210	0.03	6.44	6.5	0.40
10	240	0.12	6.84	7.0	1.76
100	150	0.45	5.64	6.1	7.41
1,000	104	1.80	5.03	6.8	26.34
10,000	79	3.62	4.69	8.3	43.51
100,000	27	6.64	4.00	10.6	62.40
1,000,000	27	14.30	4.00	18.3	78.15

a: Initial fill and fission gas pressure assumed to be 4 MPa at 27°C.
DTN: MO0001SPAICC48.037

This pressure build-up from fission gases and helium just discussed, can lead to stress that can lead to possible Delayed Hydride Cracking (DHC) and strain failure of the cladding, resulting in the release of gas and particulate spent fuel into the free volume of the spent fuel canister. If the cladding remains intact, but very small pathways are present in the cladding due to stress-corrosion cracking or whatever mechanisms, then this helium and/or other gases in the fuel-clad gap may be transported through molecular

flow into the free volume of the canister. This addition of gas can affect the time dependent pressure and depressurization times discussed in the previous chapter. Additionally, in many higher burnup fuels, the fuel expands and the cladding creeps down. These two phenomena may cause the fuel-clad gap to disappear. In such a case, the fission and decay gases will exist within the porous, cracked fuel matrix and the fuel rod plenum. The pathways through which the gas can flow within this matrix may allow for continuum, slip, transition, or molecular flows, depending on the physical dimensions of the pathway. These flow regimes are generally categorized according to the Knudsen number associated with the system defined as [5.7]

$$Kn = \frac{\lambda}{L} \tag{5.2}$$

where λ is the mean free path of the gas, defined as [5.8]

$$\lambda = \frac{1}{\sqrt{2} n \pi d_m^2} \tag{5.3}$$

and L is a characteristic length of the system which for the purposes of this study will be considered to be the distance across the pathway through which the gas is flowing. In Eq. 5.3, d_m is the collision diameter of the gas and n is the number density of the gas. If it is assumed that the pathway through which the gases are flowing is a circular tube, then the characteristic length will be the diameter of the tube. For very small Knudsen number values, gas flows can be described with continuum models using the Navier-Stokes

equations. As the Knudsen number increases above the value 0.1 however, the error associated with continuum models gets very large, and for Knudsen number values greater than 0.2, molecular models must be employed to describe the flows. The higher the value of the Knudsen number, the fewer particle-particle interactions occur and the gas can be modeled as being in the free molecular flow regime. In order to provide a feel for the conditions within the spent fuel canister for which the gas transport will be in the free molecular flow, transition, slip, and continuum regimes, Table 5.3 has been constructed. This table lists the mean free path of helium at temperatures and pressures that may exist within the spent fuel canister.

Table 5.3: Mean Free Paths and Knudsen Number Values for Various System Parameters

Pressure = 4 MPa, tube diameter = 0.1 µm			Pressure = 2 MPa, tube diameter = 0.1 µm			Pressure = 4 MPa, tube diameter = 0.01 µm			Pressure = 2 MPa, tube diameter = 0.01 µm		
T (K)	λ (nm)	Kn	T (K)	λ (nm)	Kn	T (K)	λ (nm)	Kn	T (K)	λ (nm)	Kn
600	10.1	0.101	600	20.2	0.202	600	10.1	1.01	600	20.2	2.02
500	8.4	0.084	500	16.8	0.168	500	8.4	0.84	500	16.8	1.68
400	6.72	0.067	400	13.4	0.134	400	6.72	0.672	400	13.4	1.34
300	5.05	0.0504	300	10.1	0.101	300	5.05	0.504	300	10.1	1.01
Pressure = 4 MPa, tube diameter = 1 nm			Pressure = 2 MPa, tube diameter = 1 nm			Pressure = 3 MPa, tube diameter = 0.1 µm			Pressure = 1 MPa, tube diameter = 0.1 µm		
T (K)	λ (nm)	Kn	T (K)	λ (nm)	Kn	T (K)	λ (nm)	Kn	T (K)	λ (nm)	Kn
600	10.1	10.084	600	20.2	20.2	600	13.4	0.1344	600	40.3	0.403
500	8.4	8.403	500	16.8	16.8	500	11.2	0.112	500	33.6	0.336
400	6.72	6.722	400	13.4	13.4	400	8.96	0.0896	400	26.9	0.269
300	5.05	5.042	300	10.1	10.1	300	6.72	0.0672	300	20.2	0.202
Pressure = 3 MPa, tube diameter = 0.01 µm			Pressure = 1 MPa, tube diameter = 0.01 µm			Pressure = 3 MPa, tube diameter = 1 nm			Pressure = 1 MPa, tube diameter = 1 nm		
T (K)	λ (nm)	Kn	T (K)	λ (nm)	Kn	T (K)	λ (nm)	Kn	T (K)	λ (nm)	Kn
600	13.4	1.344	600	40.3	4.03	600	13.4	13.44	600	40.3	40.3
500	11.2	1.12	500	33.6	3.36	500	11.2	11.2	500	33.6	33.6
400	8.96	0.896	400	26.9	2.69	400	8.96	8.96	400	26.9	26.9
300	6.72	0.672	300	20.2	2.02	300	6.72	6.72	300	20.2	20.2

Table 5.3 shows that the Knudsen number describing the system can be very high for nano-scale flow pathways at lower pressures and higher temperatures. Table 5.2

suggests that over time, much higher pressures will develop within the fuel rod, and the temperature will drop. This information suggests that Knudsen number will be lowered with time and that intermolecular interactions will need to be accounted for in order to model the system correctly. However, if the cladding of a fuel rod is breached, and the built-up gases within the free volume of the rod are released to the free volume of the spent fuel canister, then the pressure within the fuel rod can be expected to be much closer to 0.2 MPa. At this pressure, for smaller flow pathway dimensions, free molecular flow models might describe the gas flows fairly accurately. The model that will be presented later in this chapter can be modified to account for intermolecular interactions for more accurate modeling of higher pressure systems in the future.

Before discussing the Monte Carlo program for modeling the molecular flow of gases, the sources of particulate radioactivity will be addressed. Three reports have been produced by Sandia National Laboratory in order to determine the concentration and composition of radioactivity in spent fuel transportation casks [5.9, 5.10, 5.11]. These reports isolate three separate sources of radioactivity within the container and each report is dedicated to one of these sources. The three identified sources are activated corrosion build-up on the outside of fuel rods known as Chalk River Unidentified Deposits or CRUD, residual contamination, and the fission and activation products located within the fuel rod cladding. Collectively, these three sources are known as the radioactive "source term" within the container. This source term has been defined as, "…the amount of dispersible radioactive species within the cask that are available for release" [5.9]. If the cladding of each of the fuel rods remains intact, then the fission and activation products are not "available for release." In this situation, the only sources of radioactivity within

the container are CRUD and residual contamination. For the sake of clarity, residual contamination is defined as, "radioactive contaminants that build up on the cask internal surfaces as a result of previous loading and transport operations" [5.10]. In the case that the canister under consideration has never been used before, there would be no residual contamination. This differentiation of particulate radioactivity sources allows for model simplification and categorization. If it is desired to create estimates of the particulate population available for suspension, the easiest model to construct will be a canister that is being used for the first time and in which all of the fuel rod cladding is intact. Additional particulates from breached fuel rods and residual contamination can then be added to the first use canister with intact fuel rod cladding case which can be treated as a baseline case.

Since the single source of particulate radioactivity in the baseline case is CRUD, it is necessary to do an investigation of the CRUD properties. As was mentioned previously, a fairly vigorous report on the properties of CRUD was created by Sandia National Laboratory in 1991 [5.9]. Some interesting characteristics of CRUD discussed in this report are discussed in the following paragraph.

There are at least two distinct types of CRUD which have been christened "flocculent" and "tenacious." The flocculent CRUD is described as, "…a fluffy, easily removed CRUD, usually found on BWR rods, and composed mainly of hematite (Fe_2O_3). The tenacious CRUD is described as, "…tightly bound to the rods, usually found on PWR rods, and composed mainly of a nickel-substituted spinel (i.e. $Ni_xFe_3\text{-}xO_4$, with $x \sim 1$) [5.9]. Thus, it seems that the CRUD contribution to the source term will be different for canisters containing BWR assemblies and those containing PWR assemblies. Since

the CRUD on BWR assemblies is more easily removed, it is reasonable to conclude that more of it will be spalled into the free volume of the canister than the CRUD on PWR assemblies. However, this may not be entirely correct. Examinations of Oconee PWR fuel between 1978 and 1982 showed that the characteristics of the CRUD changed over time while the assembly was kept in a storage pool. The Oconee CRUD transformed from tenacious to flocculent over this time period [5.9]. Thus, it appears that PWR CRUD can transform to a state in which it can be more easily removed like BWR CRUD. This transformation is not ubiquitous however, as it has only been reported in this one case. The amount of CRUD that is deposited on fuel rods varies between reactors and between irradiations at the same reactor. The main parameter affecting CRUD build-up seems to be water chemistry. In fact, improvements in water chemistry have already resulted in smaller CRUD deposits and it is expected that this trend will continue into the future. For the sake of being conservative, one can assume for modeling purposes that all of the CRUD is of the flocculent type and is easily spalled and suspended by the fill gas in the free space within the container.

Thus, when modeling particulate suspension behavior within a spent fuel canister, it is important to consider the quantity of CRUD in the container and the propensity of that CRUD to become suspended. The Sandia report regarding residual contamination simply adds to the quantity of dispersible CRUD within the canister and claims that this amount is a function of the previous uses of the canister [5.10].

The third Sandia report addresses the radioactive material that exists within the confines of the fuel rod cladding [5.11]. This material is divided into three categories: gases such as Krypton-85 and tritium, volatile species such as Cs-134 and Cs-137, and

nonvolatile species consisting of fuel particles. These materials are formed in the fuel matrix and the majority of them stay in the fuel matrix. The transport of the materials out of the matrix is believed to be through the mechanism of diffusion and that this diffusion can only take place during the first five years after discharge from the reactor for thermal reasons. If a breach in the cladding forms, gases and volatile species are assumed to burst through the cladding into the free volume of the spent fuel canister. During this burst, some particulate matter is suspended in the free volume of the spent fuel canister as well. No additional releases are believed to occur after equilibrium conditions between the external and internal cladding environments are reached. This belief may not be true if helium continues to build up within the fuel matrix, leading to molecular transports and pressurized pockets that may eventually rupture. It is claimed that during a rupture event, roughly 0.003% of the fuel contained in a rod appears to be released as fines. The amount of material from each of the three categories released during a rupture event appears to be independent of the location on the fuel rod of the rupture. After the rupture event and subsequent rod depressurization, the gaseous and volatile materials are assumed to be homogeneously dispersed throughout the free volume in the spent fuel canister. A large quantity of the fines is assumed to come out of suspension due to gravitational settling and deposition on surfaces. In fact, 90% of the particulate matter ejected during a rupture event is assumed to settle within a few inches of the breach and 10% is assumed to be widely distributed and is conservatively assumed to be suspended for “long” periods of time. Although some rods may fail due to stress associated with built-up pressure, the majority of clad ruptures are assumed to occur due to pellet-clad interaction (PCI) induced stress-corrosion cracking. All forms of breach formation

except for oxidation are assumed to occur slowly and to produce pinholes or cracks varying in size from 1 to 30 micrometers. In experiments where spent fuel was purposely oxidized to U_3O_8 at 480ºC, 100% of the tritium inventory was released, 4 to 6% of the Kr-85 inventory was released, and only 0.1 to 0.2% of the ruthenium, cesium, and cerium was released. The oxidation did turn the fuel into a powder form that may be much more dispersible and contribute significantly to the fines source term. For temperatures not exceeding 350ºC, further releases from the oxidized fuel are considered inconsequential.

The data summarized above from the third Sandia report discusses the physical form, location, and mobility of the radioactive material contained within the fuel rod cladding. If a quantitative analysis of the inventory of radioactive materials within the fuel rod is desired, it can be generated with the ORIGEN code or the ORIGEN-ARP module in the SCALE code discussed in Chapter 3. The quantity and form of the radioactive material having been discussed, it is now necessary to discuss the behavior of this material once it reaches the free volume of the spent fuel canister. The gases will become mixed with the helium backfill gas within the canister. The volatile materials will remain mixed with the backfill gas as well until the temperature drops to the extent that they are condensed out. The particulate matter however, is the most interesting of the three material forms. In order to describe the particulate matter behavior, several parameters must be considered. These parameters include the pressure, temperature and bulk motion of the fill gas in the container. In addition, it is important to know the size and quantity of particulates that are present in the container and the mechanisms through which they can be suspended in the fill gas. Regarding the conditions of the fill gas, there are two bounding conditions: tranquil settling and infinitely stirred settling.

In the case of tranquil settling, it is assumed that the fill gas is completely still and that there is no bulk motion. In this case, the particles suspended in the fill gas simply settle to the bottom of the container at a terminal velocity under the influence of gravity. In this scenario, the particles must initially be suspended by a mechanical force. This means that after the container is placed in its final storage position, and there are no outside forces, the particles will simply settle. Once the particles settle and attach to a surface, if there is no outside physical mechanism for dispersion, they will not enter re-suspension in the fill gas. Thus, if a breach occurs, the aerosol particles will not be present for plugging. On the other hand, they will not be present for release to the environment either. Depending on the size of the breach and the differential pressure between the inside and outside of the container, the breach may cause enough disturbance in the fill gas to create currents strong enough to cause re-suspension. If there are no external forces or internal fill gas drafts, then the time that it takes for a particle to settle out of suspension after the initial suspending event is simply equal to the height of the particle above the settling surface divided by the particle's terminal settling velocity. A more precise assessment is to say that the time that it takes for the particle to settle out of suspension in still tranquil air after the event that caused the particles original suspension is given by the equation:

$$t_s = \frac{h}{V_{TS} - (V_{TS} - V_0)e^{-t/\tau}} \tag{5.4}$$

where t_s is the settling time of the particle, h is the height that the particle is suspended above the settling surface, V_{TS} is the terminal settling velocity of the particle, V_0 is the

initial vertical velocity of the particle due to the suspending event, t is the elapsed time after the suspending event, and τ is the relaxation time of the particle. The relaxation time of the particle is, "…the time required for a particle to adjust or "relax" its velocity to a new condition of forces" [5.8]. In other words, it is the time that it takes for the velocity of the particle to change from its current value to the terminal settling velocity.

The case of infinitely stirred settling is much closer to the case that was modeled in the previous chapter. In this case, it is assumed that the motion of the fill gas due to convection currents is extensive enough to cause the concentration of suspended particles to be uniform throughout the entire volume occupied by the fill gas. It is assumed that no particles adhere to the side of the container and that all particles are settling toward the bottom of the container. During any given small amount of time dt, the ratio of the number of particles that settle on the bottom of the container to the total number of particles suspended in the container is given by [5.8]:

$$\frac{dn}{n} = \frac{V_{TS}\,dt}{H} \tag{5.5}$$

where H is the height of the container. The numerator of the RHS of Eq. 5.5 is just the product of the terminal velocity of the particles and the time period being considered. Thus, this quantity is a distance. In fact, it is the height above the bottom of the container below which all particles will be forced to contact the bottom of the container during the time dt. Thus, the RHS of Eq. 5.5 is the ratio of the height of the container below which all particles are removed to the total height of the container. This quantity is equivalent

to the ratio of the number of particles removed to the total number of particles. If both sides of Eq. 5.5 are integrated, then the result is [5.8]:

$$n(t) = n_0 e^{-\frac{V_{TS} t}{H}} \tag{5.6}$$

where n_0 is the total number of suspended particles at $t = 0$. Eq. 5.6 neglects the effects of diffusion, resuspension, and deposition on walls. Notice that the time that it takes for the particles to settle out of suspension is much greater for the infinitely stirred case. Unless a fuel rod ruptures and introduces a timed-release of particles into the fill gas, the behavior of suspended particles inside the container will be bounded between Eq. 5.4 and Eq. 5.6. A more in-depth investigation into whether the particles are more closely described by Eq. 5.4 or Eq. 5.6 can be undertaken with the aid of a computational fluid dynamics program such as FLUENT®.

In regard to the characteristics of the particulates formed from CRUD, the Sandia report on CRUD contribution to the source term [5.9] reviewed over 200 documents for this information. This report concluded that as of January 1991, the only detailed information of CRUD particle size distributions available was from a study of spent fuel from the Quad Cities reactor. The information regarding this CRUD was gathered from two photomicrographs of the spent fuel and it was determined that the CRUD particle sizes belonged to a lognormal distribution. The number geometric mean diameter of this distribution was 3.0 micrometers and the standard deviation was 1.87 micrometers. The mass median diameter was determined to be 9.7 micrometers. It should be noted that the Quad Cities reactor is a BWR. The Sandia report claims that no such characterization of

the size distribution of CRUD particles from a PWR had been performed [5.9.]. Although the data regarding the particle size of the Quad Cities reactor was statistically categorized as stated above, there is another piece of information that should be considered. The SEM photomicrographs showed that the particulates were actually agglomerations of primary particles that had diameters from 0.5 micrometer to 1.0 micrometer. This is interesting because analysis from the Brunswick-2 BWR showed that the CRUD consisted of primary particulates with diameters from 0.1 micrometer to 0.3 micrometer, but that these particulates agglomerated into larger particulates with diameters from 1 micrometer to 3 micrometers. Similarly, analysis from the Monticello BWR showed that the CRUD consisted of primary particulates with diameters from 0.1 micrometer to 0.3 micrometer and these primary particulates agglomerated into larger particulates with diameters from 0.5 micrometer to 2 micrometers. Analysis from the Nine Mile Point BWR showed that the CRUD particulate size was predominately 0.1 micrometer. It should be noted that the SEM photomicrographs of the CRUD from the Quad Cities reactor were taken of the CRUD still on the cladding surface. In the case of the CRUD from Brunswick-2, Monticello, and Nine Mile Point, the SEM photomicrographs were made of CRUD that was scraped off the cladding while it was underwater and the particulates were captured on filter paper. Two SEM photomicrographs were also made of the CRUD still on the cladding of 2 PWRs. Analysis from the Point Beach PWR showed that the CRUD consisted of primary particles with diameters from 0.3 micrometer to 0.5 micrometer and these primary particles agglomerated into particles with diameters between 1 micrometer and 3 micrometers. Analysis of the H. B. Robinson PWR showed that the particulates had

diameters between 1 micrometer and 3 micrometers. An argument can be made that the sizes of particulates that would form from a physical spallation event would be different than those observed in the analysis above. This case seems especially compelling for the particulate sizes that were determined from CRUD that was scraped from the cladding under water and collected on filter paper. It is reassuring however, that the particulate sizes determined by way of this method closely match those determined from direct observation of the CRUD while it was still on the cladding.

Most of the particle sizes presented above are much too large to stay in suspension for very long inside the container. The smallest observed particulates in the analyses above had diameters of about 0.1 micrometers. A particle of this size is most likely in the Stokes flow regime for which the terminal settling velocity is defined as [5.8]:

$$V_{TS} = \frac{\rho_p d^2 g C_c}{18\mu} \tag{5.7}$$

where ρ_p is the particle density, d is the diameter of the particle, g is the acceleration due to gravity and μ is the viscosity of the suspending gas. The midrange of experimentally determined density values of CRUD is 1.1 g/cm^3 [5.9]. The viscosity of the gas is dependent on the temperature. For analysis in the Sandia report, a container gas temperature of 400K was assumed [5.9]. The viscosity of helium at 400K and 1 atmosphere is 24.29 μPa s [5.12]. This value for the viscosity can be used for the current situation because viscosity does not vary appreciably with small pressure changes.

The first step in this analysis is to determine whether or not the particle sizes to be considered here actually do behave according to Eq. 5.7. Two limitations for the use of Eq. 5.7 are that the particle Reynolds number must be less that 1.0 and the particle cannot be too small. As the size of the particle gets smaller, Eq. 5.7 must be adjusted for the effect of slip. This adjustment is made by multiplying the right hand side of Eq. 5.4 by a slip correction factor defined as [5.8]:

$$C_c = 1 + \frac{\lambda}{d}[2.34 + 1.05e^{-0.39\frac{d}{\lambda}}] \tag{5.8}$$

where λ is the mean free path defined by Eq. 5.3. In general, the validity of Eq. 5.7 starts to decline for particles with diameters less than 1 μm, so the correction factor of Eq. 5.8 must be used [5.8]. As particle sizes get too large however, the particle Reynolds number begins to become too large and Eq. 5.7 cannot be used at all. Instead, for particle Reynolds numbers larger than 1.0, the particle settling motion is described by [5.8]:

$$V_{TS} = \left(\frac{4\rho_p d_p g}{3C_D \rho_g} \right)^{\frac{1}{2}} \tag{5.9}$$

where C_D is the coefficient of drag. The equation for determining the particle Reynolds number is [5.8]:

$$\mathrm{Re} = \frac{\rho V d}{\mu} \tag{5.10}$$

where the density ρ is the density of the gas.

Table 5.4 gives the particle Reynolds number, the slip correction factor, the terminal settling velocity of the particle according to Eq. 5.7 and the slip-corrected terminal settling velocity of the particle according to the particle size for T = 400K. If we stick to the parameters that Zwahlen used in his analysis, then the value of n in Eq. 5.3 is 2.46×10^{25} molecules/m^3 [5.13]. Also, the value of the collision diameter (d_m) for helium is 2.15×10^{-10} meters [5.12]. Thus, the value of λ to be used here is 1.98×10^{-7} meters. The density of helium at 400K and 1 atmosphere is 0.04 mol/L [5.12]. For helium, a molar density of 0.04 mol/L is equal to 0.16 kg/m^3.

Table 5.4: Settling of Particles in Helium-Filled Dry Storage Container at 400K

d_p (μm)	V_{TS} (m/s)	Re	C_C	$V_{TS} \times C_C$ (m/s)
0.1	2.47E-07	1.62E-10	7.34	1.81E-06
0.2	9.86E-07	1.30E-09	4.02	3.96E-06
0.3	2.22E-06	4.39E-09	2.93	6.49E-06
0.4	3.94E-06	1.04E-08	2.39	9.44E-06
0.5	6.16E-06	2.03E-08	2.08	1.28E-05
0.6	8.88E-06	3.51E-08	1.88	1.67E-05
0.7	1.21E-05	5.57E-08	1.74	2.10E-05
0.8	1.58E-05	8.32E-08	1.63	2.58E-05
0.9	2.00E-05	1.18E-07	1.55	3.10E-05
1	2.47E-05	1.62E-07	1.49	3.68E-05
1.1	2.98E-05	2.16E-07	1.44	4.30E-05
1.2	3.55E-05	2.81E-07	1.4	4.98E-05
1.3	4.17E-05	3.57E-07	1.37	5.70E-05
1.4	4.83E-05	4.46E-07	1.34	6.48E-05
1.5	5.55E-05	5.48E-07	1.32	7.30E-05
1.6	6.31E-05	6.65E-07	1.29	8.17E-05
1.7	7.13E-05	7.98E-07	1.28	9.10E-05
1.8	7.99E-05	9.47E-07	1.26	1.01E-04
1.9	8.90E-05	1.11E-06	1.25	1.11E-04
2	9.86E-05	1.30E-06	1.23	1.22E-04
2.1	1.09E-04	1.50E-06	1.22	1.33E-04
2.2	1.19E-04	1.73E-06	1.21	1.45E-04
2.3	1.30E-04	1.98E-06	1.2	1.57E-04
2.4	1.42E-04	2.25E-06	1.19	1.70E-04
2.5	1.54E-04	2.54E-06	1.19	1.83E-04
2.6	1.67E-04	2.85E-06	1.18	1.96E-04
2.7	1.80E-04	3.20E-06	1.17	2.11E-04
2.8	1.93E-04	3.57E-06	1.17	2.25E-04
2.9	2.07E-04	3.96E-06	1.16	2.41E-04
3	2.22E-04	4.39E-06	1.15	2.56E-04

From Table 5.4, it is clear that under the conditions that are expected to be prevalent in the spent fuel container, the particles of the size we expect to encounter will be in the Stokes region. However, it appears to be necessary to use the slip correction factor for all particle sizes. This appears to be the case because the density, viscosity, and mean free path of helium under the conditions we are concerned with are different that these same properties of air at standard conditions. If we consider the slip-corrected

terminal settling velocity that appears in the final column of Table 5.4 to be the true settling velocity for the particles of various size, then we can use this value to determine the particle concentration in the container at a given time after the spalling event. If we assume that the relaxation time τ is close to zero, which is true for most aerosol particles, then Eq. 5.3 simplifies to:

$$t = \frac{h}{V_{TS}} \tag{5.9}$$

If we take the value of h to be 6.096 meters (the height of a vertical Ventilated Concrete Cask), then according to Eq. 5.9, it will take roughly 6.6 hours for all of the 3 μm particles to settle and roughly 286 days for all of the 0.1 μm particles to settle. The settling times for particles of all intermediate sizes are found between these two values.

If instead of assuming that the helium inside the spent fuel container is still, we assume that there is so much convective motion that the aerosol in the container is infinitely mixed, the particles remain suspended for a much longer time. If both sides of Eq. 5.6 are divided by n_0, then the equation gives the fraction of the particles that remain suspended at any given time. For still conditions above, it was determined that all of the particles with sizes between 0.1 μm and 3.0 μm will settle out of suspension after 286 days. According to Eq. 5.6, after that amount of time, 36.8% of the particles will remain suspended in the fill gas. Further investigation shows that according to Eq. 5.6, after 572 days (1.57 years), 13.5% of the original particles are suspended, after 1044 days (2.86 years), 1.8% of the original particles are suspended and after 2088 days (5.72 years), 0.03% of the original particles are still suspended. So, even if convection currents do

exist within the container, if there is no re-suspension occurring, then after 5 years, there will be virtually no aerosol left in suspension within the container. This leads to the conclusion that particles will not be present in the fill gas for very long. This conclusion is based on the assumption that there are not multiple events leading to aerosol spallation.

There are two situations that can change the conclusion made above. The first is that the original concentration of particles in the fill gas is higher than that expected from the CRUD contribution. The second is that a continuous source of aerosol spallation exists within the container. As mentioned above there are three sources of radioactivity within the container: CRUD, residual contamination, and the fission and activation products within the fuel rod cladding. The residual contamination only occurs in transportation casks that are being reused. As can be expected, the contribution of radioactivity from residual contamination is minor compared to the CRUD contribution. The source that has the greatest potential for radioactive particle contribution is the build-up of fission and activation products within the cladding. If breaches occur in the cladding of one or more fuel rods then the possible concentration of particulates that can be suspended within the fill gas has the possibility of being much higher. Except for restructured rim material where particle sizes are on the order of 0.1 μm, fuel grain sizes are roughly 5 μm. However, if the fuel is oxidized to U_3O_8, then much smaller fuel particle sizes are possible. These particles will be subject to the same settling conditions as the CRUD particles mentioned earlier. Thus, they will most likely only be present in significant quantities within relatively short time periods after a release event.

REFERENCES

5.1 MacLean, H.J., "Silver Transport in CVD Silicon Carbide," Ph.D Thesis, Massachusetts Institute of Technology (2004).

5.2 U.S. Department of Energy, Office of Civilian Radioactive Waste Management, "Characteristics of Potential Repository Wastes," DOE/RW-0184-R1, Volume 1, (1992).

5.3 CRWMS M&O, "Initial Cladding Condition," DN2002143802, MOL.20000523.0150 (2000).

5.4 Rothman, A.J., "Potential Corrosion and Degradation Mechanisms of Zircaloy Cladding on Spent Nuclear Fuel in a Tuff Repository," UCID-20172, Livermore, California: Lawrence Livermore National Laboratory, ACC: NNA.19870903.0039 (1984).

5.5 Manaktala, H.K., "Characteristics of Spent Nuclear Fuel and Cladding Relevant to High-Level Waste Source Term," CNWRA 93-006, NRC-02-88-005, San Antonio, Texas: Center for Nuclear Waste Regulatory Analyses, TIC: 208034 (1993).

5.6 Johnson, A.B., Jr., Gilbert, E.R., "Technical Basis for Storage of Zircaloy-Clad Spent Fuel in Inert Gases," PNL-4835, Richland, Washington: Pacific Northwest Laboratory, TIC: 9151 (1983).

5.7 Bird, G.A., Molecular Gas Dynamics and the Direct Simulation of Gas Flows, Clarendon Press, Oxford (1994).

5.8 Hinds, W.C., Aerosol Technology: Properties, Behavior, and Measurement of Airborne Particles, 2nd Ed., John Wiley & Sons, Inc., New York (1999).

5.9 Sandoval, R.P., Einziger, R.E., Jordan, H., Malinauskas, A.P., and Mings, W., "Estimate of CRUD Contribution to Shipping Cask Containment Requirements," Sandia National Laboratories, Albuquerque, NM, SAND88-1358, TTC-0811, (1/1991).

5.10 Sanders, T.L., Jordan, H., Pasupathi, V., Mings, W., and Reardon, P.C., "A Methodology for Estimating the Residual Contamination Contribution to the Source Term in a Spent-Fuel Transport Cask, " Sandia National Laboratories, Albuquerque, NM, SAND90-2407, TTC-1020, (9/1991).

5.11 Sanders, T.L., Seager, K.D., Rashid, Y.R., Barrett, P.R. , Malinauskas, A.P. , Einziger, R.E., Jordan, H., Duffey, T.A., Sutherland, S.H., and Reardon, P.C., "A Method for Determining the Spent-Fuel Contribution to Transport Cask Containment Requirements," Sandia National Laboratories, Albuquerque, NM, SAND90-2406, TTC-1019, (11/1992).

5.12 Lide, D.R., CRC Handbook of Chemistry and Physics, 82nd ed., CRC Press, New York (2001-2002).

5.13 Zwahlen, E., "Release Rate and Dose Rate Calculations of Radioactive Contaminants at the Proposed Yucca Mountain Repository," PhD Dissertation, University of California at Berkely, U.S.A. (1995).

5.14 Johnson, E.R., Saverot, P.M., Monograph on Spent Nuclear Fuel Storage Technologies, Institute of Nuclear Materials Management, Illinois (1997).

CHAPTER 6: A MONTE CARLO MODEL FOR THE SIMULATION OF FREE MOLECULAR FLOWS

6.1 INTRODUCTION

The issue of gas transport through spent fuel and cladding has significant impacts on the system under study. During irradiation within the reactor core, significant quantities of fission gases build up within the fuel. Also during and after irradiation, the decay of radioisotopes leads to the production of gases. Over long periods of time, the most significant gas is helium formed from alpha decay. Depending on the physics of a particular decay of a particular atom, the location of the created gas molecule will either be within the fuel itself or in the fuel-clad gap (if such a gap exists). The build-up of gases within the fuel rod leads to an increase in pressure. If the strain caused by this pressure build-up in conjunction with heat stress, radiation effects, and chemical corrosion leads to the formation of a breach in the cladding, then gases and particulates can be released into the interior of the container. The amount of material released will depend on the size of the breach, i.e. does a pinhole develop or does the clad unzip? This release will contribute to the radioactive source term and the interior pressure of the spent fuel container itself, which in turn will affect the depressurization time and the potential release of radioactivity to the surrounding environment.

The transport of vapors and gases through spent fuel has recently become a topic of interest for advanced fuel studies since it has been determined that silver is transported through the silicon carbide layers of TRISO fuels by way of vapor transport instead of

diffusion as was originally thought [6.1]. In the case of traditional UO_2 fuels as are being considered in this thesis, the phenomenon is of equal interest. It is known that during irradiation the fuel pellets develop many cracks and pockets. Some of these cracks are visible to the naked eye. Undoubtedly, there are also tiny cracks that are not visibly detectable. This large variation in the dimensions of the pathways for gas transport leads to the importance of studying several transport regimes. For micrometer size cracks like those studied in the previous chapters, the flow rate will be in the continuum regime. For slightly smaller cracks, the flow rate will enter the slip and transition regimes. For smaller cracks still, gases will be transported through free molecular transport.

The cracks that form within the fuel and within the cladding will most likely not be cylindrical like the pinholes studied earlier. They will in fact most likely have a high tortuosity. Several tools for developing these small-scale flows have been developed including Lattice-Boltzmann and Direct Simulation Monte Carlo (DSMC) [6.2]. In addition to the application to gas transport through spent fuels, the transport of gases and aerosols using these methods have been modeled for micro-electromechanical systems (MEMS) [6.3].

In order to study the possible release of gases from the fuel itself into the fuel-clad gap, a direct N-particle Monte Carlo program has been written in Mathematica®. This program assumes that the dimensions of flow are small enough that the gas is highly rarified allowing particle-particle collisions to be neglected. Each test particle is started at the entrance to the pathway and is tracked through collisions with the pathway wall until either being transmitted through the pathway or being reflected back through the

entrance. The theory behind the significance of this information lies in the fundamentals of the kinetic theory of gases itself.

6.2 MOLECULAR FLOWS AND TRANSMISSION FRACTIONS

When a gas molecule flowing through a small tube undergoes a collision with the tube wall, it does not reflect from the wall as a ball would rebound after such a collision. Such a collision is known as specular reflection. Instead, the molecule seems to be trapped against the wall for a brief period of time…long enough to come into thermal equilibrium with the wall…and then released. This type of collision is known as diffuse reflection. In reality, diffuse reflection is observed. Under diffuse reflection, the direction that the molecule travels after the collision is determined by the cosine law [6.4]. The cosine law states that the angle between the vector normal to the wall at the point of contact and the direction that the molecule is traveling after the collision is randomly chosen according to the rule

$$\theta = Cos^{-1}\left(\sqrt{\zeta}\right) \tag{6.1}$$

where ζ is a random real number between 0 and 1. The speed with which the molecule travels after the collision is chosen from the Boltzmann distribution

$$f[v] = \beta^3 v^3 e^{-\beta^2 v^2} \tag{6.2}$$

Although the speed affects properties such as the momentum flux of the gas through the tube, it does not affect the fraction of the molecules entering the pathway that are transmitted. Transmission is a purely geometric effect.

Figure 6.1 illustrates the flow currently being considered, where the pocket within the fuel in which the gas is created is represented by volume 1 and the fuel-clad gap is represented by volume 2. The pressure within each volume is governed by the ideal gas law

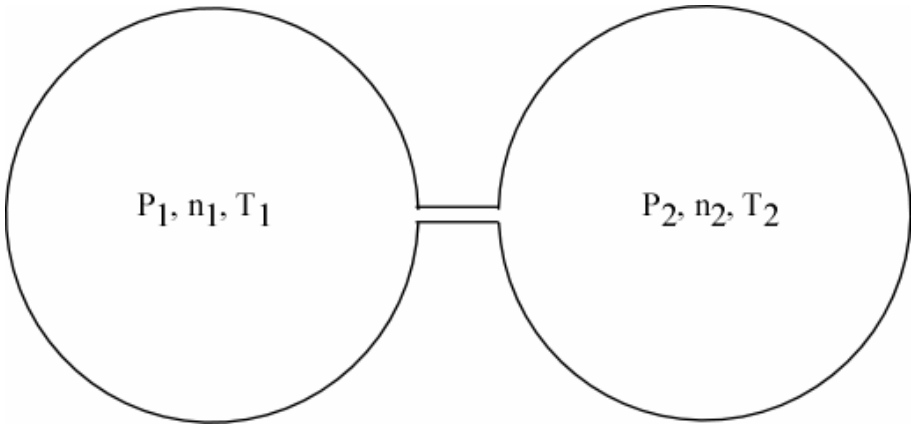

Figure 6.1: Elementary Model of Simulated Molecular Flow System

$$p_i = n_i k T_i \tag{6.3}$$

where k is Boltzmann's constant. This pressure correlates to an incidence rate of molecules impacting a surface in contact with the gas of

$$G_i = \frac{n_i \bar{v}_i}{4} \tag{6.4}$$

where $\bar{v}$ is the mean molecular speed of the gas

$$\bar{v}_i = \left(\frac{8kT_i}{\pi m} \right)^{1/2} \tag{6.5}$$

Thus, for a given system, the mass flow rate of gas into an opening with a surface area A_c is

$$\hat{J} = mGA_c \tag{6.6}$$

For a pathway connecting two volumes of unequal conditions as illustrated in Fig. 6.1, there will be a net mass flow in one direction. This net flow is equal to the difference between the flows in either direction.

If volume 2 in Fig. 6.1 were a vacuum, then the mass flow rate toward volume 1 would be zero. If the transverse dimensions of the pathway are small enough that the gas flow is in the free molecular regime however, the mass flow rate from volume 1 to volume 2 would not be equal to the rate of mass entering the connecting pathway as defined in Eq. 6.6. Instead, as discussed earlier, due to the fact that molecules striking the wall of the pathway rebound with a direction determined by the cosine law for diffuse scattering, some molecules entering the pathway will be reflected back through the entrance instead of being transmitted through the pathway into volume 2. The fraction of the molecules entering the pathway that are transmitted is represented by the parameter *w*. Taking this transmittance value into account, and considering the case that volume 2

is not a vacuum, the net flow rate through the pathway connecting volume 1 and volume 2 is expressed as

$$\vec{J} = m\left[A_{c1} \frac{n_1 \bar{v}_1}{4} w_1 - A_{c2} \frac{n_2 \bar{v}_2}{4} w_2 \right] \tag{6.7}$$

In the case that the pathway connecting the two volumes in Fig. 6.1 is straight and has a constant cross-section, Eq. 6.7 simplifies to

$$\vec{J} = A_c m\left[\frac{n_1 \bar{v}_1}{4} - \frac{n_2 \bar{v}_2}{4} \right] w \tag{6.8}$$

Substituting Eqs. 6.3 and 6.5 into Eq. 6.8 leads to the equation

$$\tilde{J} = A_c \frac{1}{\sqrt{2\pi}} \sqrt{\frac{m}{k}} \left(\frac{P_1}{\sqrt{T_1}} - \frac{P_2}{\sqrt{T_2}} \right) w \tag{6.9}$$

which simplifies under isothermal conditions to the form

$$\tilde{J} = A_c \frac{1}{\sqrt{2\pi}} \sqrt{\frac{m}{kT}} (P_1 - P_2) w \tag{6.10}$$

M. von Smoluchowski has shown that the mass flow rate through a long straight tube of arbitrary cross section should be governed by the equation [6.5]

$$\tilde{J} = \frac{1}{2(2\pi)^{1/2}} \frac{A}{L} d^{1/2} (P_1 - P_2) \tag{6.11}$$

where L is the length of the tube, d is the mass density of the gas at unit pressure, and A is defined as

$$A = \int_s \int_{-\pi/2}^{\pi/2} \frac{1}{2} \rho^2 \cos(\theta) d\theta ds \tag{6.12}$$

where "ρ represents a chord of the cross section which forms an angle θ with the normal at ds." For a tube with a circular cross section ($A_c = \pi R^2$), the value of A is $(16/3)\pi R^3$. Comparison of Eq. 6.10 with Eq. 6.11 for the case of a long straight tube of circular cross section shows that w takes the value 8R/3L which is the expected value.

For short tubes, curved tubes, or tubes with variable cross sections, Eq. 6.11 may not be valid. For these cases, in order to determine the net mass flow rate through a pathway like the one being discussed here, Eq. 6.7 must be used in conjunction with a method for determining the transmission rates. The Monte Carlo simulations discussed in this chapter present one such method for transmission rate determination.

6.3 FLOW GEOMETRY

The general flow behavior of a test particle in the Monte Carlo simulations is determined by Eq. 6.1 and Eq. 6.2. In order to expand the theory behind the simulations

further, it is necessary to address the geometry of flow. The first issue to be addressed regarding the flow geometry is the shape of the pathway entrance. For all analyses in this work, it is assumed that the entrance is a two-dimensional planar shape. For each shape, a scheme must be developed in which each test particle is given an entrance position and flow velocity that accurately represents the flow being considered. For free molecular flow, a particle has an equal chance of entering the pathway at any point on the plane that makes up the pathway entrance. Also, each particle will enter with a flow direction selected from the cosine law and a speed selected from the Boltzmann distribution. Thus for a test particle, the entrance velocity will consist of a speed chosen from Eq. 6.2 and a direction selected from Eq. 6.1 where the angle selected is the angle relative to the vector normal to the entrance plane oriented in the direction of positive flow as shown in Fig. 6.2. In addition, to the polar angle chosen from Eq. 6.1, the velocity direction needs a planar angle as well. That planar angle must be chosen from a uniform distribution

$$\varphi = 2\pi\zeta \tag{6.13}$$

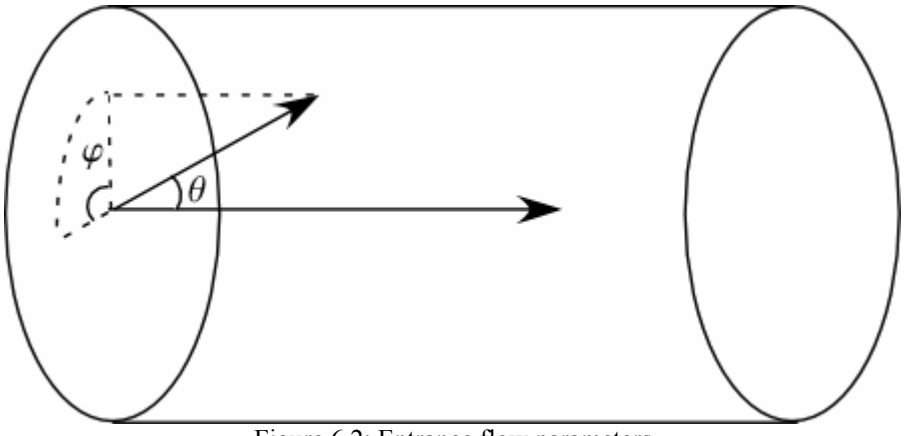

Figure 6.2: Entrance flow parameters

The particle entrance position must be selected from a uniform distribution over the entire area of the entrance plane. For some shapes of the entrance plane, such as circles, this distribution can be easily determined analytically. For instance, consider a circle with a radius R. The probability that a point chosen randomly within that circle will also be within a circle of radius r that is concentric to the larger circle is simply equal to the ratio of the areas of the two circles

$$P = \frac{\pi r^2}{\pi R^2} = \frac{r^2}{R^2} \tag{6.14}$$

Since probabilities are always assigned values between zero and one, it must be the case that $0 \leq P \leq 1$. If the value of P is selected at random, then P becomes equivalent to ζ that appears in Eq. 6.1. Thus, for the particles in the Monte Carlo simulation, the starting radial position can be determined by rearranging Eq. 6.14 into the form

$$r = R\sqrt{\zeta} \tag{6.15}$$

and evaluating for randomly selected values of ζ. The starting angular position of a test particle must be chosen from the uniform distribution given by Eq. 6.13.

For more complicated entrance geometries, explicit formulations like Eq. 6.13 and Eq. 6.15 may be very difficult to determine. In such cases, an acceptance/rejection technique can be applied. Consider the problem of selecting a random position from a uniform distribution over an ellipse. This problem is more complicated than the circular problem due to the fact that the ellipse is not radially symmetric. In order to develop the

acceptance/rejection algorithm for this particular problem, it is necessary to analyze the geometry involved. An ellipse is defined mathematically in Cartesian coordinates by the equation

$$\frac{x^2}{a^2} + \frac{y^2}{b^2} = 1 \tag{6.16}$$

where a and b are the elliptical axes. Any ellipse can be circumscribed by a rectangle with sides of length 2 a and 2 b as depicted in Fig. 6.3.

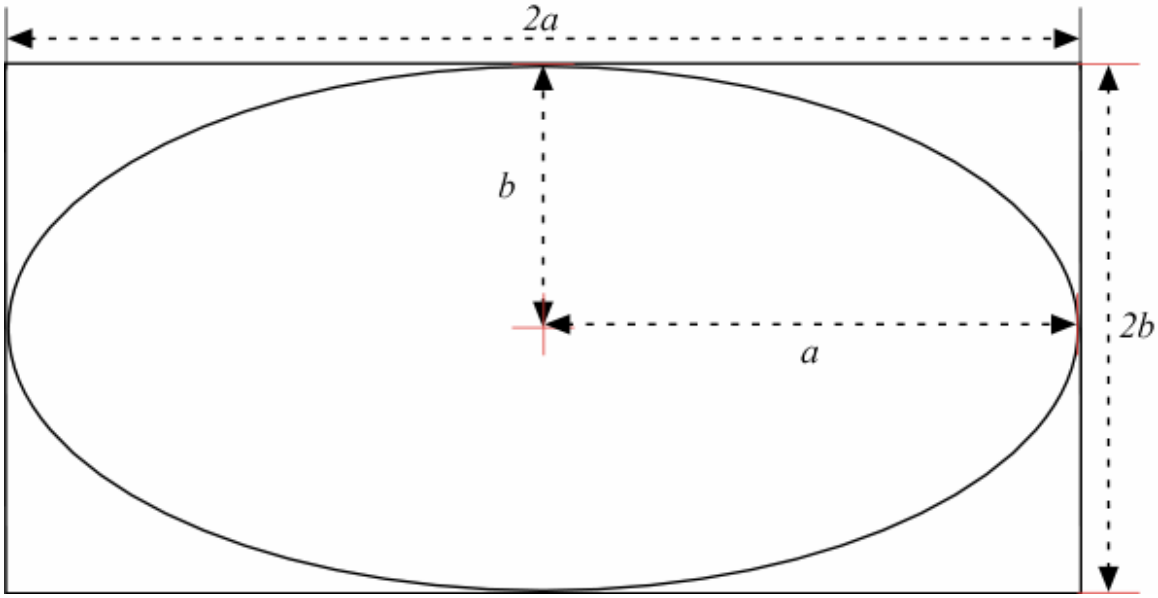

Figure 6.3: Rectangle circumscribed about an ellipse

In the algorithm for randomly selecting a point within the ellipse, an x-coordinate is randomly chosen from the distribution $-a \leq x \leq a$, and a y-coordinate is randomly chosen from the distribution $-b \leq y \leq b$, which guarantees that the point will lie within the circumscribed rectangle. The point is then checked to see whether it lies inside the

ellipse or not. If the selected values of x and y are plugged into the left hand side of Eq. 6.16 and the result is less than 1, then the point lies within the ellipse and is accepted. If the result is greater than 1, then the point lies outside the ellipse and is rejected. To demonstrate its effectiveness, this algorithm was used to generate 20,000 points within an ellipse with $a = 2$ and $b = 1$. The output of this 20,000 point generation is displayed as Fig. 6.4, which shows that the sampling is uniform across the entire area of the ellipse.

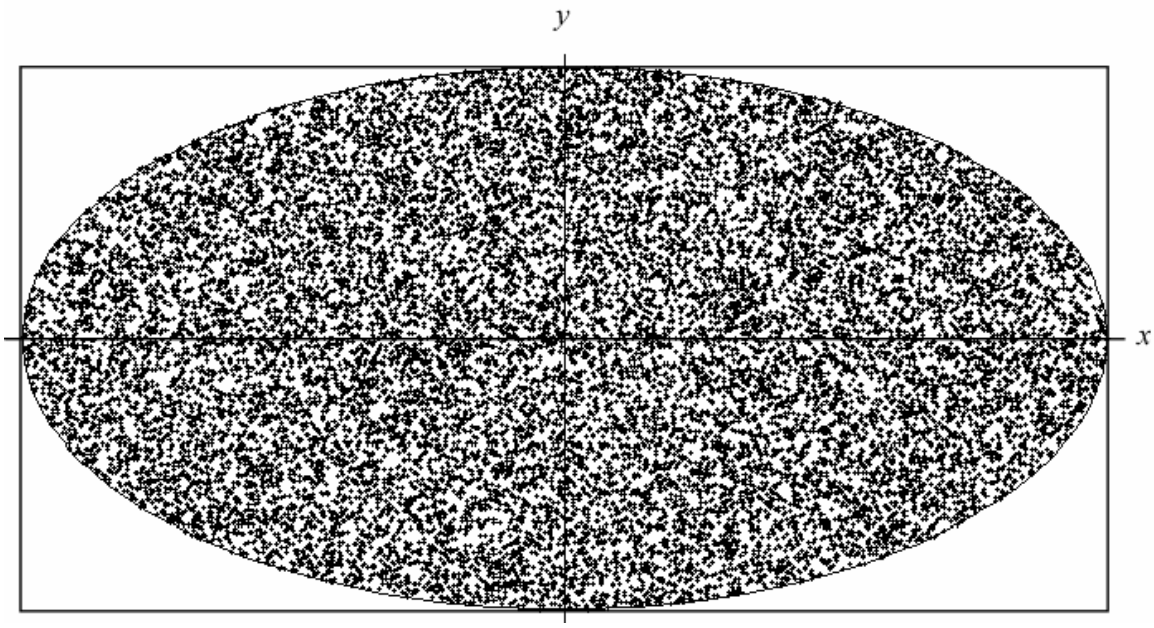

Figure 6.4: Demonstration of Initial Point Acceptance/Rejection Method for an Ellipse

After the entrance geometry is addressed, it is necessary to address the geometrical construction of the pathway itself. A three dimensional curve is conveniently expressed through the general parametric formulation [6.6].

$$\gamma[s] = \{f[s], g[s], h[s]\} \tag{6.17}$$

A tube can then be constructed about the curve by constructing a "shell" about the curve. For instance, if the tube of interest has a circular cross section of constant radius, then the "shell" can be constructed as

$$S = \gamma[s] + R\big(N[\gamma[s]] \cdot Cos[\xi] + B[\gamma[s]] \cdot Sin[\xi]\big) \tag{6.18}$$

where R is the tube radius, $0 \leq \xi < 2\pi$, B is the unit binormal vector of γ[s] defined by

$$B[\gamma[s]] = \frac{\gamma'[s] \times \gamma''[s]}{\left|\gamma'[s] \times \gamma''[s]\right|} \tag{6.19}$$

and N is the unit normal vector of γ[s] defined by

$$N[\gamma[s]] = B[\gamma[s]] \times T[\gamma[s]] \tag{6.20}$$

where T is the unit tangent vector of γ[s] defined by

$$T[\gamma[s]] = \frac{\gamma'[s]}{\left|\gamma'[s]\right|} \tag{6.21}$$

For the case γ[s] = $\{s, s^2, s^3\}$ and $R = 0.25$, then the tube created by $0 \leq s < 1$ is as appears in Fig. 6.5. Eqs. 6.19 – 6.21 are not valid for straight lines due to the fact that the second derivative of a straight line is always zero. However, two mutually perpendicular vectors that are normal to a straight line are trivial to determine. These two vectors can be used

as the normal and binormal vectors as listed in Eq. 6.18. In the case $\gamma[s] = \{s, 0, 0\}$ for instance, the unit tangent vector is simply $\{1, 0, 0\}$, the unit binormal is $\{0, 1, 0\}$, and the unit normal is $\{0, 0, 1\}$. So, for $\gamma[s] = \{s, 0, 0\}$ and R = 0.25, the tube created by $0 \leq s < 1$ is as appears in Fig. 6.6.

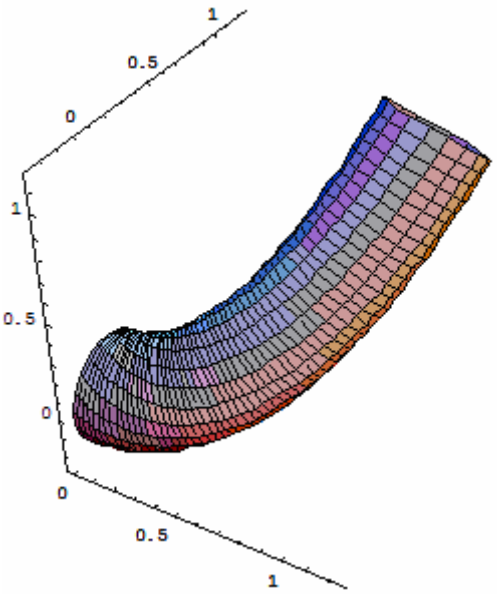

Figure 6.5: $\gamma[s]=\{s,s^2,s^3\}$, $R = 0.25$, $0 \leq s < 1$

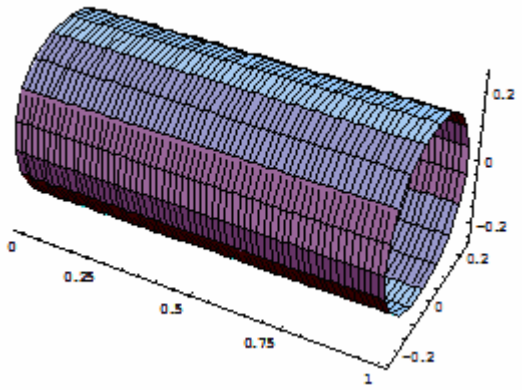

Figure 6.6: $\gamma[s] = \{s, 0, 0\}$, R = 0.25, $0 \leq s < 1$

Any three dimensional smooth tube that does not bend so tightly as to overlap itself can be constructed in this fashion. Of particular interest in the current work are helical tubes and conical tubes. A helical tube of constant radius can be constructed parametrically with the equation $\gamma[a, b, s] = \{a\ Cos[s],\ a\ Sin[s],\ b\ s\}$, where a is the inner radius of the helix and b controls the distance of separation between the successive coils of the radius. The helical tube can be constructed with Eq. 6.16 in exactly the same fashion as the curved and straight curves were. For the case of

$\gamma[3, 1, s] = \{3\ Cos[s],\ 3\ Sin[s],\ s\}$, and $R = 0.25$, then the tube created by $0 \leq s < 1$ is as appears in Fig. 6.7. This same curve is extended out to $0 \leq s < 4\ \pi$ in Fig. 6.8.

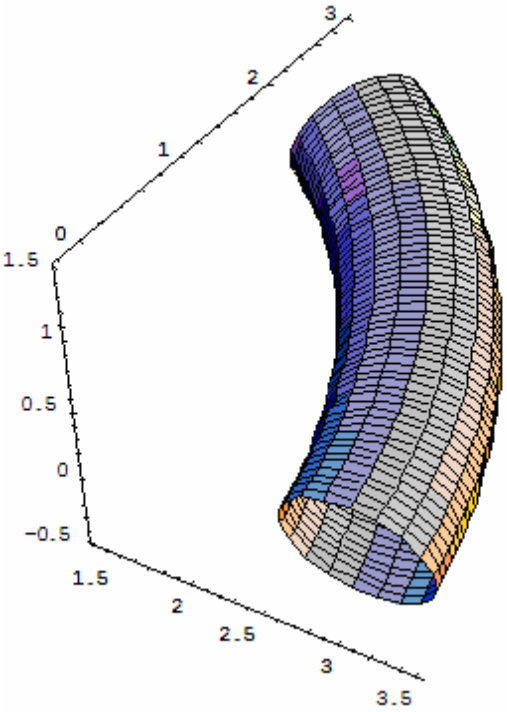

Figure 6.7: $\gamma = \{3\ Cos[s],\ 3\ Sin[s],\ s\}$, $R = 0.25,\ 0 \leq s < 1$

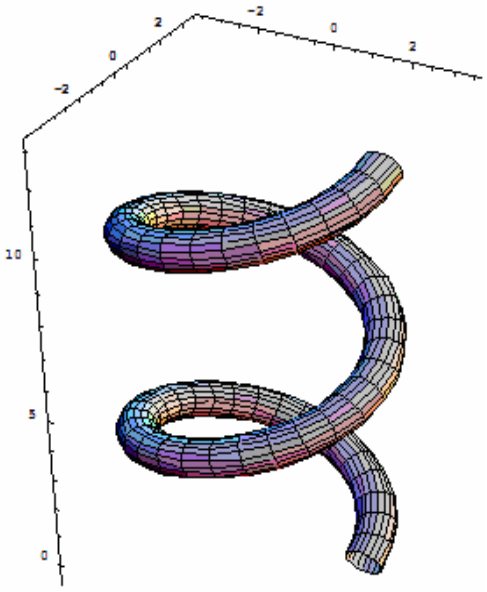

Figure 6.8: $\gamma = \{3\ Cos[s],\ 3\ Sin[s],\ s\}$, $R = 0.25,\ 0 \leq s < 4\pi$

Conical tubes are different from the tubes considered thus far in that their radii are not constant along the curve. They can easily be constructed however, if their radius is a simple function of *s*. For the straight curve that appears in Fig. 6.6 for instance, if instead of being assigned the constant value R = 0.25, the radius was assigned the functional value R[s] = s/2 + 0.1, the result would be the conical tube that appears in Fig. 6.9. The conical tube that appears in Fig. 6.9 can be slanted in the other direction by assigning the radius the value of R = (1-s)/2 + 0.1 as appears in Fig. 6.10.

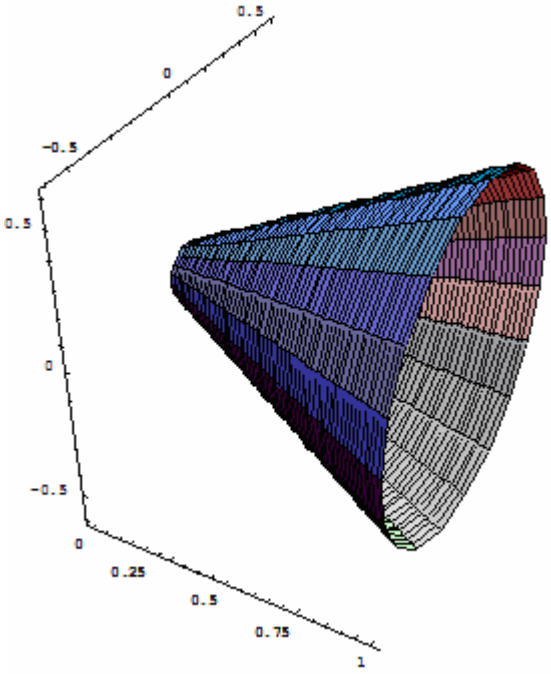

Figure 6.9: $\gamma[s] = \{s, 0, 0\}$, R = s/2 + 0.1, $0 \leq s < 1$

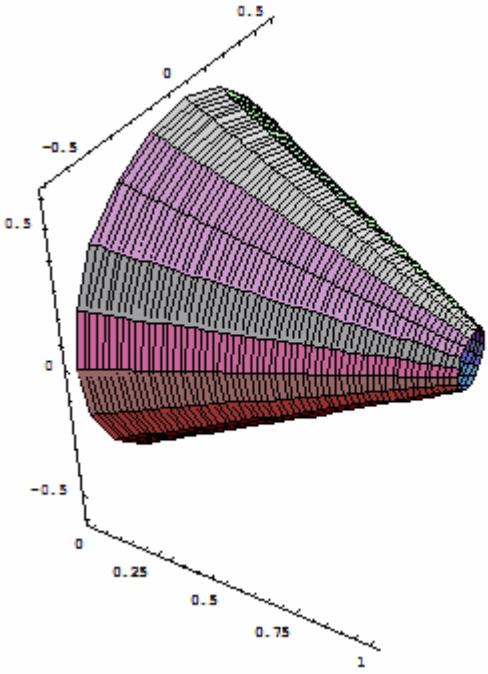

Figure 6.10: $\gamma[s] = \{s, 0, 0\}$, R = (1-s)/2 + 0.1, $0 \leq s < 1$

In general, the "shell" of the conical tube can be constructed from a straight tube where the radius is assigned the value of a straight line in the slope-intercept form:

$$R[s] = Tan[\alpha]\, s + R_0 \tag{6.22}$$

where α and R_0 are defined in Fig. 6.11.

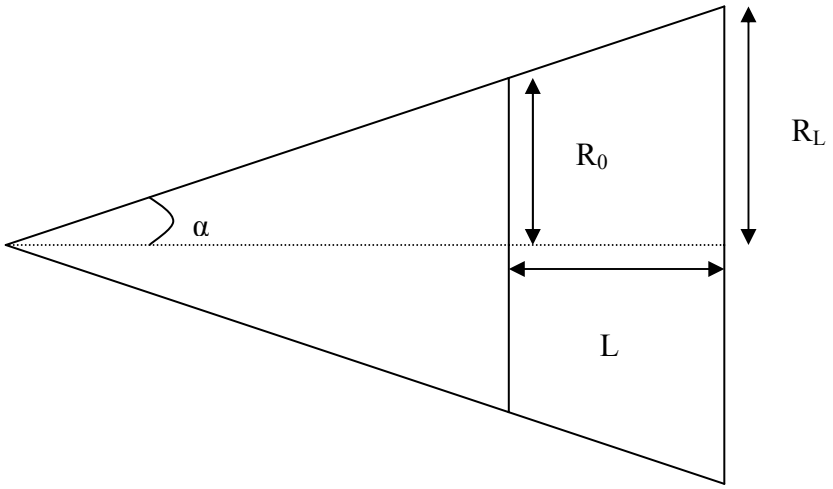

Figure 6.11: Definition of Conical Parameters [6.7]

6.4 PARTICLE TRACKING

After the appropriate tube geometry is completed, the mathematics behind the algorithm of determining the position of particle-wall collisions and the direction of particle flow after the collision must be implemented. The method for determining these values will be different for each tube geometry. The simplest geometry to address is a straight tube of constant circular cross section. For this geometry, the starting position of each test particle is determined from Eqs. 6.13 and 6.15. The initial velocity of each test particle is determined from Eqs. 6.1, 6.2 and 6.13 where the vector normal to the entrance plane as displayed in Fig. 6.2 is {1,0,0}. Given the initial particle position and velocity, the first particle-wall impact can be calculated. Each test particle is assumed to be free from the influence of other particles and thus will travel in a straight line until a collision with a wall takes place. Thus, the particle position as a function of time after entering the tube is governed by the equation

$$\{x, y, z\} = \{x_0, y_0, z_0\} + \{u_0, v_0, w_0\}t \tag{6.23}$$

where x represents the axial direction of flow, y and z represent the coordinates of the cross-section of the tube at a given axial position, u_0, v_0, and w_0 are the initial particle velocities in the x, y, and z directions respectively, and t is the time of flow. No matter where the particle is when it is within the tube, its distance from the central axis around which the tube is constructed can be determined with the two-dimensional Pythagorean Theorem

$$\delta = \sqrt{[(y_0 + v_0 t) - g[s]]^2 + [(z_0 + w_0 t) - h[s]]^2} \tag{6.24}$$

where g[s] and h[s] are the same functions that appear in Eq. 6.17. The first particle-wall collision will occur when $\delta = R$, the radius of the tube. If the axes are oriented such that the central tube axis coincides with the x-axis as is the case in Fig. 6.6, then $\gamma[s]=\{s,0,0\}$ which means that $g[s]=h[s]=0$ throughout the length of the tube, allowing Eq. 6.24 to be simplified to

$$\delta = \sqrt{(y_0 + v_0 t)^2 + (z_0 + w_0 t)^2} \tag{6.25}$$

If δ is set equal to the tube radius, then the only unknown term in Eq. 6.25 is t, allowing the equation to be easily solved. In Mathematica®, there are two built-in functions to choose from in order to solve equation (6.25) for t. One of these functions, *Solve*, solves the equation analytically, while the other function *FindRoot*, uses either Newton's

method or the secant method to numerically solve for t. In the particular case of straight tubes of constant circular cross-section, the *Solve* function is the most effective. The numerical methods of *FindRoot* are computationally faster, but they often provide extraneous roots. Selecting the desired roots and eliminating the extraneous roots complicates the code to the extent that it is better to simply use the *Solve* function. After solving Eq. 6.25 for t, the exact location of the particle-wall collision can be determined from Eq. 6.23. If $0 \leq x_c \leq L$ where L is the length of the tube and x_c is the axial position of the collision, then the new particle velocity must be determined and used to calculate the next particle-wall collision through the method outlined above. Otherwise, the particle has left through one end of the tube. In that case, the end through which the particle left is recorded to be used later to determine the correct value of w.

For the case of the straight tube of constant circular cross-section, the inward-pointing unit normal vector at the point of the particle-wall collision is simply the vector

$$n = \frac{\{x_c, 0, 0\} - \{x_c, y_c, z_c\}}{R} \tag{6.26}$$

The angle between the unit normal and the post-collision particle velocity is given by Eqs. 6.1, 6.13 and Fig. 6.2. In order to construct the post-collision particle velocity from Eqs. 6.1, 6.13 and 6.26, it is necessary to use vector rotations. The first rotation is around a vector parallel to the x-axis and passing through the particle-wall collision point. This rotation is accomplished with the rotation matrix [6.8]

$$R_x(\theta) = \begin{pmatrix} 1 & 0 & 0 \\ 0 & Cos(\theta) & -Sin(\theta) \\ 0 & Sin(\theta) & Cos(\theta) \end{pmatrix} \tag{6.27}$$

The use of the rotation matrix defined by Eq. 6.27 ensures that the normal vector is rotated about the desired axis while still preserving the unit length of the vector. The resulting vector must next be rotated about the normal vector by the angle φ defined by Eq. 6.13. This more complicated rotation is accomplished by application of the equation [6.9]

$$r' = r\ Cos[\varphi] + n\ (n \cdot r)(1 - Cos[\varphi]) + (r \times n) Sin[\varphi] \tag{6.28}$$

where r' is the unit vector pointing in the direction of the post-collision particle velocity, n is unit normal vector defined by Eq. 6.26, and r is the vector resulting from the rotation matrix (Eq. 6.27) being applied to n. These vectors and rotations are illustrated in Fig. 6.12. Thus, the new particle velocity consists of a speed defined by Eq. 6.2 and a direction defined by Eq. 6.28. The process outlined above is repeated until the particle leaves one end of the tube.

The process outlined above is only applicable to straight cylindrical tubes of constant circular cross-section. For curved tubes, tubes with cross-sections of other shapes, and tubes with cross-sections that are functions of the axial position, adjustments must be made to the algorithm presented above. With the exception of the straight tube of constant circular cross-section, the simplest tube to model is the straight conical tube

with circular cross-section. In this case, the first adjustment to be made is to insert the right-hand-side of Eq. 6.22 in for δ in Eq. 6.25, recognizing that $s = u_0 t$ and solve for t.

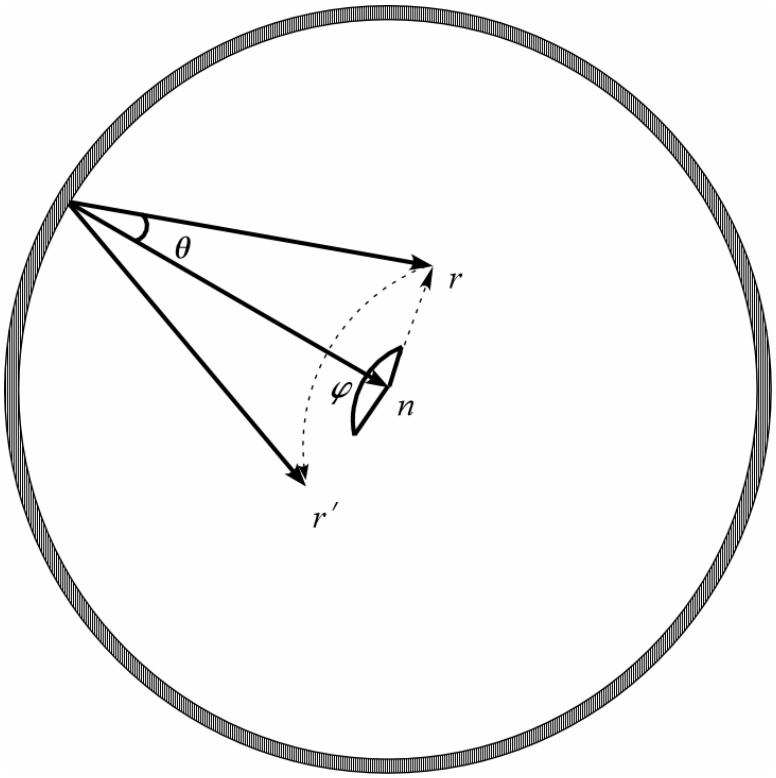

Figure 6.12: Axial View of Velocity Vector Rotations

Once the particle-wall collision point is determined, the unit normal to the wall at that point must be determined. This procedure is a bit more complicated than it was for the cylinder with a constant circular cross section. Figure 6.13 shows the geometry involved with this procedure. The parameters that appear in Fig. 6.13 are consistent with those that appear in Fig. 6.11. The first step after determining the collision point is to determine the direct unit vector from that point straight to the central axis as was done for the straight tube with the constant circular cross-section. This is done by applying Eq.

6.26, where R has been eliminated from the equation. This elimination means that the magnitude of this vector is not necessarily unity. This vector is labeled n_s in Fig. 6.13.

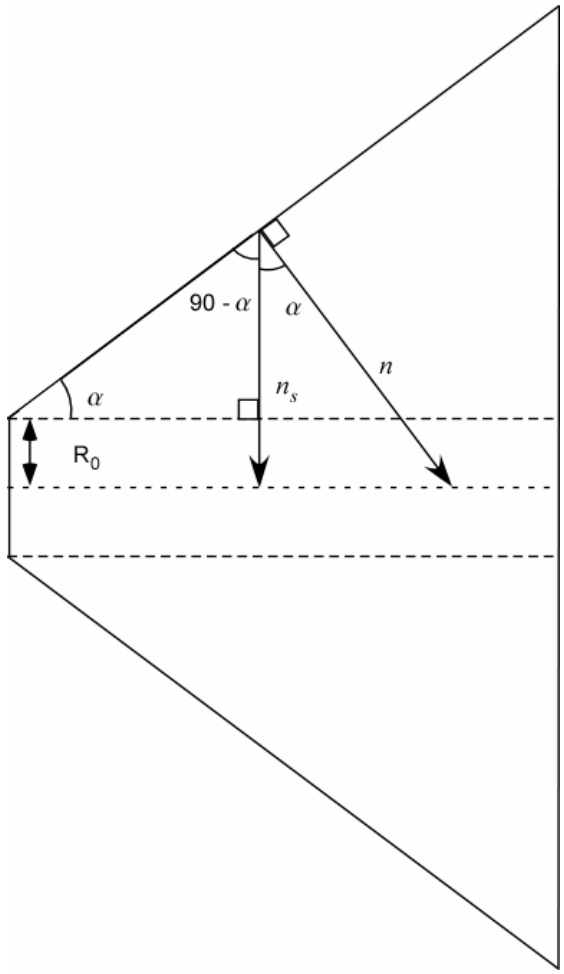

Figure 6.13: Determining the Unit Normal for a Straight Conical Tube

The components of the vector n cannot be determined by a direct application of the rotation matrix that appears in Eq. 6.27 because it is difficult to determine the correct axis around which the vector n_s needs to be rotated. However, using trigonometric identities, it can be seen that the axial component of the head of the vector n has the value $x_c + R[x_c]Tan[\alpha]$. Also, since the head of the vector n is located on the central axis of the

conical tube, the *y*- and *z*- components are both equal to zero. Thus, the vector *n* is defined as

$$n = \{x_c + RTan[\alpha],0,0\} - \{x_c, y_c, z_c\} \tag{6.29}$$

The unit vector starting at the collision point and pointing in the direction of *n* is defined as

$$\hat{n} = \frac{\{x_c + RTan[\alpha],0,0\} - \{x_c, y_c, z_c\}}{\sqrt{R^2 Tan^2[\alpha] + y_c^2 + z_c^2}} \tag{6.30}$$

In polar coordinates, this vector can be expressed as

$$\hat{n} = \{Sin[\hat{\theta}]Cos[\phi], Sin[\hat{\theta}]Sin[\phi], Cos[\hat{\theta}]\} \tag{6.31}$$

where the angles $\hat{\theta}$ and ϕ can be determined by setting the components of the vectors defined by Eqs. 6.30 and 6.31 equal to each other and solving. The rotated vector which is equivalent to the vector *r* that appears in Eq. 6.28 can now simply be written as

$$r = \{Sin[\theta + \hat{\theta}]Cos[\phi], Sin[\theta + \hat{\theta}]Sin[\phi], Cos[\theta + \hat{\theta}]\} \tag{6.32}$$

where θ is determined by Eq. 6.1. Now, the final unit vector in the direction of the post-collision particle velocity can be determined by inserting the vectors defined by Eqs. 6.31

and 6.32 into Eq. 6.28 and using a value of φ determined from Eq. 6.13. The new velocity direction can now be used to determine the next particle-wall collision and the process is continued until the x-component of the particle position is less than x_0 or greater than L.

In the case of the straight tube with a constant circular cross-section, the tube displayed both radial and axial symmetry. These symmetries made the geometry exceptionally easy to work with. In the case of the conical tube, the radial symmetry was retained while the axial symmetry was lost. This loss of symmetry led to a geometry that was a bit more difficult to work with, but manageable. Another situation in which one field of symmetry is lost and one is retained is the case of a straight elliptical tube of constant cross section. In this case, the radial symmetry is lost, but the axial symmetry is retained.

In addressing the particle tracking algorithm for an elliptical tube, the first adjustment to be made is the determining of the initial particle position. In the first two tube types discussed here, the initial position of each test particle was determined from Eqs. 6.13 and 6.15. In the case of the elliptical tube, the acceptance/rejection technique discussed alongside Figs. 6.3 and 6.4 is employed. The initial particle velocity is determined in the same fashion as it was for the first two tube geometries, by way of Eqs. 6.1, 6.2, and 6.13.

Equation 6.16 gives the equation of an ellipse in Cartesian coordinates, but an ellipse can also be constructed parametrically as

$$ell[s] = \{a\,Cos[s], b\,Sin[s]\} \tag{6.33}$$

Expressing the ellipse in parametric form allows the location of a particle-wall collision to be calculated by solving the equations

$$y_0 + v_0 t = a\,Cos[s] \tag{6.34}$$

and

$$z_0 + w_0 t = b\,Sin[s] \tag{6.35}$$

for *s* and *t*. Unfortunately, the central axis of the tube cannot be used to find the inward facing unit normal vector at the collision point for an elliptical tube. Instead, a slightly more complicated algorithm must be employed. At any given point on the surface of the tube, the unit normal vector to the plane of the cross section will be {1,0,0}. Also, the unit tangent vector to the surface at a point on the surface is given by

$$T = \frac{\frac{\partial\{a\,Cos[s], b\,Sin[s]\}}{\partial s}}{\sqrt{a^2 + b^2}} = \frac{\{-a\,Sin[s], b\,Cos[s]\}}{\sqrt{a^2 + b^2}} \tag{6.36}$$

The unit normal to the plane and the unit tangent to the surface are orthogonal to one another. The cross product of these two vectors will give an orthonormal vector to the plane formed by the unit normal to the plane and the unit tangent to the surface. The resultant vector of this cross product will be the unit normal to the surface at a point. One must be careful and note that the cross product must be done according to the right-hand

rule in order to get the inward facing unit normal as opposed to the outward facing unit normal. A series of views of particle impacts with accompanying directional vectors for free molecular flow through a straight elliptical tube are presented in Fig. 6.14. The elliptical tubes are displayed in wireframe in order to allow transparency. The different perspective views are provided to allow perception of dimension that is lacking in the three-dimensional graphics capabilities of Mathematica® 5.2. The thin lines in each of the perspectives represent the unit tangent vector to the surface, the unit normal vector to the plane, and the inward facing unit normal vector at the point of impact. The different perspectives allow for visual verification that these are indeed mutually orthogonal and do represent normal and tangent vectors. The thick lines represent the velocity vectors associated with each particle-wall impact. Each sphere that appears in the views of Fig. 6.14 represents the same particle, but successive impacts that that particle undergoes as it travels through the tube. In the particular particle simulation represented in Fig. 6.14, the particle undergoes three collisions with the tube wall before passing through the distal end of the tube. By following the post-collision velocities, it is possible to mentally reconstruct the particle path as it traversed the tube. The final particle position that is located beyond the length of the tube shows how mathematically, the tube extends forever. It is only when the particle axial position is determined to be beyond the distal end of the tube that the particle is identified as having been transmitted through the tube. The visual verification that is allowed by the perspectives in Fig. 6.14 are a demonstration of the convenience of using Mathematica® for this type of simulation as opposed to another code such as FORTRAN®.

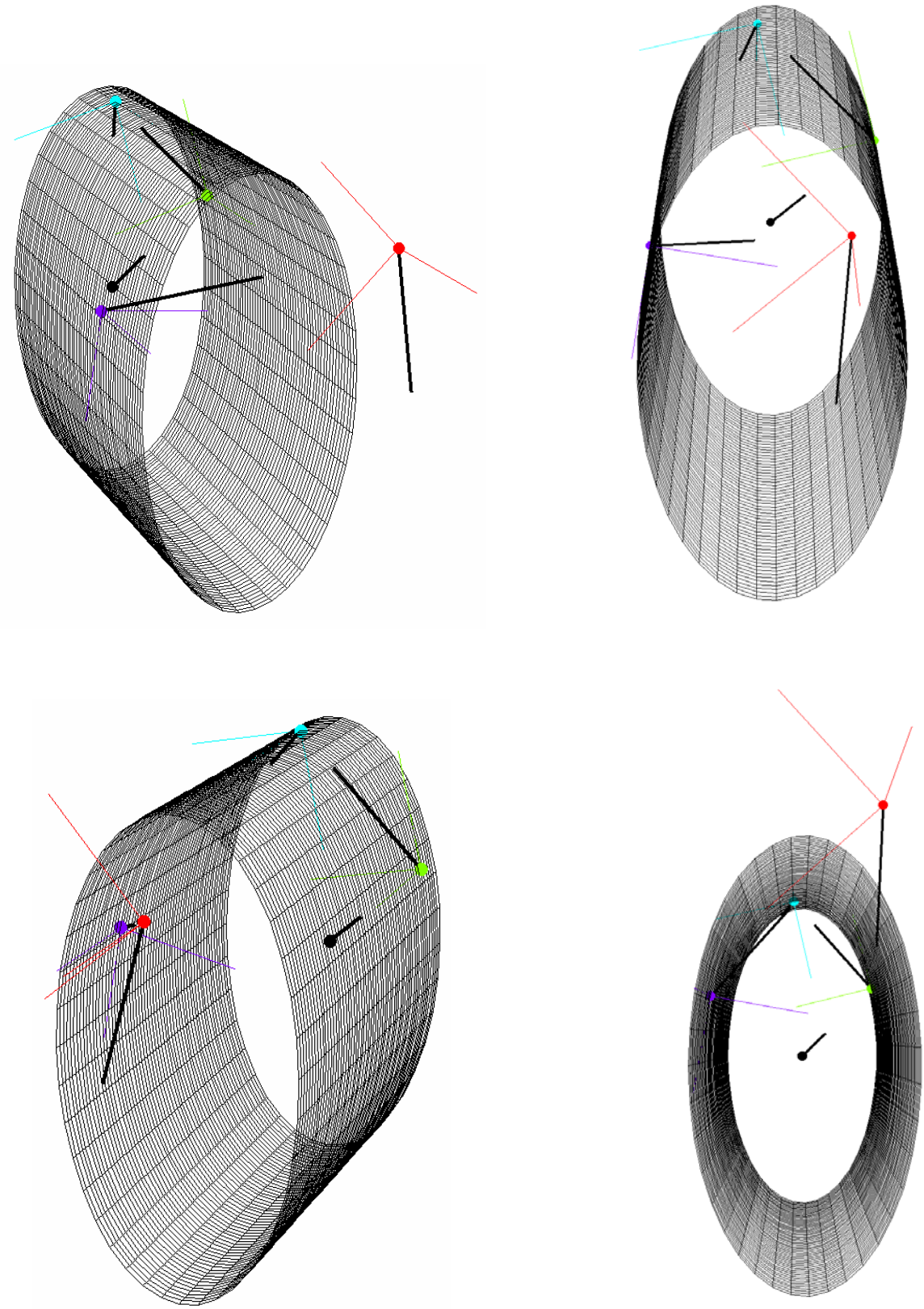

Figure 6.14: Views of Elliptical Tube with Associated Impact Vectors

All of the geometries so far have been constructed about a straight central curve that served as the tube axis. When this central curve is not straight, the geometry becomes more difficult to deal with. For this reason, only curved tubes with constant circular cross sections will be discussed in this thesis. Once again, in this case, the initial test particle position is determined from Eqs. 6.1 and 6.15. As was mentioned earlier, Mathematica® has a function for finding solutions analytically (*Solve*) and a function for finding solutions numerically (*FindRoot*). To this point, the *Solve* function has been employed in all algorithms. Unfortunately, for curved tubes, this method can give multiple solutions as is demonstrated in Fig. 6.15.

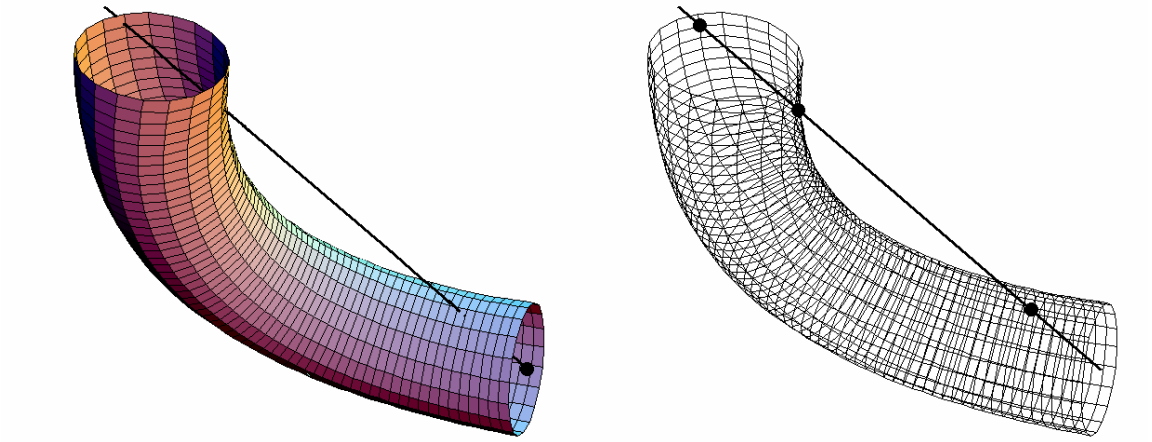

Figure 6.15: Possible Multiple Intersections of a Particle Trajectory with the Tube Wall

The numerical *FindRoot* function requires that a range be given in which to look for a desired root. Unfortunately, *FindRoot* often produces extraneous solutions and often fails to produce the correct root. In order to get around these issues, an algorithm employing the *NMinimize* command is used. This algorithm begins by selecting an initial position

and velocity for a test particle from Eqs. 6.1, 6.2, 6.13, and 6.15 just as they were selected for the straight tube of constant circular cross section. The next step in the algorithm is to move the particle forward according to Eq. 6.23 by a unit time step ($t = 1$). After this advance, the distance between the particle and the central curve is given by the three-dimensional version of Eq. 6.24

$$\delta = \sqrt{[(x_0 + u_0 t) - f[s]]^2 + [(y_0 + v_0 t) - g[s]]^2 + [(z_0 + w_0 t) - h[s]]^2} \qquad (6.37)$$

where t has been assigned a value of unity. The *NMinimize* command is then used to find the value of s for which the value of δ is minimized. If the minimum value of δ is less than the radius of the tube, then the particle is still "inside" the tube. In this case, the value of t is increased from 1 to 2 and the minimum distance from the central axis is again determined from Eq. 6.37. This process is repeated until it is determined that the minimum value of δ is greater than the tube radius and thus the particle has "left" through the wall of the tube implying that a particle-wall collision has occurred. When it is thus determined that the collision has occurred, the value of 1 is subtracted from the value of t for which the minimum value of δ is greater than the tube radius. The resulting value $t_{1,max}$ is the largest integer value of t for which the particle can travel according to Eq. 6.23 without striking the wall of the tube. The particle is next advanced from the position defined by Eq. 6.23 with the value of t set equal to $t_{1,max}$ along the same trajectory by increasing the value of t from $t_{1,max}$ to $t_{1,max} + 0.1$. The same procedure that was carried out for integer values of t is carried out until the largest value of t specified to the first decimal place is determined for which the particle has still not impacted the wall of the

tube. This procedure is then repeated for increasing values of t for the second, third, fourth,… decimal places until the desired degree of accuracy for the particle proximity to the wall is determined. This process can be described mathematically by

$$\{x_c, y_c, z_c\} = \{x_0, y_0, z_0\} + \sum_{i=0}^{n} \{u_0, v_0, w_0\}(t_{10^{-i},\max}) \tag{6.38}$$

where $t_{10^{-i},\max}$ represents the largest value of the i^{th} decimal place of t for which the particle does not strike the wall of the tube, and n defines the degree of accuracy desired in calculating the position of the particle-wall collision. The post-collision particle velocity is then determined in the same fashion that it was determined for the straight tube of constant circular cross section as described above.

Another issue to be addressed in the case of the curved tube is the problem of determining when the particle has exited the tube. For the straight tubes, this was done by determining when $x < 0$ or $x > L$. For a curved tube however, the tube does not extend its full length along the x–axis. This issue is address by tracking the value of the parameter s associated with each particle position. For a curved tube, the tube length can be defined as

$$L = \int_0^{s_{\max}} \left| \gamma'[s] \right| ds \tag{6.39}$$

When the minimum value of δ is determined for a given particle position, the value of s associated with that δ can be considered equivalent to the particle axial position. If that

value of s exceeds L as defined by Eq. 6.39, then the particle has left the distal end of the tube. If the value of s becomes negative, then the particle has been reflected back through the tube opening.

6.5 ADDITIONAL GEOMETRICAL CONSIDERATIONS

This method for simulating the free molecular flow of a gas will work for any three dimension smooth curve that does not curve so sharply relative to its radius as to cause its surfaces to overlap with themselves. Fig. 6.16 demonstrates explicitly what is meant by this statement. The two helices that are displayed in Figure 6.16 are identical except that the radius of the second helix is five times larger than the radius of the first helix. The second helix in Figure 6.16 could be used as a pathway for molecular transport, but the geometry is much more complex and the algorithm developed here cannot be used.

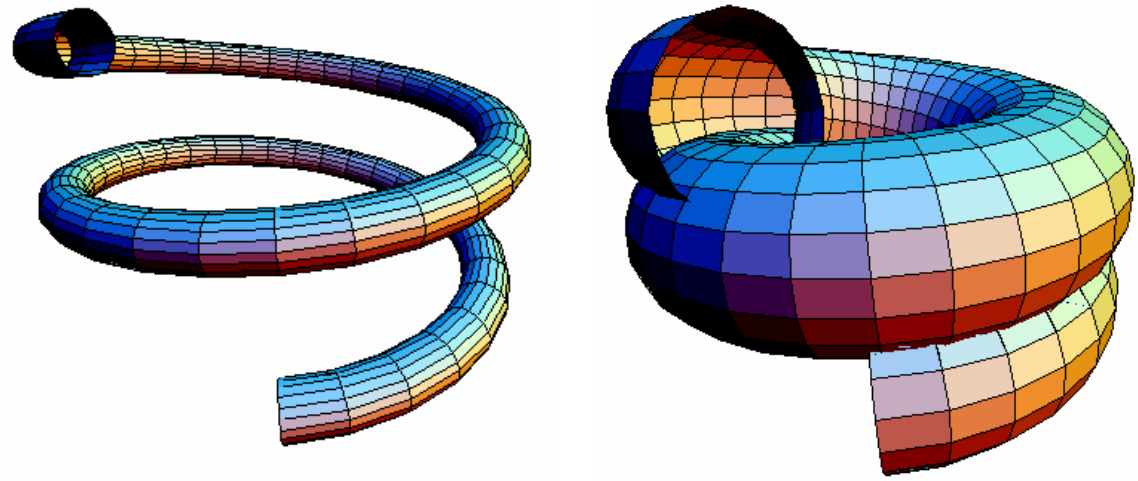

Figure 6.16: Demonstration of Surface-Overlapping for Ill-Defined Tubes

Although any smooth curve can be used to construct a curved tube with an appropriate radius as indicated, in order to generate results that are easily interpreted and compared it is necessary to choose a generic shape. In this work, the shape that was chosen for study was the helix. This shape presents a few issues as far as the geometric modeling is concerned. In general, a helical curve can be defined parametrically as

$$\gamma[s] = \{a\,Cos[s], a\,Sin[s], b\,s\} \tag{6.40}$$

and the helical tube associated with this curve is generated by adding a shell through application of Eq. 6.18. The parameter a defines the radius of curvature of the helix while the parameter b defines by how much the curve inclines or declines. For each increase of the parameter s by 2π, the curve is elevated or lowered by a distance b. Thus in order to avoid a surface overlap as demonstrated in Fig. 6.16, it is necessary that for a helical tube of length $2\pi a$ or greater, the parameter b must be greater than the tube diameter (twice the tube radius).

Although the initial position of a test particle can be generated by Eqs. 6.13 and 6.15 as indicated earlier, it is first necessary to define the plane in which the radius r and the angle φ are applicable. For example, consider a helix in which $a = 1$ and $b = 1$. A close-up view of the entrance to the tube of radius 0.1 constructed around this helix is displayed as Fig. 6.17. The entrance plane to this helix will be slanted upward with a slope of 45°. This can be verified by noticing that according to Eq. 6.40, at $s = 0$, the rate of change with respect to s in the z-direction is b, in the y-direction is a, and in the x-

direction is 0. Thus, the slope is $\text{Tan}^{-1}(1) = 45°$. Also, notice that the center of the entrance is at {1,0,0} instead of {0,0,0}.

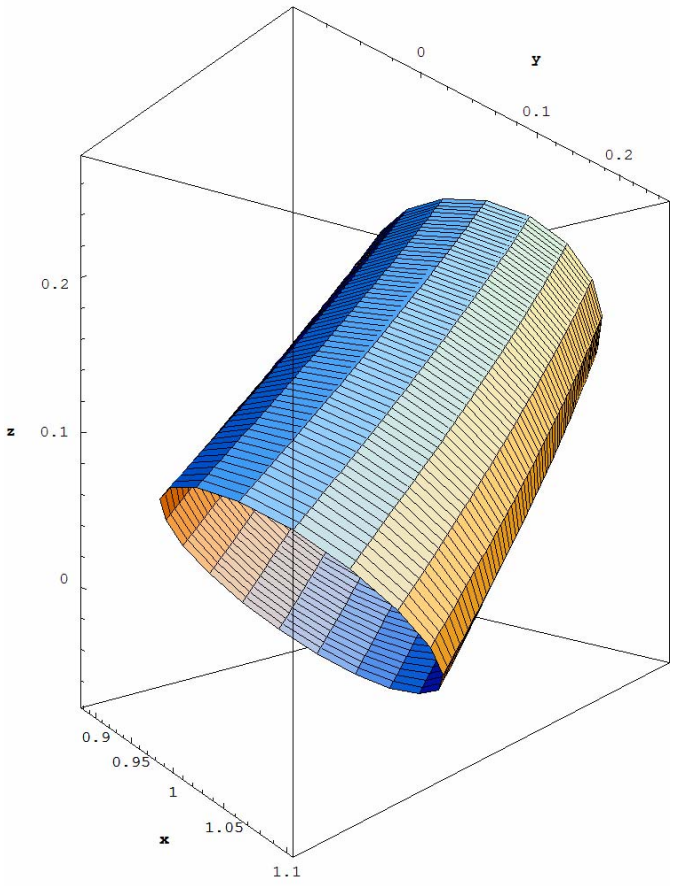

Figure 6.17: Helical Tube Entrance

The sampling of initial points can be expressed generally for a helical tube by shifting the coordinate system. Since Eq. 6.40 represents the general parametric form of a helix symmetrically wrapped about the *z*-axis, no matter what values of *a* and *b* describe such a helix, the entrance plane at $s = 0$ will always be slanted at an angle of $\text{Tan}^{-1}(b/a)$. Stated in another way, the vector tangent to the entrance plane and pointing from the center of the entrance plane into the tube will have an *x*-component of 0, a *y*-

component of a and a z-component of b. Thus, the unit tangent vector for the entrance plane has the form

$$T_{hel} = \frac{\{0, a, b\}}{\sqrt{a^2 + b^2}} \tag{6.41}$$

It is apparent that the entrance plane is bisected by the x-axis and that the rate of change of the helix with respect to s in the x-direction at $s = 0$ is 0. Thus, the vector $\{1,0,0\}$ is a unit vector in the entrance plane of the helical tube. Keeping the same labeling scheme as Eqs. 6.18 - 6.20, the vector $\{1,0,0\}$ can be dubbed the unit binormal vector for the entrance plane. The cross product of the unit binormal vector with the unit tangent vector gives the unit normal vector

$$N_{hel} = \frac{\{0, -b, a\}}{\sqrt{a^2 + b^2}} \tag{6.42}$$

Using the labeling system of Eqs. 6.41 and 6.42, the sampling distribution for the initial position of a test particle can be expressed as

$$R\sqrt{\zeta}\,(B_{hel} Sin[\varphi] + N_{hel} Cos[\varphi]) + \{a,0,0\} \tag{6.43}$$

where B_{hel} is the unit binormal $\{1,0,0\}$. This method was used to generate 1000 starting points for test particles in the helical tube of radius 1, constructed around the helix with

parameter values $a = 3$ and $b = 2$. Figure 6.18 displays four perspectives of these points plotted along with a cut-away of the helix.

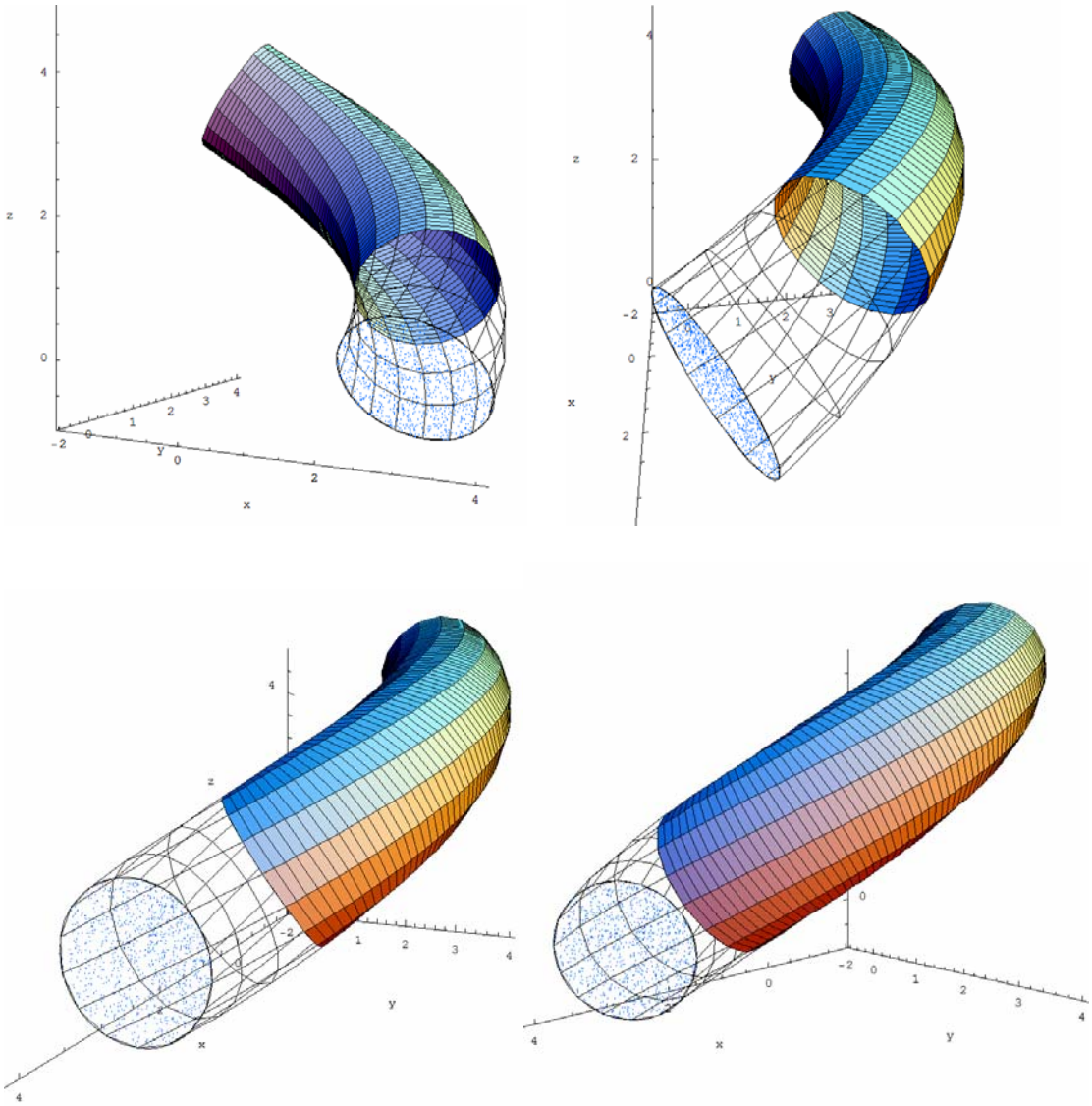

Figure 6.18: Perspectives on the Selection of Initial Points on the Entrance Plane

Just as the initial positions of the test particle for helices must be shifted, so must the initial velocities be shifted. For the straight tubes considered earlier, the direction of axial flow was always in the x-direction and thus the polar angle θ defined by Eq. 6.1 was

always taken with respect to the vector {1,0,0}. For the case of curved tubes, it has just been shown that the initial axial direction of flow is in the direction of the vector T_{hel}. Thus, the polar angles associated with the initial test particle velocities must be taken with respect to T_{hel} instead of {1,0,0} for helical tubes. To test this statement, 100 velocities were sampled using this method and the results are displayed for four different viewpoints in Fig. 6.19.

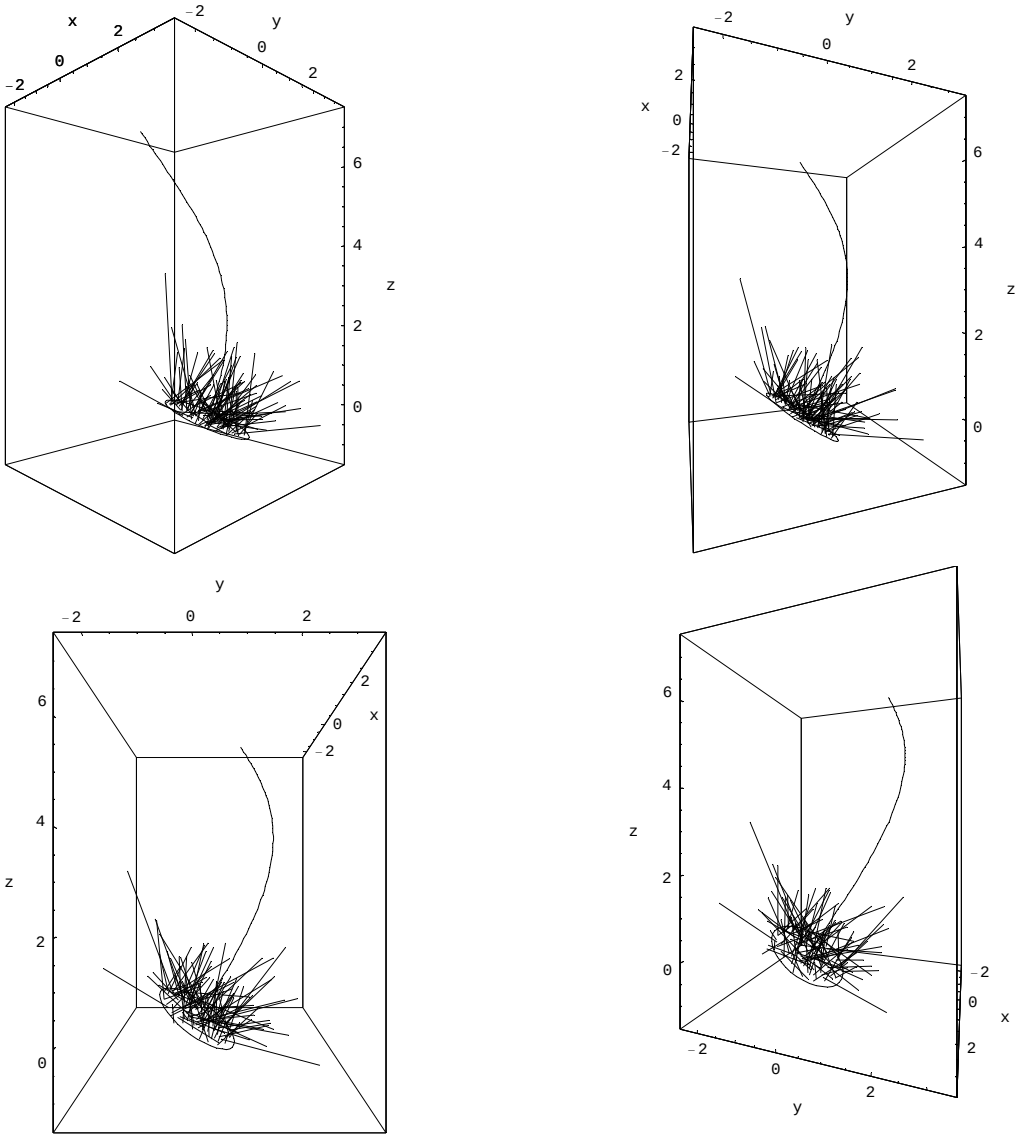

Figure 6.19: Perspectives on the Selection of Initial Velocities on the Entrance Plane

The velocities are presented in Fig. 6.19 as lines that project from the plane into the volume of the tube. No arrows are available for 3-dimensional lines in Mathematica® 5.2. The length of each line does represent the magnitude of the speed.

Although the molecular speed does not influence the value of w, it does affect aspects of the flow such as particle residence time within the tube and momentum flux from the tube. In molecular flows, the molecular speed is directly related to the temperature. The temperature in turn is directly related to the parameter β in Eq. 6.2 by the equation

$$\beta = \left(\frac{m}{2kT(s,\varphi)} \right)^{1/2} \tag{6.44}$$

where the temperature is written explicitly as a function of the wall position. Since the current model assumes diffuse scattering in which the particle comes to thermal equilibrium with the wall before being "re-emitted", a temperature variation along or around the tube wall can be implemented by substituting the position-dependent β into Eq. 6.2 when determining the post-collision speed of a test particle. A degree of caution is warranted when large temperatures are used with curved tubes in the algorithms described above. This is due to the fact that if the speed is high enough, then the particle may be allowed to "tunnel" to different parts of the tube. This effect is demonstrated in Fig. 6.20.

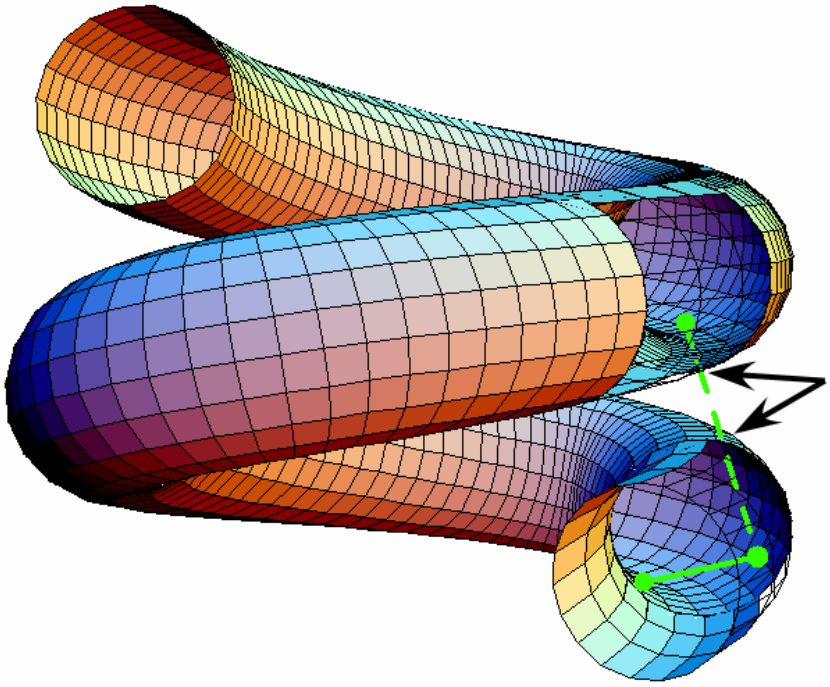

Figure 6.20: Demonstration of the "Tunneling Effect"

Figure 6.20 shows the first two steps in a simulation where the particle starts at the center of the entrance plane, travels along the trajectory denoted by the solid line, collides with the wall once, acquires a high speed due to heat transfer, and departs the wall along the trajectory denoted by the dashed line. In this case, the dashed line indicates the distance traveled when the parameter t_1 in Eq. 6.38 is set equal to unity. According to the algorithm described above for curved tubes however, the minimum distance between the test particle and the central axis of the tube is less than the radius of the tube. This indicates that the particle is still inside the tube even though in actuality it has left the tube and re-entered at the points indicated by the arrows. The algorithm will continue to advance the particle along an extension of the dashed line until it is determined that the minimum distance between the particle position and the central axis of the tube is greater than the radius of the tube, or that the particle has advanced along

the parameter s sufficiently far as to conclude that the particle has been transmitted. The result is that the particle has appeared to "tunnel" through the tube walls. This problem can be prevented by ensuring that the particle speed is low enough to limit the distance traveled or by increasing the initial value of the index i in Eq. 6.38 in order to decrease the time that a particle can travel with a given speed. For the simulations used to generate the results presented in Table 6.4, a value of 1 was taken for β. This value limited the speed that a particle could assume. In addition, the values of a, b, s, and R were chosen such that "tunneling" was improbable. The word improbable is used instead of impossible due to the fact that the selection of the speed is from a distribution and the possibility of getting an unusually high velocity is possible from time to time. Figure 6.21 shows a graphical representation of the distribution defined by Eq. 6.2 from which the post collision speeds were selected.

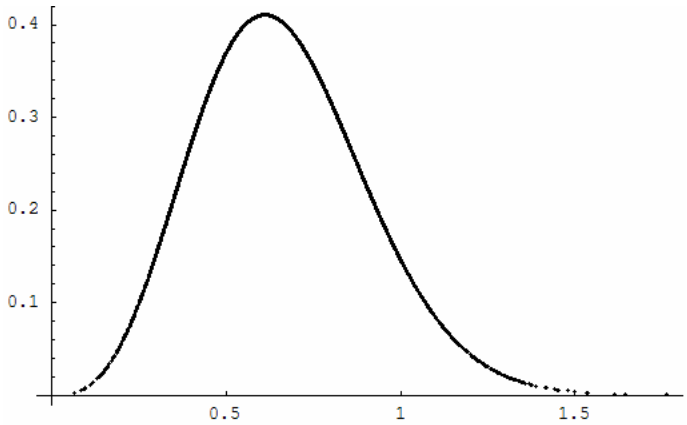

Figure 6.21: Graphical Representation of Eq. 6.2

In order to justify the results presented in Table 6.4, a visual quantitative investigation was performed for assurance that the tunneling effect did not occur. A

wireframe mesh of the shape of each helix in Table 6.4 was plotted along with the associated initial velocity vectors. These plots are shown in Fig. 6.22. The length of each helix in Fig. 6.22 is 5 and the radius is 1. Thus, they correspond to column 5 of Table 6.4. This length was used because the full geometrical nature of the helix became evident at that length and because longer lengths required more space and effectively "zoomed out" from the initial velocity vectors. For the helices in which the parameter a = 1, two different perspectives are given due to the fact that their geometries are the most likely to allow "tunneling".

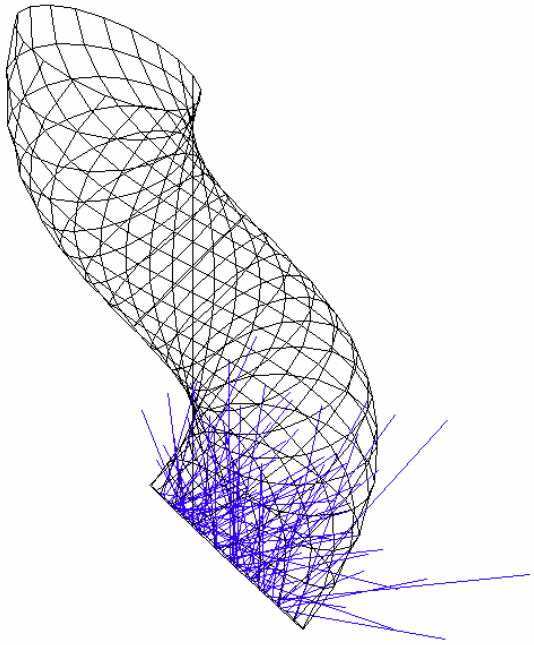

Figure 6.22a: $a = 1, b=1$

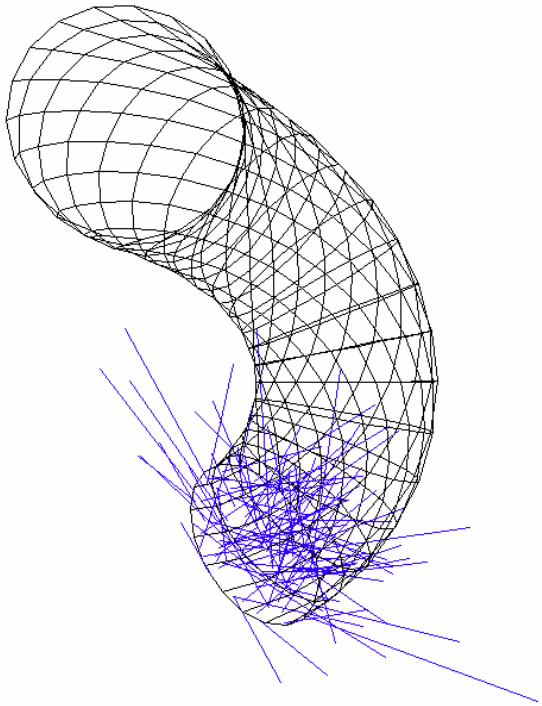

Figure 6.22b: $a = 1, b = 1$

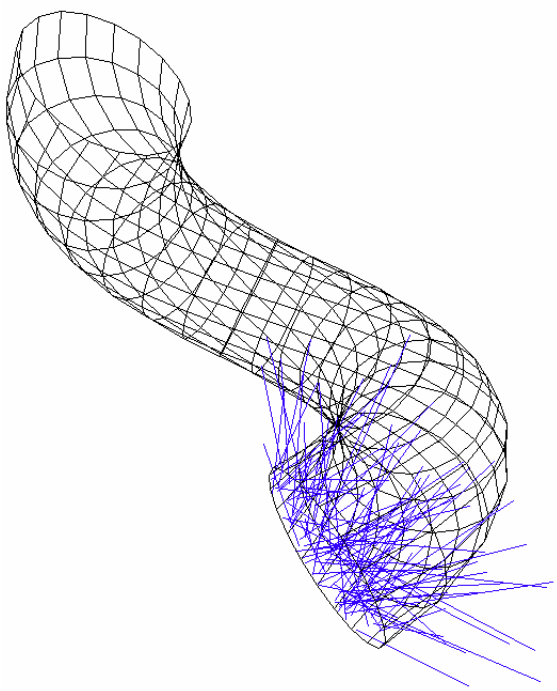

Figure 6.22c: *a = 2, b=1*

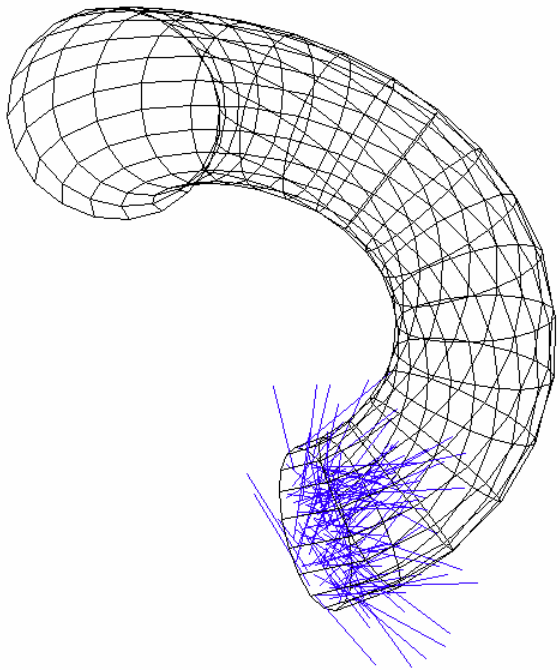

Figure 6.22d: *a = 2, b=1*

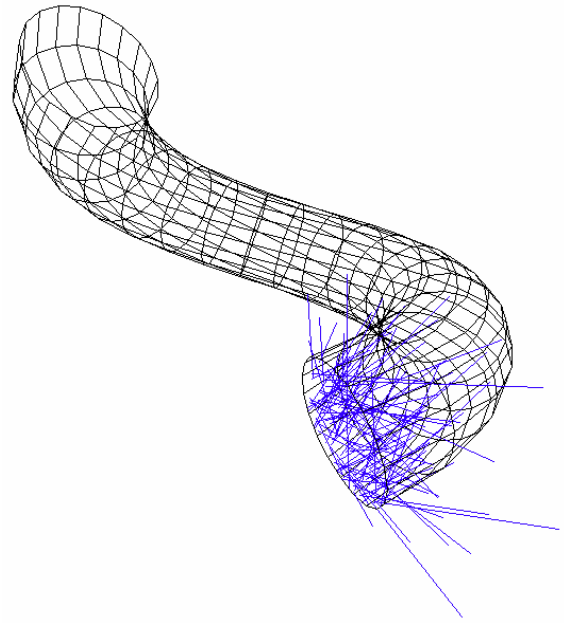

Figure 6.22e: *a = 3, b=1*

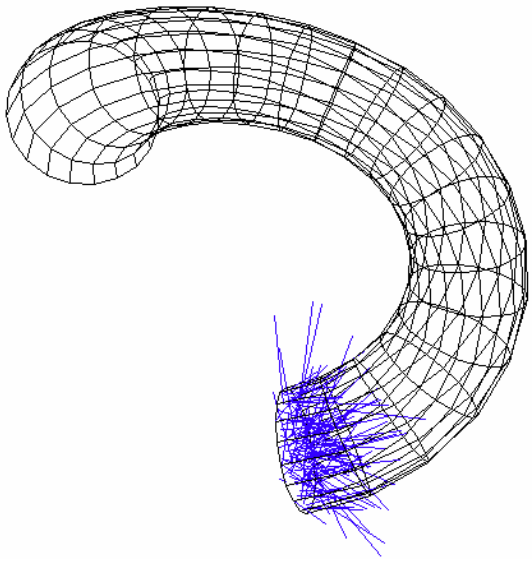

Figure 6.22f: *a = 3, b=1*

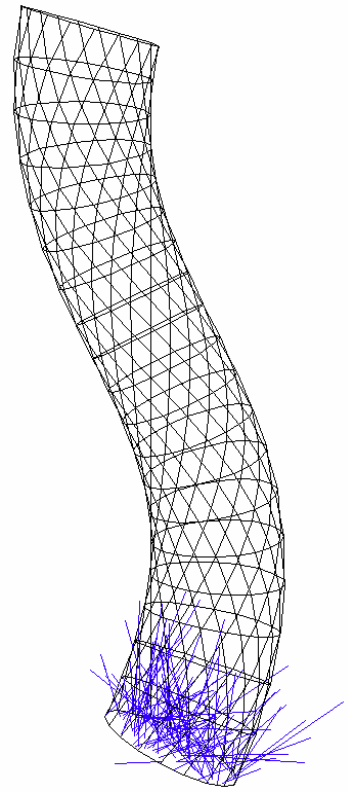

Figure 6.22g: *a = 1, b=2*

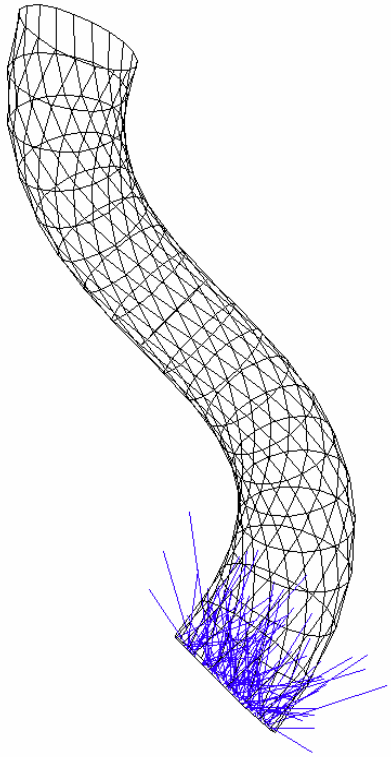

Figure 6.22h: *a = 2, b=2*

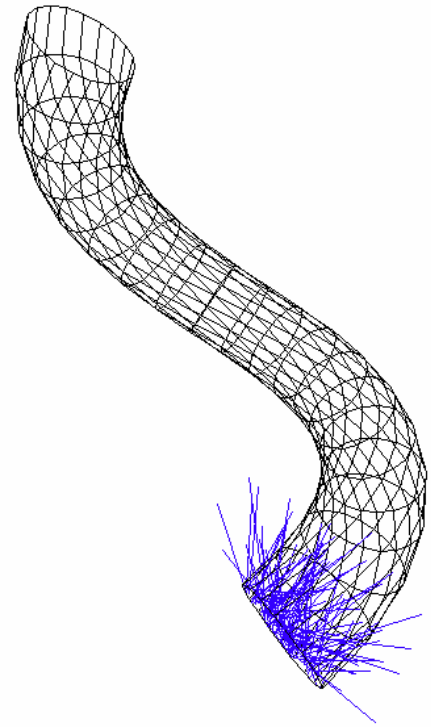

Figure 6.22i: *a = 3, b=2*

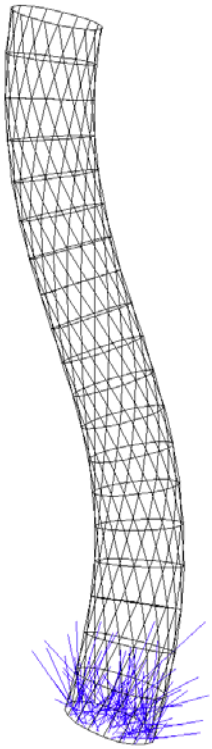

Figure 6.22j: *a = 1, b=3*

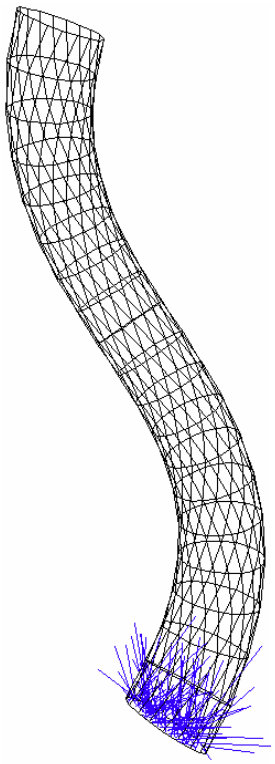

Figure 6.22k: *a = 2, b=3*

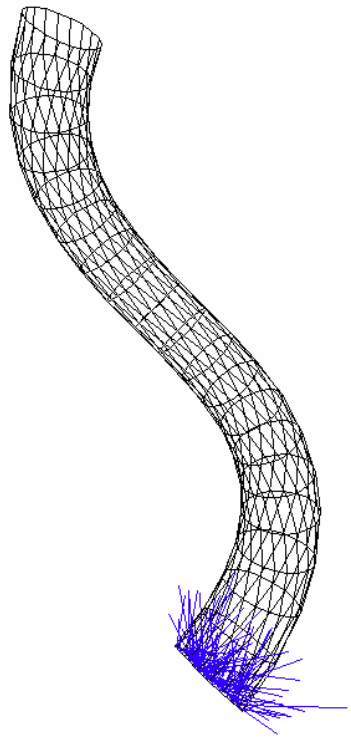

Figure 6.22l: *a = 3, b=3*

Of all of the images that appear in Fig. 6.22, the only helix for which it appears that tunneling is possible is the helix for which a =1 and b = 1 shown in Fig. 6.22a and 6.22b. It must be kept in mind however that for tunneling to occur, not only must the particle pass through the tube wall, it must also pass back into the tube through another stretch of the wall. This occurrence is exceedingly unlikely since according to the cosine law, the velocity must be oriented in the hemisphere pointing into the tube.

6.6 SIMULATION RESULTS AND ASSOCIATED RELATIVE ERRORS

Simulations were run with each of the geometries mentioned in the previous sections and the number of particles being transmitted and the number reflected were recorded. This data was used to calculate *w*. Each simulation consisted of 10,000 test particles. The results of these simulations are presented in Tables 6.1 through 6.4. Where existing calculations are available, they are listed for direct comparison with the results from the current study.

Table 6.1: Calculated Values of *w* for Straight Circular Tubes vs. those of Clausing [6.10]

L/R	Our Results	Clausing
0.1	0.9525	0.9524
1	0.6701	0.672
5	0.3089	0.3146
10	0.1928	0.1973

Table 6.2: Calculated Values of *w* for Conical Tubes vs. those of Gomez-Goni and Lobo [6.7]

Alpha	Study	L/R_0=0.1	L/R_0=1	L/R_0=5	L/R_0=10
1	Gomez-Goni	0.9541	0.6854	0.346	0.2368
	Current	0.9532	0.6882	0.3421	0.2322
30	Gomez-Goni	0.9869	0.9334	0.9081	0.9061
	Current	0.987	0.9325	0.9067	0.9055
60	Gomez-Goni	0.9986	0.9959	0.9956	0.9956
	Current	0.999	0.9955	0.9951	0.9949

Table 6.3: Calculated Values of *w* for Straight Elliptical Tubes

a	b	L/R=0.1	L/R=1	L/R=5	L/R=10
1	2	0.9606	0.7205	0.3762	0.2427
	3	0.9657	0.7257	0.399	0.2644
	4	0.9693	0.759	0.4181	0.2744

Table 6.4: Calculated Values of *w* for Helical Tubes

b	a	L/R=0.1	L/R=1	L/R=5	L/R=10
1	1	0.9518	0.669	0.2903	0.0332
	2	0.9559	0.6802	0.2807	0.0284
	3	0.9532	0.6798	0.3086	0.0345
2	1	0.9529	0.6729	0.3082	0.1841
	2	0.9481	0.669	0.3047	0.1872
	3	0.953	0.6781	0.2982	0.1764
3	1	0.9506	0.6647	0.3005	0.1883
	2	0.9523	0.6729	0.3049	0.1917
	3	0.9519	0.6706	0.3111	0.1881

The values of *w* generated in this study and displayed in Tables 6.1 through 6.4 have errors associated with them due to the fact that they were determined using Monte Carlo Techniques. Since the technique used to calculate these values so closely matches the method used by the Department of Energy's Monte Carlo N-Particle (MCNP) code for modeling particle transport, the method used for determining the relative error in the results from the MCNP code will be used here to determine the relative error in the Monte Carlo code discussed in this chapter. In the MCNP code, the relative error R_{MC} associated with the results of a simulation is defined as [6.11]

$$R_{MC} = \frac{\sigma_{MC}}{\mu_{MC}} \tag{6.45}$$

where σ_{MC} is the estimated standard deviation and μ_{MC} is the mean. In order to generate values of the mean and standard deviations, a set of simulations composed of the same number of particle histories must be run. One history refers to the simulation of one particle from entrance into to exit from the pathway. According to the Central Limit

Theorem, there is a 68% chance that the true answer to a problem lies within the range $\mu_{MC}(1\pm R_{MC})$, a 95% chance that the true answer lies within the range $\mu_{MC}(1\pm 2R_{MC})$, and a 99% chance that the true answer lies within the range $\mu_{MC}(1\pm 3R_{MC})$. An interesting characteristic of the relative error is that it is proportional to the number of histories N_{MC} through the relation

$$R_{MC} \propto \frac{1}{\sqrt{N_{MC}}} \tag{6.46}$$

Equation (6.46) can be used to determine a constant of proportionality that can be used to determine the relative error associated with simulations consisting of a large number of histories. The relation thus eliminates the necessity to run several simulations consisting of a large number of histories in order to determine the mean and the standard deviation associated with the simulation. Take for instance, the value of 0.9525 reported for w for the case L/R = 0.1 in Table 6.1. This value was determined after running 10,000 particle histories in which 9525 resulting in the particle being transmitted through the pathway. If the results from the 10,000 histories run to determine this number are divided into 1000 sets of 10 histories, the mean value of w generated from these sets is 0.9525 with a standard deviation of 0.0666. These results correspond to a relative error of 0.0699. Since N_{MC} = 10 in this case, the constant of proportionality corresponding to Eq. 6.46 is 0.2212. If the results of the 10,000 histories are instead divided into 100 sets of 100 histories, the resulting mean is 0.9525 with a standard deviation of 0.0213 corresponding to a relative error of 0.0213. The constant of proportionality can be determined from

these values to be 0.2240. If the results of the 10,000 histories are divided into 10 sets of 1000 histories, the resulting mean is 0.9525 with a standard deviation of 0.0080 corresponding to a relative error of 0.0084. These numbers imply a constant of proportionality of 0.2643. The constants of proportionality determined from each of these cases are close to the same value, but are not exactly the same. How does one decide which to use? A strong case can be made that thee constant of proportionality determined from the 1000 sets of 10 histories is the most accurate since it is determined from a larger statistical sample. However, to be conservative, one could use the largest of the three values. In this study, it has been decided to take the mean of the three values, or 0.2365 as the proportionality constant. This means that according to equation (6.???), the relative error associated with the value obtained from 1 set of all 10,000 histories should be equal to $R_{MC} = 0.2365/\sqrt{10{,}000} = 0.002365 \approx 0.0024$. This means that there is a 99% chance that the result of 0.9525 reported in Table 6.1 is within $\pm$ 0.0072 of the true answer. The result of 0.9525 is definitely within $\pm$ 0.0072 of the previously reported result of 0.9525. This experiment validates the results of the Monte Carlo program reported in this chapter. The relative errors associated with the other values in Tables 6.1 through 6.4 are presented in Tables.6.5 through 6.7. Each of the values in these tables was calculated with the same method described above.

Table 6.5: Relative Errors Associated with the Monte Carlo Results for Conical Tubes

Alpha	L/R_0=0.1	L/R_0=1	L/R_0=5	L/R_0=10
0	0.00237	0.00704	0.0133	0.01779
1	0.00186	0.00661	0.01532	0.01856
30	0.00122	0.0027	0.00361	0.00356
60	0.00035	0.00068	0.00068	0.00079

Table 6.6: Relative Errors Associated with the Monte Carlo Results for Elliptical Tubes

a	b	L/R=0.1	L/R=1	L/R=5	L/R=10
1	2	0.00899	0.00594	0.01339	0.01881
	3	0.00753	0.0059	0.01164	0.01718
	4	0.00883	0.00587	0.01113	0.01474

Table 6.7: Relative Errors Associated with the Monte Carlo Results for Helical Tubes

b	a	L/R=0.1	L/R=1	L/R=5	L/R=10
1	1	0.0099	0.01508	0.0153	0.01055
	2	0.00412	0.00652	0.00799	0.00742
	3	0.00198	0.00238	0.00604	0.00527
2	1	0.00943	0.01457	0.01416	0.0109
	2	0.00399	0.00567	0.00754	0.0061
	3	0.00177	0.00233	0.00672	0.00453
3	1	0.01252	0.01	0.01482	0.0117
	2	0.00398	0.00457	0.00532	0.00562
	3	0.00147	0.00187	0.00589	0.0047

The values of w presented in Tables 6.1 through 6.4 can be directly inserted into Eq. 6.10 in order to determine mass flow rates. It should be noted that these results are associated directly with the geometry of a given tube and are independent of the molecular speed. Although the speed of each particle simulated to generate the results in Tables 6.1 through 6.4 was determined from Eq. 6.2 after each collision with the tube wall, it is ultimately only the direction of particle motion that determines whether or not a particle will collide again with the wall or be transmitted or reflected. Thus, the four factors affecting the results in Tables 6.1 through 6.4 are the test particle initial positions, the directions of the initial velocities, the geometry of the tube, and the distribution from which the post-collision velocity is chosen (cosine law). The methods used to determine each of these factors for the simulations in this study are carefully described above so that future numerical methods and experiments can be directly compared.

6.7 CONCLUSIONS

In this chapter, a Monte Carlo model for tracking molecular gas flow through nano-scale cracks in spent fuel was successfully created. This model was modified to describe flow through straight cylindrical tubes, straight conical tubes, straight elliptical tubes, and helical tubes of constant circular cross section. The parameter of interest generated by the Monte Carlo program for each tube geometry is the transmission fraction *w*. This parameter can be used to determine the mass flow rate of the gas through the tube. Although the specifics of the program must be modified for each tube shape considered, the same principles presented in this chapter can be used to generate transmission fractions for additional geometries of interest. The accuracy of the Monte Carlo program is directly related to the number of test particles used in each simulation. Future work on this topic will focus on expanding to new tube shapes and generating more accurate results with simulations consisting of much larger number of test particles.

REFERENCES

6.1 MacLean, H.J., "Silver Transport in CVD Silicon Carbide," Ph.D Thesis, Massachusetts Institute of Technology (2004).

6.2 Bird, G.A., Molecular Gas Dynamics and the Direct Simulation of Gas Flows, Clarendon Press, Oxford (1994).

6.3 Karniadakis, G., Beskok, A., Aluru, N., Microflows and Nanoflows, Fundamentals and Simulation, Springer, New York (2005).

6.4 Knudsen, M., The Kinetic Theory of Gases, John Wiley & Sons Inc., New York (1950)

6.5. von Smoluchowski, M. "Zur kinetischen Theorie der Transpiration und Diffusion verdünnter Gase", *Annalen der Physik,* 33(4), (1910) p. 1559-1570.

6.6 Gray, A., Modern Differential Geometry of Curves and Surfaces with Mathematica®, 2nd Ed, CRC Press, Boca Raton (1998).

6.7 Gomez-Goni, J. and Lobo, P.J., "Comparison between Monte Carlo and analytical calculation of the conductance of cylindrical and conical tubes" *Journal of Vacuum Science and Technology A*, 21(4), (2003) p. 1452-1457.

6.8 Sakurai, J.J., Modern Quantum Mechanics, 2nd Edition, Addison-Wesley, New York (1994).

6.9 Goldstein, H., Poole, C., and Safko, J., Classical Mechanics, 3rd Ed., Addison Wesley, New Jersey (2002).

6.10 Clausing, P., "Über die Strömung sehr verdünnter Gase durch Röhren von beliebiger Länge," *Annalen der Physik,* 12(5), (1932) p. 961-989, in German. English translation, "The Flow of Highly Rarefied Gases through Tubes of Arbitrary Length," *Journal of Vacuum Science and Technology*, 8(5), (1971) p. 636-646.

6.11 X-5 Monte Carlo Team, MCNP – A General Monte Carlo N-Particle Transport Code, Version 5, Volume 1: Overview and Theory , Los Alamos National Laboratory, (2005)

CHAPTER 7: MODELING AEROSOL RELEASE AND PLUGGING

7.1 INTRODUCTION

The depressurization of a spent fuel canister after the formation of a small pinhole breach was discussed in Chapter 4. In the scenario discussed in Chapter 4, no radiation was released as only the helium fill gas was escaping from this canister. Thus, the main consequence of the depressurization is the loss of the inert and thermally conductive atmosphere provided by the helium. The release of radioactivity to the environment in this case is not an issue of concern. However, if a significant quantity of particulates is present in the fill gas, the scenario is much different. The radioactivity associated with suspended particles can escape through the breach along with the fill gas. The release of this radioactivity to the environment becomes a topic of concern. Also if particles suspended in the fill gas are deposited as they are transported through the breach, they may restrict the flow leading to depressurization. This chapter focuses on expanding the model presented in Chapter 4 in order to account for the presence of suspended particles in the fill gas within the spent fuel canister.

7.2 STEADY-STATE CONVECTIVE-DIFFUSIVE DEPOSITION OF PARTICLES IN FULLY-DEVLOPED LAMINAR FLOWS

In Chapter 4 the argument was made that the dimensions of the breaches being considered in this study are small enough, and the velocity generated by the pressure

differential low enough, that the gas flows under consideration will be laminar. This claim is verified quantitatively by examination of the Reynolds number

$$\mathrm{Re} = \frac{2\rho_g U_{av} a_t}{\mu} \tag{7.1}$$

where ρ_g is the mass density of the carrier gas, U_{av} is the average "bulk" velocity of the gas, μ is the viscosity of the gas, and a_t is the radius of the breach. In general, systems described by a Reynolds number less than 2100 can be consider to exhibit laminar flow. Since ideal pinhole breaches are being considered here, the geometry of concern is a straight right-cylinder with a constant circular cross section. These conditions imply that the gas flow through the breach should be described by the Poiseuille equation as claimed in Chapter 4, which dictates that the velocity distribution within the breach is characterized by [7.1]

$$u_z(r) = \frac{(P_{in} - P_{out})a_t^2}{4\mu L}\left[1 - \left(\frac{r}{a_t}\right)^2\right] = 2U_{av}\left[1 - \left(\frac{r}{a_t}\right)^2\right] \tag{7.2}$$

Equation 7.2 defines the stream velocity of the gas in the axial direction at a radial distance r from the center of the cylindrical breach. The radial and angular velocities of the gas flow are considered non-existent. According to Eq. 7.2 the velocity of a molecule of the gas at a defined radial position will be pointed in the axial direction and have a constant value as the particle travels axially along the breach. Although this description is valid for macroscopic analysis, it is known from the kinetic theory of gases that this is

not an accurate description of molecular motion. Instead, each gas molecule is traversing a tortuous, chaotic path at any given time or location. However, when the motions of all of the gas molecules are averaged together, the resultant bulk velocity corresponds well to Eq. 7.2. If a particle, similar in size to a gas molecule happens to be suspended within the gas and carried into the breach, then its behavior would mimic that of a gas molecule. The particle would have an axial motion determined by its radial position in the breach, and tortuous, chaotic radial and angular motions. The axial motion described here is known as the convective motion of the particle, while the particle motion in the radial and angular directions is known as the Brownian diffusion of the particle. If the particle being considered here is much larger, then the particle inertia and acceleration due to gravity start to affect the particle motion. Just as the laminar flow of the gas was verified with the Reynolds number defined by Eq. 7.1, the degree to which the convective flow velocity of a particle departs from the convective flow velocity of the carrier gas due to the particle inertia is quantified by the Stokes number [7.2]

$$Stk = \frac{\rho_p d_p^2 C_c U}{18 \mu a_t} \quad for\ \mathrm{Re}_0 < 1.0 \tag{7.3}$$

where Re_0 is the particle Reynolds number defined in the same way as Eq. 7.1 but with the particle density and particle velocity replacing the gas density and gas velocity. For the case *Stk « 1*, the particle tends to follow the fluid velocity streamline exactly while for *Stk > 1* the particle tends to deviate significantly from the streamlines due to inertial motion. In Eq. 7.3, the parameter d_p refers to the particle diameter and the parameter C_c

is the Cunningham slip correction factor which has been experimentally determined to be [7.3]

$$C_c = 1 + \frac{\lambda}{d_p}\left[2.34 + 1.05e^{-0.39\frac{d_p}{\lambda}}\right] \tag{7.4}$$

where λ is the mean free path of the carrier gas. Although Eq. 7.4 counteracts the trend in Eq. 7.3 for particle diameter, it is apparent that in general, the smaller the particle, the more likely it is that the particle convective motion will match the bulk convective motion of the carrier gas in the immediate vicinity of the particle. However, the smaller the particle, the more the particle behaves like an individual gas molecule and thus the greater the effect of Brownian diffusion on the particle motion. The Brownian diffusion of a large number of particles through a gas can be described macroscopically by the equation

$$J = -D\nabla n \tag{7.5}$$

where n is the number density of the aerosol particles and D is Einstein's diffusion coefficient [7.4]

$$D = \frac{kTC_c}{6\pi\mu a} \tag{7.6}$$

where k is Boltzmann's constant, T is the absolute temperature of the carrier gas, and a is the particle radius. Einstein's original diffusion coefficient did not include the Cunningham slip correction factor.

If the particles are small enough, the inertia associated with their motion and the effects of gravity will be negligible. If the carrier gas is isothermal, then motion due to thermal gradients will be non-existent. If there are no electric charges on the particles, then there will be no electromagnetically induced particle motion. Under these circumstances, the motion of particles suspended in a carrier gas can be described solely by the convective motion of the particle which is directly coupled to the convective motion of the carrier gas, and the diffusion due to Brownian motion. In the case that the aerosol under consideration is flowing through a straight, right-cylindrical breach with a constant circular cross section, the convective motion of the particle can be described by Eq. 7.2 and the diffusive motion can be described by Eq. 7.5. If it is assumed that a particle is deposited once it comes into contact with the tube wall, then the steady-state particle continuity equation retaining only the convective and diffusive terms for fully developed laminar flow in a straight tube of circular cross section can be written in cylindrical coordinates in the non-dimensional form [7.5]

$$(1-\hat{r}^2)\frac{\partial \hat{n}}{\partial \hat{x}} = \frac{1}{Pe}\frac{1}{\hat{r}}\frac{\partial}{\partial \hat{r}}\left(\hat{r}\frac{\partial \hat{n}}{\partial \hat{r}}\right) \tag{7.7}$$

with the boundary conditions

$$\hat{n}(\hat{r},0) = 1 \quad and \quad \hat{n}(1,\hat{x}) = 0 \tag{7.8}$$

where

$$\hat{r} = \frac{r}{a_t} \quad , \quad \hat{x} = \frac{x}{a_t} \quad , \quad \hat{n} = \frac{n}{n_0} \quad , \quad Pe = \frac{a_t U}{D} \tag{7.9}$$

This equation has been solved analytically using separation of variables and eigenfunction expansion in order to provide the well known expression [7.6]

$$P(\hat{x}) = 0.81919e^{-7.312\hat{x}/Pe} + 0.0975e^{-44.62\hat{x}/Pe} + 0.0325e^{-113.8\hat{x}/Pe} + ... \tag{7.10}$$

where P represents the fraction of the particles entering the tube that reach the axial distance $\hat{x}$ without being deposited on the tube wall. This solution is well established and is analogous to the more well-known Graetz problem of heat transfer [7.7].

Some authors prefer to write Eq. 7.10 in the form [7.8]

$$P(z) = 0.819e^{-\alpha} + 0.0975e^{-6.1\alpha} + 0.0325e^{-16\alpha} + ... \tag{7.11}$$

where

$$\alpha = \frac{3.66\pi Dz}{Q} \tag{7.12}$$

and Q is the aerosol volumetric flow rate through the tube. The volumetric flow rate is related to the velocity U and the tube radius a_t through the equation

$$Q = \frac{U\pi a_t^2}{2} \tag{7.13}$$

Substituting Eq. 7.9 into Eq. 7.10 and Eq. 7.12 and 7.13 into Eq. 7.11 and recognizing that *z* in Eq. 7.12 is the same parameter as *x* in Eq. 7.9 allows for the direct comparison of the exponents that occur in Eq. 7.10 and Eq. 7.11

$$\frac{-7.312\,Dx}{a_t^2U} \approx \frac{-7.32\,Dz}{a_t^2U}, \quad \frac{-44.62\,Dx}{a_t^2U} \approx \frac{-44.652\,Dz}{a_t^2U}, \quad \frac{-113.8\,Dx}{a_t^2U} \approx \frac{-117.12\,Dz}{a_t^2U}$$

These comparisons show that the exponents are nearly the same. It is apparent that Eq. 7.10 is the more accurate equation with Eq. 7.11 being an approximation. However, the differences in the two equations do not really become apparent until the third exponent. The third term in the series of Eq. 7.10 and 7.11 is nearly negligible compared to the first two terms. Since the difference between the exponents in the third terms of the equations is so small, the difference in the results from the two equations is nearly imperceptible.

When modeling aerosol flows and reading published reports on the subject, it is convenient to be able to convert between the exponential terms in Eq. 7.11 that contain the volumetric flow rate and the exponential terms in Eq. 7.10 that contain the flow velocity. In order to show the direct relationship between the two flow rates, Eqs. 7.9 and 7.13 are substituted into Eq. 7.10 to form

$$P(x) = 0.81919e^{-7.312(\pi x D/2Q)} + 0.0975e^{-44.62(\pi x D/2Q)} + 0.0325e^{-113.8(\pi x D/2Q)} + \ldots \tag{7.14}$$

Also, combining Eq. 7.2 and Eq. 7.13 leads to the equation

$$Q = \frac{(P_{in} - P_{out})\pi a_t^4}{8\mu L} \tag{7.15}$$

If the pressure inside the tube is assumed to be the arithmetic average of the inlet and the outlet pressures, and the temperature within the tube is assumed to be equal to the tube wall temperature, then according to the ideal gas law,

$$\frac{n}{V} = \left(\frac{P_{in} + P_{out}}{2}\right)\frac{1}{RT_w} \tag{7.16}$$

The molar flow rate through the breach is equal to the product of the volumetric flow rate and the molecular density of the flowing fluid. Thus, the molar flow rate should result from the product of Eq. 7.15 and Eq. 7.16, or

$$\frac{Qn}{V} = \dot{n} = \left(\frac{(P_{in} - P_{out})\pi a_t^4}{8\mu L}\right)\left(\left(\frac{P_{in} + P_{out}}{2}\right)\frac{1}{RT_w}\right) = \left(\frac{(P_{in}^2 - P_{out}^2)\pi a_t^4}{16\mu L R T_w}\right) \tag{7.17}$$

which is equivalent to Eq. 4.2.

In Eq. 7.7, it has been assumed that diffusion in the axial direction can be neglected. This assumption has been shown to be valid for systems in which the Péclet number, *Pe*, is much greater than 1 [7.9]. It has also been shown that for values of *Pe* less than or equal to 100, the effect of axial diffusion is significant only for a length equal

to two and one-half times the breach diameter from the breach entrance and can be neglected for axial distances farther from the entrance [7.10]. In the systems studied in this thesis, the length of the breach (1 cm) is several orders of magnitude greater than the diameter of the breach (10 – 100 μm). In Eq. 7.7, the angular diffusion has been neglected as well. The significance of this assumption will be discussed in Chapter 8. In order to put the parameters involved in the discussion to this point in quantitative terms, Tables 7.1 through 7.8 have been constructed from the equations above. In each of the cases below, the temperature is assumed constant throughout the tube and the parameters are calculated at a pressure value equal to the arithmetic mean of the inlet pressure and atmospheric pressure.

Table 7.1: P_{in} = 1.87 atm, T = 558 K, fill gas = helium, a_t = 5 μm, L = 1 cm

d_p nm	1	5	10	50	100	500	1000
U (m/s)	1.792	1.792	1.792	1.792	1.792	1.792	1.792
μ (μPa s)	30.74	30.74	30.74	30.74	30.74	30.74	30.74
λ (nm)	258	258	258	258	258	258	258
Kn	0.0516	0.0516	0.0516	0.0516	0.0516	0.0516	0.0516
C_c	875.2	175.5	88.1	18.1	9.37	2.46	1.66
D (m^2/s)	2.33E-05	9.33E-07	2.34E-07	9.63E-09	2.50E-09	1.31E-10	4.42E-11
P(L)	0	0	0	1.24E-07	0.014	0.689	0.835
Re	0.073	0.073	0.073	0.073	0.073	0.073	0.073
Pe	0.385	9.6	38.27	931.021	3598	68442	202585

Table 7.2: P_{in} = 1.87 atm, T = 558 K, fill gas = helium, a_t = 25 μm, L = 1 cm

d_p nm	1	5	10	50	100	500	1000
U (m/s)	44.81	44.81	44.81	44.81	44.81	44.81	44.81
μ (μPa s)	30.74	30.74	30.74	30.74	30.74	30.74	30.74
λ (nm)	258	258	258	258	258	258	258
Kn	0.0103	0.0103	0.0103	0.0103	0.0103	0.0103	0.0103
C_c	875.2	175.5	88.1	18.1	9.37	2.46	1.66
D (m^2/s)	2.33E-05	9.33E-07	2.34E-07	9.63E-09	2.50E-09	1.31E-10	4.42E-11
P(L)	0	0.072	0.447	0.904	0.937	0.949	0.949
Re	9.14	9.14	9.14	9.14	9.14	9.14	9.14
Pe	48.13	1200	4784	116378	449748	8.56E+06	2.53E+07

Table 7.3: P_{in} = 1.87 atm, T = 558 K, fill gas = helium, a_t = 50 μm, L = 1 cm

d_p nm	1	5	10	50	100	500	1000
U (m/s)	179.2	179.2	179.2	179.2	179.2	179.2	179.2
μ (μPa s)	30.74	30.74	30.74	30.74	30.74	30.74	30.74
λ (nm)	258	258	258	258	258	258	258
Kn	0.0052	0.0052	0.0052	0.0052	0.0052	0.0052	0.0052
C_c	875.2	175.5	88.1	18.1	9.37	2.46	1.66
D (m^2/s)	2.33E-05	9.33E-07	2.34E-07	9.63E-09	2.50E-09	1.31E-10	4.42E-11
P(L)	0.018	0.745	0.884	0.946	0.948	0.949	0.949
Re	73.1	73.1	73.1	73.1	73.1	73.1	73.1
Pe	385.041	9600	38270	931021	3.60E+06	6.84E+07	2.03E+08

Table 7.4: P_{in} = 1.87 atm, T = 400 K, fill gas = helium, a_t = 50 μm, L = 1 cm

d_p nm	1	5	10	50	100	500	1000
U (m/s)	224.4	224.4	224.4	224.4	224.4	224.4	224.4
μ (μPa s)	24.55	24.55	24.55	24.55	24.55	24.55	24.55
λ (nm)	185	185	185	185	185	185	185
Kn	0.0037	0.0037	0.0037	0.0037	0.0037	0.0037	0.0037
C_c	627.6	126	63.3	13.2	6.9	2	1.46
D (m^2/s)	1.50E-05	6.01E-07	1.51E-07	6.28E-09	1.65E-09	9.55E-11	3.48E-11
P(L)	0.116	0.827	0.914	0.948	0.949	0.949	0.949
Re	159.9	159.9	159.9	159.9	159.9	159.9	159.9
Pe	749.1	18657	74276	1.79E+06	6.81E+06	1.18E+08	3.23E+08

Table 7.5: P_{in} = 1.87 atm, T = 558 K, fill gas = air, a_t = 5 μm, L = 1 cm

d_p nm	1	5	10	50	100	500	1000
U (m/s)	1.878	1.878	1.878	1.878	1.878	1.878	1.878
μ (μPa s)	29.33	29.33	29.33	29.33	29.33	29.33	29.33
λ (nm)	89.03	89.03	89.03	89.03	89.03	89.03	89.03
Kn	0.0178	0.0178	0.0178	0.0178	0.0178	0.0178	0.0178
C_c	302.4	60.96	30.78	6.669	3.687	1.438	1.21
D (m^2/s)	8.43E-06	3.40E-07	8.58E-08	3.72E-09	1.03E-09	8.01E-11	3.37E-11
P(L)	0	0	0	2.51E-03	0.165	0.773	0.862
Re	0.1046	0.1046	0.1046	0.1046	0.1046	0.1046	0.1046
Pe	1.1144	27.642	109.48	2527	9141	117209	2.79E+05

Table 7.6: P_{in} = 1.87 atm, T = 558 K, fill gas = air, a_t = 25 μm, L = 1 cm

d_p nm	1	5	10	50	100	500	1000
U (m/s)	49.61	49.61	49.61	49.61	49.61	49.61	49.61
μ (μPa s)	29.33	29.33	29.33	29.33	29.33	29.33	29.33
λ (nm)	89.03	89.03	89.03	89.03	89.03	89.03	89.03
Kn	0.0036	0.0036	0.0036	0.0036	0.0036	0.0036	0.0036
C_c	302.4	60.96	30.78	6.669	3.687	1.438	1.21
D (m^2/s)	8.43E-06	3.40E-07	8.58E-08	3.72E-09	1.03E-09	8.01E-11	3.37E-11
P(L)	6.23E-10	0.352	0.689	0.932	0.944	0.949	0.949
Re	13.08	13.08	13.08	13.08	13.08	13.08	13.08
Pe	139.3	3455	13685	3.16E+05	1.14E+06	1.47E+07	3.48E+07

Table 7.7: P_{in} = 1.87 atm, T = 558 K, fill gas = air, a_t = 50 μm, L = 1 cm

d_p nm	1	5	10	50	100	500	1000
U (m/s)	187.8	187.8	187.8	187.8	187.8	187.8	187.8
μ (μPa s)	29.33	29.33	29.33	29.33	29.33	29.33	29.33
λ (nm)	89.03	89.03	89.03	89.03	89.03	89.03	89.03
Kn	0.0018	0.0018	0.0018	0.0018	0.0018	0.0018	0.0018
C_c	302.4	60.96	30.78	6.669	3.687	1.438	1.21
D (m^2/s)	8.43E-06	3.40E-07	8.58E-08	3.72E-09	1.03E-09	8.01E-11	3.37E-11
P(L)	0.221	0.862	0.925	0.948	0.949	0.949	0.949
Re	104.6	104.6	104.6	104.6	104.6	104.6	104.6
Pe	1114.39	27642	1.10E+05	2.53E+06	9.14E+06	1.17E+08	2.79E+08

Table 7.8: P_{in} = 1.87 atm, T = 400 K, fill gas = air, a_t = 50 μm, L = 1 cm

d_p nm	1	5	10	50	100	500	1000
U (m/s)	237.5	237.5	237.5	237.5	237.5	237.5	237.5
μ (μPa s)	23.2	23.2	23.2	23.2	23.2	23.2	23.2
λ (nm)	63.8	63.8	63.8	63.8	63.8	63.8	63.8
Kn	0.00128	0.00128	0.00128	0.00128	0.00128	0.00128	0.00128
C_c	216.95	43.87	22.24	4.974	2.857	1.305	1.149
D (m^2/s)	1.50E-05	2.22E-07	5.62E-08	2.51E-09	7.22E-10	6.59E-11	2.90E-11
P(L)	0.419	0.901	0.936	0.949	0.949	0.949	0.949
Re	233.41	233.41	233.41	233.41	233.41	233.41	233.41
Pe	2167	53583	2.11E+05	4.73E+06	1.65E+07	1.80E+08	4.09E+08

Tables 7.1 through 7.8 provide some insight into the values of parameters involved in the analyses being conducted. The tables were generated for both helium and air to provide a comparison between particle behavior in the helium environment of the spent fuel canisters and the more familiar particle behavior in air. The tables also bring to light the limits on the application of Eq. 7.10 to the problem of nano-particulate transport through micro-breaches. For smaller particles and smaller breach radii, axial diffusion is not negligible and thus Eq. 7.10 may not be accurate. Thus, there are lower bounds for the applicability of Eq. 7.10 for both particle size and breach size. However, it should be noticed that the only case in Tables 7.1 through 7.8 in which the value of *Pe* is small enough for this bound to apply is the case of one nm particles in a helium suspending gas flowing through a 5 micrometer breach.

There are also upper bounds to the applicability of Eq. 7.10. Although the Reynolds number for each system described in Tables 7.1 through 7.8 are all low enough that laminar flow is maintained, there is an upper limit to the breach size for each system. For instance, the breach size at which the Reynolds number predicts that the flow will become turbulent (*Re = 2100*) is given in Table 7.9. Of course, the validity of Eq. 7.10 is

dependent on the flow being described by fully developed laminar flow, not on the flow "not being turbulent". Before turbulent flow is attained, the flow will be in the transition regime which does not correspond to the flow profile associated with fully developed laminar flow. Transition flow will occur in a system for which the value of the associated Reynolds number is less than 2100. In the cases presented in Tables 7.1 through 7.8, the Reynolds numbers are low enough that transition flow should not be occurring.

Table 7.9: Breach Radii Corresponding to Turbulent Flow

Table	7.1 through 7.3	7.4	7.5 through 7.7	7.8
Radius (μm)	154	118	136	104

There are upper bounds to the particle size for which Eq. 7.10 is valid as well. For instance, the particle size obviously cannot exceed the diameter of the breach radius. In fact, in order for Eq. 7.10 to be truly valid, the particle size cannot be anything other than zero. In the derivation of Eq. 7.10, it is effectively assumed that a particle is deposited on the breach wall when the position of the center of the particle coincides with a position on the breach wall. Thus, the physical interpretation of the mathematical model is that each of the particles being modeled has a radius of zero. If the size of the particle relative to the size of the breach is very small, then the error associated with the model is minimal. However, if the size of the particle is within a couple of orders of magnitude of the size of the breach, then errors can start to be apparent. Once a particle of this size is deposited, it can significantly obstruct the local velocity profile of the carrier gas. This phenomenon is addressed in more depth in the next chapter. This

phenomenon is erased in the current model since it is assumed that no matter what the size of the particle, the deposited volume is evenly distributed in an annulus along the breach wall. Although this assumption is in no way physical, it does allow the Eq. 7.2 to be applied appropriately to the system.

The particle size at which gravitational settling becomes important is another upper bound to the applicability of the current model. In order to get a quantitative feel for this limit, the physical distance that a particle can be expected to move due to the mechanisms of convection, diffusion, and gravitational settling have been calculated. These distances are compared for various systems in Table 7.10. The distance traveled by a particle due to convection is equal to the product of the convective velocity, given by Eq. 7.2, and the length of the time interval. The distance traveled by a particle due to gravitational settling is equal to the product of the terminal settling velocity, given by Eq. 5.7 and the length of the time interval. The distance traveled by a particle due to Brownian diffusion is a bit more difficult to determine. The solution to the instantaneous point source diffusion problem is [7.1, 7.11]

$$n(r,t) = \frac{1}{(4\pi Dt)^{1/2}} e^{\frac{-(r-r_0)^2}{4Dt}} \tag{7.11}$$

where n represents the number of particles that have diffused from the position of the point source, r_0, to a position r some distance from r_0 at time t after the initiation of diffusion. Equation 7.11 can be integrated over r in order to determine what fraction of the initial particles are still located within the sphere with its center at r_0 and a radius of r at time t. For Table 7.10, the distance used for diffusion is that distance for which 50%

of the particles lie within this sphere. The time step used to generate the data for comparison in Table 7.10 was one μs. The system parameters used in Table 7.1 are used in Table 7.10 since they provide a lower limit for the distance traveled by the particle due to convection. Thus, the limiting size value due to gravitational settling determined for the conditions in Table 7.1 will be applicable to the conditions in Tables 7.2 through 7.8 as well. The average convective velocity, which is equal to one-half the peak convective velocity, was used to determine the particle distance traveled due to convection in Table 7.10. The particle density used to determine the terminal settling velocity is 1.1 g/cm^3, which is consistent with the value for CRUD presented in chapter 5. The density of spent fuel is approximately 11 g/cm^3 which is roughly one order of magnitude larger than the density of CRUD. In the current model, the adjustment of the particle mass density in order to account for the difference between spent fuel particles and CRUD particles will only affect the particle motion due to gravitational settling. The change in particle density affects the settling velocity linearly, so the distance traveled due to settling in Table 7.10 can be increased by one order of magnitude for consideration of fuel particles instead of CRUD particles.

Table 7.10: Comparison of Particle Distance Traveled Due to Competing Mechanisms

d_p (μm)	Convection (nm)	Diffusion (nm)	Settling (nm)
1	896	53.1	0.0324
2	896	33.3	0.102
3	896	26.1	0.2108
4	896	22.1	0.3588
5	896	19.5	0.5459
6	896	17.6	0.7719
7	896	16.2	1.037
8	896	15	1.341
9	896	14.1	1.684
10	896	13.3	2.066

As analyzed in Table 7.10, gravitational settling does not really need to be considered since even when the particle diameter is equal to the breach diameter, the motion due to diffusion is more than 6.5 times greater than the motion due to settling. However, if spent fuel particles are being considered instead of CRUD particles, then the motion due to settling is of the same order of magnitude as the motion due to diffusion for 4 μm particles. Table 7.10 also demonstrates that the distance traveled due to convection is much larger than the distance traveled due to either diffusion or settling. In the case where the breach is oriented horizontally however, this is mostly irrelevant since the motion due to convection is perpendicular to the motion due to diffusion and settling. At lower temperatures, the diffusion coefficient will be lower, while the effect of gravitation will be largely unaffected except for the adjustment associated with the slip correction factor. The slip correction factor influences the diffusion coefficient equally, however. Still, the distance traveled due to diffusion presented in Table 7.10 is a defined average from a statistical distribution. By the definition used to generate the diffusion data, one-half of all particles travel further than the reported value during a time step.

The distance traveled by a particle due to diffusion during a time step can easily be between 0 and more than twice the value presented in Table 7.10 or more.

The particles considered in this chapter are less than or equal to 1 μm. Thus, the effects of gravitational settling will be neglected in the rest of the models that are prepared. However, the model developed in the next chapter will be able to characterize aerosol flows in which gravitational settling is significant for future work.

Another limitation of the use of Eq. 7.10 is demonstrated by the fact that in Tables 7.2 through 7.4 and Tables 7.6 though 7.8 the transmission fraction for larger particles seems to be maximized at 0.949. Remember that Eq. 7.10 is the eigenfunction expansion solution to Eq. 7.7 and is thus in reality an infinite series. As presented, only the first three terms have been retained. Under most circumstances, these three terms are effective in providing accurate answers since the additional terms contribute only very small values. However, in the case where the transmission value reaches the maximum value of 0.949, additional terms should be added for accurate results. Table 7.11 lists values from each of the terms in Eq. 7.10 for the conditions presented in Table 7.2 to provide a quantitative feel for the limits of use for the equation and conditions in which additional terms are necessary.

Table 7.11: Comparison of Terms in Equation (7.10) for Conditions in Table 7.2

Particle Size d_p (nm)	First Term	Second Term	Third Term
1	0	0	0
5	0.07159	3.39E-08	1.09E-18
10	0.44449	0.00234	2.40E-06
50	0.79886	0.08364	0.02198
100	0.81388	0.09371	0.02937
500	0.81891	0.0973	0.03233
1000	0.8191	0.09743	0.03244

Table 7.11 demonstrates that for larger particles, each of the terms in Eq. 7.11 tends to approach the value of its leading coefficient. However, in each case, the first term is by far the dominant term. In fact, for particles with sizes less than or equal to 10 nm, there is very little contribution from any other terms. This indicates that Eq. 7.10 is much more accurate for smaller particles than it is for larger particles. When the particle size reaches 1 μm, the third term contributes 3.4% of the answer and is equal to 33.3% of the second term. Thus for many cases, the first three terms in the eigenfunction expansion solution to Eq. 7.7 are sufficient. However, as was just pointed out, sometimes more terms are necessary. Equation 7.10 expanded to 6 terms is [7.12]

$$P(\hat{x}) = 0.81919e^{-7.312\hat{x}/Pe} + 0.0975e^{-44.62\hat{x}/Pe} + 0.0325e^{-113.8\hat{x}/Pe} + 0.0154e^{-215.2\hat{x}/Pe} - 0.0030e^{-348.6\hat{x}/Pe} + 0.0002e^{-513.9\hat{x}/Pe} \ldots \quad (7.12)$$

The effect of these additional terms on the results from Table 7.11 are presented in Table 7.12. For large particles, the fourth term in the expansion contributes roughly 1.6% of

the result and is thus significant. The fifth term contributes only very minimally and the sixth term is inconsequential for even the largest particles considered.

Table 7.12: Table 7.11 with Additional Terms

d_p (nm)	1st Term	2nd Term	3rd Term	4th Term	5th Term	6th Term
1	0	0	0	0	0	0
5	0.07159	3.39E-08	1.09E-18	0	0	0
10	0.44449	0.00234	2.40E-06	2.36E-10	-6.58E-16	0
50	0.79886	0.08364	0.02198	0.00735	-0.00091	2.90E-05
100	0.81388	0.09371	0.02937	0.01272	-0.0022	0.00012
500	0.81891	0.0973	0.03233	0.01525	-0.00295	0.00017
1000	0.8191	0.09743	0.03244	0.01535	-0.00298	0.00017

Another limitation of Eq. 7.10 is that it is a steady state solution to the equations of motion for aerosol flow through a cylindrical tube and thus provides no information regarding time-dependence. However, the equations used so far can be modified to account for changes in the flow radius of the tube due to particle deposition over time. Due to the complexity involved with the applicable equations, it was more convenient at first to develop a discrete model characterizing particle flow and deposition. This model and its results have been published and presented [7.13]. After dealing with the system of equations for a period of time however, a system of equations that can be solved simultaneously has been developed. Both the discrete and the continuous models are described below.

7.3 TIME-DEPENDENT COUPLED PROBLEM OF AEROSOL FLOWS AND PARTICLE DEPOSITION

7.3.1 A DISCRETE MODEL

In the discrete model, the value of x in Eq. 7.10 is set equal to the length of the tube L, the value of U is determined from Eq. 7.2 where $U = 2U_{av}$, and D is determined from Eq. 7.6. The aerosol is allowed to flow through the breach for a time Δt at steady state, and then the number of particles deposited during this time is determined from Eq. 7.10. The number of deposited particles is used to determine to what extent the flow area of the breach has been constricted. A new flow velocity is then determined and the process is repeated. This procedure and the results it has produced are described below.

The first step in the discrete time-dependent algorithm is to solve Eqs. 4.13 – 4.15 as they were solved in Chapter 4 for a time period Δt without taking into account the presence of the aerosol particles. The results of this calculation will be the time-dependent temperature ($T(t)$), pressure ($P(t)$), and number of moles of gas ($n_{cv}(t)$) within the spent fuel container over the time period Δt. The time-dependent molar flow rate through the breach is simply equal to the negative time-derivative of $n_{cv}(t)$ ($-\frac{dn_{cv}(t)}{dt} = \dot{n}(t)$). The time-dependent volumetric flow rate through the breach can be constructed by

$$Q(t) = \frac{\dot{n}(t)V}{n} = -\frac{dn_{cv}(t)}{dt}\left(\frac{2RT(t)}{P(t)+P_{out}}\right) \tag{7.18}$$

Since Eqs. 7.10 and 7.11 are steady-state equations, it is necessary to determine a steady-state value of Q to be used with them. This value can be constructed from Eq. 7.18 through the operation

$$Q = \frac{\int_{\Delta t} -\frac{dn_{cv}(t)}{dt}\left(\frac{2RT(t)}{P(t)+P_{out}}\right)dt}{\Delta t} \tag{7.19}$$

The same averaging procedure can be used to determine the average temperature, viscosity, and mean free path of the gas over the period Δt. The average values can be used in Eqs. 7.4 and 7.6 to determine the correct value of D over the period Δt. This value of D and the value of Q determined from Eq. 7.19 can be substituted into Eq. 7.11 to determine the fraction of particles entering the breach that pass through and the fraction that are deposited. In order to determine the number of particles that are deposited in the breach, it is necessary to know the concentration of particles suspended in the carrier gas. The product of this concentration, the gas flow rate, the length of the time interval, and *P(L)* will be the total number of particles or particle mass deposited within the tube during the time interval. If the particle concentration is known in units of number density, then the result will be the total number of particles deposited. If the size of each particle is known, then the total volume of particles deposited can be determined. If the particle concentration is known in units of mass density, then the total volume of particulates deposited within the breach during the time interval can be determined from the mass density of the particles. It is this total volume of deposited particles during the time interval that is desired. If it is assumed that the total volume of deposited particles

(V_{dep}) is deposited evenly along the length of the breach and around the circumference of the breach, then the flow radius of the tube after the time interval will become

$$r(\Delta t) = \sqrt{\frac{1}{\pi}\left(\pi a_t^2 - \frac{V_{dep}}{L}\right)} \tag{7.20}$$

Using this new radius instead of a_t, the entire process outlined above can be repeated until the tube is "plugged" or pressure equilibrium is reached, or whatever desired measure of completion is achieved.

The assumption that the total volume of the deposited particles is deposited in a uniform annulus against the tube wall along the length of the tube is not realistic. However, the assumption does provide an easy mechanism for calculating the effect of particle deposition during flow. In addition, the assumption is conservative. In reality, the particles will be deposited with "gaps" between them due to the particle geometry and will be preferentially deposited at certain points within the tube. These phenomena will cause plugging to occur faster in reality than in this model. The argument can be made that this model is not conservative however, due to the fact that it is assumed that 100% of the particles that come into contact with the tube wall are deposited and now deposited particles are re-suspended. However, the model can easily be adjusted to account for these concerns by multiplying the calculated values of *P(L)* by the fraction of particles that are assumed to stick. This fraction can also be adjusted to account for an assumed particle re-suspension rate.

7.3.2 A CONTINUOUS MODEL

The smaller the value of Δt used in the discrete algorithm above, the more accurate the results will be. This is due to the fact that the model will more accurately reflect the continuum behavior of reality. The reason that the discrete method was developed in the first place was due to the fact that it was initially too difficult to determine a continuous solution to the equations that govern the aerosol flow and particle definition. Having already been developed, the discrete model can now serve as a foundation for constructing the continuous model. From Chapter 4 and from the discussion above, it is known that the flow of gas from the spent fuel container is governed by Eqs. (4.13) – (4.15). These three equations ultimately have the three unknowns $T(t)$, $P(t)$, and $n_{cv}(t)$ which can be determined as continuous functions of time. Although these three functions constitute a continuous model, they were averaged over discrete time intervals in order to determine particle deposition characteristics.

The first step in advancing from the discrete model to the fully continuous model is to construct a continuous model for describing the particle deposition during each time interval in the discrete model. If, during the discrete time interval, the temperature and the pressure differential are constant, then the model of aerosol flow through the breach taking particle deposition into account can be written as a system of three equations with three unknowns. The three unknowns in this system of equations are $r(t)$, $U(t)$, and $\widetilde{P}(t)$ representing the time-dependent tube radius, flow velocity, and transmission fraction. The transmission fraction is the same as that defined by Eqs. 7.10 and 7.11, but is represented here with a tilde to distinguish it from the pressure. Since constant

temperature and pressure differential are assumed in this case, the diffusion coefficient can be taken to be a constant over a given time step. In addition, there is no interest in the particle deposition as a function of axial position. The transmission ratio will be determined for the value of *x* equal to the length of the tube in all cases. Thus, $\widetilde{P}(t)$ can be expressed in an alternative form of Eq. 7.10 written as

$$\begin{aligned}\widetilde{P}(t) &= 0.81919\,e^{-7.312\left(DL/U(t)r(t)^2\right)} + 0.0975\,e^{-44.62\left(DL/U(t)r(t)^2\right)} \\ &+ 0.0325\,e^{-113.8\left(DL/U(t)r(t)^2\right)} + 0.0154\,e^{-215.2\left(DL/U(t)r(t)^2\right)} + \\ &0.0030\,e^{-348.6\left(DL/U(t)r(t)^2\right)} + 0.0002\,e^{-513.9\left(DL/U(t)r(t)^2\right)} + \ldots\end{aligned} \tag{7.21}$$

The velocity *U(t)* can be taken directly from Eq. 7.2 to be

$$U(t) = \frac{(P_{in} - P_{out})r(t)^2}{4\mu(t)L} \tag{7.22}$$

The equation for *r(t)* is a bit more involved. The time-dependent volumetric flow rate of the aerosol through the breach can be fashioned after Eq. 7.13 to be

$$Q(t) = U_{av}(t)\pi\, r(t)^2 = \frac{U(t)\pi\, r(t)^2}{2} \tag{7.23}$$

If *n* is the number density of the particles suspended in the gas, then the number rate of particles being deposited within the breach is described by

$$\#(t) = \frac{nU(t)\pi\, r(t)^2}{2}\left(1 - \widetilde{P}(t)\right) \tag{7.24}$$

For monodisperse spherical aerosol particles with a diameters of d_p, the rate of particle deposition is transformed into a rate of volume deposition according to

$$V_{dep}(t) = \frac{nU(t)\pi\, r(t)^2}{2}\left(1 - \widetilde{P}(t)\right)\left(\pi\frac{d_p^3}{6}\right) = \frac{nU(t)\pi^2 r(t)^2 d_p^3}{12}\left(1 - \widetilde{P}(t)\right) \tag{7.25}$$

Assuming the same uniform volume deposition as before, the rate of volume deposition is converted to a rate of flow area restriction according to

$$A_{dep} = \frac{V_{dep}}{L} \tag{7.26}$$

Finally, the time dependent flow radius can be written as

$$r(t) = \sqrt{\left(a_t^2 - \int_{\Delta t}\frac{nU(t)\pi\, r(t)^2 d_p^3}{12\,L}\left(1 - \widetilde{P}(t)\right)dt\right)} \tag{7.27}$$

Thus, the system of three time-dependent equations with three unknowns for characterizing aerosol flow through a breach at constant temperature and a constant pressure differential consists of Eqs. 7.21, 7.22, and 7.27. Since for a time step in the discrete model, the pressure differential, the temperature, and the effective tube radius are

known and constant, the peak flow velocity can be directly calculated from Eq. 7.22. Additionally, the diffusion coefficient can be directly calculated from Eq. 7.6 and the value of $\widetilde{P}(t)$ can be subsequently calculated from Eq. 7.21. For the discrete case, Eq. 7.26 can be combined with Eq. 7.27 to give

$$r(t) = \sqrt{\left(a_t^2 - \frac{A_{dep}}{\pi} \right)} \tag{7.28}$$

which is equivalent to Eq. 7.20. Thus, at the end of the time step, the new flow radius can be calculated from Eq. 7.28. The process can the be repeated with the substitutions $r(t) = r_2(t)$ and $a_t = r_1(t)$ for the discrete model. These indices can be continually replaced in this fashion for succeeding repetitions.

Although the system of equations consisting of Eqs. 7.21, 7.22, and 7.27 is difficult to solve analytically, the system can be solved numerically with Mathematica® in the exact same fashion as Eqs. 4.13 – 4.15 were solved in Chapter 4. In order to achieve this, these equations are reformulated in differential form. Using the chain rule, Eq. 7.21 can be written in the form

$$\begin{aligned} \widetilde{P}'(t) = & -5.98992\, DLe^{-7.312\left(DL/U(t)r(t)^2\right)}\beta - 4.35045\, DLe^{-44.62\left(DL/U(t)r(t)^2\right)}\beta \\ & - 3.6985\, DLe^{-113.8\left(DL/U(t)r(t)^2\right)}\beta - 3.3141\, DLe^{-215.2\left(DL/U(t)r(t)^2\right)}\beta \\ & - 1.0458\, DLe^{-348.6\left(DL/U(t)r(t)^2\right)}\beta - 0.10278\, DLe^{-513.9\left(DL/U(t)r(t)^2\right)}\beta - \ldots \end{aligned} \tag{7.29}$$

where

$$\beta = \left(-U(t)^{-2} r(t)^{-2} U'(t) - 2U(t)^{-1} r(t)^{-3} r'(t)\right) \tag{7.30}$$

Equation 7.22 can be written in differential form as

$$U'(t) = \frac{(P_{in} - P_{out}) r(t) r'(t)}{2\mu L} \tag{7.31}$$

It is much easier to derive a new differential form for the time-dependent radius of the tube than to take the derivative of Eq. 7.27. Using Eqs. 7.25 and 7.26, the rate of change in the flow area of the tube can be determined. The flow area of the tube at any time is simply $\pi\ r(t)^2$ so the rate of change in the flow area as particles are deposited is $2\ \pi\ r(t)\ r'(t)$. Equating this to the rate of change in the flow area determined from Eqs. 7.25 and 7.26 results in

$$2\pi r(t) r'(t) = -\frac{nU(t)\pi^2 r(t)^2 d_p^3}{12L}\left(1 - \widetilde{P}(t)\right) \tag{7.32}$$

which can be rearranged to form

$$r'(t) = -\frac{nU(t)\pi r(t) d_p^3}{24L}\left(1 - \widetilde{P}(t)\right) \tag{7.33}$$

Equations 7.29, 7.31, and 7.33 form a set of three differential equations with three unknowns. In order to solve them with *NDSolve* in Mathematica®, it is necessary to

specify the initial conditions of the functions we are trying to construct. These are easily found by setting t = 0 in Eqs. 7.21, 7.22, and 7.27. The results of the numerical integration are the radius of the tube, the flow velocity, and the transmission fraction as a function of time. The necessary inputs of this model are the pressure differential, the temperature, the number density of the particles suspended in the gas, and the diameter of the particles.

For the discrete model, the flow was considered to be at steady state and thus a constant diffusion constant was assumed. Since the length of time step being considered is exceptionally small, this assumption will not make much of a difference. However, in moving to the fully continuous model, the diffusion constant can be assumed to change with time. Essentially, this means that Eqs. 7.29 and 7.30 must be replaced respectively by

$$\begin{aligned}\widetilde{P}'(t) = &-5.98992\, Le^{-7.312\left(D\,L/U(t)r(t)^2\right)}\beta - 4.35045\, Le^{-44.62\left(D\,L/U(t)r(t)^2\right)}\beta \\ &- 3.6985\, Le^{-113.8\left(D\,L/U(t)r(t)^2\right)}\beta - 3.3141\, Le^{-215.2\left(D\,L/U(t)r(t)^2\right)}\beta \\ &- 1.0458\, Le^{-348.6\left(D\,L/U(t)r(t)^2\right)}\beta - 0.10278\, Le^{-513.9\left(D\,L/U(t)r(t)^2\right)}\beta - \ldots\end{aligned} \tag{7.34}$$

and

$$\beta[t] = -\frac{D'[t]}{r[t]^2 U[t]} + \frac{2D[t]r'[t]}{r[t]^3 U[t]} + \frac{D[t]U'[t]}{r[t]^2 U[t]^2} \tag{7.35}$$

This implies that Eqs. 7.4 and 7.6 must be introduced as functions of time and time-dependent equations for the viscosity and the mean free path must be introduced. Since

these parameters are functions of temperature and pressure, not time, a time-dependent temperature and a time-dependent pressure must be introduced. Both of these quantities are provided by the original model from Chapter 4 consisting of Eqs. 4.13 – 4.15. The entire list of equations discussed above (4.13 – 4.15, 7.11, 7.33 – 7.35) can be combined into one model and solved simultaneously using the previously described numerical methods available in Mathematica®. In this way a complete continuous model for spent fuel canister depressurization including the effects of particulate release and deposition can be constructed.

7.4 PARTICLE DEPOSITION MODEL RESULTS

Table 7.13 lists the general mass and number concentrations associated with common aerosols. The mass concentrations are compiled from published data [7.2] and the number concentrations associated with each particle size are calculated using a density of 1.1 g/cm^3 which was asserted as the density of CRUD particles in chapter 5. The number concentrations in Table 7.13 are listed in units of $\#/cm^3$ and the numbers will be six orders of magnitude larger when expressed in units of $\#/m^3$.

Table 7.13: Particulate Concentration Comparisons

	Background	Urban Air – Upper Bound	Fog	Rain	Dust Storm
Mass conc.	10^{-5} g/cm^3	10^{-3} g/cm^3	0.01 g/cm^3	0.1 g/cm^3	1 g/cm^3
#/cm^3 for d_p = 1 nm	1.74E+16	1.74E+18	1.74E+19	1.74E+20	1.74E+21
#/cm^3 for d_p = 5 nm	1.39E+14	1.39E+16	1.39E+17	1.39E+18	1.39E+19
#/cm^3 for d_p = 10 nm	1.74E+13	1.74E+15	1.74E+16	1.74E+17	1.74E+18
#/cm^3 for d_p = 50 nm	1.39E+11	1.39E+13	1.39E+14	1.39E+15	1.39E+16
#/cm^3 for d_p = 100 nm	1.74E+10	1.74E+12	1.74E+13	1.74E+14	1.74E+15
#/cm^3 for d_p = 500 nm	1.39E+08	1.39E+10	1.39E+11	1.39E+12	1.39E+13
#/cm^3 for d_p = 1 μm	1.74E+07	1.74E+09	1.74E+10	1.74E+11	1.74E+12

The range of concentrations and particle sizes in Table 7.13 is sufficient to cover the conditions considered in this work. In fact, the analyses in this chapter will focus on concentrations less than or equal to the smallest concentration appearing in Table 7.13. These small concentrations are used because plugging of the small breaches being considered occurs very rapidly. For instance, according to Table 7.1, all of the 1, 5, and 10 nm particles entering a 5 μm breach under the conditions being considered will be deposited. For large particle concentrations and large deposition fractions, the flow area of a breach is rapidly closed. This rapid restriction of flow area is demonstrated in Fig. 7.1 in the form of the decrease in the effective flow radius of the breach due to particle deposition.

Figure 7.1 presents the change in flow radius with respect to time predicted by both the discrete model (Δt = 1 s) and the continuous model. In the case presented in Fig. 7.1, there is little apparent difference between the two models over the 1.5 hour time period covered. During this period, the effective flow radius has decreased from 5 μm to roughly 2.66 μm, effectively cutting the flow area by roughly 72%. Since the

transmission ratio is zero for this case, no particulate radioactivity is released and the breach is clogged so rapidly, there is not a noticeable drop in canister pressure. For higher concentrations of 1 nm particles, the breach clogs even faster with no particulate release.

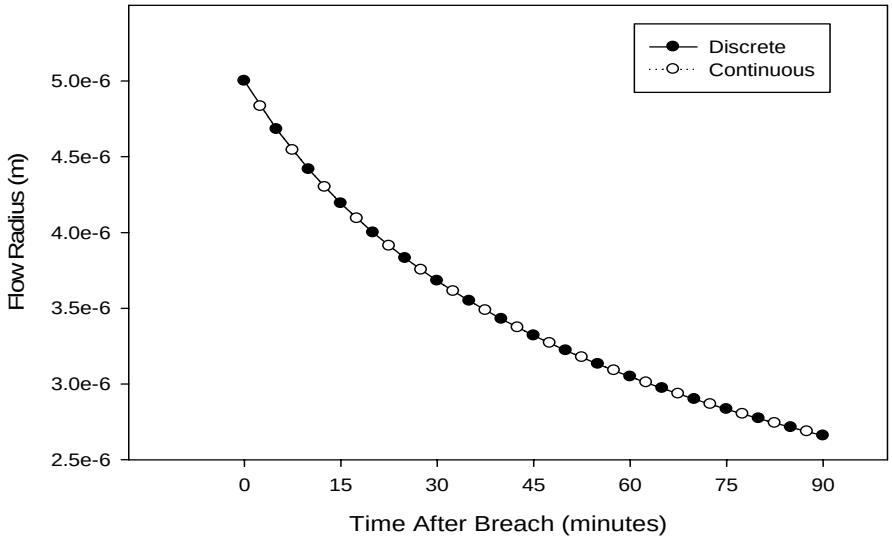

Figure 7.1: Comparison of Time-Dependent Radius for r = 5 μm, d_p = 1 nm, n = 10^{22} #/m^3, Δt = 1s for Discrete Model

Figure 7.1 shows that in one particular case, the discrete and the continuous models match nearly perfectly. Even in this case however, there is more to the story. The discrete model used to generate Fig. 7.1 took 54 minutes to compute the data whereas the continuous model took only 0.26 seconds. This begs the question, why use the discrete model at all? To answer this question fully, more data about how the continuous model is truly performing must be generated. Table 7.14 lists the values of $\widetilde{P}(t)$, U(t), and r(t) for the first ten minutes of the time period represented in Fig. 7.1.

Table 7.14: Continuous Model Parameters

t (minutes)	$\tilde{P}(t)$	$U(t)$ m/s	$r(t)$ μm
1	-9.46E-20	1.71	4.88
2	-9.59E-20	1.63	4.77
3	-9.56E-20	1.56	4.67
4	-9.56E-20	1.5	4.57
5	-9.56E-20	1.44	4.48
6	-9.56E-20	1.39	4.4
7	-9.56E-20	1.34	4.32
8	-9.56E-20	1.29	4.24
9	-9.56E-20	1.24	4.17
10	-9.56E-20	1.2	4.1

The values in Table 7.14 decline in an expected way and the time-dependent velocity values correspond well to the time-dependent values of the radius. The transmission fractions however, are obviously incorrect. A negative transmission value means that more particles are being deposited during transit than are actually entering the breach. In order to understand the cause of this anomaly, it must first be pointed out that the transmission rate for the case presented in Table 7.1 is incorrect. It is listed as 0, but in reality it is some positive number greater than zero but much less than 1. For what it's worth, Mathematica® calculates it to be $1.8213 \times 10^{-16495}$. The time-derivative of $\tilde{P}(t)$ at $t = 0$ is equal to -6.796×10^{-21}. This value represents the change in the fraction of particles being transmitted through the breach per second. Thus, even within the first fraction of a second, the transmission fraction is negative in the continuous model. However, the discrete model does not use the time-derivative of the transmission equation and thus does not exhibit this problem. Thus, the discrete model can be used as a cross-check on the continuous model. Although the transmission factor is negative for

the case presented in Fig. 7.1, it is so small that it is essentially zero and does not noticeably impact the result. Figure 7.2 presents a case that is quite different.

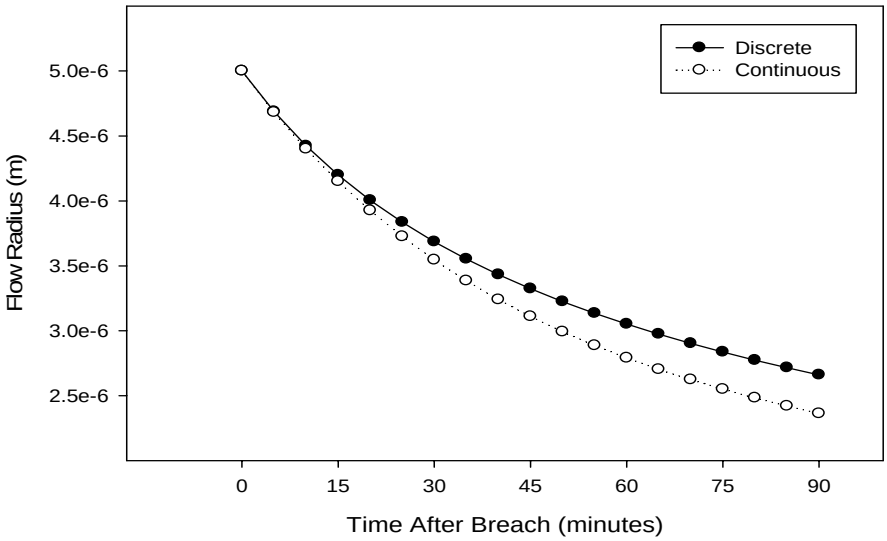

Figure 7.2: Comparison of Time-Dependent Radius for r = 5 μm, d_p = 100 nm, n = 10^{16} #/m^3, Δt = 1s for Discrete Model.

In the case chosen for Fig. 7.2, the difference between the discrete and the continuous models is very apparent. This case is interesting because the transmission rate associated with it is on the same order of magnitude as the time rate of change of the transmission rate. Table 7.15 lists these values for different times.

Table 7.15: Transmission Rates and Their Rates of Change for the System in Figure 7.2

T (minutes)	$\widetilde{P}(t)$	$\widetilde{P}'(t)$/s
0	0.0339	-0.000226
30	-0.3566	-0.000142
60	-0.4945	-0.000018
90	-0.5037	-3.71E-07

The data in Table 7.15 indicate that a large portion of the discrepancy between the models that appears in Fig. 7.2 may be to the negative transmission coefficients that occur in the continuous model. Unfortunately, the derivatives that occur in the NDSOLVE function of Mathematica® must be continuous functions. This mandate disallows the use of "If" statements to remove the negative transmission rates. One method of improving this issue in the continuous model is to search for the point in time in the model at which the transmission rate turns negative. The model should be accurate up until that point. Unfortunately in some cases like the one in Fig. 7.2, the transmission rate turns negative almost immediately. In this case, another method that can be used is to use the continuous model with Eq. 7.34 replaced by $\widetilde{P}'(t) = 0$. In a case where the transmission rate turns negative only after a significant amount of time has passed since the breach formation, the model with Eq. 7.34 can be used up until that point in time, and the model with the $\widetilde{P}'(t) = 0$ substitution can be used after that time. If Eq. 7.34 is replaced with the suggested substitution, then the resulting curves representing the effective flow radius as a function of time generated by the discrete and continuous models are as presented in Fig. 7.3. These curves show that continuous model with the substitution of a time rate of change of zero for the transmission fraction produces much closer results to the discrete model in this case than does the original continuous model. However, it is not apparent which of the curves in Fig. 7.3 is more accurate. The small discrepancy between the two curves could either be caused by the error associated with taking discrete instead of continuous steps or an error manifested by setting the time rate of change of the transmission fraction equal to zero.

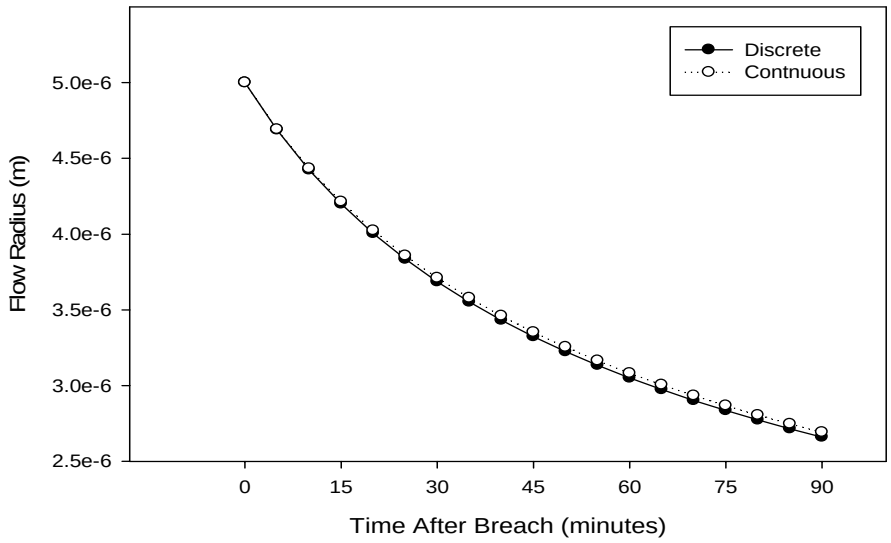

Figure 7.3: Comparison of Time-Dependent Radius for r = 5 μm, d_p = 100 nm, n = 10^{16} #/m^3, Δt = 1s for Discrete Model, $\widetilde{P}'(t)$=0 for Continuous Model

Figure 7.4 shows the flow radii predicted by the continuous model for the various particle sizes listed in the second column of Table 7.13. Notice that the curves for the 1, 5, and 10 nm particles are virtually on top of one another. This is an expected result due to the fact that in each case, the same volume of particles is being transported into the breach and none of the entering particles are transmitted. This means that the same volume of particles is being deposited in each case. Since the transmission fraction for the 50 nm and the 100 nm cases are virtually zero as well, it is expected that the curves for theses particle sizes should almost match those of the 1, 5, and 10 nm particles. The transmission fraction of the 500 nm and 1000 nm particles are significantly higher, which projects change in the flow radius over time should decline less rapidly in cases considering particles of this size.

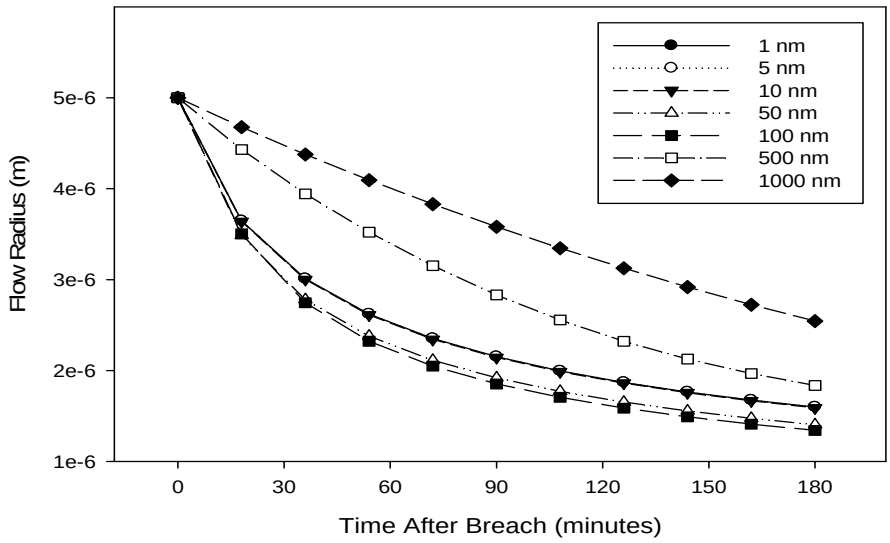

Figure 7.4: Comparison of the Flow Radii Predicted by the Continuous Model Considering Plugging Due to the Particle Sizes and Concentrations Listed in the Second Column of Table 7. 13

The discrepancy seen in Fig. 7.4 is due to the negative transmission fractions of significant magnitude that were just discussed. The curves for the 500 and 1000 nm cases are higher as expected. The adjustment suggested earlier for substituting in a time rate of change of zero for the transmission fraction once the rate of change becomes negative can be made for the continuous model cases used to generate Fig. 7.4. The results of the models with these substitutions are shown in Fig. 7.5. The curves for the smaller particle sizes for which the transmission fraction is zero or near zero now align as was conjectured.

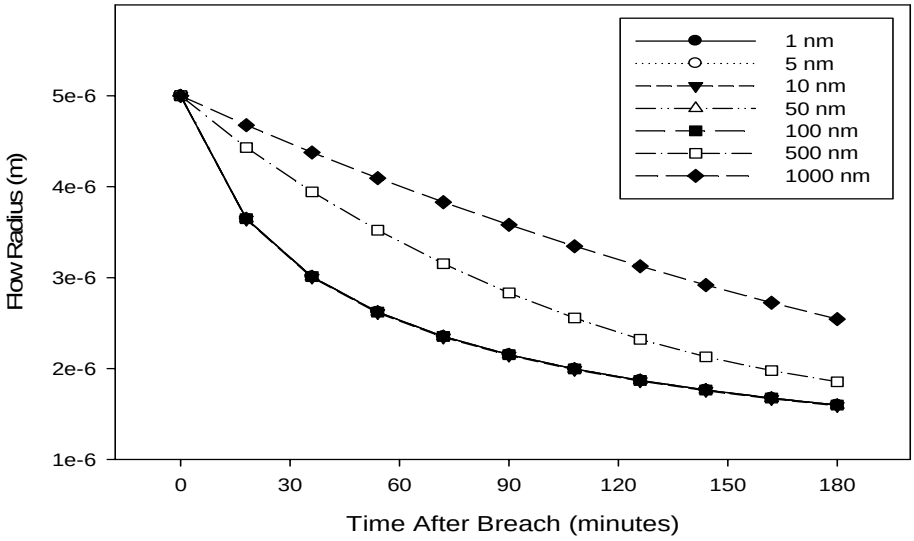

Figure 7.5: Comparison of the Flow Radii Predicted by the Continuous Model Considering Plugging Due to the Particle Sizes and Concentrations Listed in the Second Column of Table 7.13 with Corrections for the Time-Derivative of the Transmission Fraction

In Fig. 7.5, the same mass (and therefore the same volume) of particulate is flowing through the breach for each particle size. Since the transmission fraction for the two largest particle sizes are greater than zero, fewer of the particles are deposited within the breach and thus the flow radius decreases less rapidly. Associated with this phenomenon is the fact that particles are being released from the canister. The number of particles released during a period of time can be calculated from the model. Just as the number of particles being deposited within the breach as a function of time is determined from Eq. 7.24, the number of particles being transmitted through the breach as a function of time is determined from

$$\#(t) = \frac{nU(t)\pi\, r(t)^2}{2}\,\tilde{P}(t) \tag{7.36}$$

In order to determine the total number of particles released over a time interval, it is necessary to integrate Eq. 7.36 over the interval. This seems daunting since the right hand side of Eq. 7.36 is the product of three functions of time. However, the continuous model generates numerical solutions for *U(t)*, *r(t)* and $\widetilde{P}'(t)$, in the form of interpolating functions. Thus, the number of particles leaving at a given time is known in the form of the product of three interpolating functions. This allows for the number of particles released over a period of time to be determined by numerically integrating the product of the interpolating functions and negates the necessity to evaluate the integral of the right hand side of Eq. 7.36 analytically. The results of this numerical integration are that over the three hour period represented in Figs. 7.4 and 7.5, 1.538 x 10^{10} particles with a diameter of 500 nm would be released and 3.478 x 10^{10} particles with a diameter of 1000 nm would be released. These numbers seem large, but due to the small size of each particle, the total mass of the released particles in these two cases amount to 1.1 mg and 20 mg respectively.

In the cases just considered for various particle sizes, the breach size of 5 μm ultimately constrained the system. The small breach size restricted the flow velocity of the fill gas and the quantity of suspended particles from the container. This restriction leads to slow canister depressurization, low particle losses, and rapid plugging. The scenario changes however for the larger breaches whose associated parameter values are listed in Tables 7.2 and 7.3. These scenarios will be analyzed here using the continuous model due to its computational expediency and due to the fact that we now have methods of characterizing its validity.

The next system to be considered is the system presented in Table 7.2. All parameter values for this system are equal to those in the system just discussed, except that the breach radius has been expanded from 5 μm to 25 μm. Due to the increased flow area, this system will depressurize more rapidly. If no deposition of particles occurs within the breach, then this system will depressurize in approximately 2.28 years. According to Table 7.2, if 1 nm particles are suspended in the fill gas, it will remain true that all of the particles that enter the breach will be deposited. If the 1 nm particles are suspended at a concentration of 10^{16} particles/cm^3 as suggested by Table 7.13, then their deposition within the breach will significantly slow the depressurization. The first interesting phenomenon in this case is that since the flow area and velocity through it are so much greater than in the 5 μm case, a much larger number of particles enter the breach. Since all of these particles are deposited, the effective breach radius shrinks rapidly. This effect will be true for the larger particles as well, but to a lesser extent due to higher transmission fractions. Figure 7.6 shows the change in effective flow radius through the breach due to particle deposition during the first 10 minutes after the formation of a breach with a radius of 25 μm. Figure 7.7 presents the same data as Fig. 7.6 but for a longer period of time after the breach formation.

The data presented in Figs. 7.6 and 7.7 as well as the rest of the figures in this chapter, have already been adjusted in order to remove negative transmission fractions. To show the importance of this correction, Table 7.16 lists the transmission fractions at several different points in time for each of the particle sizes under consideration for the 25 μm breach case. Table 7.17 expands the data for the larger particles presented in Table 7.16 to a longer time period.

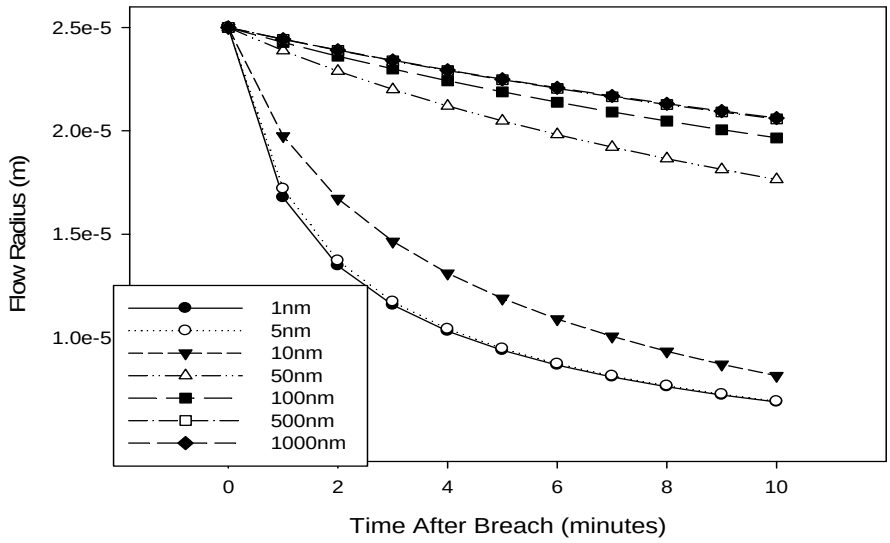

Figure 7.6: Comparison of the Time Dependent Effective Flow Radii for a 25 μm Breach Predicted by the Continuous Model Considering Plugging Due to the Particle Sizes and Concentrations Listed in the Second Column of Table 7.13 with Corrections for the Time-Derivative of the Transmission Fraction

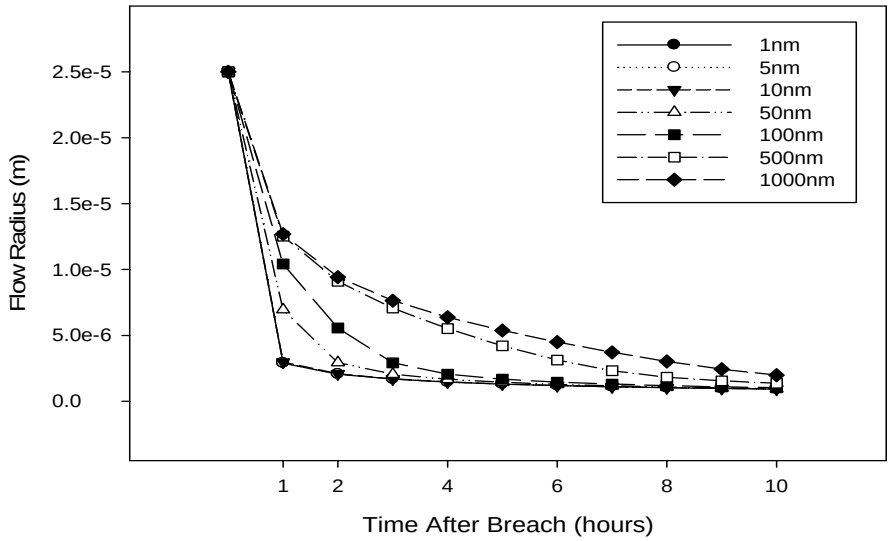

Figure 7.7: Comparison of the Flow Radii Predicted by the Continuous Model Considering Plugging Due to the Particle Sizes and Concentrations Listed in the Second Column of Table 7.13 with Corrections for the Time-Derivative of the Transmission Fraction

Table 7.16: Comparison of Transmission Fractions for the 25 μm Breach Case

t (minutes)	1 nm	5 nm	10 nm	50 nm	100 nm	500 nm	1 μm
0	3.78E-21	0.126	0.5175	0.9215	0.9506	0.9611	0.9616
1	-0.281	0.0449	0.4955	0.9209	0.9504	0.9611	0.9615
2	-0.5933	-0.0645	0.4648	0.9202	0.9502	0.9611	0.9615
3	-0.7858	-0.1906	0.4267	0.9194	0.95	0.961	0.9615
4	-0.8349	-0.3277	0.3823	0.9186	0.9498	0.961	0.9615
5	-0.8403	-0.467	0.3326	0.9178	0.9495	0.961	0.9615
6	-0.8405	-0.5931	0.2778	0.9168	0.9493	0.9609	0.9615
7	-0.8405	-0.6901	0.2182	0.9158	0.949	0.9609	0.9614
8	-0.8405	-0.7518	0.1542	0.9147	0.9487	0.9609	0.9614
9	-0.8405	-0.7843	0.0862	0.9136	0.9484	0.9608	0.9614
10	-0.8405	-0.7987	0.0154	0.9123	0.9481	0.9608	0.9614

Table 7.17: Comparison of Transmission Fractions for Two-hour Period

t (minutes)	10 nm	50 nm	100 nm	500 nm	1 μm
0	0.5175	0.9215	0.9506	0.9611	0.9616
12	-0.1277	0.9096	0.9475	0.9607	0.9613
24	-0.4285	0.8849	0.9422	0.96	0.961
36	-0.4292	0.8397	0.9342	0.9591	0.9606
48	-0.4292	0.7622	0.9225	0.958	0.96
60	-0.4292	0.6376	0.9053	0.9566	0.9594
72	-0.4292	0.4494	0.8803	0.9549	0.9586
84	-0.4292	0.2112	0.8443	0.9528	0.9577
96	-0.4292	0.0306	0.7932	0.9504	0.9567
108	-0.4292	-0.0284	0.7219	0.9476	0.9555
120	-0.4292	-0.0366	0.6244	0.9443	0.9541

Tables 7.16 and 7.17 show that although the transmission fractions turn negative for the case of a 25 μm breach, they tend to do so after a longer period of time than they did for the case of the 5 μm breach. The time-dependent transmission fractions for the various particle sizes flowing through a 25 μm breach over the first ten minutes after breach formation are presented in Fig. 7.8.

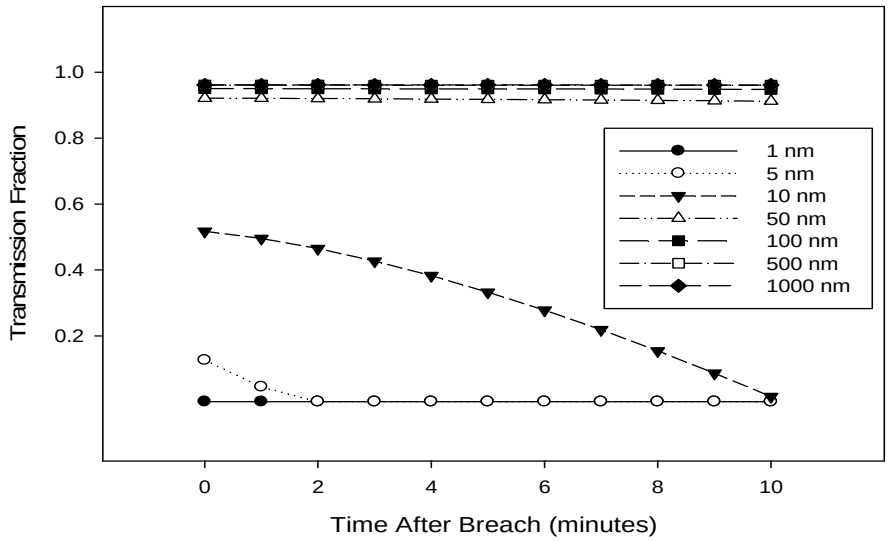

Figure 7.8: Comparison of the Transmission Fractions Predicted by the Continuous Model Considering Plugging Due to the Particle Sizes and Concentrations Listed in the Second Column of Table 7.13 with Corrections for the Time-Derivative of the Transmission Fraction

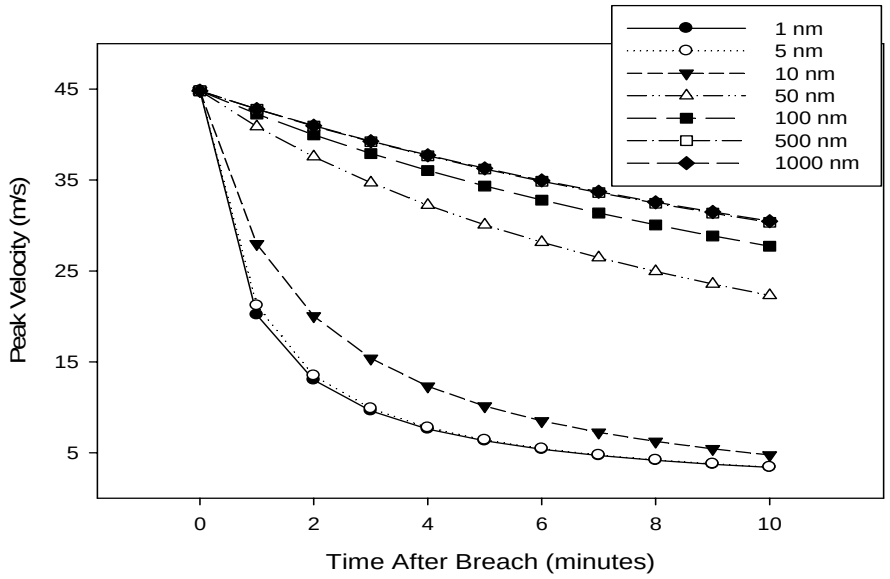

Figure 7.9: Comparison of the Peak Velocities Predicted by the Continuous Model Considering Plugging Due to the Particle Sizes and Concentrations Listed in the Second Column of Table 7.13 with Corrections for the Time-Derivative of the Transmission Fraction

The change in effective flow radii in the case of a 50 μm breach, for parameter values described in Table 7.3, are presented in Fig. 7.10. Figure 7.11 protracts the data in

Fig. 7.10 to a longer time period and highlights the rapid blocking of the breach flow area due to particle deposition. Figure 7.12 shows the time-dependent transmission fractions for each of the particle sizes and illustrates that the transmission fractions for the larger particles over the first ten minutes after the formation of a 50 μm breach remain high. The transmission fractions presented in Fig. 7.12 seem to conflict with the diminishing flow radii presented in Figs. 7.8 and 7.9. However, there is no conflict as the reason for the rapid decrease in flow radius is attributed to the high quantity of particles entering the breach. Since the suspended particle concentration is constant, the number of particles entering the breach can be correlated to the time-dependent carrier gas velocity shown in Fig. 7.13.

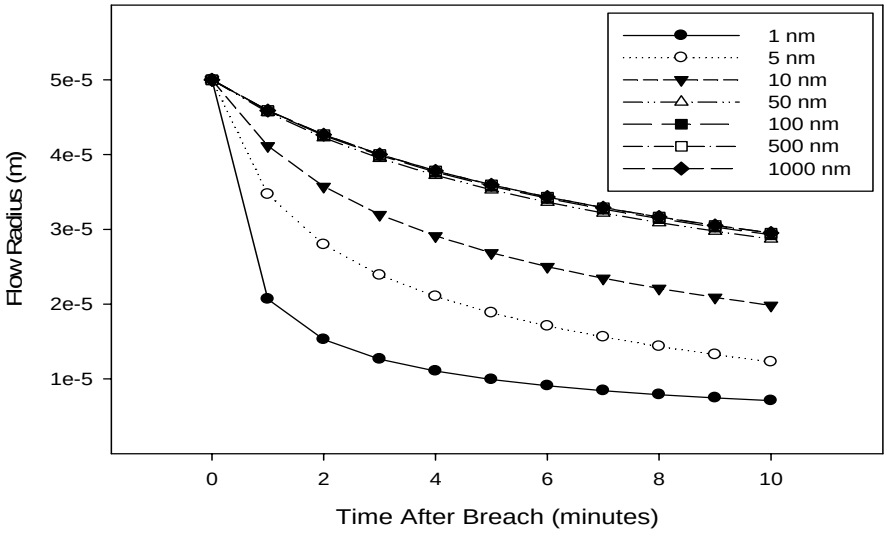

Figure 7.10: Comparison of the Flow Radii Predicted by the Continuous Model Considering Plugging Due to the Particle Sizes and Concentrations Listed in the Second Column of Table 7.13 with Corrections for the Time-Derivative of the Transmission Fraction

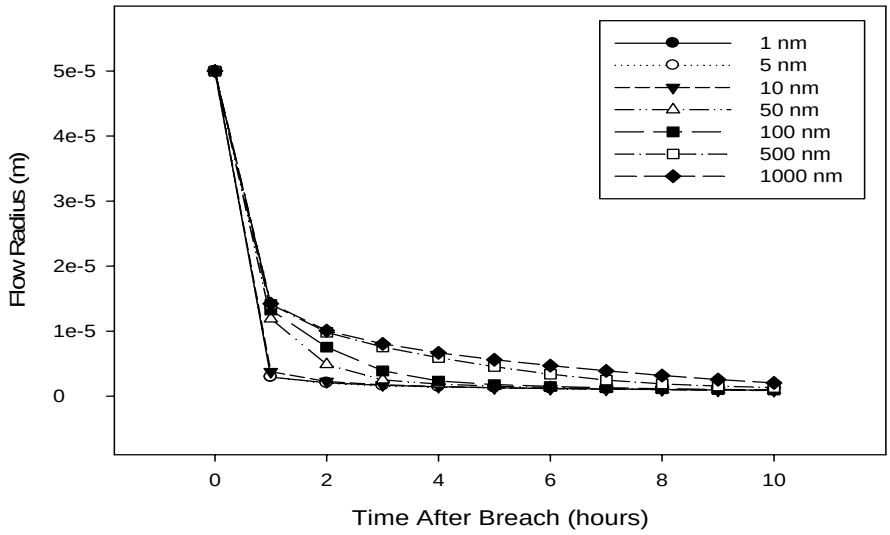

Figure 7.11: Comparison of the Flow Radii Predicted by the Continuous Model Considering Plugging Due to the Particle Sizes and Concentrations Listed in the Second Column of Table 7.13 with Corrections for the Time-Derivative of the Transmission Fraction

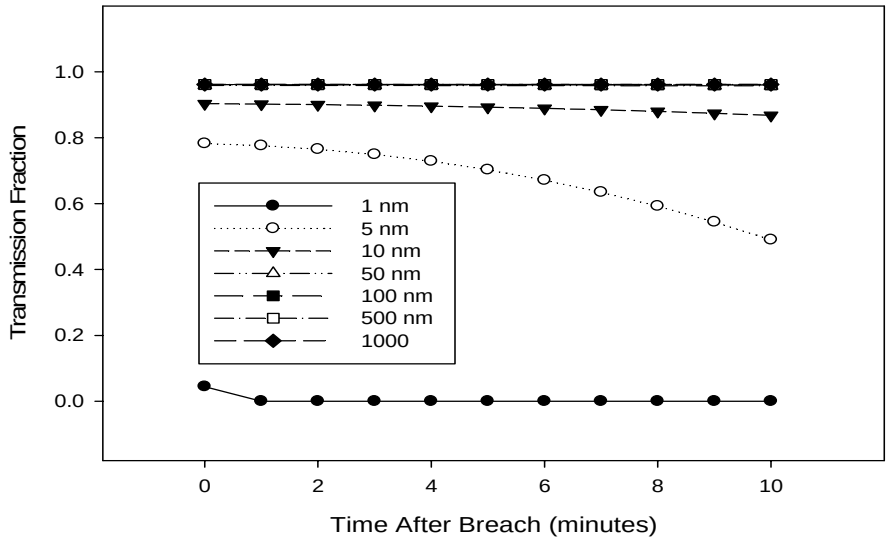

Figure 7.12: Comparison of the Transmission Fractions Predicted by the Continuous Model Considering Plugging Due to the Particle Sizes and Concentrations Listed in the Second Column of Table 7.13 with Corrections for the Time-Derivative of the Transmission Fraction

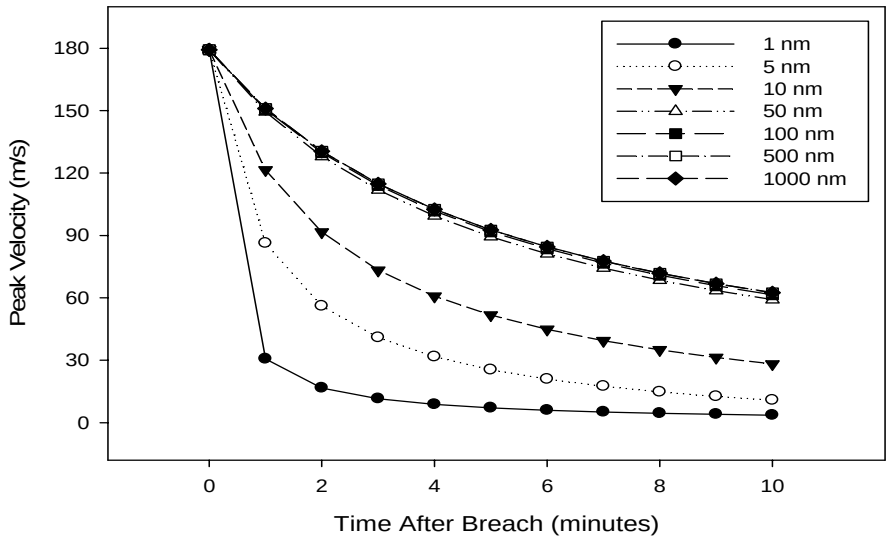

Figure 7.13: Comparison of the Peak Velocities Predicted by the Continuous Model Considering Plugging Due to the Particle Sizes and Concentrations Listed in the Second Column of Table 7.13 with Corrections for the Time-Derivative of the Transmission Fraction

In addition to the breach size and the particle size, the particle concentration is a parameter that produces interesting result for different values. The case of a 25 μm breach with 100 nm particles suspended for 286 days as indicated in Chapter 5 was modeled for several different particle concentrations to illustrate the effect that the concentration has on the behavior of the system. The resulting time-dependent effect on flow radii for the various particle concentrations over a 2 year period after the breach formation are presented in Fig. 7.14. The corresponding time-dependent canister pressures for the various particle concentrations for the same 2 year time period are displayed in Fig. 7.15. Figure 7.16 extends the time period over which the canister pressure is tracked to 500 years. Figure 7.17 displays the rate at which particles are flowing through the breach in units of the number transmitted per second during the 286 day suspension time. If the particle release rates in Fig. 7.17 are integrated, then the total number of particles released and corresponding mass losses are presented in Table 7.18.

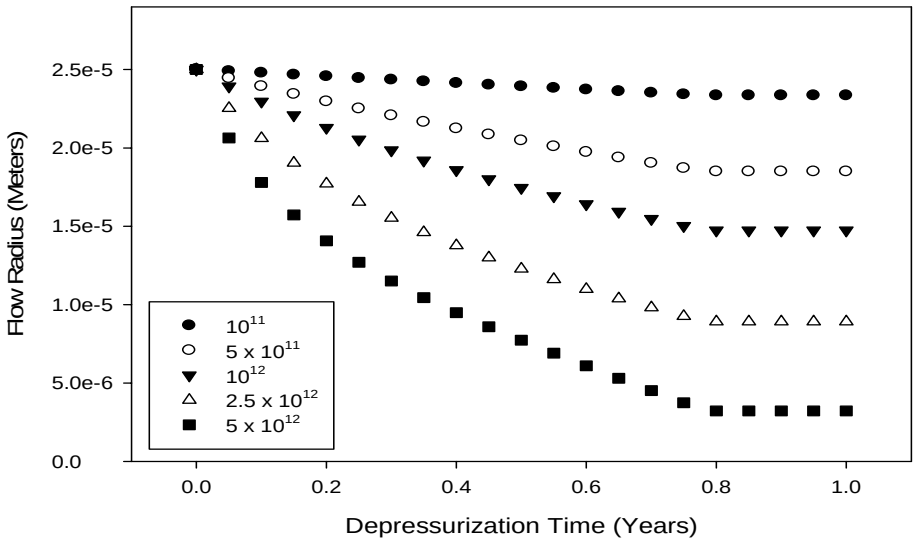

Figure 7.14: Comparison of the Effective Flow Radii Predicted by the Continuous Model Considering Plugging Due to the Particle Sizes and Concentrations Listed in the Second Column of Table 7.13 with Corrections for the Time-Derivative of the Transmission Fraction

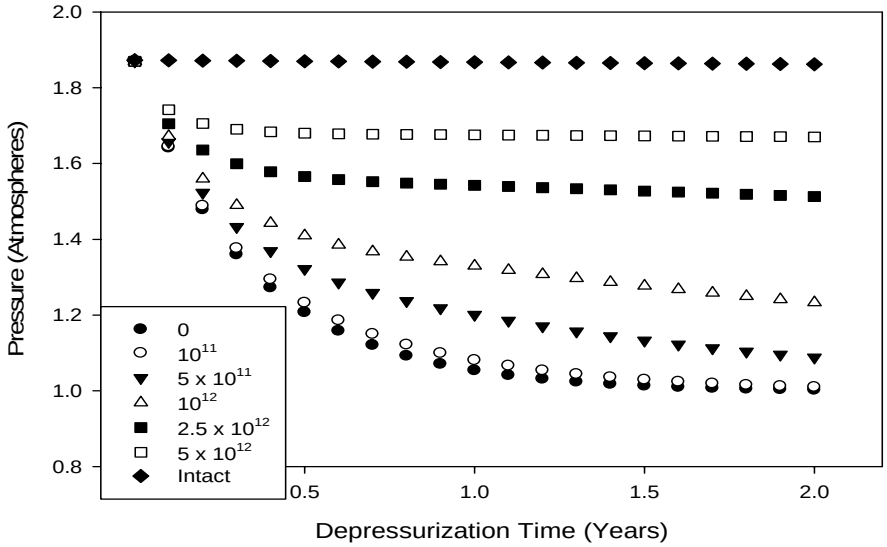

Figure 7.15: Comparison of the Canister Pressures Predicted by the Continuous Model Considering Plugging Due to the Particle Sizes and Concentrations Listed in the Second Column of Table 7.13 with Corrections for the Time-Derivative of the Transmission Fraction

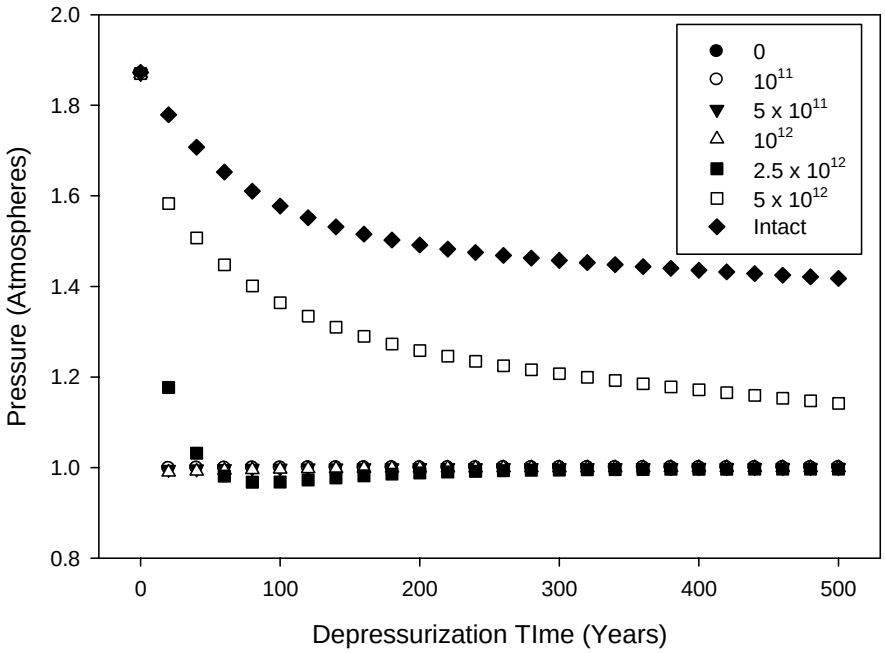

Figure 7.16: Comparison of the Canister Pressures Predicted by the Continuous Model Considering Plugging Due to the Particle Sizes and Concentrations Listed in the Second Column of Table 7.13 with Corrections for the Time-Derivative of the Transmission Fraction

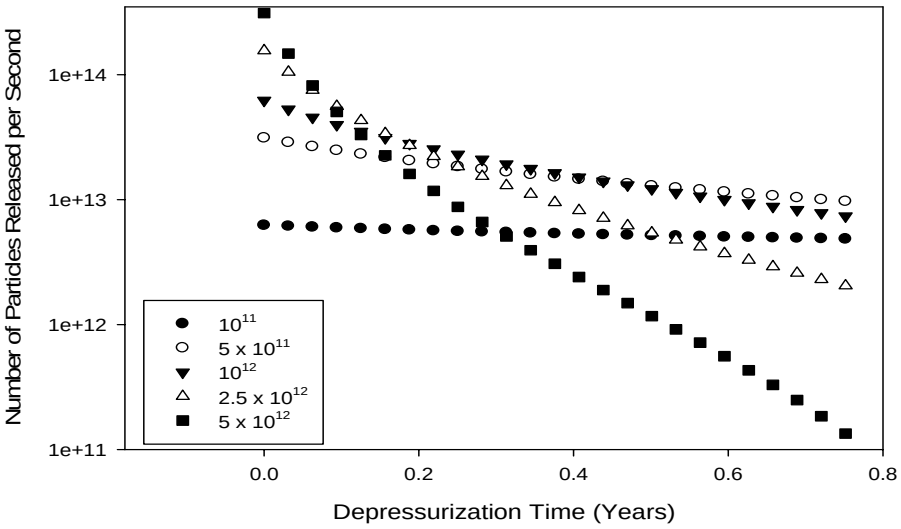

Figure 7.17: Comparison of the Particle Release Rates Predicted by the Continuous Model Considering Plugging Due to the Particle Sizes and Concentrations Listed in the Second Column of Table 7.13 with Corrections for the Time-Derivative of the Transmission Fraction

Table 7.18: Particles Lost Over Depressurization Time

number/cm^3	100 days	200 days	286 days
1.0E+11	5.04E+19	9.61E+19	1.33E+20
5.0E+11	2.00E+20	3.26E+20	4.06E+20
1.0E+12	3.13E+20	4.46E+20	5.12E+20
2.5E+12	4.51E+20	5.27E+20	4.51E+20
5.0E+12	5.27E+20	5.49E+20	5.02E+20

Table 7.18 introduces an interesting realization. According to the continuous model discussed in this chapter, in order to achieve the effects seen in Figs. 7.14 through 7.17, it is necessary for a very large quantity of particles to be suspended in the fill gas. For instance, if the 100 nm particles are suspended at a concentration of 10^{11} particles/cm^3, then over the first 100 days after the formation of the breach, 5.04 x 10^{19} particles are predicted to be lost. This number correlates to a loss of 29 kg of particles. This number is too large because in reality, the suspended particle concentration will decrease with time as the particles settle and diffuse out of suspension. Thus, in order to accurately describe the scenarios described in this chapter, the model should be modified so that the total number of particles entering a breach does not exceed the total number of particles suspended within the canister. This issue could best be addressed by expanding the information presented in Chapter 5 to create an accurate model of particle suspension and settling as a function of time within the spent fuel canister.

If the time-dependent suspended particle concentrations and suspension times can be deliberately determined for particular breach and particle sizes, then they can be used to deliver interesting results. The time-dependent suspended particle concentration is one of many aspects of the model that can be expanded in order to improve its applicability and accuracy. Another improvement can be made by accurately determining the sticking

fractions of particles that collide with the wall and the rate of resuspension of deposited particles. Using supported values for sticking fractions and resuspension rates would make the model truly conservative. Thermal gradients and electrical charges could also be incorporated into the model to determine more accurate transport conditions and particle behavior. Additionally, particle agglomeration can be considered.

Gravitational settling of particles was ruled out with physical arguments in this chapter. In order for settling to play an appreciable role in particle motion, the particle must be larger than those considered thus far. If the particles are much larger, then two adjustments to the model must be considered. First, the particle size must be accounted for. In the current form of the model, the aerosol particles are treated at mathematical points with no spatial dimensions. Thus, the position associated with each particle is actually just the center of the particle and a particle-wall impact is defined as the time when this point coincides with a point on the breach wall. This is an acceptable assumption when the particle diameter is only a small fraction of the tube diameter. However, the error associated with this treatment becomes large when the particle size is a significant fraction of the size of the breach diameter. To adjust the model so that the particle-wall collision occurs when the particle surface impacts the breach wall instead of when the particle center impacts the breach wall, the tube radius a_t should be replaced by the value $(a_t - d_p/2)$. The convective velocity of the particle can still be assumed to be determined by Eq. 7.2 where the position r coincides with the position of the center of the particle. Unfortunately, the radius of the tube cannot be replaced with the suggested substitution in all calculations due to the fact the full radius of the tube is necessary in order to determine the velocity of the tube. One way to adjust for the non-zero particle

radii is to insert the value of ($r - d_p/2$) in for the value of r in the boundary condition (Eq. 7.8). Another possibility is to leave the model intact as it currently is, but determine a new method for calculating the transmission fraction that is independent of the current model. One new method of determining the transmission fraction with the newly determined system parameters will be the primary focus of Chapter 8. The second adjustment that should be considered when modeling larger particles is that the use of larger breaches will lower the ratio of the particle diameter to breach diameter. Unfortunately, as discussed earlier, the breach size is limited to sizes that allow for the implementation of Eq. 7.2 for the description of the velocity profile. Thus, if larger breaches or alternative breach shapes are to be considered, new velocity profiles must be provided. The development and use of alternative velocity profiles will also be discussed in detail in Chapter 8.

Finally, in the derivation of Eq. 7.10, the axial and angular diffusion were neglected. Although it was shown in this chapter that only in extreme cases will the axial diffusion be of importance, the model in the next chapter will be capable of accounting for it. The importance of the neglect of the angular diffusion is that since convective motion is considered to be only in the axial direction, all ability to track particle angular velocity and position were lost. This loss, along with the limited geometry to which Eq. 7.2 could be applied, necessitated the assumption of uniform particle deposition. The model developed and described in the next chapter will be able to account for angular particle motion, 3-D particle position, and any other shortcomings of the models developed in this chapter.

7.5 CONCLUSIONS

This chapter expanded the model constructed in Chapter 4 to account for the presence of suspended particulates. The model is able to track the time-dependent effect of particle deposition within a breach. It is capable of monitoring the number of moles within the canister, the velocity through the breach, the radius of the breach, the transmission fraction of the particulates through the breach, the canister pressure, and the canister temperature at any time after the formation of the through-wall breach in the canister. Although the model successfully accounts for the presence of suspended particles, it has several limitations. The Monte Carlo model of aerosol flows presented in the next chapter will provide a means of removing some of these limitations.

REFERENCES

7.1 Bird, R.B., Stewart, W.E., Lightfoot, E.N., Transport Phenomena, 2nd Edition, John Wiley & Sons, Inc., New York (2005).

7.2 Hinds, W.C., Aerosol Technology, 2nd Ed. John Wiley & Sons, Inc., New York (1999).

7.3 Allen, M.D., Raabe, O.G., "Slip Correction Measurements of Spherical Solid Aerosol Particles in an Improved Millikan Apparatus," *Aerosol Science and Technology,* 4 (1985) p. 269-286.

7.4 Einstein, A., Investigations on the Theory of the Brownian Movement, Dover Publications Inc., New York (1956). Translated from Einstein, A., *Annalen der Physik.,*17 (1905) p. 549.

7.5 Williams, M.M.R., Loyalka, S.K., Aerosol Science, Pergamon Press, New York (1991).

7.6 Gormley, P.G., Kennedy, M., "Diffusion from a Stream Flowing though a Cylindrical Tube," *Proceedings of the Royal Irish Academy,* 52 (1949) p. 163-169.

7.7 Graetz, L., "Ueber die Warmeleitungsfahigkeit von Flussigkeiten," *Annalen der Physik und Chemie*, 25 (1885) 337.

7.8 Williams, M.M.R., "Fission Product Retention in Narrow Leak Pathways," A Report to the European Atomic Energy Community (9/1994).

7.9 Ingham, D.B., "Diffusion of Aerosols from a Stream Flowing through a Cylindrical Tube," *Journal of Aerosol Science*, 6 (1975) p. 125-132.

7.10 Tan, C.W., Hsu, C.J., "Diffusion of Aerosols in Laminar Flow in a Cylindrical Tube," *Journal of Aerosol Science*, 2 (1971) p. 117-124.

7.11 Carslaw, H.S., Jaeger, J.C., Conduction of Heat in Solids, 2nd edition, Oxford University Press (1959) p. 257.

7.12 Personal communication with S.K. Loyalka (06/05/2007).

7.13 Casella, A.M., Loyalka, S.K., Hanson, B.D., "Plugging Effects on Depressurization Time in Dry Storage Containers with Pinhole Breaches," *ANS Transactions*, 95 (2006) p. 209-210.

CHAPTER 8: A MONTE CARLO MODEL FOR TRACKING AEROSOL FLOWS THROUGH BREACHES

8.1 INTRODUCTION

In the previous chapter, a model of the transport of aerosol particles through breaches was constructed based on the continuity equation defined by Eqs. 7.7 – 7.9. These equations were combined to form Eq. 7.10 which determines the fraction of particles entering a tube that are transmitted or deposited within the tube. There are many constraints on the applicability of Eq. 7.10 and subsequently on the models described in Chapter 7. These constraints included the following:

- The breach must be a straight right-cylinder of constant circular cross section so that Eq. 7.2 would be applicable.
- The particle deposition within the breach must be assumed to be uniform axially and circumferentially in order to preserve the constant circular cross section of the flow path.
- The flow must be laminar in order to justify the use of the Poiseuille equation of flow.
- The particles must be small enough to justify neglecting the effect of gravitational settling and particle inertia.
- The Péclet number must be large enough to justify neglecting axial diffusion within the tube.
- There can be no particle charging or thermal gradients or gradients of any other kind within the tube. If these charges or gradients are present, then the forces they exert on the particles must be taken into consideration.

Obviously, a general model taking into account every force affecting particle motion would be too complex to construct and utilize. An excellent example of the simplification of the system in order to obtain useful results is the neglect of all forces except convective motion and diffusion in order to generate Eq. 7.10. Unfortunately, any model using such simplifications must be used responsibly to characterize only the systems to which it is closely applicable. In this chapter, a more general approach to modeling particle motion will be constructed. An attempt will be made to keep this model as general as possible or to suggest how to reconstruct generality when simplifications are made. This model will utilize the Monte Carlo methods used to model molecular movements through passageways considered in Chapter 6.

8.2 MATHEMATICAL THEORY OF PARTICLE MOTION

The generalized particle continuity equation is [8.1]

$$\frac{\partial n}{\partial t} + \underline{\nabla} \bullet \underline{J} = 0 \tag{8.1}$$

where the underscores represent vector quantities and

$$\underline{J} = \underline{J}_c + \underline{J}_d + \underline{J}_T + \underline{J}_D + \underline{J}_e + \ldots \tag{8.2}$$

where $\underline{J}$ represents the particle current due to all mechanisms and the terms on the right hand side represent respectively the currents induced by convection, diffusion,

thermophoresis, diffusiophoresis, external forces, and whatever additional forces may be present. Each current in Eq. 8.2 can be written in operator form according to

$$\underline{J}_c = \underline{u}\, n \quad \underline{J}_d = -D\underline{\nabla} n \quad \underline{J}_T = \underline{u}_T n \quad \underline{J}_D = \underline{u}_D n \quad \underline{J}_e = \underline{u}_e n \quad \ldots \tag{8.3}$$

It is at this point that every non-negligible force influencing particle motion must be introduced into the equation. If the only two non-negligible mechanisms of particle motion are convection and diffusion, and the system is at steady-state, then the continuity equation becomes

$$\hat{\underline{u}} \bullet \hat{\underline{\nabla}} \hat{n} = \frac{1}{Pe} \hat{\underline{\nabla}}^2 \hat{n} \tag{8.4}$$

If the convective particle motion is due to fully developed flow in a straight tube of constant circular cross section and the diffusion part is only in the radial and angular directions (axial diffusion neglected), then the continuity equation take the form of Eq. 7.7. However, it was pointed out in the last chapter that for very small particles and very small tube radii, even if the flow is fully developed, the Péclet can be too small to neglect axial diffusion. In the case that axial diffusion is not negligible, Eq. 8.4 becomes

$$(1-\hat{r}^2)\frac{\partial \hat{n}}{\partial \hat{x}} = \frac{1}{Pe}\left(\frac{1}{\hat{r}}\frac{\partial}{\partial \hat{r}}\left(\hat{r}\frac{\partial \hat{n}}{\partial \hat{r}}\right) + \frac{\partial^2 \hat{n}}{\partial \hat{x}^2}\right) \tag{8.5}$$

Equation 8.5 is more difficult to solve than equation 7.7. It should be pointed out at this point that in cylindrical coordinates, the complete Laplacian takes the form

$$\nabla^2 \hat{n} = \frac{1}{\hat{r}} \frac{\partial}{\partial \hat{r}} \left(\hat{r} \frac{\partial \hat{n}}{\partial \hat{r}} \right) + \frac{1}{\hat{r}^2} \frac{\partial^2 \hat{n}}{\partial \hat{\theta}^2} + \frac{\partial^2 \hat{n}}{\partial \hat{x}^2} \tag{8.6}$$

The second term on the right hand side of Eq. 8.6 represents the change with respect to the planar angle at any axially position. It is neglected for the sake of simplification in order to solve the equation in order to produce Eq. 7.7. This is the reason that Eq. 7.10 provides no information regarding the angular dependence of particle deposition. In fact, in moving from Eq. 7.7 to Eq. 8.5, the angular dependence has remained absent. If it is desired to track the effect of angular dependence, the second term on the right hand side of Eq. 8.6 must remain within the particle continuity equation to be used. The term on the left hand side of Eq. 8.5 is the convective term. In Eq. 8.5, this term represents fully developed laminar flow through a straight tube of constant circular cross section. If the flow volume were of any other shape, or slip effects or effects of turbulence or the effects of particle inertia were present, then the convective term would have to be adjusted accordingly.

In addressing particle behavior in a bulk macroscopic fashion as has been described in the preceding paragraphs, it eventually becomes necessary to solve a partial differential equation with designated boundary conditions. This can be very difficult if not currently impossible. In order to create a more general method of addressing aerosol flows, a microscopic approach can be utilized and a model constructed from the bottom up. This model is based on the Langevin equation of individual particle motion [8.2].

$$m\frac{du}{dt} = -6\pi a\mu(u - v) + A(t) + K(r,t) \tag{8.7}$$

where u is the particle velocity, v is the local carrier gas velocity, $A(t)$ is the "force" that causes a particle to move according to Brownian motion, and $K(r,t)$ represents other outside forces, of which the most commonly considered is gravity. If the particle is small enough to justify neglecting the inertia associated with its motion, then the convective particle motion will follow a streamline of the carrier gas. In this case $u = v$ and the first term on the right hand side of Eq. 8.7 vanishes. It is for this reason that it is preferable to model small particles. Also, if the particles are very small, then the effect of gravitational settling is negligible. If this is the case, and if no electrical charges or physical gradients are present, then the third term on the right hand side of Eq. 8.7 is negligible. In the case that the particles being considered are small enough to neglect these terms, the second term on the right had side of Eq. 8.7 will be very significant. As was seen in the previous chapter, smaller particles have much larger diffusion coefficients than larger particles.

Equation 8.7 represents a force balance on a particle. Integrating this equation once with respect to time will give a momentum balance, and integrating it again will give a continuity equation. The first integration where the first and third terms on the right hand side have been neglected gives

$$u(t) = u(0) + \frac{1}{m}\int_0^t A(t)dt \tag{8.8}$$

and the second integration gives

$$x(t) = x(0) + u(0)\Delta t + \frac{1}{m}\iint_{\Delta t} A(t)dt^2 \tag{8.9}$$

The third term on the right hand side of Eq. 8.9 looks strange but its interpretation is straightforward. *A(t)* is a "force" associated with the Brownian motion of the particle. Since the force applied to a particle is equal to the product of the mass of the particle and the acceleration the particle experiences as an effect of the force, the integral of *A(t)* over a time interval divided by the particle mass will yield the velocity of the particle imposed by the Brownian "force". The integral over time of this velocity will yield the change in position of the particle due to Brownian motion. One way to represent this change in position is a random selection from the Gaussian distribution using the initial particle position as the mean and the root of the product of twice the diffusion coefficient and the time step over which the particle is moving as the standard deviation. This is readily seen when the Gaussian distribution function (Eq. 8.10) is directly compared to the solution of the problem of instantaneous diffusion from a point source (Eq. 8.11).

$$P(x) = \frac{1}{\left(\sqrt{2\pi}\sigma\right)^3} e^{\frac{-(x-\mu)^2}{2\sigma^2}} \tag{8.10}$$

$$n(r,t) = \frac{1}{(4\pi Dt)^{3/2}} e^{\frac{-(r-r_0)^2}{4Dt}} \tag{8.11}$$

The right hand side of Eq. 8.10 directly matches the right hand side of Eq. 8.11 for the case $\mu = r_0$ and $\sigma = (2Dt)^{1/2}$. Thus, the change in position due to Brownian motion for a

given time step (the third term on the right hand side of Eq. 8.9) can be represented as a random sampling from Eq. 8.11. Thus for a given time step, the change in the position of a particle can be represented by

$$x(t) = x(0) + u(0)\Delta t + Random[n(r,t)] \tag{8.12}$$

where *n(r,t)* is defined by Eq. 8.11. Equations 8.10 and 8.11 are three-dimensional distributions. If the problem can be simplified such that particle diffusive motion in one or two dimensions can be neglected, then one- and two-dimensional distributions can be used. These equations are respectively

$$n(r,t) = \frac{1}{(4\pi Dt)^{1/2}} e^{\frac{-(r-r_0)^2}{4Dt}} \tag{8.13}$$

$$n(r,t) = \frac{1}{4\pi Dt} e^{\frac{-(r-r_0)^2}{4Dt}} \tag{8.14}$$

where *r* represents the distance traveling along the line, or within the plane or space defined by the dimensions involved.

8.3 BENCHMARKS

The easiest way to develop the equations discussed thus far in this chapter into a model is to attempt to recreate the model from the previous chapter and to compare the

two. Thus, to start out, it will be assumed that the only two relevant mechanisms of particle motion are convection and diffusion. In addition, it can be assumed that axial diffusion is negligible.

The model to be constructed here is an N-particle Monte Carlo code that will track each test particle individually through successive time steps. During each time step, the motion of the particle due to the influence of each mechanism must be considered. In the current case, the only mechanisms to consider are convection and diffusion. At the beginning of a time step, the axial convective velocity of a test particle is determined from Eq. 7.2. The convective motion during the time step is then just equal to $u_z(r)\Delta t$. The diffusive motion during the time step is simply sampled from Eq. 8.14 after the convective motion is accounted for. This calculation is consistent with Eq. 8.12. The diffusive motion is in the radial direction. In this case, since the quantity of relevance is the actual distance from the central axis of the tube, it is possible to determine a particle-wall collision with only the magnitude of *r*. However, *r* is related to the *y* and *z* directions in the cross-section plane of the tube by the Pythagorean Theorem. Thus, the value of *r* in equation can be replaced by the value $\sqrt{y^2+z^2}$. With this substitution, we can effectively track the angular position of the particle.

In addition to tracking the particle through time steps, it is necessary to determine the initial starting position of each test particle as it enters the breach. It is desired that the sampling of initial test particle positions to be consistent with the initial conditions prescribed by Eq. 7.8. If the axial velocity across the entrance cross section were constant, then the sampling would be the same as that described by Eq. 6.15. However, since the velocity profile is assumed to be fully developed at the entrance to the tube, and

the number density at the entry to the tube is uniform as stipulated by Eq. 7.2, the probability that an entering particle will have a radial position $0 \leq r \leq \hat{r}$ is determined by

$$P = \frac{\int_0^{\tilde{r}} \left(1 - \frac{r^2}{a_t^2}\right) 2\pi r dr}{\int_0^{a_t} \left(1 - \frac{r^2}{a_t^2}\right) 2\pi r dr} = 2\left(\frac{\tilde{r}}{a_t}\right)^2 - \left(\frac{\tilde{r}}{a_t}\right)^4 \tag{8.15}$$

which when solve for $\tilde{r}$, leads to the expression

$$\tilde{r} = a_t \sqrt{1 - \sqrt{1 - P}} \tag{8.16}$$

Thus, the initial position *x(0)* for a given particle will have an axial position of zero, and a radial position determined from Eq. 8.16. Equation 8.16 is actually a probability distribution and the value of $\hat{r}$ is determined by evaluating the expression with the value of *P* randomly chosen from the continuous real distribution [0,1]. The starting planar angle of a particle is chosen randomly from the continuous real distribution [0, 2 π).

Before using the Monte Carlo program to predict aerosol flow behavior, it is necessary to benchmark the results it generates against the results of existing models. The most convenient results to be used for this purpose are those generated by Eq. 7.10. Currently, the breach is taken to be a right circular cylinder 50 μm in diameter and 1 cm in length. The pressure at the entrance to the tube is 1.8 atmospheres and the pressure at the exit is 1 atmosphere. It is assumed that the flow out of the tube is unrestricted and the possibility of choked flow is neglected. The system is assumed to be isothermal and the

assigned temperature is 558K. Flowing through the micropath, is a monodisperse aerosol consisting of spherical particles 10 nm in diameter suspended in helium. Under these conditions, the slip-corrected diffusion coefficient is determined to be 2.34 x 10^{-7} m^2/s and the average bulk fluid velocity U is 44.81 m/s. Equation 7.10 predicts that for this system, the ratio of the number of particles leaving the tube without being deposited to the number of particles entering the tube is 0.447.

In order to run the Monte Carlo program, it is necessary to select a time step Δt. In order to determine the correct value of Δt, and to determine the error caused by choosing an incorrect value, the Monte Carlo program was run for several different values of Δt. Due to the fact that the Monte Carlo program is statistical in nature, ten simulations of 1000 particles were run for each Δt and the mean value as well as the relative error associated with that mean value were recorded. The results of this test are shown in Table 8.1.

Table 8.1: 1000 Particle Simulations

Δt (μs)	Mean	Rel. Error
10	0.4829	0.0565305
5	0.4767	0.0373698
1	0.4634	0.0348289
0.5	0.4475	0.0489953
0.1	0.4472	0.0260946

The relative error is too high for each of the time steps in Table 8.1, so 10 simulations with 10,000 particles were run for higher precision. The results from these simulations are presented in Table 8.2. The ten sets of simulations consisting of 10,000 particles each that were used to generate the data in Table 8.2 were treated as one

simulation of 100,000 particles in Table 8.3. The relative errors associated with the values presented as Means in Table 8.3 were generated using the statistical methods described in Chapter 6.

Table 8.2: 10,000 Particle Simulations

Δt (μs)	Mean	Rel. Error
10	0.48799	0.0099932
5	0.47372	0.0072989
1	0.45722	0.0085561
0.5	0.45668	0.0101227
0.1	0.45078	0.010795

Table 8.3: 100,000 Particle Simulations (Extrapolated)

Δt (μs)	Mean	Rel. Error
10	0.48799	0.0044066
5	0.47372	0.0030225
1	0.45722	0.0030943
0.5	0.45668	0.0040503
0.1	0.45078	0.0030116

Table 8.1 demonstrates that the smaller the time step and the larger the number of test particles, the more accurately the Monte Carlo program replicates the results from Eq. 7.10. These relationships are intuitive. The Brownian diffusion modeled by Eqs. 7.5 and 7.6 is a continuous process in which $\Delta t \rightarrow 0$.

Due to the collisions with carrier gas molecules which cause Brownian motion, the direction and magnitude of the particle velocity due to diffusion is changing at such a rapid rate, the true description of the process has to be continuous and not discrete. Unfortunately, the Monte Carlo program is discrete by nature as each consecutive

diffusion step must be selected from a Gaussian distribution. Figure 8.1 demonstrates that each diffusion step can be in any direction. The smaller the time interval associated with a diffusion step, the smaller the circle in which the diffusion step is likely to take place. If the time step is too large, then the particle may travel too far and strike the breach wall in the simulation, whereas in reality, the particle may have changed directions several times over the simulated time step. Figure 8.2 shows a test particle trajectory due to diffusive motion in a typical Monte Carlo simulation. Notice how drastically the diffusion steps differ in direction and magnitude. If the simulation time step were much smaller, there would be more diffusion steps and more directional changes. The motion in Fig. 8.2 is for a particle with a diffusion coefficient of 10^{-8} m^2/s and a time step of 10 μs. The distance of the particle from the central axis at each time step during the same simulation that generated the results for Fig. 8.8 is displayed in Fig. 8.9.

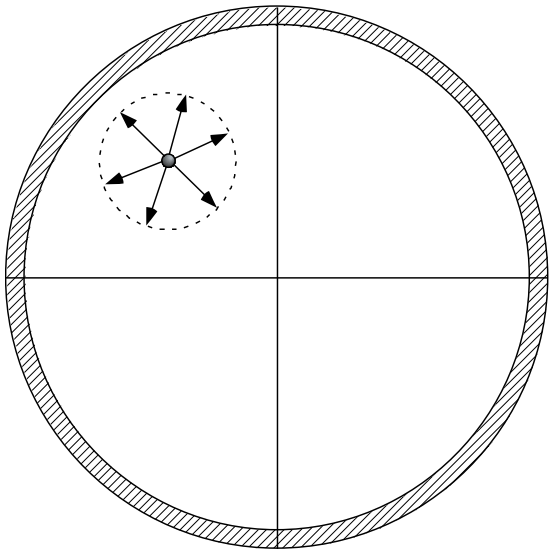

Figure 8.1: Particle Step Range

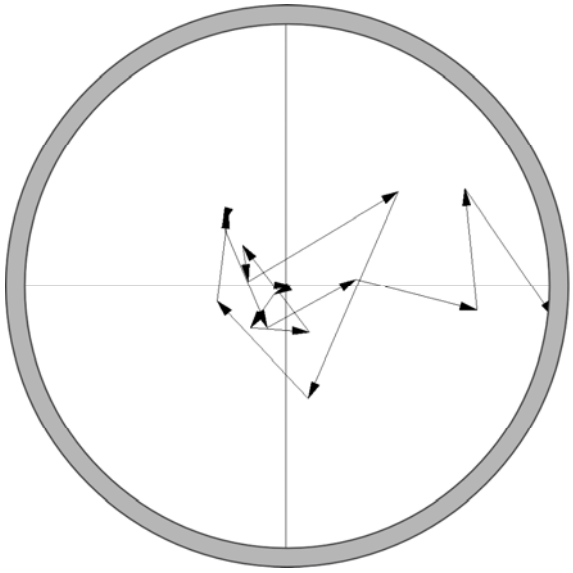

Figure 8.2: Traced Particle Pathway

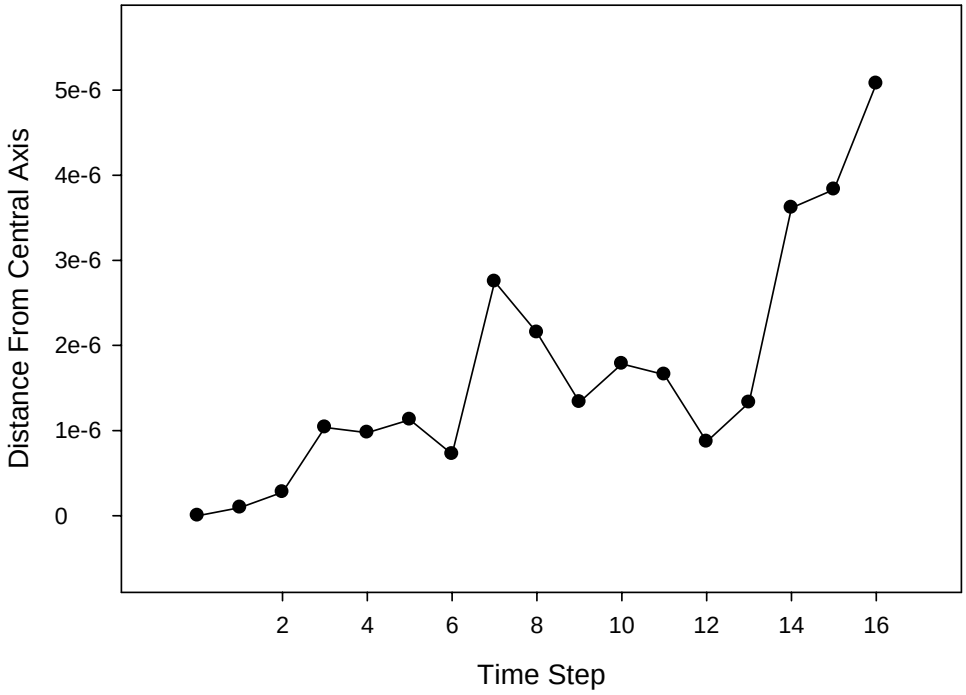

Figure 8.3: Particle Distance from the Central Axis at Each Time Step

In addition to improved results for smaller simulated time steps, it is a statistical property of Monte Carlo programs that the higher the number of test particles, the higher the accuracy of the result. Thus, when running simulations with the Monte Carlo program, it is important to use a Δt that is small enough and a number of test particles that is large enough to produce an accurate result. Unfortunately, both decreasing Δt and increasing the number of test particles are computationally expensive decisions.

8.4 IMPROVEMENTS TO THE STRAIGHT BREACH MODEL

During a Monte Carlo simulation, each test particle is tracked from its initial position at the breach entrance until it impacts the breach wall or passes through the far

end of the breach. If the particle impacts the wall, then the impact position in three-dimensions is recorded. Thus, this method allows particle "clumping" at deposition sites due to the stochastic nature of Brownian diffusion can be recorded. This is already an improvement in the results from the models presented in Chapter 7, in which it had to be assumed that for a given axial slice of the tube, the particle deposition pattern more resembled the one displayed in Fig. 8.4 rather than the one displayed in Fig. 8.5. In Figs. 8.1 and 8.2, there are 35 particles each with a diameter that is roughly equal to one-twelfth the diameter of the breach. Thus, for a breach with a 10 μm diameter, these particles would have diameters of about 0.833 μm. As far as the analyses in this thesis are concerned, these are large particles. In such a case, where so few particles are needed to completely coat the inner circumference of the breach, it is much more probable that a non-uniform deposition pattern resembling that in Fig. 8.5 would occur as opposed to a uniform deposition pattern like Fig. 8.4.

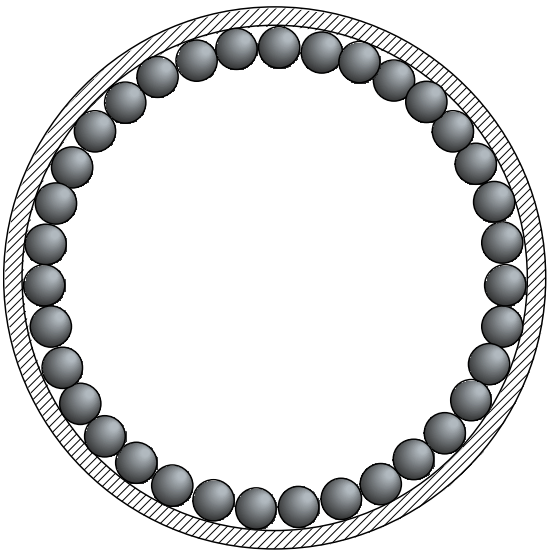

Figure 8.4: Uniform Circumferential Deposition

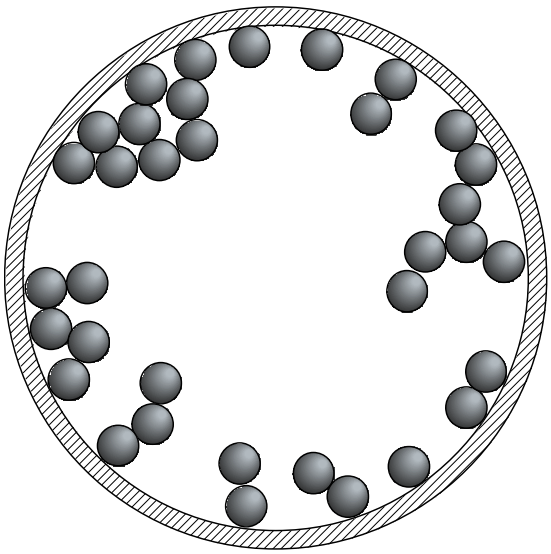

Figure 8.5: Random Circumferential Deposition

Due to the limitations of the equations used in the models in chapter six, the deposition pattern is actually modeled as it appears in Fig. 8.6. If the particles under consideration were much smaller, and quantity of particles being considered was much, much larger, then the pattern of particle deposition pattern may look like the one in Fig. 8.6. Another issue to be considered is the fact that for a given axial ring of the tube, the particle deposition will be in three-dimensions like Fig. 8.7 as opposed to a two-dimensional pattern as is implied by Figs. 8.4 and 8.5. In the models of Chapter 7, the particles deposited in three-dimensions like those shown in Fig. 8.7 are spread into a smooth uniform like the one shown in Fig. 8.6 along the length of the tube. If the change in flow due to the change in the surface geometry associated with particle deposition is not taken into account, then successive particle deposition positions can be recorded in three dimensions with the Monte Carlo program. Once again, this aspect alone makes the Monte Carlo program an improvement over the Chapter 7 models. The degree to which the deposited particles do affect the flow through the tube is smaller when the particle size is smaller. However, the effect of the stochastic nature of particle deposition is less for the larger particle numbers that are associated with flow restriction and plugging due to particle deposition.

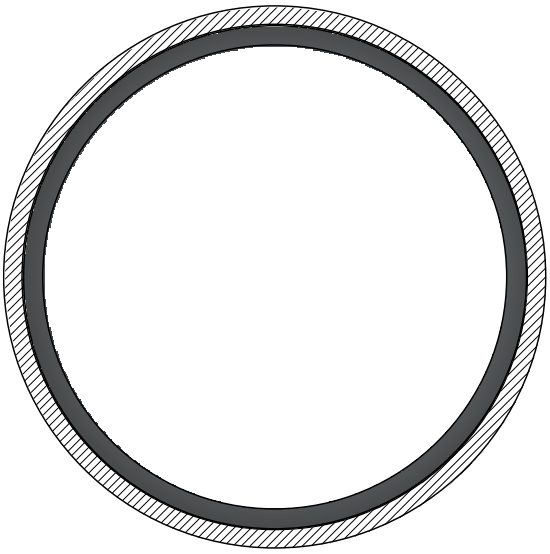

Figure 8.6: Deposition Pattern of Chapter 7 Models

Figure 8.7: 3-Dimensional Deposition Pattern

Table 8.1 shows that with the correctly chosen time step and number of test particles, the Monte Carlo program can match the results for the particle transmission fraction of Eq. 7.10. In addition to comparing the fraction of transmitted particles, it is beneficial to compare other results that can be generated by the models. For instance, if the breach through which the aerosol is flowing is divided into rings along its axis, the number of particles that are determined to be deposited on each ring can be compared. Consider 1000 test particles run through a tube with a length of 1 cm under the same conditions used to generate the data in Table 8.1. The tube is divided into 10 axial rings, each with a length 1 mm. The number of particles predicted to be deposited by the Monte Carlo program is compared to the number predicted by Eq. 7.10 in Fig. 8.8. In Fig. 8.9, the same comparison is made for the same data, but with the tube divided into 20 axial rings, each with a length of 0.5 mm. Figs. 8.8 and 8.9 show how closely the

Monte Carlo program results follow the analytical results – even if the number of test particles is as small as 1000.

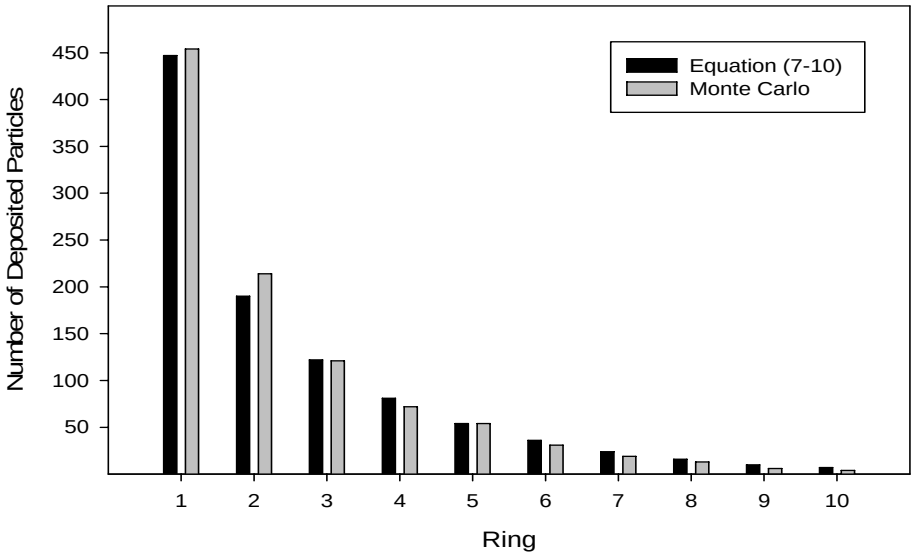

Figure 8.8: Comparison of Results for 1000 Test Particles and 10 Axial Rings

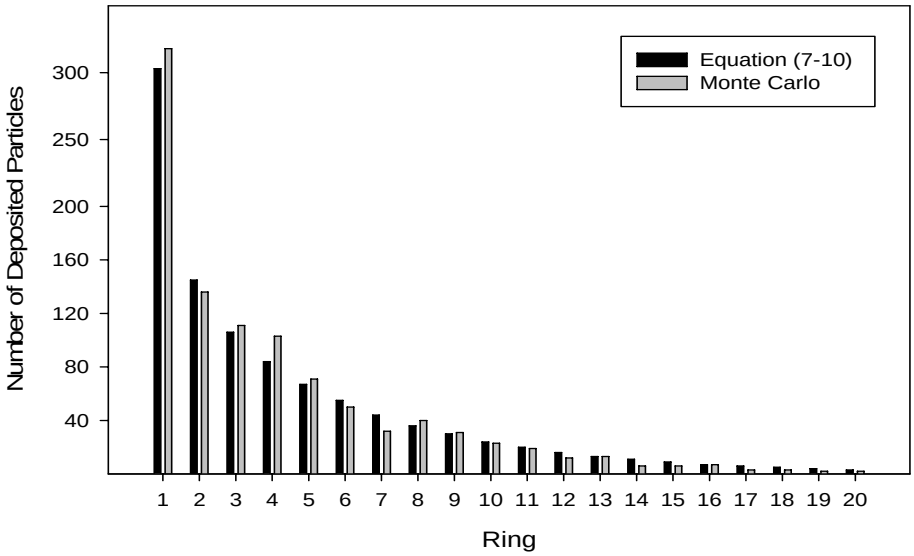

Figure 8.9: Comparison of Results for 1000 Test Particles and 20 Axial Rings

Although Figs. 8.8 and 8.9 show that the trend in the results for axial deposition from the Monte Carlo program match those from Eq. 7.10 nicely, there are still some discrepancies. These discrepancies become more apparent for smaller sample sizes. For instance, in Fig. 8.8, the number of particles deposited in ring 1 is roughly the same from both models. However, when that ring is split into two as it was for Fig. 8.9, the discrepancies in each half start to stand out. In ring 1 of Fig. 8.8, the number of particles deposited is about 450 in each model. However, in rings 1 and 2 of Fig. 8.9, the number of particles deposited is roughly 320 and 140 respectively. These smaller sample sizes cause differences in the models to become more apparent. If the tube were to be divided into even more axial rings, these differences would become more noticeable. This realization once again underscores the necessity to consider the plugging of a breach by a large number of small particles in a distinctly different way than the plugging of a breach by a small number of large particles.

In Fig. 8.2, it is evident that in the Monte Carlo model, the circumferential point of impact is recorded. If each axial ring is divided into sectors defined by planar angles, then the deposited particles in a given axial ring can be binned and compared. The process of dividing a ring into bins is demonstrated in Fig. 8.10. The particles that are deposited in a sector of the ring defined by the angle $\alpha - \beta$ can be determined if the coordinates of their deposition position are such that $a_t\text{Cos}[\alpha] \leq x < a_t\text{Cos}[\beta]$ and $a_t\text{Sin}[\beta] \leq y < a_t\text{Sin}[\alpha]$. Once the Monte Carlo simulation is run, then each ring can be searched for particle "clumps" in this fashion.

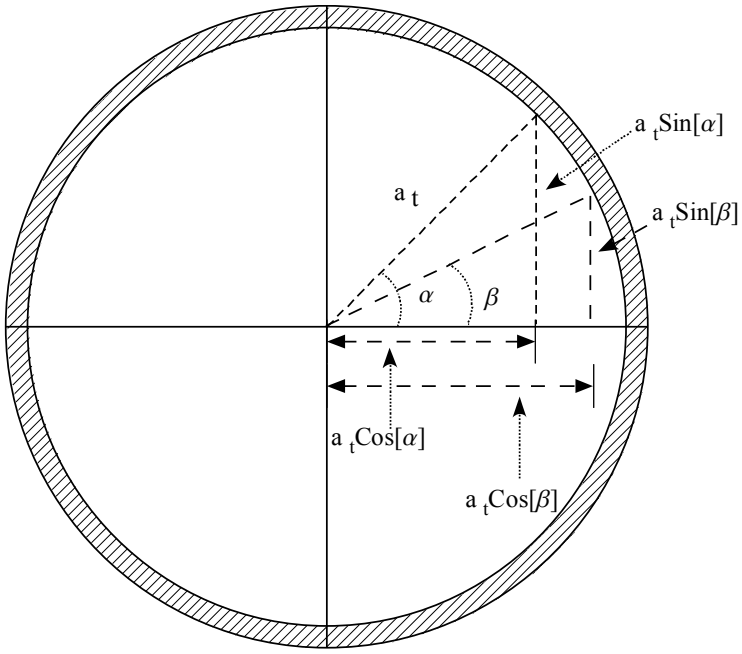

Figure 8.10: Dividing an Axial Ring into Bins According to Planar Angle

In applying the methodology portrayed in Figure 8.10, if β is taken to be a factor of 2π, and α is taken to be 2β, the sectors spanned by β and $\alpha - \beta$ will be the same. A third sector past that spanned by $\alpha - \beta$ is $3\beta - 2\beta$. This process of advancing sectors can be repeated until the entire circle is spanned, providing bins of equal size for particle deposition characterization. The size of these bins can be as large or as small as desired in order to determine the characteristic of deposition that is under consideration. In addition, sectors of arbitrary size and position can be scanned for deposition clumps. As a test case, consider the first axial ring of the system used to generate Figure 8.8.

If the ring is divided into left ($x < 0$) and right ($x > 0$) hemispheres, it is discovered that of the 454 particles deposited on the ring, 233 are in the right hemisphere and 221 are in the left. Dividing the ring into quadrants, labeled in the traditional fashion of the upper-right quadrant labeled I, and labels increasing counter-clockwise, the deposition pattern is discovered to be I-115, II-120, III-101, IV-118. Thus, although the

bias is to the right of the tube, it is not focused in one particular quadrant. If only the first half of the first axial ring (the first axial ring in Figure 8.9) is similarly divided into quadrants, the deposition pattern is discovered to be I-86, II-81, III-68, IV-83. The pattern of the bias to the right hemisphere is thus seen to be in the first half of the first axial ring. The bias seen in this simulation is not consistent for repeated simulations. Results from this type of simulation may indicate very uniform deposition or very non-uniform deposition patterns. The degree of differentiation between different sectors on a given axial ring will generally be greater for smaller quantities of test particles in a simulation. Since plugging due to a smaller number of particles occurs for larger particle sizes, it is once again asserted here that plugging due to small numbers of large particles in a stochastic process as opposed to the generally steady-uniform process of plugging due to large numbers of smaller particles (a process which for the most part is well defined by Eq. 7.10).

The results presented in Figs. 8.8 and 8.9 are statistical in nature as has been claimed earlier. Thus, each simulation with identical input parameters to those used to generate Figs. 8.8 and 8.9 will have varying results. In order to study this phenomenon, simulations identical to the one used to generate the results for Figs. 8.5 and 8.6, were run and the results presented in the Figs. 8.11 through 8.28. The data from all ten simulations are combined to produce Figs. 8.29 and 8.30. As expected, the results associated with the larger sample size of 10,000 particles have smaller deviations from the results generated by Eq. 7.10 than the simulations with a smaller sample size of 1,000. The results from larger and larger sample sizes are expected to agree more and more closely with the results from Eq. 7.10.

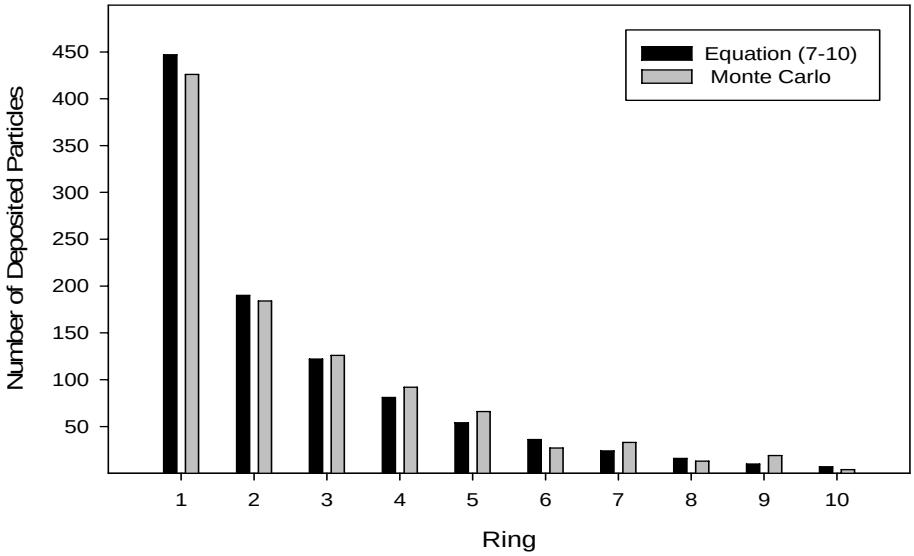

Figure 8.11: Comparison of Simulation 2 Results for 10 Axial Rings

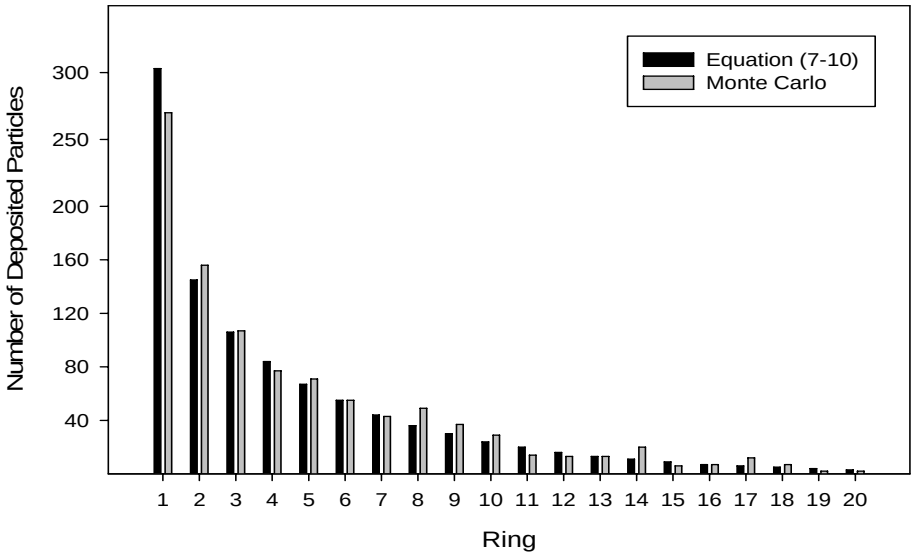

Figure 8.12: Comparison of Simulation 2 Results for 20 Axial Rings

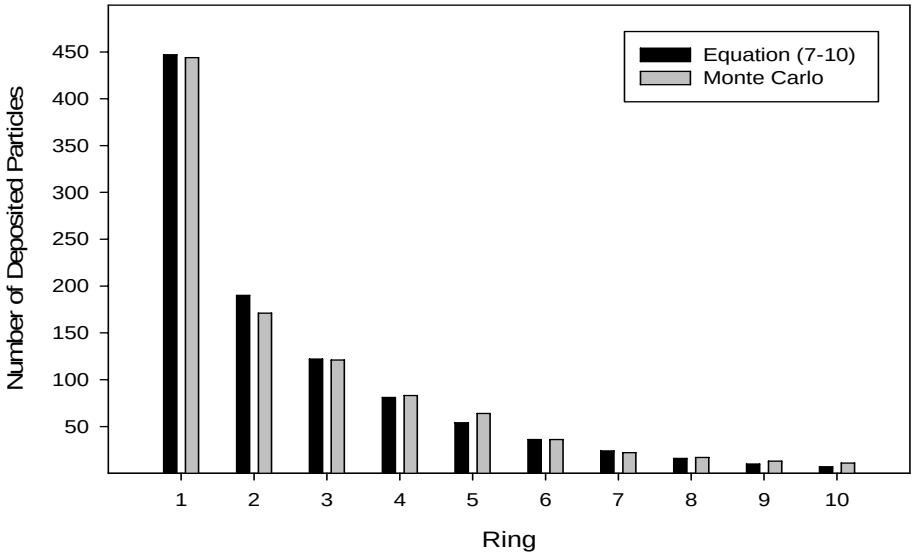

Figure 8.13: Comparison of Simulation 3 Results for 10 Axial Rings

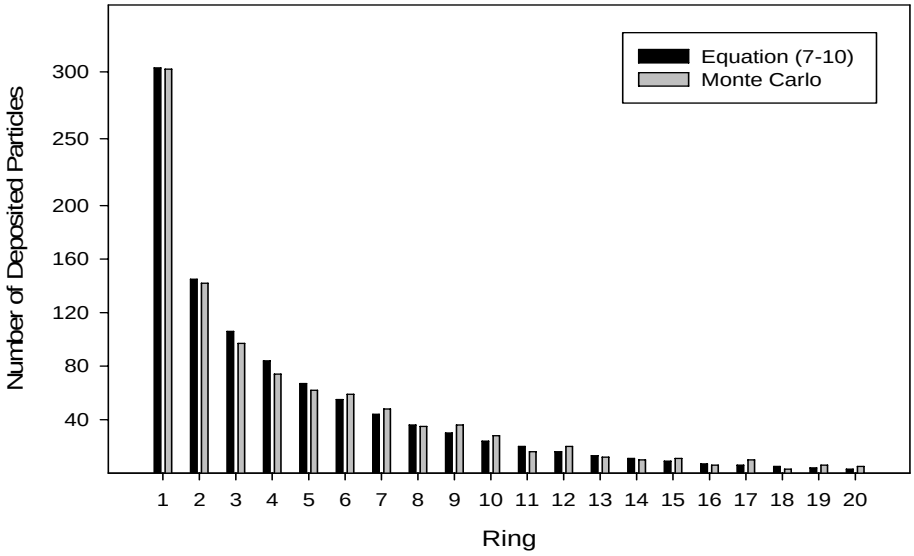

Figure 8.14: Comparison of Simulation 3 Results for 20 Axial Rings

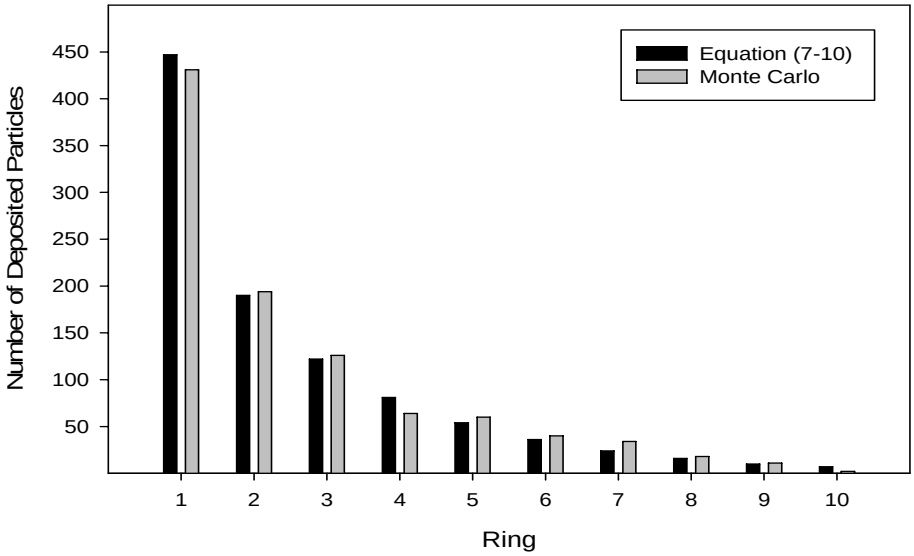

Figure 8.15: Comparison of Simulation 4 Results for 10 Axial Rings

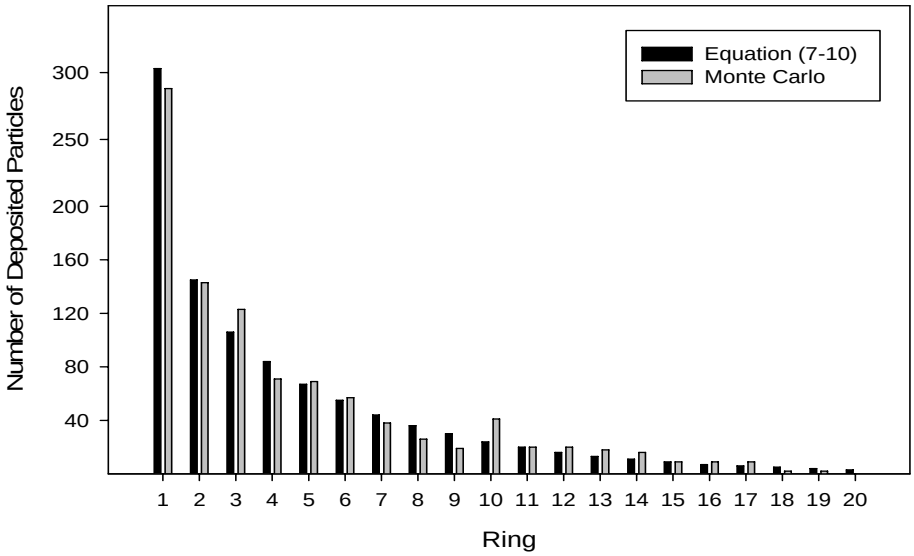

Figure 8.16: Comparison of Simulation 4 Results for 20 Axial Rings

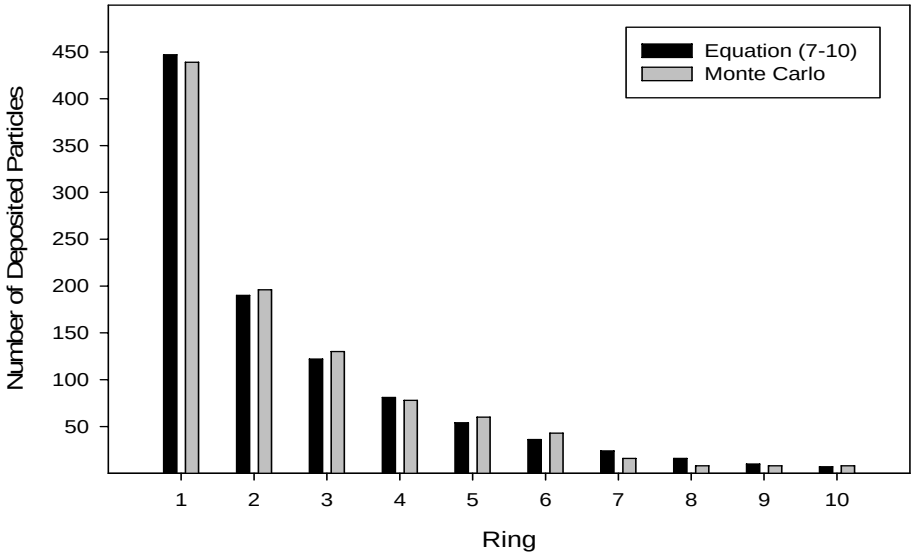

Figure 8.17: Comparison of Simulation 5 Results for 10 Axial Rings

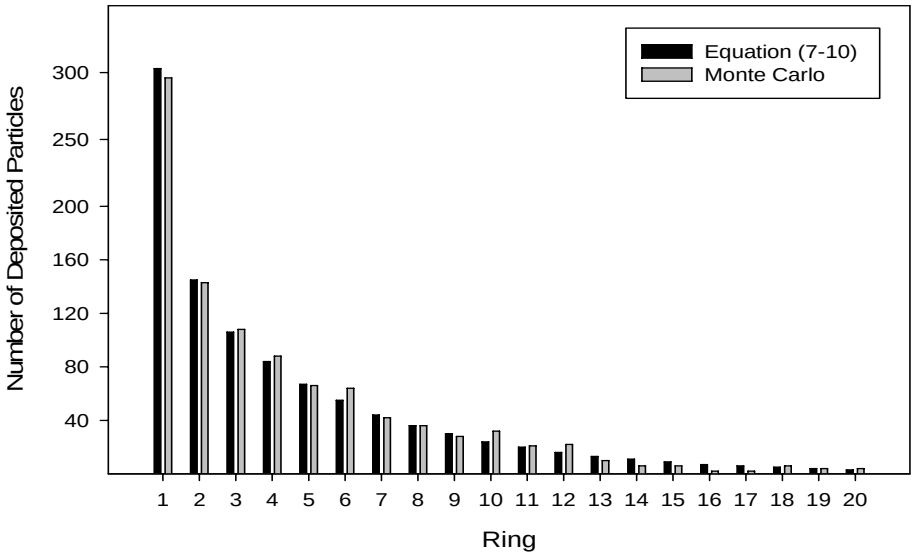

Figure 8.18: Comparison of Simulation 5 Results for 20 Axial Rings

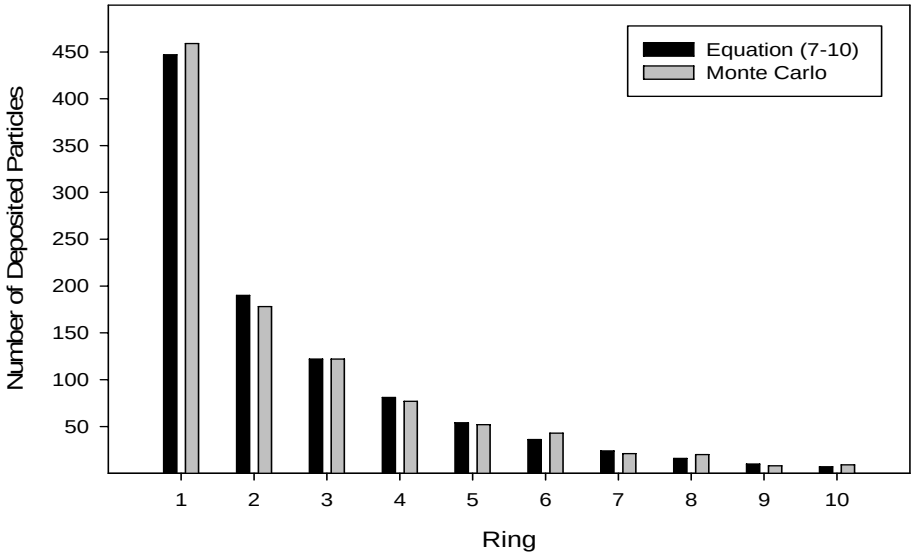

Figure 8.19: Comparison of Simulation 6 Results for 10 Axial Rings

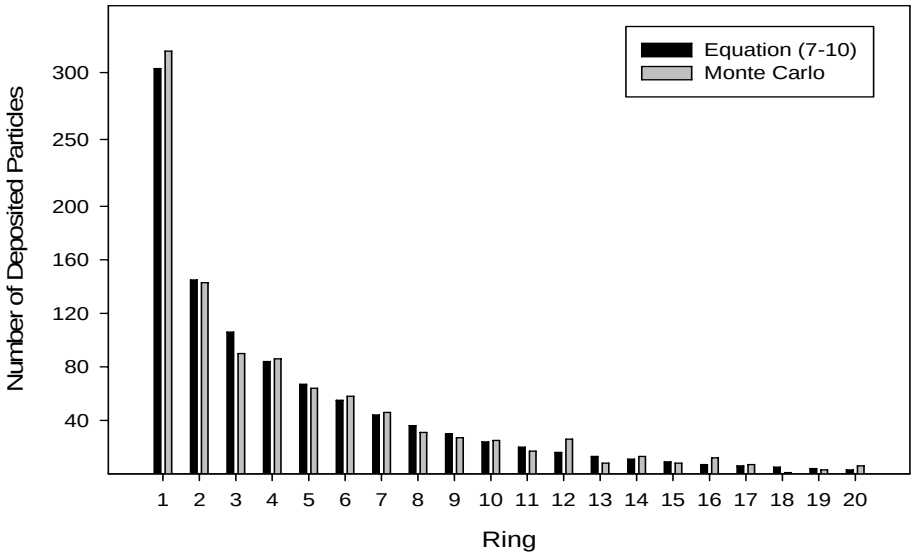

Figure 8.20: Comparison of Simulation 6 Results for 20 Axial Rings

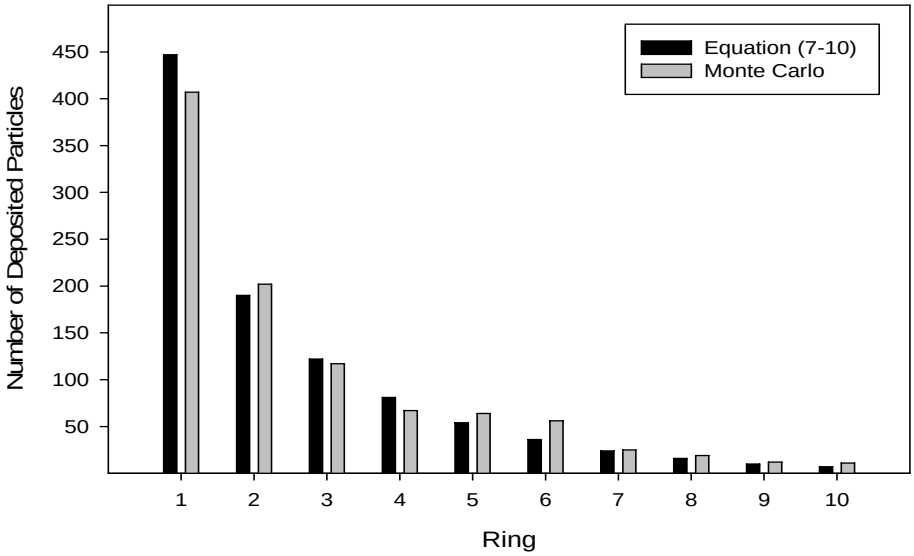

Figure 8.21: Comparison of Simulation 7 Results for 10 Axial Rings

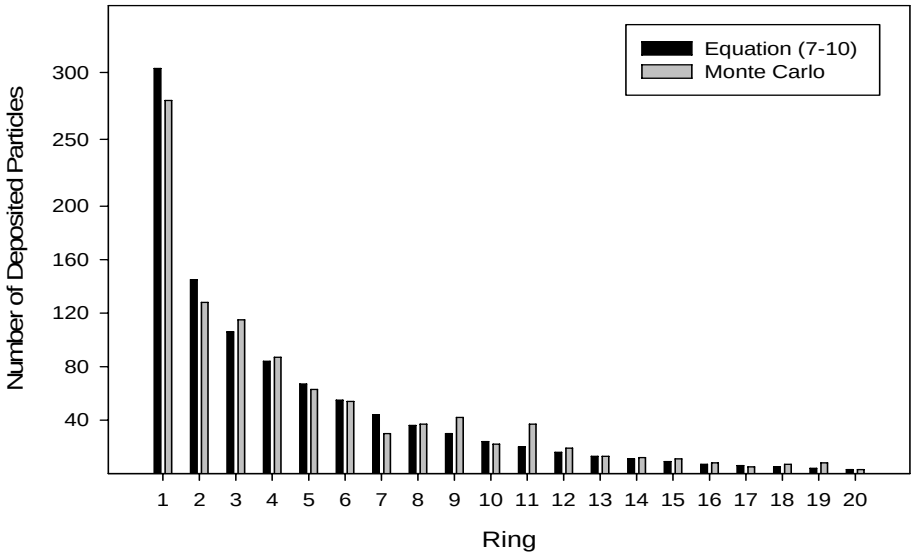

Figure 8.22: Comparison of Simulation 7 Results for 20 Axial Rings

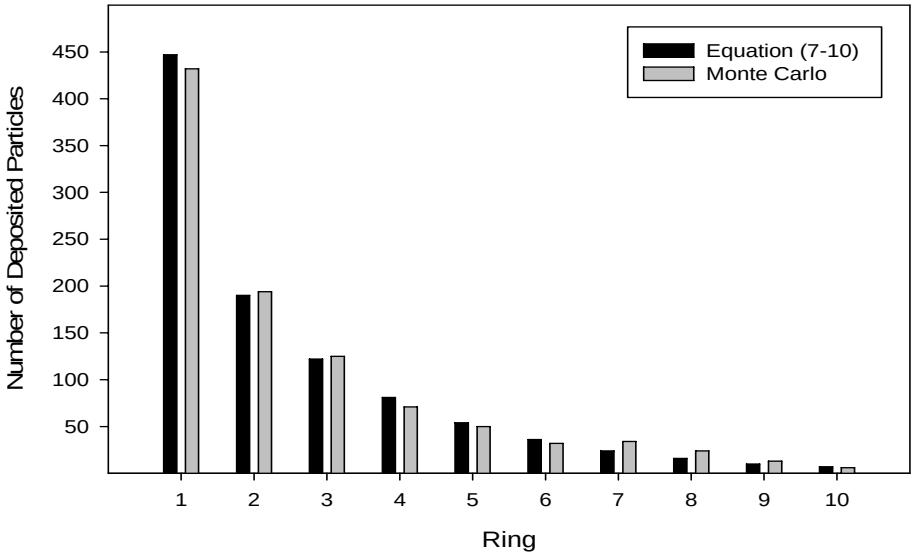

Figure 8.23: Comparison of Simulation 8 Results for 10 Axial Rings

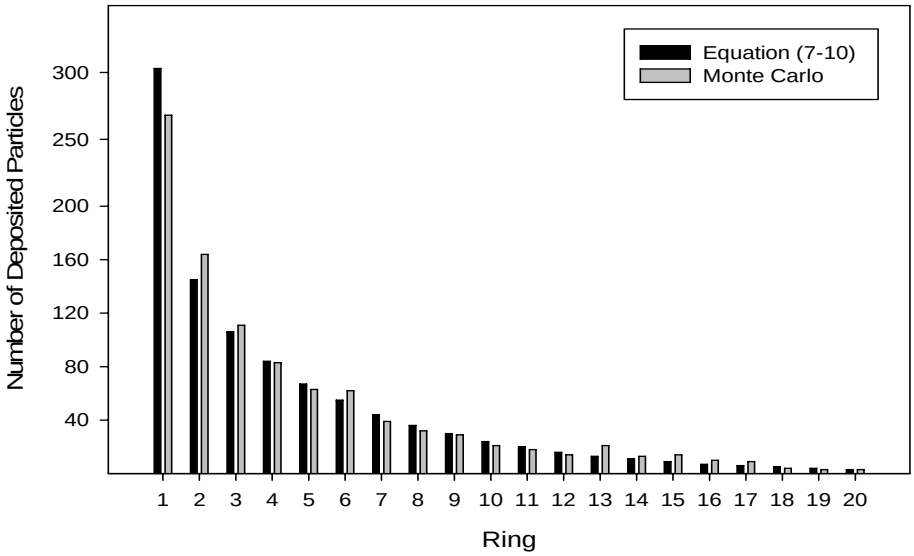

Figure 8.24: Comparison of Simulation 8 Results for 20 Axial Rings

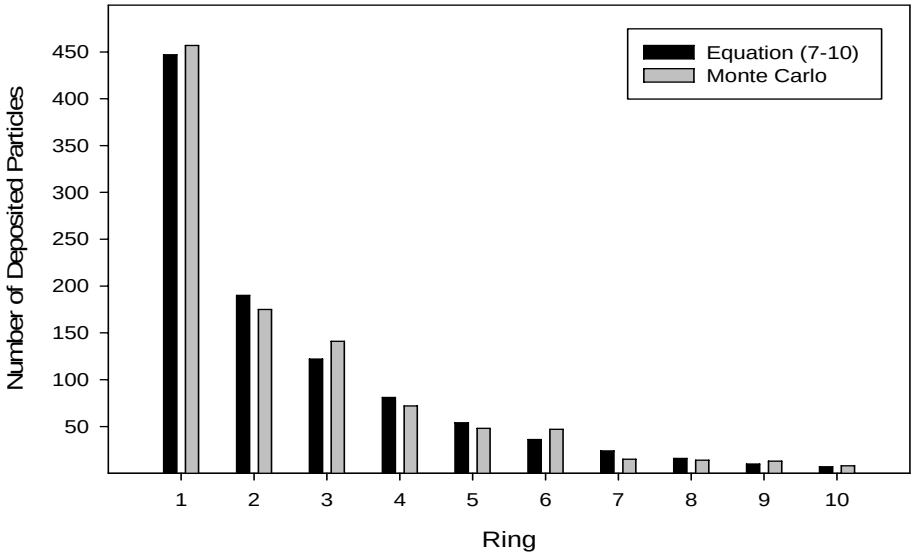

Figure 8.25: Comparison of Simulation 9 Results for 10 Axial Rings

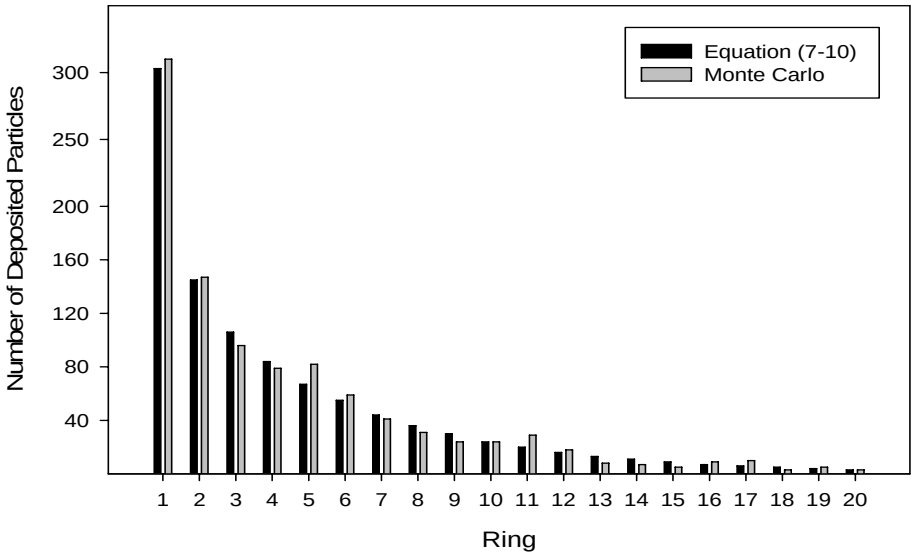

Figure 8.26: Comparison of Simulation 9 Results for 20 Axial Rings

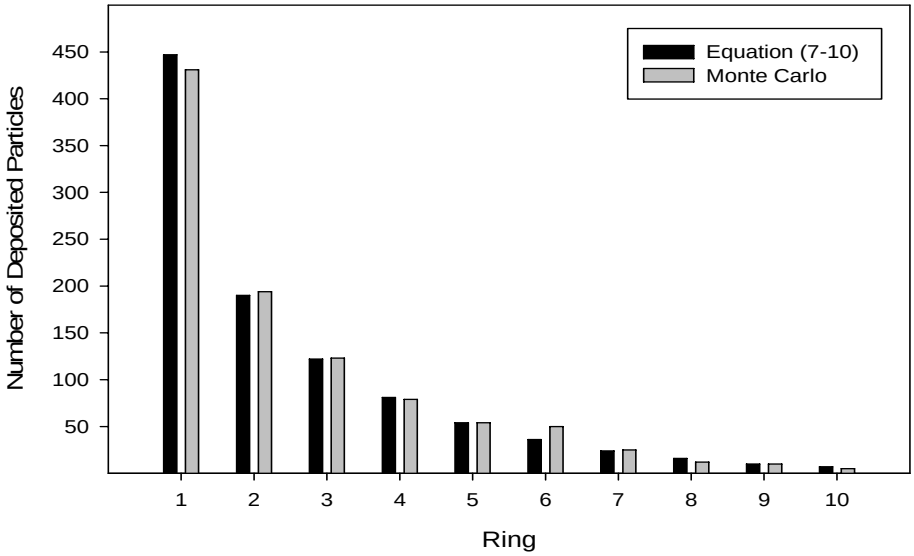

Figure 8.27: Comparison of Simulation 10 Results for 10 Axial Rings

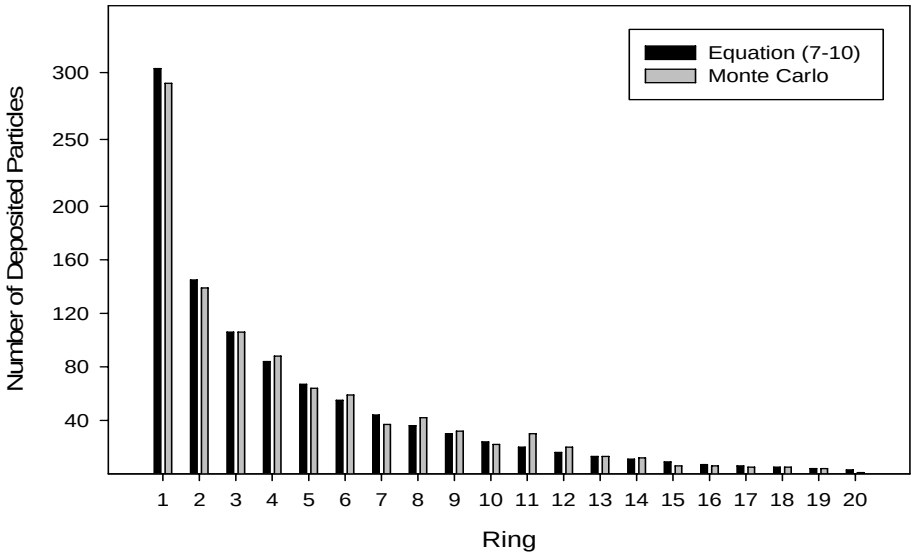

Figure 8.28: Comparison of Simulation 10 Results for 20 Axial Rings

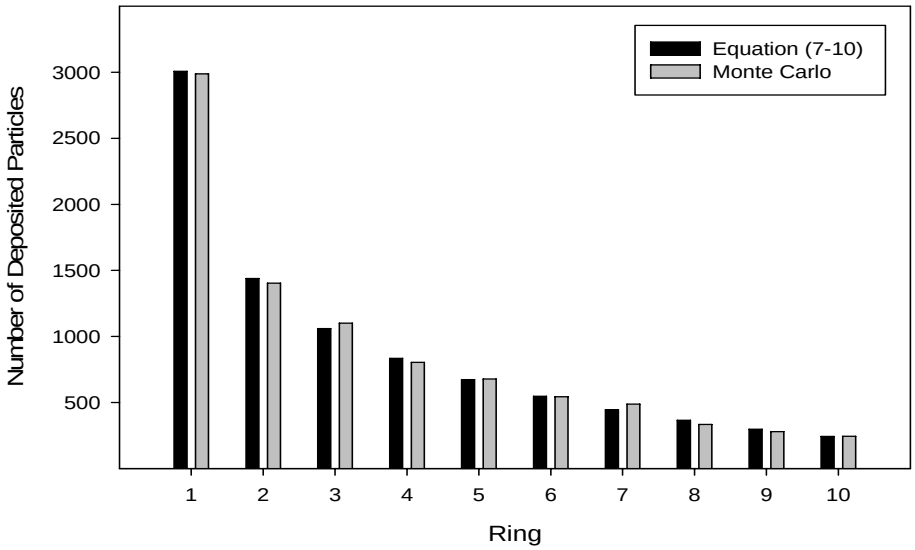

Figure 8.29: Comparison of Combined Results from Simulations 1 - 10 for 10 Axial Rings

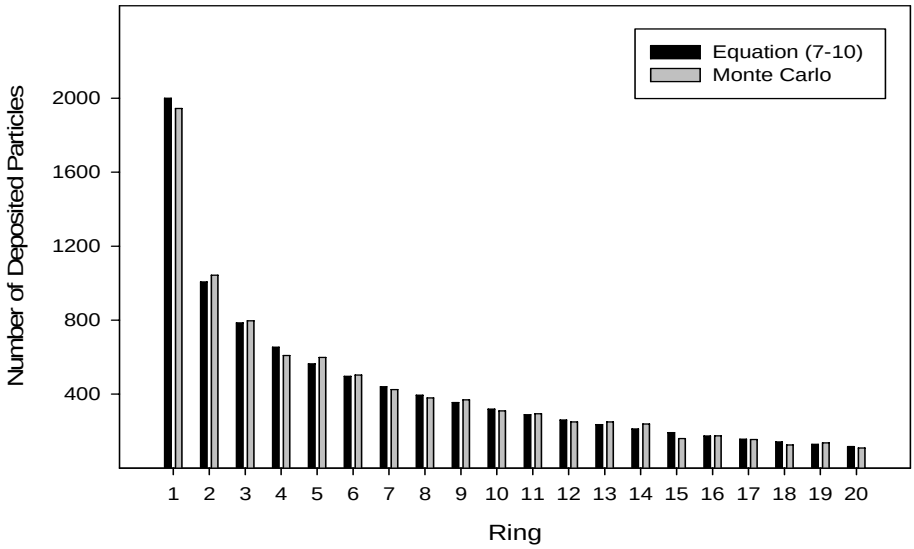

Figure 8.30: Comparison of Combined Results from Simulations 1 - 10 for 20 Axial Rings

Table 8.4 shows the statistical mean and standard deviation for the 10-ring case determined from the ten simulations discussed here. Table 8.5 provides the same information, but for the 20 ring case. Table 8.6 compares the percentage that the standard

deviation makes of the mean for the 10-ring case and the 20-ring case. The differences in these values are not consistent due to the low number of particles in the sample size. In this case, the sample size is the number of particles deposited in the ring being considered. The purpose of Table 8.6 is to demonstrate quantitatively the statistical nature of particle deposition for small sample sizes. A larger percentage of the mean that the standard deviation makes up for a given ring, indicates a higher the variability in that result for the different simulations. Once again, this phenomenon is unimportant for a large number of small particles, but for large particles that can close of the flow area with only a small number of particles, this effect is significant.

Table 8.4: Deposition Statistics for 10-Ring Case

Ring	Mean	Std. Dev.	Ring	Mean	Std. Dev.
1	438	16.1	6	40.5	9.13
2	190.2	13.2	7	24.4	7.18
3	125.2	6.6	8	15.8	4.66
4	75.5	8.15	9	11.3	3.65
5	57.2	6.41	10	6.8	3.08

Table 8.5: Deposition Statistics for 20-Ring Case

Ring	Mean	Std. Dev.	Ring	Mean	Std. Dev.
1	293.9	18	11	22.1	7.4
2	144.1	10	12	18.4	4.33
3	106.6	9.41	13	12.9	4.07
4	83.6	9.12	14	11.5	4.48
5	67.5	6.1	15	8.2	2.97
6	57.7	4	16	7.6	2.72
7	39.6	5.68	17	7.2	3.33
8	35.9	6.57	18	4.1	2.08
9	30.5	6.69	19	3.9	1.97
10	26.7	6.15	20	2.9	1.79

Table 8.6: Standard Deviation Percentage of Mean

Ring	10-Ring Case	20-Ring Case	Ring	20-Ring Case
1	3.68%	6.11%	11	33.49%
2	6.94%	6.96%	12	23.51%
3	5.27%	8.84%	13	31.53%
4	10.80%	10.91%	14	38.94%
5	11.20%	9.03%	15	36.27%
6	22.55%	6.93%	16	35.74%
7	29.44%	14.34%	17	46.20%
8	29.51%	18.31%	18	50.71%
9	32.33%	21.93%	19	50.49%
10	45.35%	23.02%	20	61.79%

Figures 8.11 through 8.30 and Tables 8.2 through 8.4 analyze the axial deposition patterns and statistics generated from the Monte Carlo program. The following figures analyze the corresponding circumferential deposition patterns and statistics. Figure 8.31 displays the number of particles deposited in each quadrant of each axial ring in Fig. 8.8.

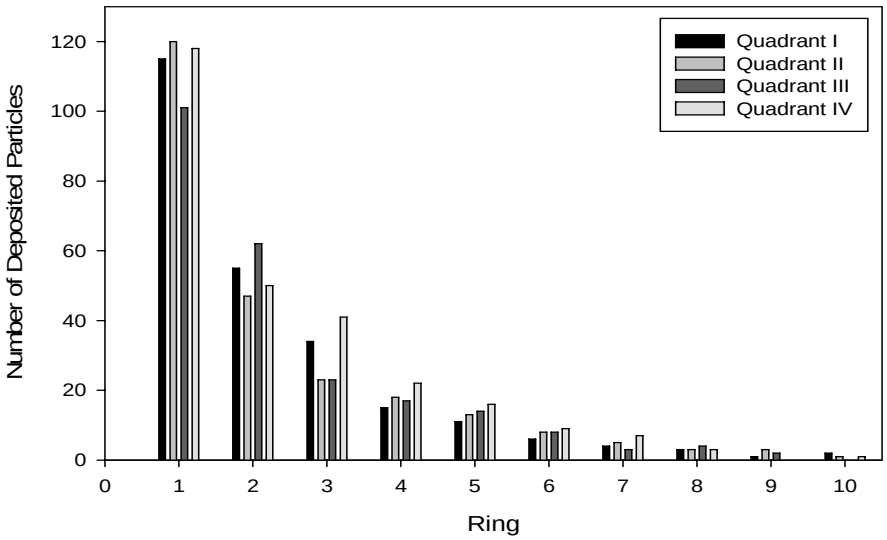

Figure 8.31: Circumferential Deposition Patterns for Each Axial Ring in Fig. 8.8

Figure 8.31 shows that there is preferential circumferential deposition, particularly in ring number 3. Since more particles are deposited in the first axial ring than in all other rings combined, it is more likely that a flow blocking structure will form there. Figure 8.32 displays the number of particles deposited in each quadrant of the first axial ring of each of the ten simulations represented in Figs. 8.8 through 8.28.

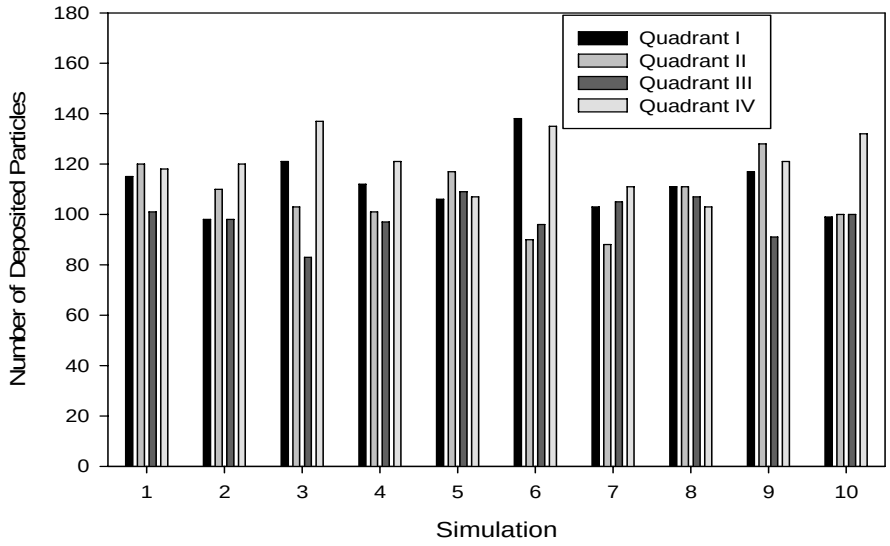

Figure 8.32: Circumferential Deposition Patterns in the First Axial Ring of the 10 Simulations in Figs. 8.8 through 8.28

Some circumferential deposition patterns in Fig. 8.32 are fairly flat such as those in simulations 1, 5, and 8, whereas some are show preferential deposition such as those in simulations 3, 6, 9, and 10. Although some of the deposition patterns in Fig. 8.32 show preferential circumferential deposition, each quadrant represents a deposition surface that extends for the 1 mm length of each axial ring. In order to decrease the area of the deposition surface to better pinpoint "clumps", the circumferential deposition pattern in the first half of the first axial ring in each simulation is displayed in Fig. 8.33.

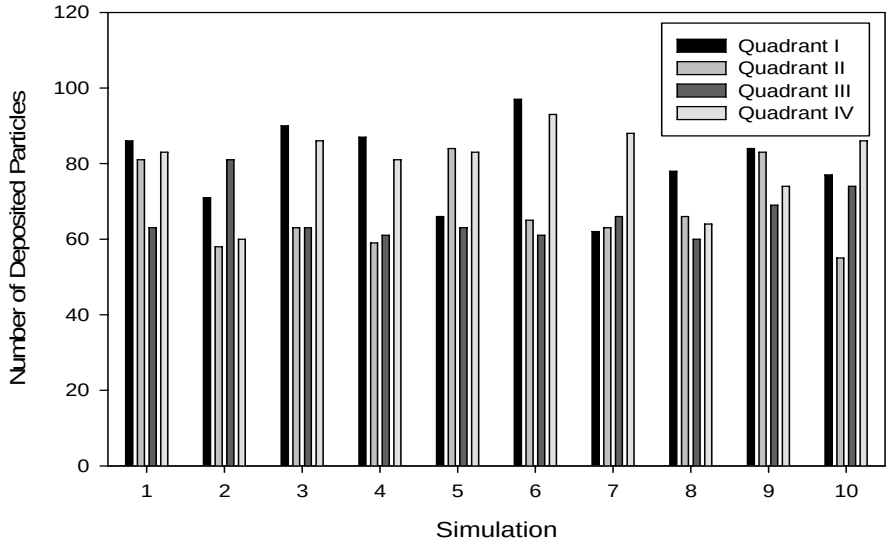

Figure 8.33: Circumferential Deposition Patterns in the First Half of the First Axial Ring of the 10 Simulations in Figs. 8.8 through 8.28

Nearly every pattern displayed in Fig. 8.33 exhibits preferential deposition in one or two quadrants of the represented half-ring. The process of scanning shorter axial rings and smaller circumferential sectors will allow for detection of exceptionally high deposition spots. Figures 8.34 through 8.39 provide a more in-depth deposition scan of the 10,000 simulated particles represented in Figs. 8.29 and 8.30. Figures 8.34 through 8.36 show that there is a definite bias in the first 0.1 mm of the breach toward the right half of the breach since the first quadrant contains the most deposited particles and the fourth quadrant contains the second most deposited particles. The bias stays either in the first quadrant or some sector that is composed of part of the first quadrant and part of the second quadrant as the sector angle is varied. In the first 0.01 mm of the breach, the bias remains and is more pronounced.

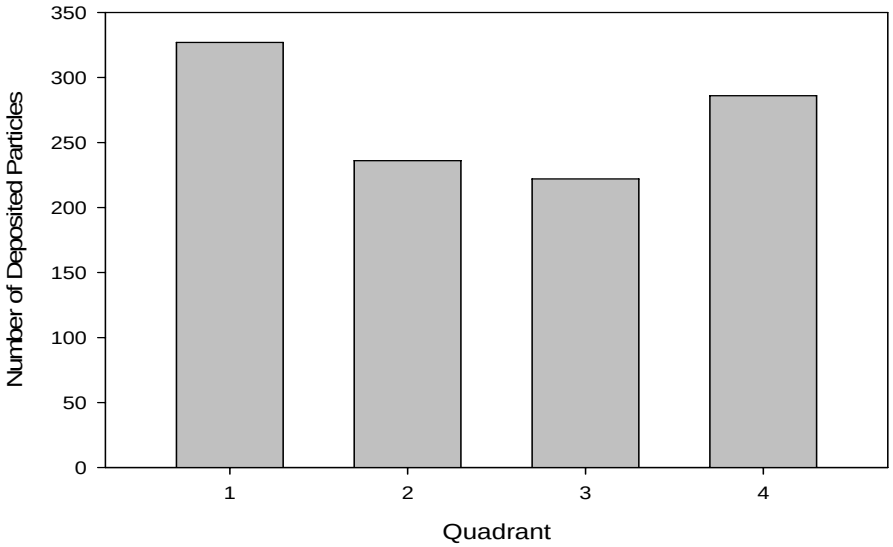

Figure 8.34: Deposition by Quadrant in the First 0.1 mm of the Breach

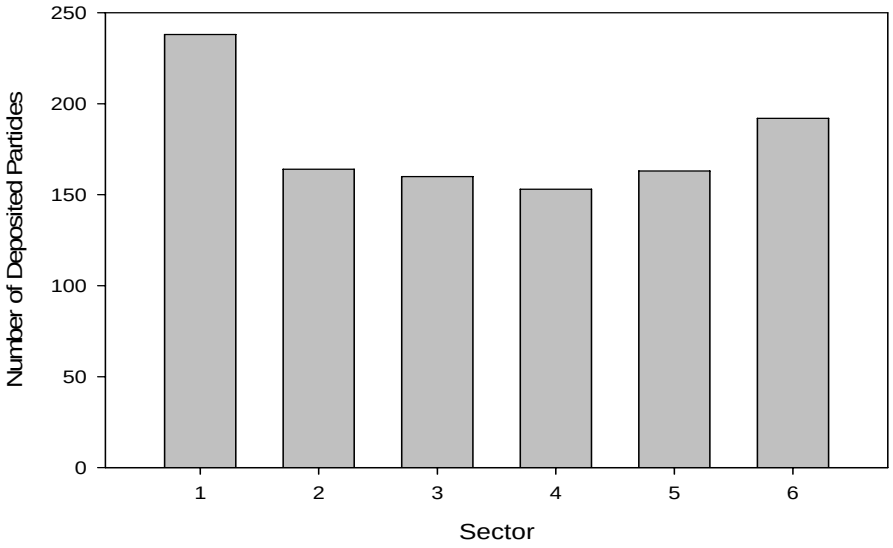

Figure 8.35: Deposition by Sector (Sector Angle = $\pi/3$) in the First 0.1 mm of the Breach

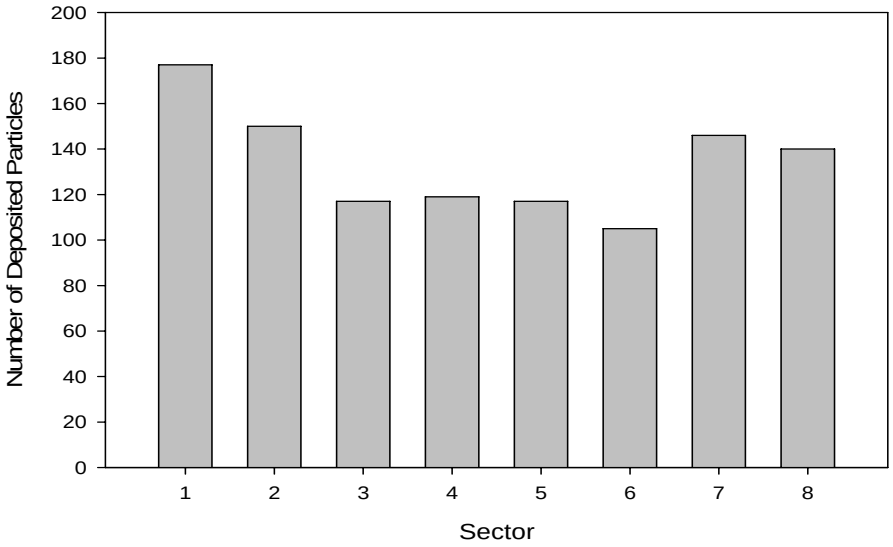

Figure 8.36: Deposition by Sector (Sector Angle = π/4) in the First 0.1 mm of the Breach

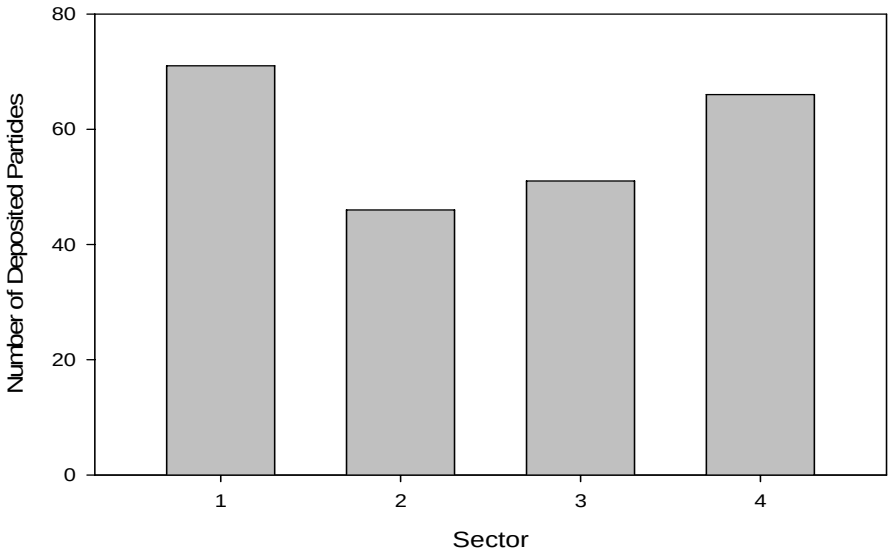

Figure 8.37: Deposition by Quadrant in the First 0.01 mm of the Breach

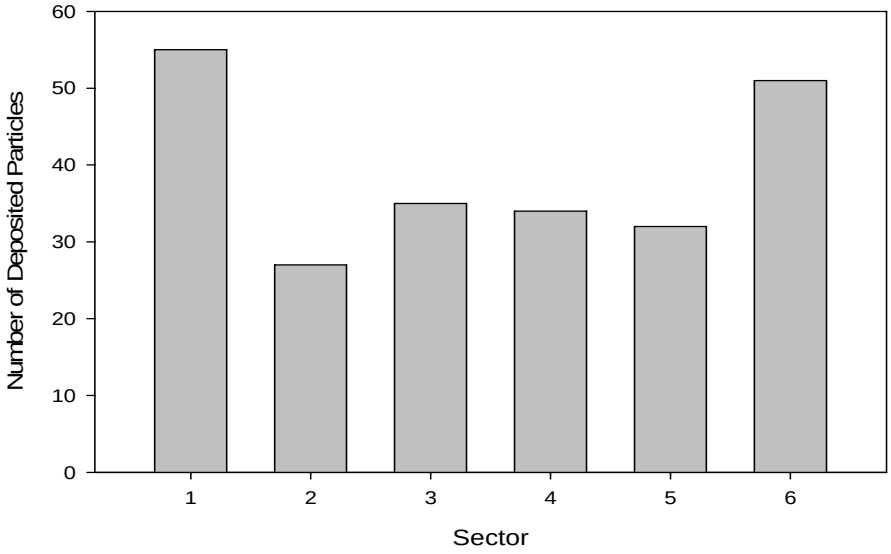

Figure 8.38: Deposition by Sector (Sector Angle = π/3) in the First 0.01 mm of the Breach

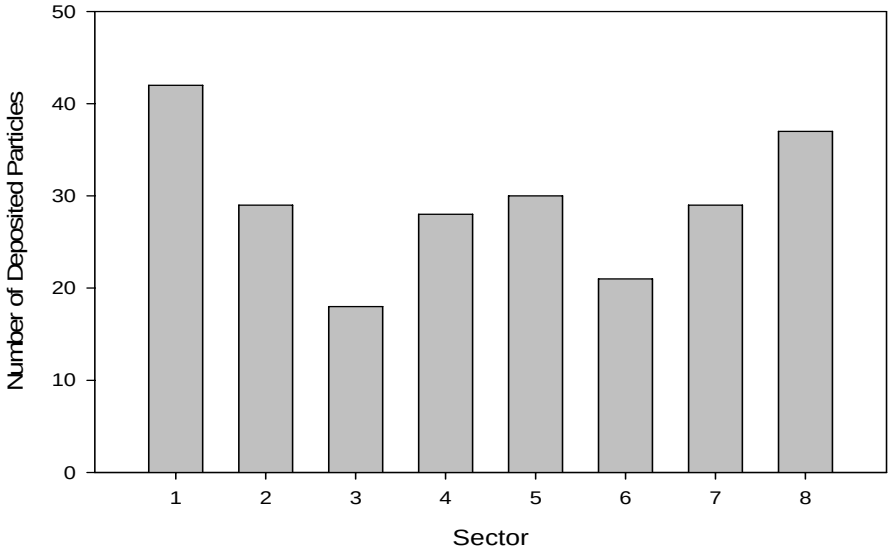

Figure 8.39: Deposition by Sector (Sector Angle = π/4) in the First 0.01 mm of the Breach

In Fig. 8.39, each deposition area considered has an axial length of 10 μm and a circumferential length of 3.93 μm corresponding to an area of 39.3 μm^2. Each particle considered has a diameter of 0.5 μm constituting a collision area of 0.786 μm^2. The 42

particles deposited in the first sector of Fig. 8.39 constitute a total deposition area of 31.4 μm^2 which is nearly equal to the deposition area. Most likely, some of the particles will be deposited upon one another, contributing to the foundation of a flow blocking structure. The deposition search demonstrated in Figs. 8.34 through 8.39 can be continued to more precise deposition areas all the way down to exact particle deposition positions. The results of such a search can be used to construct a deposition structure. Of course, in the current model, the presence of deposited particles was not accounted for in the deposition of other particles. This model can be expanded to account for this and other phenomena.

Thus far, the ability of the Monte Carlo program to reproduce the results of the analytical solution and to track the circumferential deposition position as well as the axial deposition position has been demonstrated. The ability of the program to expand upon these results will now be explored. One of the drawbacks of the analytical solution that was discussed in chapter six was that the particles were assumed to be mathematical points with no physical size. Although simplifications still must be made, the Monte Carlo can account for finite particle diameters.

There are three fundamental issues to be addressed when adjusting the Monte Carlo program to deal with finite particles. The first of these issues stems from the fact that the three dimensional coordinate associated with a particle position coincides now not with the entire particle, but only with the particle center. Thus, a particle-wall collision no longer occurs when the particle "position" coincides with a coordinate that lies on the breach wall. Instead, the collision occurs when that "position" of the particle coincides with a coordinate located a distance equal to $d_p/2$ from the breach wall. Thus,

collisions must be tracked for a particle radial distance from the central axis of $a_t - d_p/2$ instead of a distance a_t. This implies that the particle velocity in the axial direction due to convection is equal to zero when the particle "position" is a distance equal to the particle radius from the wall instead of at the wall.

This leads to the second issue which is the determination of the velocity to assign to the particle when it is located at any given radial position. The simplest solution is to assign the particle the velocity associated with the fluid stream velocity at the radial position where the center of the particle is located. This is an approximation however since the fluid will be moving faster at the edge of the particle that is closer to the central axis of the breach and will be moving slower at the edge of the particle that is closer to the breach wall. This disparity in the velocity at different points on the particle, which is now being treated as a finite sphere, will likely place a torque on the particle which will cause it to rotate. This spinning motion will probably have some affect on the trajectory of the particle. The extent to which this effect influences the particle motion is likely a function of the particle size and it is a reasonable conclusion that it will affect larger particles to a greater extent due to the greater difference in the velocities on opposite sides of the particle. This effect however will not be addressed in this thesis. In this work, the velocity associated with a particle will be assumed to be the same as it would be if the particle were simply still a mathematical point. Thus, the convective axial velocity will still be determined from Eq. 7.2 except that the velocity jumps abruptly to zero at the radial position equal to $(a_t - d_p/2)$. This profile is distinctly different from the profile that would result if a_t were to be replaced by $(a_t - d_p/2)$ in Eq. 7.2. The incorrect

profile created by this substitution is shown in Fig. 8.40 alongside the profile created by Eq. 7.2. Figure 8.41 displays the correct profile along with the profile created by Eq. 7.2.

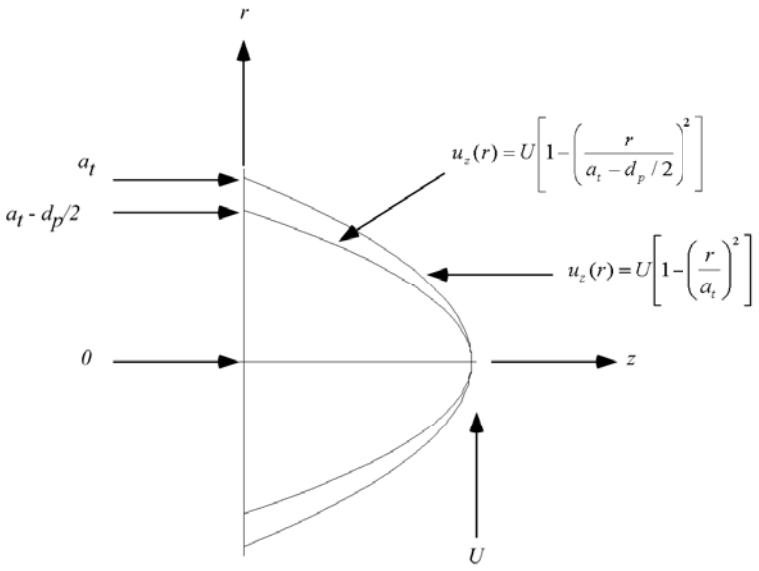

Figure 8.40: Flow Profiles Resulting from Eq. 7.2 and Substitution

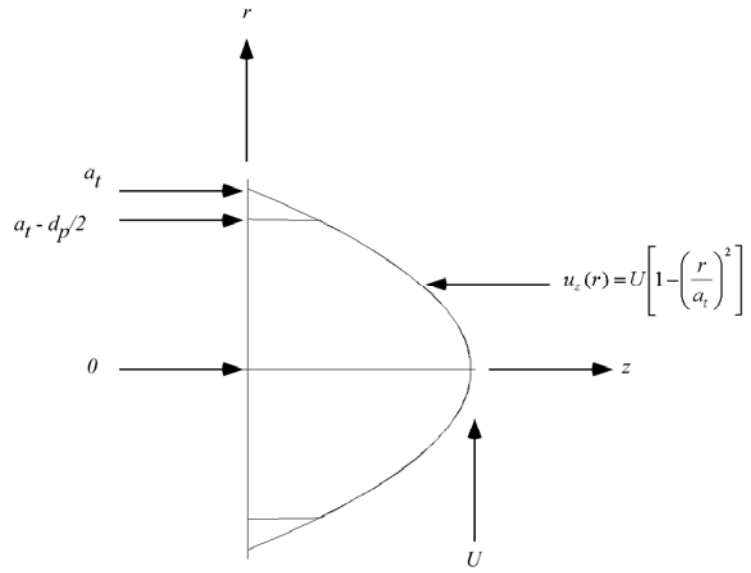

Figure 8.41: Desired Profile Beside the Profile from Eq. 7.22

The justification of using the velocity profile suggested by Fig. 8.41 relies heavily on the idea that the fluid velocity profile through the breach would be the same regardless of whether the particles were present or not. As the particles get larger however, this becomes less and less true. In fact drafts and eddies will form around the larger particles, causing local turbulence that can affect the entire flow velocity distribution. The velocity profile suggested in Fig. 8.41 is also based on the assumption, as previously stated, that the particle convective motion is solely determined by the fluid convective motion. As the particles get larger, this too comes in to doubt. It has been well known for some time that aerosol particle motion is heavily influenced by objects located in close proximity to the particle. When these proximal objects are much larger than the particles and the carrier fluid flow is along the objects surface, the object appears to be a wall. Thus, the influence of the object's presence on the convective motion of a suspended particle is often referred to as the "wall effect". This effect is a function of the shape of the object and the proximity of the object to the suspended particle. The presence of the wall tends to increase the resistance to the forward motion of the particle by the factor $1+b\frac{d_p}{2x}$ where x is the distance from the center of the particle to the wall surface and b is a coefficient that depends on the proximal object. This factor is relevant for the case where $\frac{d_p}{2x} > 0.1$. The value of b has been determined to be 2.1 for a particle moving along the axis of an infinitely long cylinder [8.3]. For a particle with a diameter equal to or larger than 0.5 μm and a breach with a diameter equal to 10 μm, the ratio $\frac{d_p}{2x}$ is always greater than 0.1. This provides insight into how prevalent this effect is for some

of the cases that have been discussed in this thesis. For the larger of the particle sizes and the smaller of the breach sizes considered thus far in this work, and for the particle concentrations considered, it is also likely that the presence of other particles will influence the motion of particles within close proximity due to collisions or fluid flow disruption. Particle-particle interaction, particle disruption of flow, and the wall effect are beyond the current scope of the programs used to generate results in this thesis. These phenomena can ultimately be implemented in the current programs, but the time and computational expense make implementing the effects of these phenomena in the programs topics of future work. As far as relative difficulty, the addition of wall effects to the program is relatively easy and computationally inexpensive, while addressing particle disruption of flow and particle-particle interactions are much more difficult and computationally time consuming.

The third issue is the determination of the starting position of a test particle. Since mathematically, a particle can no longer be assigned a radial position between (a_t – d_p/2) and a_t, the test particle initial position can no longer be assigned by Eq. 8.16. Instead, a new generating equation must be created as

$$P = \frac{\int_0^{\tilde{r}} 2U_{av}\left(1-\frac{r^2}{a_t^2}\right)2\pi r\,dr}{\int_0^{a_t-\frac{d_p}{2}} 2U_{av}\left(1-\frac{r^2}{a_t^2}\right)2\pi r\,dr} = \frac{2a_t^2\tilde{r}^2-\tilde{r}^4}{2a_t^2\left(a_t-\frac{d_p}{2}\right)^2-\left(a_t-\frac{d_p}{2}\right)^4} \tag{8.17}$$

which results in the initial position generating function

$$\tilde{r} = a_t \sqrt{1 - \sqrt{1 - \Omega P}} \tag{8.18}$$

where

$$\Omega = \frac{\left(a_t - \frac{d_p}{2}\right)^2 \left(2a_t^2 - \left(a_t - \frac{d_p}{2}\right)^2\right)}{a_t^4} \tag{8.19}$$

Adjusting the program used to generate the deposition results presented in this chapter so far by substituting Eq. 8.18 and 8.19 for Eq. 8.16 and replacing the impact parameter a_t by ($a_t - d_p/2$), the limited effects of particle size described above can be modeled. The case that has the greatest probability of demonstrating the effects of particle size is the case in which the ratio of particle size to breach radius is large and the transmission ratio has a value in which deviations from the standard result can be observed. An excellent case for study suggested from Table 7.1 is the case of 500 nm particles suspended in helium flowing through a breach with a 5 μm radius. In this case, the transmission ratio is 0.689 and additional terms in the expansion do not change this value. Increased deposition due to particle size, if present, should be observable in this case. A simulation of 10000 particles was run using 0.1 μs time steps for the program that takes particle size into consideration. The mean transmission fraction was 0.6598 with a relative error of 0.0079. This result implies that the particle radius effect is

observable. However, even in cases in which the conditions are ideal to observe this phenomenon, its effect although observable, is not that substantial.

Another issue that was promised in the last chapter to be resolved with the Monte Carlo program in this chapter is accounting for axial diffusion. Adjusting the program to account for axial diffusion is very simple. The diffusion step in three dimensions is taken according to Eq. 8.11. This step is used with the realization that $r = \sqrt{x^2 + y^2 + z^2}$ and this fact can be used along with Eq. 8.13 to separate the diffusion steps in each of the spatial dimensions through the relation

$$\begin{aligned} n(r,t) &= \frac{1}{(4\pi Dt)^{3/2}} e^{\frac{-(r-r_0)^2}{4Dt}} = \frac{1}{\left((4\pi Dt)^{1/2}\right)^3} e^{\frac{-(x-x_0)^2-(y-y_0)^2-(z-z_0)^2}{4Dt}} \\ &= \left(\frac{1}{(4\pi Dt)^{1/2}} e^{\frac{-(x-x_0)^2}{4Dt}} \right) \left(\frac{1}{(4\pi Dt)^{1/2}} e^{\frac{-(y-y_0)^2}{4Dt}} \right) \left(\frac{1}{(4\pi Dt)^{1/2}} e^{\frac{-(z-z_0)^2}{4Dt}} \right) \end{aligned} \tag{8.20}$$

Thus, the diffusion steps in each direction can be selected from a one-dimensional Gaussian distribution. The only adjustment to the Monte Carlo program then, is that after the convective step for each time step, a diffusive step in the axial direction is added to the diffusive steps in the two spatial directions of the plane perpendicular to axial flow. The only case in Tables 7.1 through 7.8 for which the Péclet number suggests axial diffusion might have an effect is the case of 1 nm particles suspended in helium flowing through a breach with a radius of 5 μm. Unfortunately, the transmission fraction for this case is zero. Although the conditions do no indicate that axial diffusion should be

observable, the case of 100 nm particles suspended in helium flowing through a breach with a radius of 5 μm was simulated, accounting for axial diffusion. For a simulation of 10,000 particles, the transmission fraction was determined from the Monte Carlo program to be 0.0152 with a relative error of 0.0820. The relative error is so high because the mean number being determined is so low. The resulting transmission fraction is close to the value of 0.014 returned from Eq. 7.10. In order to get better values for comparisons, a situation where the Péclet number is less than 1 and the transmission fraction is reasonable can be devised. Although this simulation is not completed here, the methodology developed so far in this chapter can be used to accomplish it.

8.5 EXPANSION OF THE MONTE CARLO METHOD TO A CURVED TUBE

Another drawback to the model presented in chapter six was that it was confined to a right cylindrical flow pathway of constant circular cross-section. Effectively, the model could be used for any pathway for which a constant axial velocity profile could be provided. The Monte Carlo Program is limited in a similar fashion. The flow profile must be provided as a function of radial and axial position in order to determine the convective step for a particle. This flow profile can be generated with a computational fluid dynamics code such as FLUENT. Some work has been done however, toward determining velocity profiles that deviate only slightly from the Poiseuille velocity profile through the use of perturbation methods. For curves bent in a torroidal shape, the dimensionless numbers that describe the flow are the Reynolds number, the curvature

ratio, and the Dean number. The Reynolds number is still defined by Eq. 7.1, and the curvature ratio and Dean number are defined respectively as

$$R_0 = \frac{R_b}{a_t} \tag{8.21}$$

$$De = \frac{\mathrm{Re}}{\sqrt{R_0}} \tag{8.22}$$

The spatial dimensions a_t, the tube radius, and R_b, the radius of curvature of the tube displayed in Fig. 8.42.

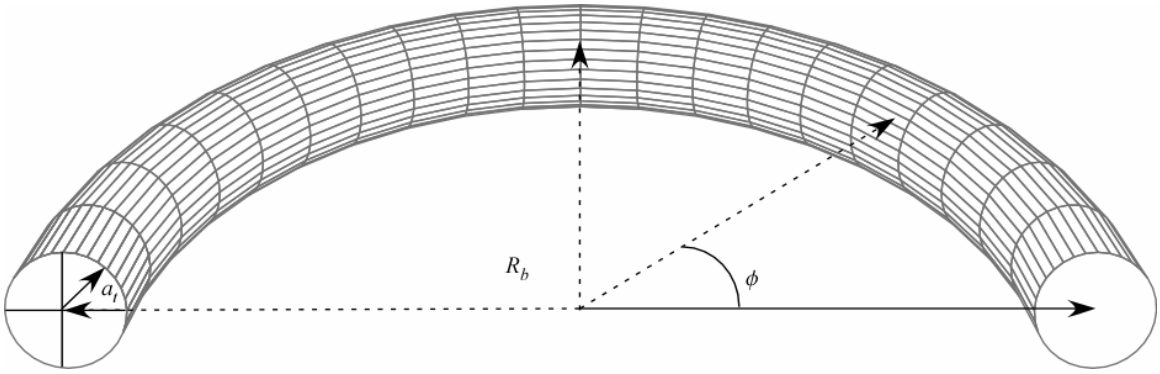

Figure 8.42: Parameters Associated with Torroidal Tube Geometry

The equation describing the torroid that appears in Fig. 8.42, using the same parameters, is

$$\gamma(R_b, \phi) = \{R_b Cos(\phi), R_b Sin(\phi), 0\} \tag{8.23}$$

The radius of curvature R_b, and angle ϕ that appear in Fig. 8.42 effectively determine the arc-length of the tube. This can be seen by application of Eq. 6.39. If it is desired that the central curve of the tube have a length of 1 cm in order to allow direct comparison with the simulations involving straight tubes, then according to Eq. 6.39,

$$0.01 = \int_0^{\hat{\phi}} \sqrt{\gamma'(R_b,\phi).\gamma'(R_b,\phi)}\,d\phi = \int_0^{\hat{\phi}} \sqrt{R_b^2(Cos^2(\phi)+Sin^2(\phi)}\,d\phi = R_b\hat{\phi} \tag{8.24}$$

Thus, for a defined radius of curvature, the value of the angle ϕ that generates a central curve of the desired length can be determine. In the Monte Carlo program for modeling flow through straight tubes that was just described, the axial position of a particle in the tube was tracked with the parameter "s" that was used to generate the parametric equation of the "curve". In Eq. 8.24 above however, the parameter used to create the parametric equation of the torroid is ϕ. Using Eq. 6.39 as demonstrated above, it can be shown that the distance "s" traveled along the central curve is related to the radius of curvature R_b and to the central angle ϕ through the relationship

$$s = R_b\phi \tag{8.25}$$

The three-dimensional coordinates of any position within the torroid can thus be expressed in the form {s, x, y}, where "s" determines the axial distance along the central curve and "x" and "y" define the Cartesian coordinates of the circular cross section at the

axial position "s". Notice in Fig. 8.42 that if the "x" coordinate at any "s" position is not equal to zero, then the distance from that position to the central point from which the radius of curvature originates is not equal to R_b. Instead, this distance is "R_b + x", which means that the length of a curve parallel to the central curve and in the with a "y" position of zero with have a length equal to $(R_b + x)\,\phi$ instead of $R_b\,\phi$. This effect is more prominent for tubes with higher R_b/a_t ratios, which is why the parameter R_0 defined by Eq. 8.21 carries such importance. Notice as $R_b \rightarrow \infty$, the tube becomes straight and the effect of curvature diminishes. Also, as the radius of the tube decreases, the variation due to the "x" position becomes less important. Since the velocity profile defined in Eq. 7.2 is only for laminar flow through straight, cylindrical tubes, it should closely approximate the flow through circular tubes for which the value of R_0 is large. As this value becomes smaller, the deviations from the flow profile described by Eq. 7.2 will become more and more important. It is important to characterize the flow within a curved tube in order to estimate these effects.

It has been asserted that the critical value of the Reynolds number below which the flow can be characterized as laminar for flow through a curved tube can be determined with the relation

$$\mathrm{Re}_{cr} = 2 \times 10^4 \times R_0^{-0.32} \tag{8.26}$$

for the range $15 < R_0 < 860$. For values of R_0 larger than 860, Re_{cr} "practically coincides" with the critical Reynolds number for a straight pipe [8.4]. Tubes with R_0 values less than 15 have too high of a degree of bend for consideration in this paper.

Although the flow in a torroidal tube may be laminar, the velocity profile of the flow may significantly differ from that of a straight tube. As a fluid flows through a torroidal tube, the axial velocity profile becomes skewed toward the outside wall of the tube. In addition, a secondary flow develops in the tube. It has been noted that the intensity of the secondary flow is directly associated with the value of the Dean number [8.5]. This assertion has been explored in detail and the secondary flows associated with varying classes of Dean number have been studied [8.6]. Dean himself noted that for small values of the Dean number, the axial and secondary flows can be represented respectively as perturbations from the equations of flow in straight circular tubes with the equations [8.7, 8.8, 8.9]

$$u_z(r',\theta) = W_0 w = W_0 \sum_{n=0}^{\infty} \left(\frac{1}{576} De \right)^n w_n(r',\theta) \tag{8.27}$$

$$u_{r',\theta}(r',\theta) = \frac{\nu}{a_t r'} \psi = \frac{\nu}{a_t} \sum_{n=1}^{\infty} \left(\frac{1}{576} De \right)^n \psi_n(r',\theta) \tag{8.28}$$

where r' is the ratio r / a_t, θ is the angle relative to the plane of symmetry, and W_0 is the peak axial velocity defined as U in Eq. 7.2. These parameters are displayed in Fig. 8.43 which also displays the transverse velocities in the same configuration and notation as that used by Dean [8.8, 8.9]. The velocity component U is oriented in the direction of the radial vector r and V is oriented perpendicular to U as shown. The velocity component W is perpendicular to both U and V and thus point in the direction of axial flow.

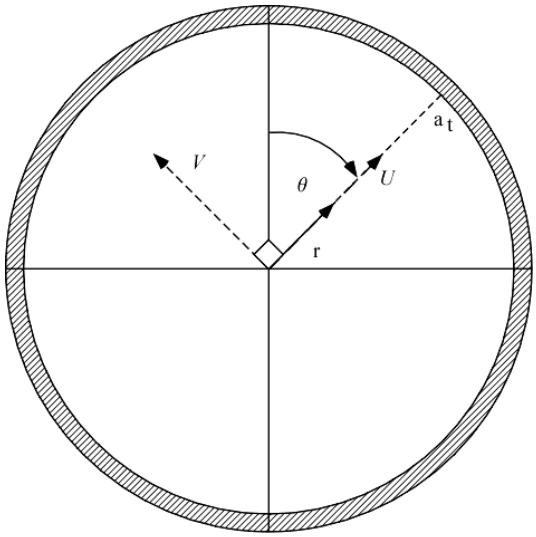

Figure 8.43: Velocity Components Associated with Flow in a Torroidal Tube

It should be noted that $n = 0$ in Eqs. 8.27 and 8.28 corresponds to Poiseuille flow defined by Eq. 7.2. Explicitly, the terms corresponding to the subscript "1" in the expansions of Eqs. 8.27 and 8.28 can be written in the form [8.9]

$$w_1 = \left(4r' - 9r'^3 + 6r'^5 - r'^7\right)\cos(\theta) \tag{8.29}$$

$$\psi_1 = \left(\frac{19}{40}r' - r'^3 + \frac{3}{4}r'^5 - \frac{1}{4}r'^7 + \frac{1}{40}r'^9\right)\sin(\theta) \tag{8.30}$$

In this work, the focus is on systems for which the Dean number is very small. Thus, the deviation of the flow from the Poiseuille flow described by Eqs. 8.29 and 8.30 should be minimal. In addition, the remaining terms in the expansions of Eqs. 8.27 and 8.28 for which $n > 1$, can be neglected. Although Eqs. 8.27 through 8.30 quantify the perturbations from Poiseuille flow, in the form presented above, they do not explicitly define flow direction. In order to obtain this information, it is necessary to quickly

review the method that Dean used to determine these equations. He started his analysis from the continuity equation, which he wrote as [8.8]

$$\frac{\partial U}{\partial r}+\frac{U}{r}+\frac{U\sin(\theta)}{a_t+r\sin(\theta)}+\frac{1}{r}\frac{\partial V}{\partial \theta}+\frac{V\cos(\theta)}{R+r\sin(\theta)}=0 \tag{8.31}$$

In the limit that a_t/R_b is very small, this equation is simplified to

$$\frac{\partial U}{\partial r}+\frac{U}{r}+\frac{1}{r}\frac{\partial V}{\partial \theta}=0 \tag{8.32}$$

Since the derivative terms in Eq. 8.32 are taken with respect to different variables, in order for the equation to be solved, it must be true that

$$U=-\frac{1}{r}\frac{\partial f(r,\theta)}{\partial \theta} \tag{8.33}$$

and

$$V=\frac{\partial f(r,\theta)}{\partial r} \tag{8.34}$$

In the process of solving these equations, he used the following relationships to put the equations in a non-dimensional form

$$f=\nu\psi \tag{8.35}$$

$$W = W_0 w \tag{8.36}$$

$$r = a_t r' \tag{8.37}$$

where ν is the kinematic viscosity. These relationships are what lead to the coefficient terms in Eqs. 8.27 and 8.28. Thus, the equations for the velocity for any point in the tubes considered in this paper can be determined from Eqs. 8.27 through 8.37 to be

$$W(r',\theta) = W_0\left[1 - r'^2 + \frac{De}{576}\left(\frac{19}{40}r' - r'^3 + \frac{3}{4}r'^5 - \frac{1}{4}r'^7 + \frac{1}{40}r'^9\right)\sin(\theta)\right] \tag{8.38}$$

$$U(r',\theta) = \frac{\nu}{a_t r'}\left[\frac{De}{576}\left(4r' - 9r'^3 + 6r'^5 - r'^7\right)\sin(\theta)\right] \tag{8.39}$$

$$V(r',\theta) = \frac{\nu}{a_t}\left[\frac{De}{576}\left(4 - 27r'^2 + 30r'^4 - 7r'^6\right)\cos(\theta)\right] \tag{8.40}$$

Notice that the velocity components are functions of the radial and angular position, but are independent of the axial position along the tube. This is a result of Dean making the simplifying assumption that the change in velocity with respect to axial position is negligible. It is now possible to use Eq. 8.38 through Eq. 8.40 to the extent to which the Poiseuille flow is perturbed for a given system.

These equations were used to construct a Monte Carlo program that operates in the same fashion as the program for straight tubes described earlier in this chapter. The only differences between the two programs where the equation defining the central curve, the equation determining the velocity profile, and the method of determining whether or not a test particle has left the tube. The transmission fractions for torroidal tubes of various curvature ratios calculated with the Monte Carlo program, are listed in Table 8.7. For each of the cases simulated to generate the results in Table 8.7, the tube radius was 5 μm, the particle diameter was 0.5 μm, the suspending gas was helium, and there were 10,000 test particles.

Table 8.7: Transmission Fraction as a Function of Curvature Ratio

R_0	P	Rel. Error	De
200000	0.6920	0.0057	0.0002
20000	0.6815	0.0065	0.0005
2000	0.6314	0.0076	0.0016
200	0.5400	0.0105	0.0052
20	0.3652	0.0118	0.0163

Table 8.7 demonstrates the predicted transmission fractions for the limits of applicability of the Monte Carlo Program. The curvature ratio of 200,000 simulates a straight tube for which the transmission fraction determined from Eq. 7.10 is 0.689. According to Eq. 8.26, the critical Reynolds number for torroidal tubes is only good for curvature ratios greater than 15, so a curvature ratio of 20 is pushing that limit. Table 8.7 also lists the value of the Dean number corresponding to each simulated system. The correlation of higher Dean number for lower curvature ratio is very apparent. The trend seems straight forward except that it is expected that the transmission fraction for a tube with a curvature ratio of 20 should be lower than the transmission fraction for a tube with

a curvature ratio of 200. It is a possibility that the assumption that the Dean number is small enough to neglect terms of order greater than 1 in Eqs. 8.38 through 8.40 is not valid for tubes with curvature ratios as low as 20. In order to gain more insight into this phenomenon, the deposition patterns for the tubes of various curvature ratios were analyzed. Figure 8.44 shows the axial deposition pattern for the various cases. In each case, the tube was divided axially into ten rings. Figures 8.45 through 8.54 show the circumferential deposition patterns in quadrants for each of these ten axial rings.

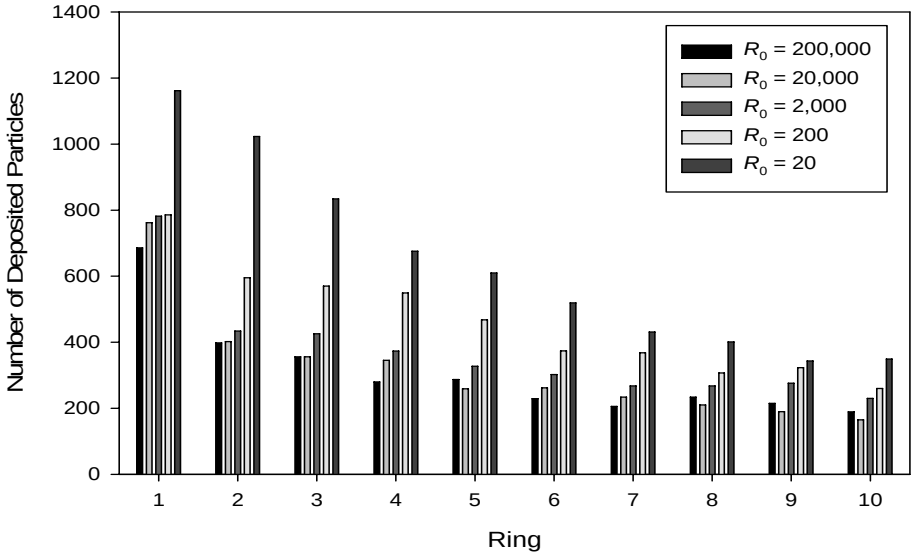

Figure 8.44: Axial Deposition Patterns for Curved Tubes

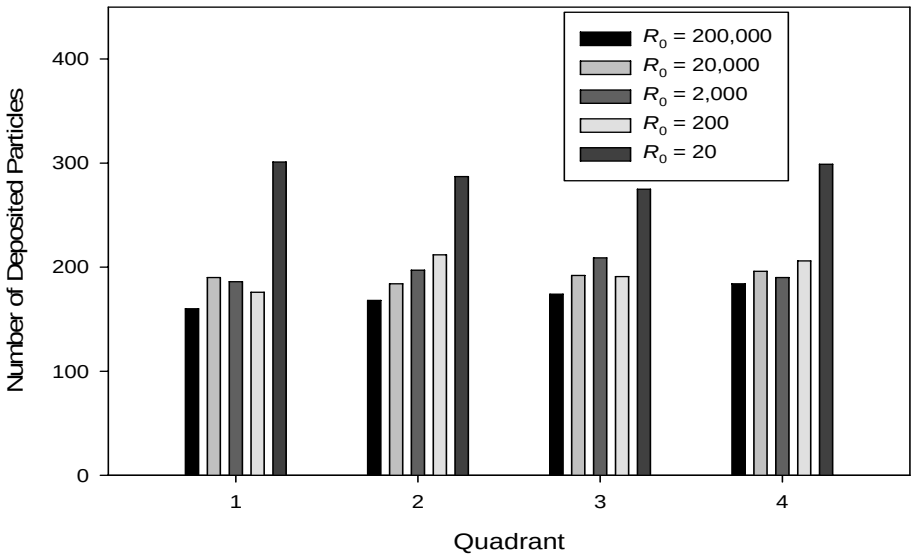

Figure 8.45: Circumferential Deposition Patterns for the First mm of Curved Tubes

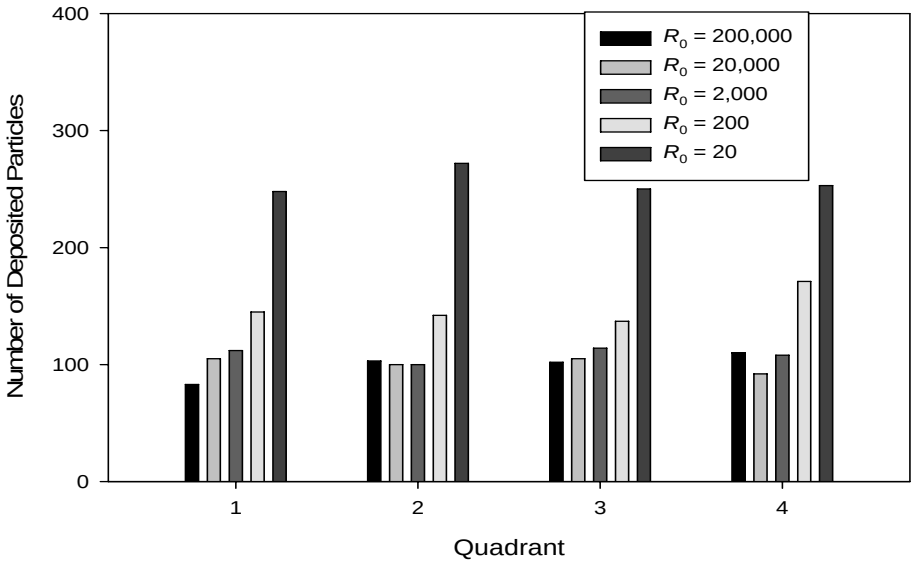

Figure 8.46: Circumferential Deposition Patterns for the Second mm of Curved Tubes

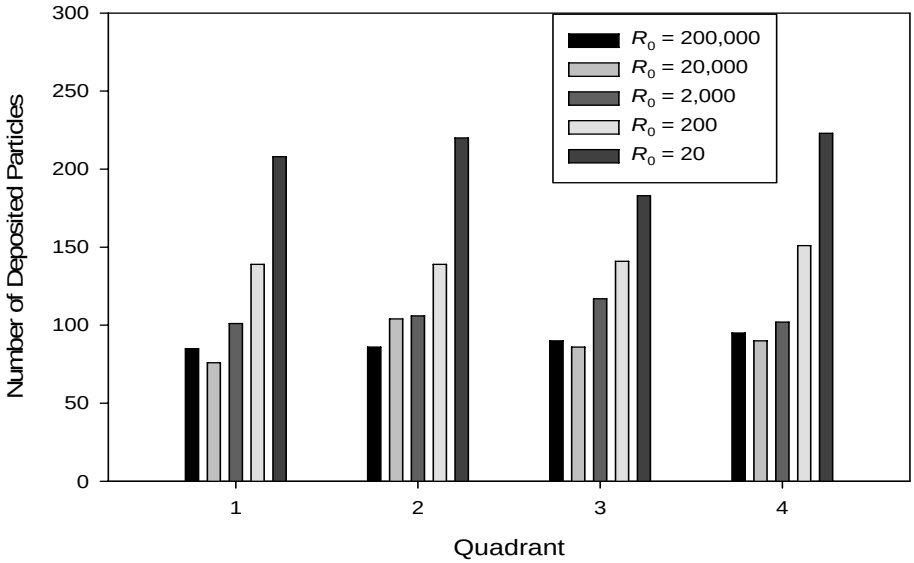

Figure 8.47: Circumferential Deposition Patterns for the Third mm of Curved Tubes

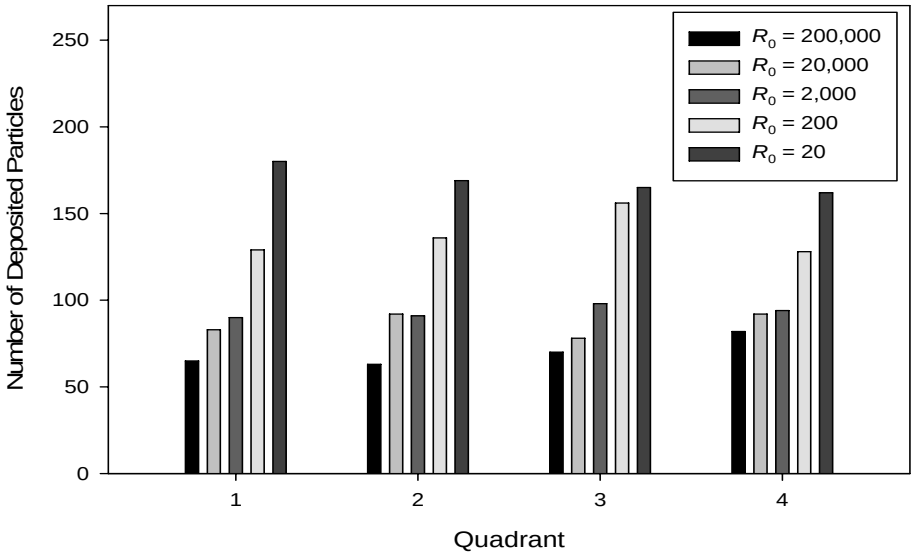

Figure 8.48: Circumferential Deposition Patterns for the Fourth mm of Curved Tubes

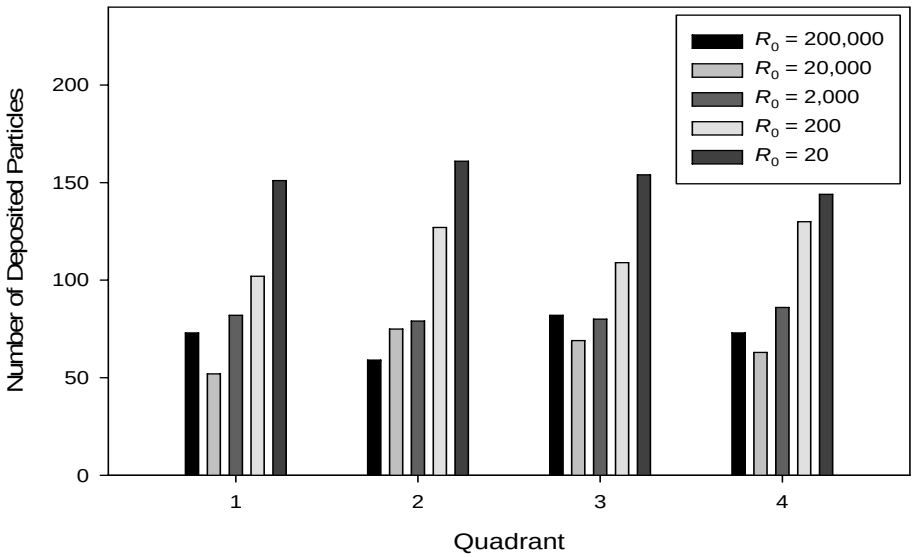

Figure 8.49: Circumferential Deposition Patterns for the Fifth mm of Curved Tubes

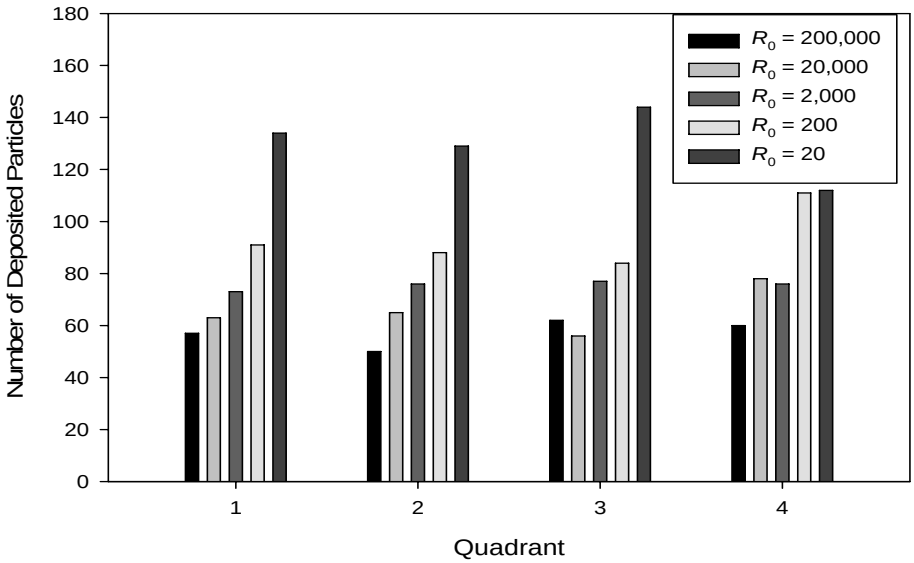

Figure 8.50: Circumferential Deposition Patterns for the Sixth mm of Curved Tubes

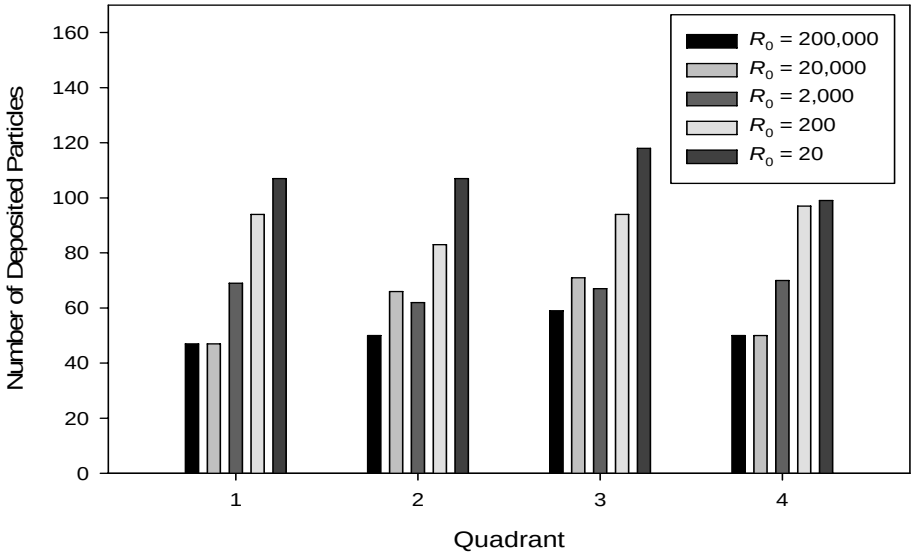

Figure 8.51: Circumferential Deposition Patterns for the Seventh mm of Curved Tubes

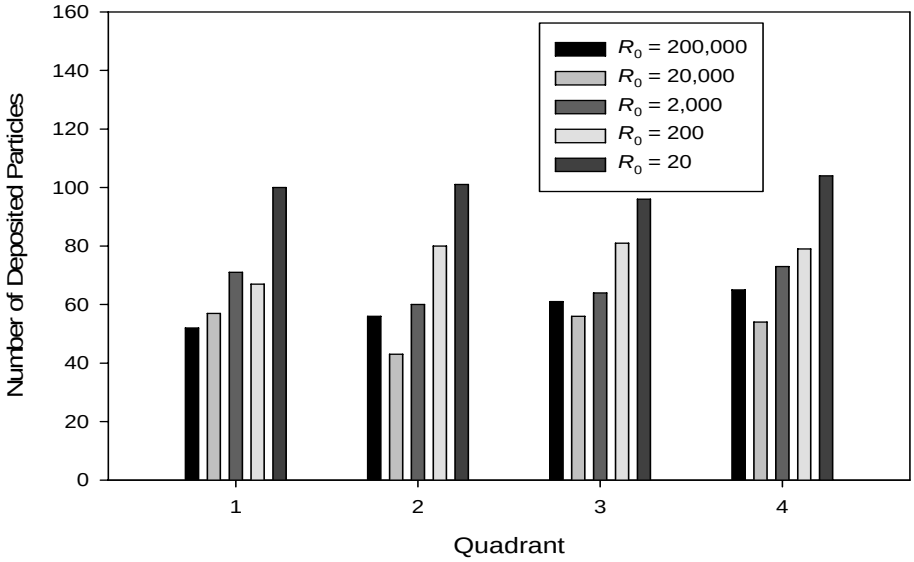

Figure 8.52: Circumferential Deposition Patterns for the Eighth mm of Curved Tubes

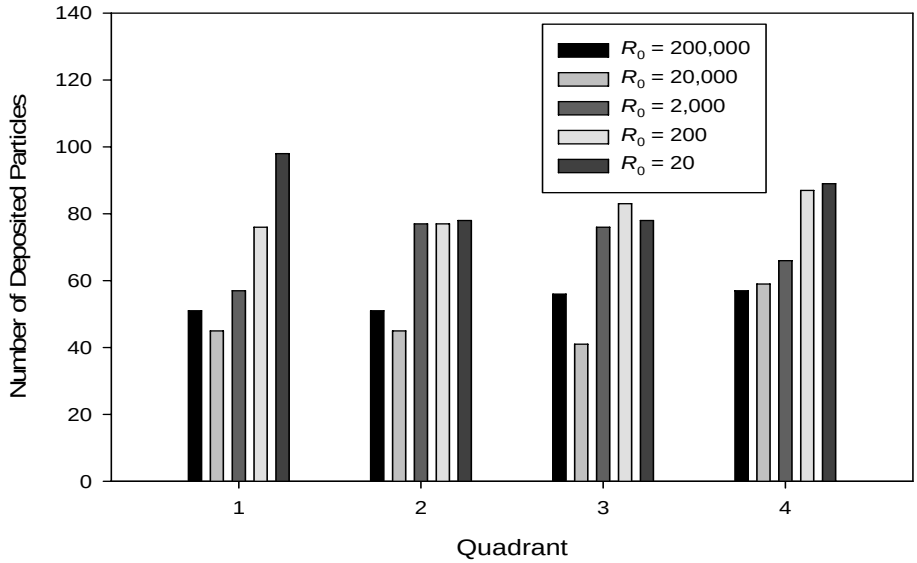

Figure 8.53: Circumferential Deposition Patterns for the Ninth mm of Curved Tubes

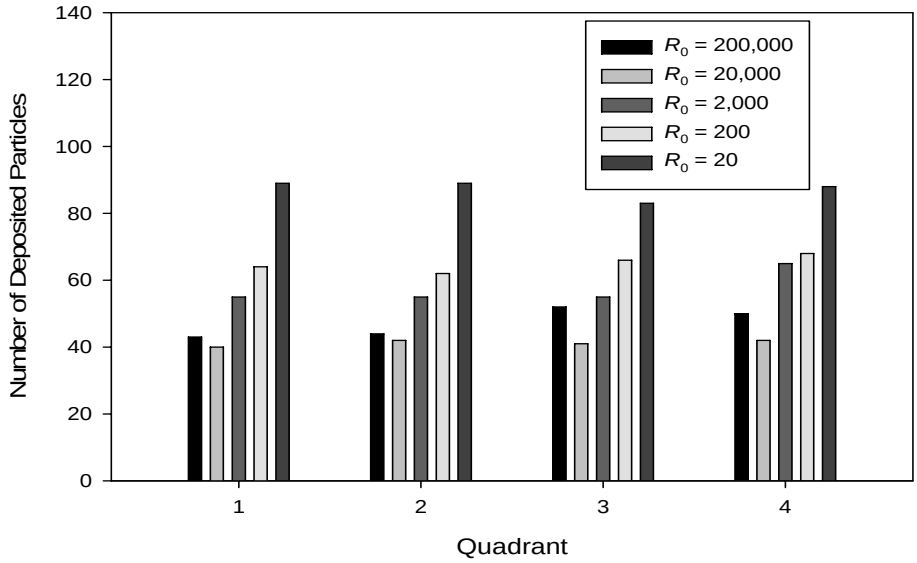

Figure 8.54: Circumferential Deposition Patterns for the Last mm of Curved Tubes

Figures 8.44 through 8.54 show that the axial deposition pattern for curved tubes seems to be nearly the same as the pattern for straight tubes. The only distinct trend that

can be gathered from Fig. 8.44 through 8.54 is: the smaller the curvature ratio, the lower the transmission fraction. There does not seem to be a consistent circumferential deposition bias for any given curvature ratio or axial position. Care should be taken from this result however, due to the fact that for tubes with small curvature ratios, the surface area of the outer wall is larger than the surface area of the inner wall. This means that there should be a circumferential deposition bias toward quadrants I and IV for each axial ring. This bias should be more apparent for tubes with smaller curvature ratios. The lack of a deposition bias toward quadrants I and IV actually implies a possible deposition bias toward quadrants II and III of the inner wall. Further investigation into this phenomenon in pending.

8.6 CONCLUSIONS

In this chapter, a method of expanding the model of aerosol flows through a small breach was presented. Although only convective and diffusive motions were considered in this chapter, more mechanisms of particle motion could be inserted into the model. The advancements developed in this chapter allow for the tracking of three dimensional particle deposition patterns along the interior of a breach. This ability was not available in the model constructed in Chapter 7. The model in this chapter also allows for consideration of the effects of axial and angular diffusion, as well as particle size effects. A procedure for expanding the modeling of particle convective motion in straight tubes to convective motion in torroidal tubes was also presented. This procedure can be used as a guide to determining convective motion through differently shaped tubes as well.

Ultimately, the model constructed in this chapter can be expanded to consider as many mechanisms of particle motion as is desired. The results presented here explore only a part of the parametric space that can be studied with the model.

REFERENCES

8.1 Williams, M.M.R., Loyalka, S.K., Aerosol Science, Pergamon Press, New York (1991).

8.2 Chandrasekhar, S., *Reviews of Modern Physics*, 15 (1943) p. 1-89.

8.3 Fuchs, N.A., The Mechanics of Aerosols, Pergamon Press, New York (1964) p. 23-24, 1964.

8.4 Ito, H., "Friction Factors for Turbulent Flow in Curved Pipes," *Journal of Basic Engineering*, 81 (1959) p. 123-129.

8.5 Humphrey, J.A.C., Iacovides, H., Launder, B.E., "Some Numerical Experiments on Developing Laminar Flow in Circular-Sectioned Bends," *Journal of Fluid Mechanics*, 154 (1985) 357-375.

8.6 Berger, S.A., Talbot, L., Yao, L., "Flow in Curved Pipes," *Annual Review of Fluid Mechanics*, 15 (1983) p. 461-512.

8.7 Dean, W. R., "Note on the Motion of Fluid in a Curved Pipe," *Philosophical Magazine and Journal of Science*, 20 (1927) p. 208-223.

8.8 Dean, W.R., "The Stream-Line Motion of Fluid in a Curved Pipe," *Philosophical Magazine and Journal of Science*, 30 (1928) p. 673-693.

8.9 Van Dyke, M., "Extended Stokes series: laminar flow through a loosely coiled pipe," *Journal of Fluid Mechanics*, 86 (1978) p. 129-145.

CHAPTER 9: CONCLUSION AND FUTURE WORK

In this thesis, a range of gaseous and aerosol flow phenomena have been explored in conjunction with applicability to dry storage containers. In the process of constructing the models presented in this thesis, a great deal of effort was expended in pursuing different pathways. The thesis presents the fundamental findings from the constructed models in a concise way. This chapter presents some suggestions for future work for expanding the applicability of the models presented in this thesis.

The first suggestion for advancement is a thorough characterization of the thermal conditions within the spent fuel canister. The results of Chapters 3 and 4 underscore the importance of this information. As was suggested in Chapter 3, the use of a computational fluid dynamics code such as FLUENT® might be useful in this endeavor. In addition to determining the temperature of the fill gas in the canister, it would be helpful to determine whether or not convective currents develop within the canister. These two pieces of information would be particularly helpful in determining depressurization and particle suspension times.

After determining the thermal and convective conditions, the next area for improvement is the consideration of the release of fission gases and helium from breached fuel rods on canister depressurization times. The gas build-up and release discussed in Chapters 5 and 6 can be used to estimate the quantity of gas available for release from individual fuel rods. This can be combined with data from studies regarding clad rupture and unzipping [9.1 - 9.5] under any conditions of interest to determine a total

quantity of gas release to the free volume of the canister. Modeling of the effects of the addition of this gas on the canister depressurization time could provide interesting results.

Many improvements can be made to the free molecular flow model presented in Chapter 6. The most direct is to improve the statistics associated with the results by increasing the number of test particles in each simulation. This will require a significant amount of computational power and time. The model can also be extended to additional geometries. The post-collision velocity distributions can be varied as a function of position on the breach wall. The most direct case of such a variation is a temperature dependence on the axial position along the tube. Introducing intermolecular collisions into the model would provide an advancement in the applicability of the program.

For the model of plugging and particulate release presented in Chapter 7, the most direct progression would be to run an array of simulations with various particle concentrations, particle sizes, settling times, and breach radii. A time-dependent suspended particle concentration could be introduced into the continuous plugging model. However, the function describing the time-dependent particle concentration can be complex, depending on the number of parameters considered. However, a simpler function can be constructed using only the gravitational settling equation discussed in Chapter 5. This function can be expanded to model polydisperse particle suspensions instead of the monodisperse suspensions considered in this thesis. The settling times for these suspensions can be adjusted to account for non-spherical particle shapes. In addition, a dynamic polydisperse suspension can be modeled by adding the effects of agglomeration. Direct Simulation Monte Carlo models have recently been created to describe this phenomenon [9.6, 9.7].

The effects of charges generated by radioactive decay could be another point of interest. Charging and thermal effects can be considered in the flow through the breach in addition to the effects of these phenomena within the canister. The behavior of the particles after escaping the canister may also be of interest. The plugging and depressurization models of Chapter 7 are limited in that they only consider the uniform axial and circumferential deposition of aerosol particles. This limitation stems from the necessity to have a velocity profile of the carrier gas. One possible way to retain the structure of the Chapter 7 model, but expand its geometrical accuracy is to use a more accurate axial deposition pattern. According to Eq. 7.10, the deposition pattern should be approximately exponential. This could be estimated by assuming a conical deposition pattern and using perturbation methods to alter the Poiseuille flow equation in order to describe the flow through the cone [9.8 – 9.12]. Such perturbation methods used by Dean were discussed to determine the velocity profile in slightly bent tubes in Chapter 8. A parabolic deposition pattern would be more accurate than the conical deposition pattern. The velocity profile for the parabolic tube would then have to be developed [9.13].

The velocity profiles discussed for use in the continuous plugging model could also be used in the Monte Carlo program. There are several concepts associated with fluid flow through curved tubes that could be incorporated into the existing Monte Carlo model [9.14-9.26]. Of particular interest in expanding the Monte Carlo program is to move from torroidal tubes to helical tubes. This advancement involves a considering many complicated aspects of fluid flow that can be neglected in flow through straight or torroidal tubes [9.27 – 9.34]. The additional consideration of particle motion phenomena and particle-particle interactions as well as interacting particle-fluid two-phase flows is

another area of interest. [9.35 – 9.65] The addition of realistic particle two-phase flow including inertial particle effects would allow for the direct comparison of computational results with experimental results.

The models developed in their current state allow for simulation of aerosol release through breaches in spent fuel containers. The model predicts depressurization time, plugging, temperature, pressure, fill gas loss, and flow velocity while allowing for multiple parameters such as breach length, breach radius, particle size, initial physical conditions within the canister, and rate of heat deposition within the fill gas to be varied. Although much research has been performed, the additions to this work discussed in this chapter would also provide valuable insight into the behavior of spent fuel canisters that have developed small through-wall breaches.

REFERENCES

9.1 CRWMS M&O, "Initial Cladding Condition," DN2002143802, MOL.20000523.0150 (2000).

9.2. Rothman, A.J., "Potential Corrosion and Degradation Mechanisms of Zircaloy Cladding on Spent Nuclear Fuel in a Tuff Repository," UCID-20172, Livermore, California: Lawrence Livermore National Laboratory, ACC: NNA.19870903.0039 (1984).

9.2 Manaktala, H.K., "Characteristics of Spent Nuclear Fuel and Cladding Relevant to High-Level Waste Source Term," CNWRA 93-006, NRC-02-88-005, San Antonio, Texas: Center for Nuclear Waste Regulatory Analyses, TIC: 208034 (1993).

9.3 Johnson, A.B., Jr., Gilbert, E.R., "Technical Basis for Storage of Zircaloy-Clay Spent Fuel in Inert Gases," PNL-4835, Richland, Washington: Pacific Northwest Laboratory, TIC: 9151 (1983).

9.4 Einziger, R. E., Tsai, H., Billone, M.C., Hilton, B.A., "Examination of Spent Pressurized Water Reactor Fuel Rods after 15 Years in Dry Storage," *Nuclear Technology*, 144 (2003) p. 186 – 200.

9.5 Palaniswaamy, G., Loyalka, S.K., "Direct Simulation Monte Carlo Aerosol Dynamics: Coagulation and Collisional Sampling," *Nuclear Technology*, 156 (2006) p. 29-38.

9.6 Palaniswaamy, G., Loyalka, S.K., "Direct Simulation Monte Carlo Aerosol Dynamics: Collisional Sampling Algorithms," *Annals of Nuclear Energy*, 34 (2007) p. 13-21.

9.7 Hemmy, A.S., "The Flow of Viscous Liquids through Slightly Conical Tubes," *Proceedings of the Physical Society of London*, 34 (1921) p. 22-26.

9.8 Bond, W.N., "Viscous Flow through Wide-Angled Cones," *Philosophy Magazine*, 6 (1925) p. 1058-1066.

9.9 Bond, W.N., "Theory of Liquid Flow through Cones," *Proceedings of the Physical Society of London*, 40 (1927) p. 1-6.

9.10 Dryden, H. et al., Hydrodynamics, Dover (1956) p. 469-470.

9.11 Vatistas, G.H., Ghaly, W.S., "Converging and Diverging Flow in Narrow Conical Passages," *Acta Mechanica*, 136 (1999) p. 209-222.

9.12 Betyaev, S.K., "Conical and Quasi-Conical Incompressible Fluid Flows," *Fluid Dynamics*, 38 (2003) p. 581-591.

9.13 Hawthorne, W.R., "Secondary Circulation in Fluid Flow," *Proceedings of the Royal Society of London, Series A, Mathematical and Physical Sciences*, 206 (1951) p. 374- 387.

9.14 Hanks, R.W., "Velocity Profile Development in the Entrance Region of a Right Circular Cylinder with Slip at the Walls," *The Physics of Fluids*, 6 (1963) p. 1645-1648.

9.15 Greenspan, D., "Secondary Flow in a Curved Tube," *Journal of Fluid Mechanics*, 57 (1973) p. 167-176.

9.16 Murata, S., Miyake, Y., and Inaba T., "Laminar Flow in a Curved Pipe with Varying Curvature," *Journal of Fluid Mechanics*, 73 (1976) p. 735-752.

9.17 Smith, F.T., "Steady Motion within a Curved Pipe," *Proceedings of the Royal Society of London, Series A, Mathematical and Physical Sciences*, 347 (1976) p. 345-370.

9.18 Mohanty, A.K., Asthana, S.B.L., "Laminar Flow in the Entrance Region of a Smooth Pipe," *Journal of Fluid Mechanics*, 90 (1978) p. 433-447.

9.19 Soh, W.Y., Berger, S.A., "Laminar Entrance Flow in a Curved Pipe," *Journal of Fluid Mechanics*, 148 (1984) p. 109-135.

9.20 Humphrey, J.A.C., Iacovides, H., Launder, B.E., "Some Numerical Experiments on the Developing Laminar Flow in Circular-sectioned Bends," *Journal of Fluid Mechanics*, 154 (1985) p. 357-375.

9.21 Dombrowski, N., Foumeny, E.A., Ookawara, S., Riza, A., "The Influence of Reynolds Number on the Entry Length and Pressure Drop for Laminar Pipe Flow," *The Canadian Journal of Chemical Engineering*, 71 (1993) p. 472-476.

9.22 Šašić, R., Šašić, S., "A New Approach to the Velocity Field Investigation in Case of the Entry Flow in Curved Pipes with Circular Cross Section," *Acta Mechanica*, 140 (2000) p. 103-117.

9.23 Guan, X., Martonen, T.B., "Flow Transition in Bends and Applications to Airways," *Journal of Aerosol Science*, 31 (2000) p. 833-847.

9.24 Boiron, O., Deplano, V., Pelissier, R., "Experimental and Numerical Studies on the Starting Effect on the Secondary Flow in a Bend," *Journal of Fluid Mechanics*, 574 (2007) p. 109-129.

9.25 Akbarinia, A., Behzadmehr, A., "Numerical Study of Laminar Mixed Convection of a Nanofluid in Horizontal Curved Tubes," *Applied Thermal Engineering*, 27 (2007) p. 1327-1337.

9.26 Wang, C.Y., "On the Low-Reynolds-Number Flow in a Helical Pipe," *Journal of Fluid Mecanics*, 108 (1981) p. 185-294.

9.27 Germano, M., "On the Effect of Torsion on a Helical Pipe Flow," *Journal of Fluid Mechanics*, 125 (1982) p. 1-8.

9.28 Germano, M., "The Dean Equations Extended to a Helical Pipe Flow," *Journal of Fluid Mechanics*, 203 (1989) p. 289-305.

9.29 Yamamoto, K., Yanase, S., Yoshida, T., "Torsion Effect on the Flow in a Helical Pipe," *Fluid Dynamics Research*, 14 (1994) 259-273.

9.30 Zabielski, L., Mestel, A.J., "Steady Flow in a Helically Symmetric Pipe," *Journal of Fluid Mechanics*, 370 (1998) p. 297-320.

9.31 Yamamoto, K., Yanase, S., Yoshida, T., "Erratum Torsion Effect on the Flow in a Helical Pipe," *Fluid Dynamics Research*, 24 (1999) p. 309-311.

9.32 Gammack, D., Hydon, P.E., "Flow in Pipes with Non-Uniform Curvature and Torsion," *Journal of Fluid Mechanics*, 433 (2001) p. 357-382.

9.33 Yamamoto, K., Aribowo, A., Hayamizu, T., Hirose, T., Kawahara, K., "Visualization of the Flow in a Helical Pipe," *Fluid Dynamics Research*, 30 (2002) p. 251-267.

9.34 Davies, C.N., "Diffusion and Sedimentation of Aerosol Particles from Poiseuille Flow in Pipes," *Aerosol Science*, 4 (1973) p. 317-328.

9.35 Cheng, Y., Wang, C., "Inertial Deposition of Particles in a Bend," *Aerosol Science*, 6 (1975) p. 139-145.

9.36 Batchelor, G.K., "Brownian Diffusion of Particles with Hydrodynamic Interactions," *Journal of Fluid Mechanics*, 74 (1976) p. 1-29.

9.37 Crane, R.I., Evans, R.L., "Inertial Deposition of Particles in a Bent Pipe," *Journal of Aerosol Science*, 8 (1977) p. 161-170.

9.38 Sutter, S.L., Johnston, J.W., Owzarski, P.C., Mishima, J., Schwendiman, L.C., "Depleted Uranium Dioxide Powder Flow through Very Small Openings," Nuclear Technology, 52 (1981) p. 100-104.

9.39 Morewitz, H.A., "Leakage of Aerosols from Containment Buildings," *Health Physics*, 42 (1982) p. 195-207.

9.40 Ingham, D.B., "Diffusion of Aerosols from a Stream Flowing through a Short Cylindrical Pipe," *Journal of Aerosol Science*, 15/5 (1984) p. 637-641.

9.41 Aylor, D., Ferrandino, F.J., "Rebound of Pollen and Spores During Deposition on Cylinders by Inertial Impaction," *Atmospheric Environment*, 19/5 (1985) p. 803-806.

9.42 Pui, D.Y.H., Romay-Novas, F., Liu, B.Y.H., "Experimental Study of Particle Deposition in Bends of Circular Cross Section," *Aerosol Science and Technology*, 7 (1987) p. 301-315.

9.43 Tsai, C., Pui, D.Y.H., "Numerical Study of Particle Deposition in Bends of a Circular Cross-Section-Laminar Flow Regime," *Aerosol Science and Technology*, 12 (1990) p. 813-831.

9.44 Cohen, B.S., Asgharian, B., "Deposition of Ultrafine Particles in the Upper Airways: An Empirical Analysis," *Journal of Aerosol Science*, 21/6 (1990) p. 789-797.

9.45 Ingham, D.B., "Diffusion of Aerosols in the Entrance Region of a Smooth Cylindrical Pipe," *Journal of Aerosol Science*, 22/3 (1991) p. 253-257.

9.46 Stopford, P.J., Williams, M.G., "The Modeling of Aerosol Sampling by Fine Capillaries and Small Orifices," AEA Technology, AEA D&R 0158, TRDP(91)P15 (1992).

9.47 Williams, M.M.R., "Particle Deposition and Plugging in Tubes and Cracks (With Special Reference to Fission Product Retention)," *Progress in Nuclear Energy*, 28/1 (1994) p.1-60.

9.48 Williams, M.M.R., "Fission Product Retention in Narrow Leak Pathways, III. A Review of Aerosol Transport and Deposition through Conduits," A Report to the European Atomic Energy Community under Contract No. FI3S-CT92-0007 (1994).

9.49 Morton, D.A.V., Mitchell, J.P., "Aerosol Penetration through Capillaries and Leaks: Experimental Studies on the Influence of Pressure," *Journal of Aerosol Science*, 26/3 (1995) p. 353-367.

9.50 Clement, C.F., "Aerosol Penetration through Capillaries and Leaks: Theory," *Journal of Aerosol Science*, 26/3 (1995) p. 369-385.

9.51 Martonene, T., Zhang, Z., Yang, Y., "Particle Diffusion with Entrance Effects in a Smooth-Walled Cylinder," *Journal of Aerosol Science*, 27/1 (1996) p. 139-150.

9.52 Williams, M.M.R., "Numerical and Analytical Studies of Aerosol Particle Deposition around Complex Shapes," AEA Technology, AEAT-5471 Issue 1 (1998).

9.53 Williams, M.M.R., "The Transmission Efficiency of Aerosol Particles Passing through a Multi-Leg Crack Incorporating Bends and Constrictions," AEA Technology, AEAT-5470 Issue 1 (1999).

9.54 Wang, J., Flagan, R.C., Seinfeld, J.H., "Diffusional Losses in particle Sampling Systems Containing Bends and Elbows," *Journal of Aerosol Science*, 33 (2002) p. 843-857.

9.55 Sato, S., Chen, D., Pui, D.Y.H., "Particle Transport at Low Pressure: Deposition in Bends of a Circular Cross-Section," *Aerosol Science and Technology*, 37 (2003) p. 770-779.

9.56 Shi, H., Kleinstreuer, C., Zhang, Z., Kim, C.S., "Nanoparticle Transport and Deposition in Bifurcating Tubes with Different Inlet Conditions," *Physics of Fluids*, 16/7 (2004) p. 2199-2213.

9.57 Tyree, C.A., Allen, J.O., "Diffusional Particle Loss Upstream of Isokinetic Sampling Inlets," *Aerosol Science and Technology*, 38 (2004) p. 1019-1026.

9.58 Sharp, K.V., Adrain, R.J., "On Flow-Blocking Particle Structures in Microtubes," Microfluidics and Nanofluidics, 1 (2005) p. 376-380.

9.59 Tiwari, P., Antal, S.P., Podowski, M.Z., "Three-Dimensional Fluid Mechanics of Particulate Two-Phase Flows in U-Bend and Helical Conduits," Physics of Fluids, 18 (2006) Art. No. 043304.

9.60 Khalizov, A.F., Earle, M.E., Johnson, W.J.W., Stubley, G.D., Sloan, J.J., "Modeling of Flow Dynamics in Laminar Aerosol Flow Tubes," *Journal of Aerosol Science*, 37 (2006) p. 1174-1187.

9.61 Breuer, M., Baytekin, H.T., Matida, E.A., "Prediction of Aerosol Deposition in 90° bends using LES and an Efficient Lagrangian Tracking Method," *Journal of Aerosol Science*, 37 (2006) p. 1407-1428.

9.62 Yook, S., Pui, D.Y.H., "Experimental Study of Nanoparticle Penetration Efficiency through Coils of Circular Cross-Sections," *Aerosol Science and Technology*, 40 (2006) p. 456-462.

9.63 Poesio, P., Ooms, G., Cate, A.T., Hunt, J.C.R., "Interaction and Collisions Between Particles in a Linear Shear Flow Near a Wall at Low Reynolds Number," *Journal of Fluid Mechanics*, 555 (2006) p.113-130.

9.64 Marshall, J.S., "Particle Aggregation and Capture by Walls in a Particulate Aerosol Channel Flow," *Aerosol Science*, 38 (2007) p. 333-351.

9.65 Longest, P.W., Xi, J., "Effectiveness of Direct Lagrangian Tracking Models for Simulating Nanoparticle Deposition in the Upper Airways," *Aerosol Science and Technology*, 41 (2007) p. 380-397.

VITA

Andrew Casella was born on April 9, 1979 in Joplin, Missouri. After graduating from Webb City High School in 1997, he enrolled as an engineering student at the University of Missouri-Columbia where he obtained a B.S. in Chemical Engineering and a B.S. in Mathematics in December, 2001. He continued his studies at the University of Missouri-Columbia, receiving a M.S. in Nuclear Engineering with an emphasis in Medical Physics in December, 2003. He performed the research for his Masters degree at the University of Missouri Research Reactor (MURR). Upon completion of his Masters study, he remained at the University of Missouri and started the work that culminated in this thesis. During his doctoral studies, Andrew held a position as a mathematics instructor at Moberly Area Community College before obtaining funding in the form of a Department of Energy Nuclear Engineering and Health Physics Fellowship. He also completed a summer internship with the Nuclear Criticality Safety Group at BWX Technologies in 2004 and a practicum as a student researcher at Savannah River National Laboratory (SRNL) in 2005. In addition, he attended the inaugural World Nuclear University Summer Institute in Idaho Falls, Idaho in 2005. Andrew moved to Richland, WA in January, 2006 in order to complete the research for this thesis at Pacific Northwest National Laboratory (PNNL). He has chosen to remain in Richland after completing his Ph.D., having accepted a staff position at PNNL in the Radiomaterials Chemistry Group within the Environmental Technology Directorate.